Developing novel immunotherapeutic approaches to Pancreatic Ductal Adenocarcinoma (PDAC)

Giampiero Valenzano

Green Templeton College
University of Oxford

Thesis submitted for the degree of *Doctor of Philosophy* in *Cancer Science*

Michaelmas 2025

Supervisor

Professor Eric O'Neill (University of Oxford)

The work presented in this thesis was performed at the Department of Oncology, Old Road Campus Research Building, University of Oxford. This study was funded by Cancer Research UK through a Clinical Research Training Fellowship at the Oxford Cancer Centre. Additional funding was provided in part by Pancreatic Cancer UK.

To my husband Eddie

For showing me what love *really* is

ABSTRACT

Pancreatic ductal adenocarcinoma (PDAC) is a major clinical challenge due to late diagnosis, high metastatic potential, and resistance to conventional therapies. This thesis explores novel immunotherapeutic strategies aimed at improving outcomes in PDAC.

First, a multiparametric flow cytometry panel was developed to comprehensively profile immune alterations in pancreatic tumours and systemic compartments in a mouse model of disease. Using this and other tools, a subset of natural killer (NK) cells expressing markers of tissue retention was identified in mice receiving multimodal therapy; this subset might support anti-tumour immunity indirectly through T cell modulation. Subsequently, another combination regimen was investigated, comprising focal adhesion kinase (FAK) inhibition and T cell immunoreceptor with Ig and ITIM domains (TIGIT) blockade, which demonstrated trends towards enhanced survival and tumour control. Additionally, an *in vitro* protocol was established to generate cytotoxic NK cells expressing tissue retention markers, which successfully homed to pancreatic tissue *in vivo*, providing a potential strategy for adoptive NK cell transfer in pre-invasive or early-stage PDAC. Finally, using a different mouse model of disease with slower tumour development revealed progressive accumulation of innate and adaptive lymphocytes during early tumourigenesis. Collectively, these findings provide preliminary support for two conceptual shifts in PDAC immunotherapy that may inform future clinical studies: one towards NK-cell based therapies, and another towards early/preventative interventions.

ACKNOWLEDGEMENTS

I am not the biggest fan of the acknowledgements page in theses. It is not the concept of acknowledgements *per se* that I do not wholeheartedly espouse (quite the opposite, in fact), but rather the way some people use it as an excuse to hide them all there, in the hope that those mentioned will, someday, feel acknowledged. I'm more of a "shout it in their face" kind of guy and, as a result, the people named on this page will not be surprised to find themselves here. Yet, as the Latins would say, *repetita iuvant*.

As this is the only section of this thesis where I can treat myself to the luxury of saying pretty much whatever I most please, in the order that most makes sense in my head, I will start by thanking my family. I feel I owe them, since the day I got onto a plane for my first medical school interview in the UK in December 2013 and, upon landing, I opened my suitcase to find an electricity provider advertisement meticulously cut out from a magazine and even more meticulously slipped inside said suitcase.

"You are the energy we believe in"

And it could very well have said: "You are the energy we will blindly and passionately support over the next twelve years, despite not having the faintest clue about things like: why you turned down that offer from the UK medical school you'd so eagerly prepared for, why all your doctor friends are now working in hospitals while you're spending your days in a lab… unpaid, and what it is you actually do"—for all that it mattered.

To those wondering, I do have an answer to these questions. To the first: it was the naïve (and, in retrospect, utterly arrogant) conviction that I would only leave my country for Oxbridge—anything else would not be worth it. (This kind of naivety and arrogance can only be forgiven when you are 17.) To the second: it was the slightly less naïve (and, in retrospect, slightly less arrogant) conviction that I could actually make it into Oxbridge—if only I had mastered my flow cytometry and presentation skills (this kind of naivety and arrogance is what makes you relocate to Sweden for an unpaid lab internship fresh out of medical school). To the third: well, that is thoroughly discussed in the coming chapters.

Next on my acknowledgement list (and this is where I stop blabbering and do what more serious Oxford students do) is my supervisor, Eric. Thank you for allowing me to dive deeply and freely into the world of research, granting me permission to follow my relentless curiosity wherever it led, and for accompanying me on these journeys of discovery. Thank you for showing me that a supervisor can care about your life both inside and outside the lab, and for bestowing upon me your deepest trust whenever you introduced me as a “young medical oncologist” to the many, far more qualified scientists and clinicians I was fortunate to interact with over these three years.

Thanks to the unbelievably amazing people in the EON lab, including people whose paths diverged at one point or another (yes, Simei, you do come to mind before everyone else). I normally tend not to single people out, but I feel some people deserve extra credit; these are (in no specific order):

Ash, for his “coffee” trips; Tess, for the constant supply of hugs, sweets, and medicines; Shannon, for always and forever being my glamorous surgical assistant; Alice, for just being an icon-trailblazer-inspiration; and Keaton, for not laughing at me when, reviewing a CT scan of a mouse, I pointed at a grey outline and asked how the tumour could have implanted so high up in the chest (it was the heart).

Thanks to the other people in Oncology/RRI and the Green Building, including (again in no specific order): Pash, for the constant cheerleading; Chris, Magda, and Doug, for their help with mouse work; Tanusya and Berna, for their tips on NK cell culture; Brittany, for helping with cell transduction and sorting; and Hala, for the flow antibodies and cell irradiation. As is often said, sometimes it does indeed take a village.

Thanks to Sabrina, witness at my wedding and at my highest and lowest points in life, the one person I single-handedly have to thank for getting to the end of my DPhil (barely) healthy and intact. I know people often say, “I would not have made it without you,” but I truly mean it: I very simply would not have.

Thanks to Ricardo, for bearing with my “super busy” times with grace and kindness, without ever pointing out that there never were any times that were not “super busy.” You are tangible proof that the best people in Oxford do not actually attend Oxford University (there, I said it).

And lastly, thank you, Giulia and Carlo, for giving me not only a house but a home when I most needed one (and when would that be, if not during the final stretch of the write-up?), for always treating me like family, and for showing me the kind of grown-up I aspire to be.

Post scriptum

In a late edit of this section, I felt I must also extend my gratitude to: (I) the human sample donors, who agreed to donate parts of their bodies for the advancement of science; (II) the poor mice, who did not agree to donate parts of their bodies for the advancement of science but contributed greatly nevertheless; and (III) a renowned AI-powered language model, for clarifying my rambling first-draft thoughts so coherently that now every single sophisticated word in this thesis might look suspicious. I will never forgive you for taking away em dashes (my favourite punctuation mark since the dawn of time, certainly since before the dawn of yours). Years of passionate reading and academic writing courses to develop an elevated style of my own—made up of amidsts, amongsts, and wherebys—have brought me to a day when the style (never the content) of a beautifully written sentence might be mistaken for your own creation. A cost I will painfully have to accept, given that after all those years of reading and courses, I still cannot remember whether one should compare something *with* or *to* something else, and for that sort of thing you just nail it every time.

TABLE OF CONTENTS

LIST OF FIGURES

LIST OF TABLES

LIST OF ABBREVIATIONS

ADCC	Antibody-dependent cellular cytotoxicity
APC	Antigen presenting cell
BaEV	Baboon endogenous virus
BSA	Bovine serum albumin
CAF	Cancer-associated fibroblast
CCL5	C–C motif chemokine ligand
CCR5	C–C motif chemokine receptor 5
CD	Cluster of differentiation
cDC	Conventional dendritic cell
cDC1	Type 1 conventional dendritic cell
cDC2	Type 2 conventional dendritic cell
CFSE	Carboxyfluorescein succinimidyl ester
CI	Complexity index
CX3CR1	CX3C motif chemokine receptor 1
CXCL10	CXC motif chemokine ligand 10
CXCL16	CXC motif chemokine ligand 16
CXCR3	CXC motif chemokine receptor 3
CXCR6	CXC motif chemokine receptor 6
CTLA-4	Cytotoxic T lymphocyte antigen 4
DAPI	4',6-diamidino-2-phenylindole
DCM	Dead cell marker
DMEM	Dulbecco's Modified Eagle Medium
dMMR	Deficient mismatch repair
DNAM-1	DNAX Accessory Molecule-1
ECM	Extracellular matrix
EDTA	Ethylenediaminetetraacetic acid

ELISA	Enzyme-linked immunosorbent assay
EOMES	Eomesodermin
FAK	Focal adhesion kinase
FFPE	Formalin-fixed, paraffin-embedded
FBS	Foetal bovine serum
FlowSOM	Flow self-organising map
FMO	Fluorescence minus one
FOLFIRINOX	5-fluorouracil, leucovorin, irinotecan, oxaliplatin
FOXP3	Forkhead box P3
GEMM	Genetically engineered mouse model
GM-CSF	Granulocyte-Monocyte colony stimulating factor
Gy	Gray
GzmA	Granzyme A
GzmB	Granzyme B
GzmK	Granzyme K
HBBS	Hanks' balanced buffer solution
HEPES	4-(2-hydroxyethyl)-1-piperazineethanesulfonic acid
HLA	Human leukocyte antigen
HRP	Horseradish peroxidase
IDO	Indoleamine 2,3-dioxygenase
IHC	Immunohistochemistry
IL-12	Interleukin-12
IL-15	Interleukin-15
IL-18	Interleukin-18
IL-2	Interleukin-2
IL-21	Interleukin-21
ILC1	Type 1 innate lymphoid cell

ILC2	Type 2 innate lymphoid cell
ILC3	Type 3 innate lymphoid cell
IR	Irradiation
KC	*Pdx-1*-Cre;LSL-*Kras*$^{G12D/+}$
KLRG-1	Killer cell lectin-like receptor subfamily G member 1
KPC	LSL-*Kras*$^{G12D/+}$;LSL-*Trp53*$^{R172H/+}$;*Pdx-1*-Cre
MDSC	Myeloid-derived suppressor cell
MFI	Mean fluorescence intensity
mg	Milligram
MHC	Major histocompatibility complex
mL	Millilitre
mM	Millimolar
M-MDSC	Monocytic myeloid-derived suppressor cell
MRI	Magnetic resonance imaging
MSI-H	Microsatellite instability–high
NK	Natural killer
NKG2A	Natural Killer Group 2, member A
NKG2C	Natural Killer Group 2, member C
NKG2D	Natural Killer Group 2, member D
NKp46	Natural Killer Protein 46
NOD	Non obese diabetic
PanIN	Pancreatic intraepithelial neoplasia
PBMC	Peripheral blood mononuclear cell
PBS	Phosphate-buffered saline
PDAC	Pancreatic ductal adenocarcinoma
PEG300	Polyethylene glycol 300
PD-1	Programmed death protein 1

PD-L1	Programmed death ligand 1
PDX	Patient-derived xenograft
PMN-MDSC	Polymorphonuclear myeloid-derived suppressor cell
pNET	Pancreatic neuroendocrine tumour
RBC	Red blood cell
R2G2	Rag2/IL2RG double-knockout
RPMI	Roswell Park Memorial Institute 1640
ROI	Region of interest
SARRP	Small animal radiation research platform
SD	Standard deviation
SI	Similarity index
SIR	Stain index reduction
S1PR1	Sphingosine-1-phosphate receptor 1
TGF-β	Transforming growth factor beta
THL	Translational Histopathology Laboratory
TIGIT	T cell immunoreceptor with Ig and ITIM domains
TIM-3	T cell immunoglobulin and mucin-domain containing-3
TMB	3,3',5,5'-Tetramethylbenzidine
TME	Tumour microenvironment
TNF-α	Tumour necrosis factor α
Tp53	Tumour protein p53
TRAIL	TNF-related apoptosis-inducing ligand
Treg	Regulatory T cell
TRM	Tissue-resident memory T cell
trNK	Tissue-resident natural killer cell
µg	Microgram
µL	Microlitre

Chapter 1

Introduction

1.1

Pancreatic cancer

1.1.1 Classification

Pancreatic cancer is a highly heterogeneous disease that encompasses a spectrum of malignant neoplasms arising from both the exocrine and endocrine components of the pancreas. The vast majority of cases (approximately 90%) are pancreatic ductal adenocarcinomas (PDACs), which originate from the exocrine epithelium of the pancreatic ducts (Kamisawa et al. 2016). PDAC (often referred to simply as pancreatic cancer) is an invasive carcinoma with irregular glandular architecture, characterised by a propensity for early invasion and frequent vascular or perineural invasion. Based on the degree of glandular differentiation, PDAC is commonly graded as well- (G1), moderately- (G2), or poorly-differentiated (G3) (Garcia et al. 2013).

An inconspicuous proportion of cases of pancreatic cancer are caused by pancreatic neuroendocrine tumours (pNETs) (Halfdanarson et al. 2008). These neoplasms arise from the endocrine islets of Langerhans and therefore secrete hormones such as insulin, glucagon, and somatostatin. These neoplasms are biologically and clinically distinct from PDAC, often displaying a more indolent course, though aggressive variants exist.

Whereas most pNETs develop sporadically, several hereditary cancer syndromes have been described that predispose to their development, including Multiple Endocrine Neoplasia type 1, von Hippel-Lindau disease, neurofibromatosis type 1, and tuberous sclerosis (Falconi et al. 2016).

Other, rarer exocrine malignancies exist, including the cystic tumours of the pancreas, a group that comprise both benign and malignant entities (Karoumpalis and Christodoulou 2016). The presence of cystic pancreatic lesions has also been associated with hereditary cancer syndromes.

1.1.2 Aetiology and epidemiology

Pancreatic cancer is one of the deadliest malignancies worldwide, with a 5-year overall survival rate of less than 10% and a median survival of approximately 4 months (Rawla et al. 2019). Global incidence is estimated at around 495,000 new cases per year, corresponding to roughly 2.6% of all cancers, while mortality approaches 466,000 deaths per year, highlighting the exceptionally high fatality rate of this disease (Sung et al. 2021). These figures are expected to rise, with pancreatic cancer projected to become the second deadliest malignancy by 2030, after lung cancer (Rahib et al. 2014).

The disease predominantly affects individuals over 65 years of age, with a median age at diagnosis of 70 years, and shows a mild male predominance (Ilic and Ilic 2016). Cigarette smoking remains the single most important modifiable risk factor, accounting for about 20-25% of cases and conferring a 2- to 3-fold increase in risk compared to non-smokers (Bosetti et al. 2012).

Excess alcohol consumption, obesity, and diets rich in processed meats and saturated fats have all been linked to an increased risk, likely through metabolic and inflammatory mechanisms (Genkinger et al. 2015; Naudin et al. 2025). The long-held belief that consumption of dairy products could increase risk has been disproven (Genkinger et al. 2014).

Chronic pancreatitis has been extensively studied as a predisposing condition for pancreatic cancer, and specifically for PDAC (Lowenfels et al. 1993). Multiple longitudinal cohort studies and meta-analyses have shown that individuals with chronic pancreatitis have a lifetime risk that is markedly increased (estimated between 5- and 20-fold higher than the general population), depending on duration and genetic predisposition (Krejs 2010; Kirkegård et al. 2017). The proposed mechanisms include nonspecific chronic inflammatory stress and repeated epithelial injury promoting neoplastic transformation of ductal cells. Acute pancreatitis has also been linked to PDAC; however, in patients with acute pancreatitis, the risk of pancreatic cancer peaks within the first 2 months following symptom onset, likely reflecting cases in which pancreatitis represents an early manifestation of an underlying early tumour. Thereafter, the risk declines progressively and approaches that of the general population approximately 10 years after diagnosis (Sadr-Azodi et al. 2018).

The relationship between diabetes mellitus and pancreatic cancer has long been controversial. In early reports, diabetes and impaired glucose tolerance were observed in 75% of patients with PDAC (Permert et al. 1993).

It is now accepted that, on the one hand, new-onset diabetes frequently represents a signpost of an early, occult pancreatic tumour, especially in adults older than 50 (Andersen et al. 2017; Khalaf and Ali 2022); on the other hand, long-standing type-2 diabetes is an ascertained risk factor conferring a nearly 2-fold increased risk, likely stemming from chronic inflammatory and metabolic derangements in the pancreas (Song et al. 2015).

Approximately 5-10% of all pancreatic cancers are hereditary. Germline mutations in *BRCA2*, *BRCA1*, *PALB2*, *ATM*, *CDKN2A*, *MLH1*, *MSH2*, *MSH6*, and *STK11* contribute to familial predisposition and account for the increased risk observed in syndromes such as Peutz–Jeghers and Lynch (Kastrinos et al. 2009; Korsse et al. 2013). Carriers of these mutations have gene-dependent lifetime risks in the range of 10-20%, which can rise when combined with environmental risk factors such as smoking or obesity.

1.1.3 Current standard of care

There are four recognised classes of PDAC, including resectable, borderline resectable, locally advanced/unresectable, and metastatic disease (Callery et al. 2009) (**Figure 1.1**).

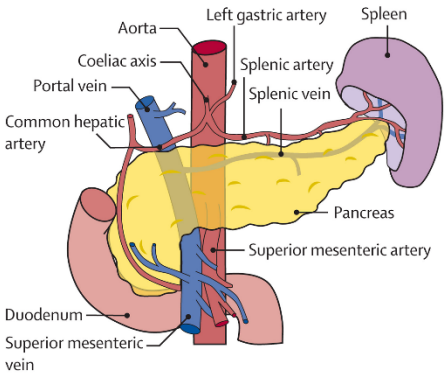

	Superior mesenteric artery	Coeliac axis	Common hepatic artery	Portomesenteric venous axis
Resectable	No involvement	No involvement	No involvement	≤180° contact without vein contour irregularity
Borderline resectable	≤180° contact	≤180° contact	Any contact without extension to CA or hepatic artery bifurcation*	≤180° contact with vein contour irregularity OR >180° contact without vein contour irregularity or thrombosis, but reconstructable OR Any contact with inferior vena cava
Locally advanced	>180° contact	>180° contact OR any contact of the CA with aortic involvement	Any contact with extension to CA and/or hepatic artery bifurcation	No reconstructable involvement due to tumour contact or occlusion (either due to tumour or bland thrombus)
Metastatic	Distant metastatic disease, regardless of vascular involvement of the primary tumour			

Figure 1.1 – PDAC classification based on resectability criteria
Resectability criteria introduced by the National Comprehensive Cancer Network (NCCN) guidelines (version 2.2024) and later updated by Callery et al. Reproduced with permission from *Stoop et al., Lancet, 2025 (Figure 1) – Licence Number 6140790078935*.

About 60% of cases are already metastatic at presentation (L. Huang et al. 2019), with only a minority of patients (approximately 15-20%) presenting with resectable tumours at diagnosis, largely due to the combination of three factors: (I) the absence of an effective screening programme, (II) the lack of sensitive and specific biomarkers for early detection, and (III) the slow and insidious development of symptoms, a consequence of the pancreas' deep retroperitoneal location. Early manifestations such as weight loss, abdominal or back pain, new-onset diabetes, or neuropsychiatric symptoms are vague and rarely lead to prompt diagnosis (**Figure 1.2**). More recognisable symptoms like jaundice usually indicate involvement of the biliary tract and therefore locally advanced disease.

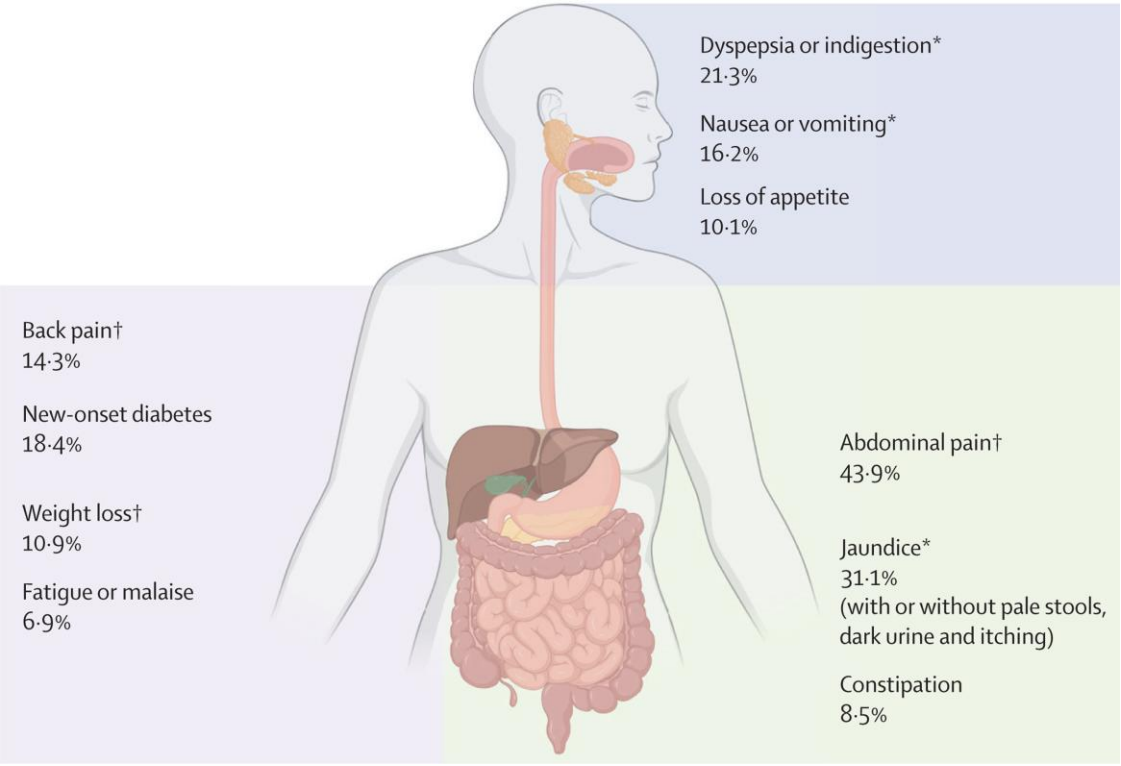

Figure 1.2 – PDAC symptoms by district involved
Blue: upper gastrointestinal tract; green: lower gastrointestinal tract; indigo: systemic manifestations. Reproduced with permission from *Stoop et al., Lancet, 2025 (Figure 3) – Licence Number 6140790078935*.

For resectable PDAC, surgical resection with curative intent remains the mainstay of treatment (T. Conroy et al. 2023), typically via pancreatoduodenectomy (also known as Whipple procedure) for cancer of the head, or distal pancreatectomy for cancer of the neck or tail. Surgery is invariably followed by adjuvant chemotherapy, which consists of FOLFIRINOX (5-fluorouracil, leucovorin, irinotecan, oxaliplatin) for fit patients, and gemcitabine/capecitabine for older/unfit patients (**Figure 1.3**).

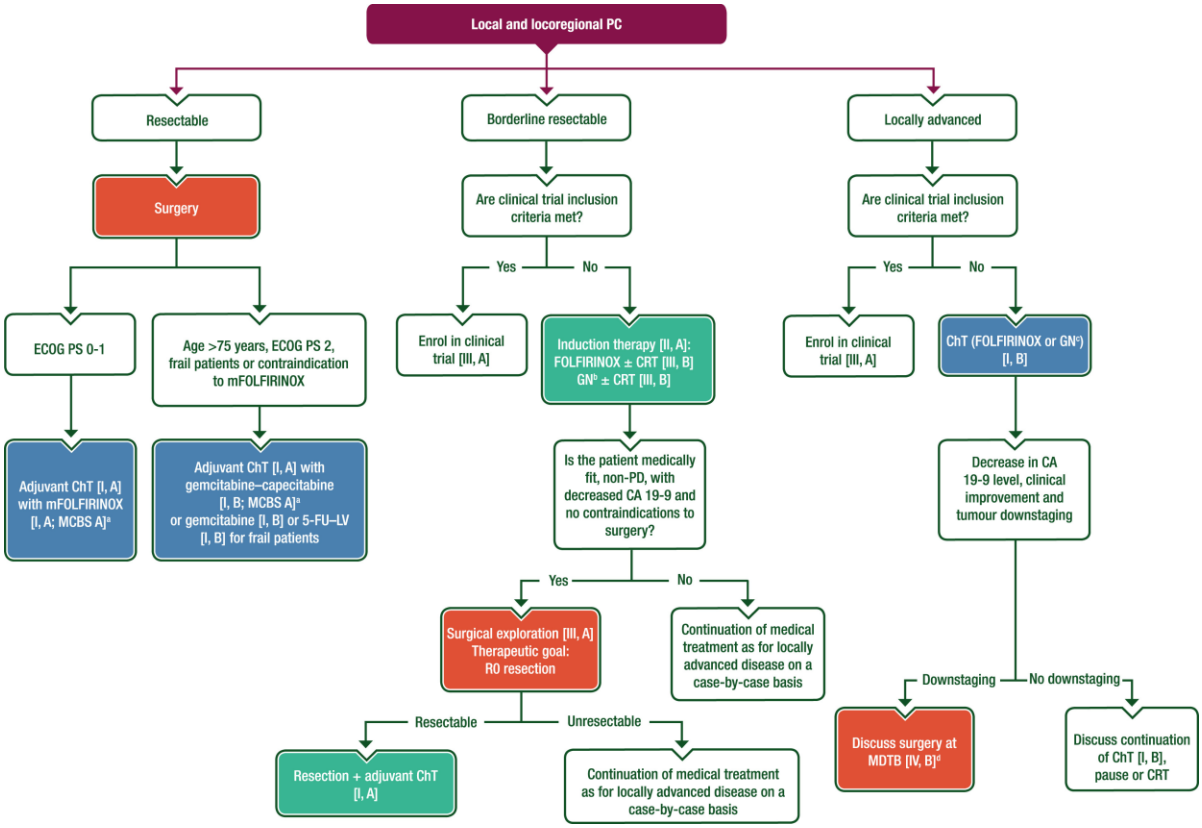

Figure 1.3 - Treatment for local and locoregional pancreatic cancer

European Society for Medical Oncology (ESMO) Clinical Practice Guidelines. Orange: surgery; blue: systemic anticancer therapy; green: combination of treatments; white: other aspects of management. 5-FU, 5-fluorouracil; CA 19-9, carbohydrate antigen 19-9; ChT, chemotherapy; CRT, chemoradiotherapy; ECOG, Eastern Cooperative Oncology Group; FOLFIRINOX, leucovorin–5-fluorouracil–irinotecan–oxaliplatin; GN, gemcitabine–nab-paclitaxel; LV, leucovorin; MCBS, ESMO-Magnitude of Clinical Benefit Scale; MDTB, multidisciplinary tumour board; mFOLFIRINOX, modified FOLFIRINOX; PC, pancreatic cancer; PD, progressive disease; PS, performance status; R0, no tumour at the margin. Reproduced with permission from *Conroy et al., Annals of Oncology, 2023 (Figure 2) – Licence Number 6141360176423*.

In borderline resectable cases, i.e., those patients where vascular involvement precludes upfront surgery, neoadjuvant chemotherapy (commonly FOLFIRINOX or gemcitabine/nab-paclitaxel) is employed to downstage the tumour, followed by surgery as above in patients who respond well to treatment. For locally advanced (unresectable) or metastatic PDAC, treatment is palliative, with systemic chemotherapy

(FOLFIRINOX or gemcitabine plus nab-paclitaxel) aimed at prolonging survival and maintaining quality of life (**Figure 1.4**). Chemoradiation and enrolment in clinical trials are also options that may be offered to selected patients.

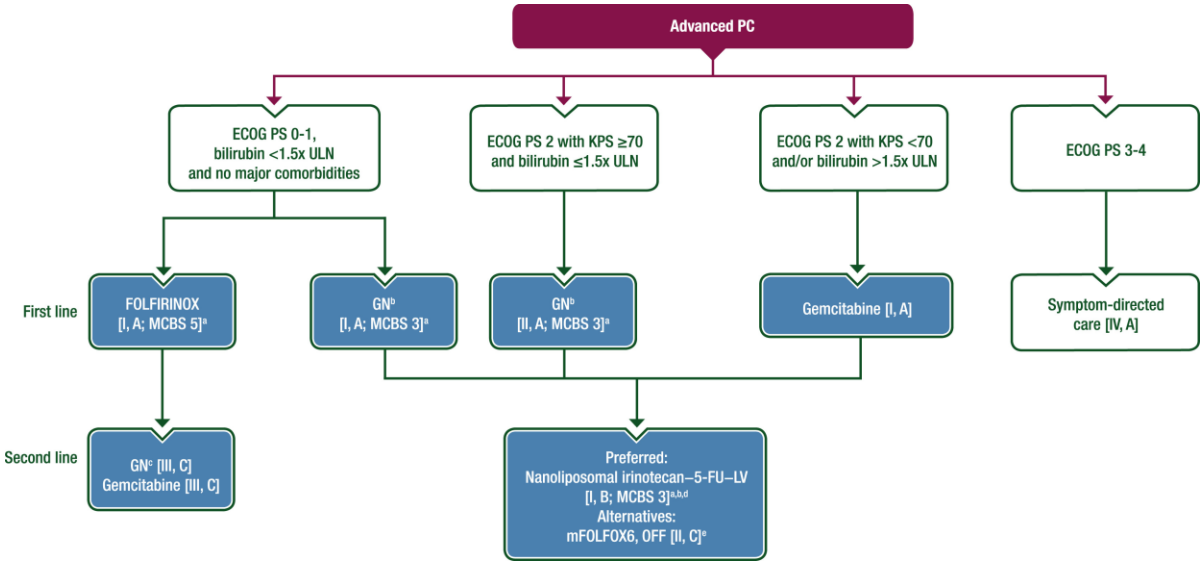

Figure 1.4 – Treatment for advanced or metastatic pancreatic cancer
European Society for Medical Oncology (ESMO) Clinical Practice Guidelines. Blue: systemic anticancer therapy; white: other aspects of management. 5-FU, 5-fluorouracil; ECOG, Eastern Cooperative Oncology Group; FOLFIRINOX, leucovorin–5-fluorouracil–irinotecan–oxaliplatin; GN, gemcitabine–nab-paclitaxel; KPS, Karnofsky performance status; MCBS, ESMO-Magnitude of Clinical Benefit Scale; LV, leucovorin; mFOLFOX6, modified leucovorin–5-fluorouracil–oxaliplatin; OFF, oxaliplatin–fluorouracil–leucovorin; PC, pancreatic cancer; PS, performance status; ULN, upper limit of normal. Reproduced with permission from *Conroy et al., Annals of Oncology, 2023 (Figure 3) – Licence Number 6141360176423*.

1.1.4 Immunotherapy

In the context of cancer, immunotherapy refers to the use of therapeutic agents that enhance or restore the immune system's capacity to recognise and eliminate malignant cells. Unlike conventional cytotoxic therapies that directly (and often non-selectively) block cancer proliferation,

immunotherapies modulate cellular and/or soluble components of the immune response to cancer cells.

Immune checkpoint inhibition is an immunotherapeutic strategy that releases inhibitory brakes on anti-tumour immune responses by blocking receptor–ligand interactions that normally restrain immune effector cells (Pardoll 2012). These receptors are expressed on a variety of immune cells—notably, but not exclusively, $CD8^+$ T cells, $CD4^+$ T cells, and natural killer (NK) cells—and engage ligands expressed on tumour cells and stromal cells. When engaged, these interactions dampen effector cell activity, thereby blunting anti-tumour immunity.

Checkpoint inhibitors currently in clinical use are monoclonal antibodies targeting either checkpoint receptors, such as nivolumab (Brahmer et al. 2012) and pembrolizumab (Reck et al. 2016), which target Programmed death protein 1 (PD-1), and ipilimumab (Hodi et al. 2010), which targets Cytotoxic T-lymphocyte antigen 4 (CTLA-4), or their ligands, such as atezolizumab (Rittmeyer et al. 2017) and durvalumab (Antonia et al. 2017), which target Programmed death ligand 1 (PD-L1). Additional inhibitory receptors, including T cell immunoreceptor with Ig and ITIM domains (TIGIT) and T cell immunoglobulin and mucin-domain containing-3 (TIM-3), are under active clinical investigation as targets for checkpoint blockade (Cho et al. 2022; Gutierrez et al. 2025).

The only approved immune checkpoint inhibitor for PDAC is the anti–PD-1 antibody pembrolizumab, which may be offered exclusively to patients with metastatic, microsatellite instability-high (MSI-H) or mismatch repair–deficient (dMMR) cancer (less than 1% of cases), and only as a second- or later line of therapy (**Figure 1.5**). In all other settings, both single- (Royal et al. 2010; Brahmer et al. 2012; Herbst et al. 2014) and dual (O'Reilly et al. 2019) checkpoint blockade have invariably led to failure of obtaining objective responses.

Combining immune checkpoint blockade with other therapies (such as neoadjuvant chemotherapy, transforming growth factor β, TGF-β, inhibition, or stroma-targeted approaches) has produced objective responses of only 5-20% and a median overall survival rate of less than 9 months (Aglietta et al. 2014; Weiss et al. 2017; Melisi et al. 2019; Kamath et al. 2020; Wang-Gillam et al. 2022). Some trials were discontinued due to lack of clinical benefit (Zhen et al. 2022; Renouf et al. 2022). Comparable response rates were registered in trials of immune checkpoint blockade combined with radiotherapy (Xie et al. 2020; Parikh et al. 2021).

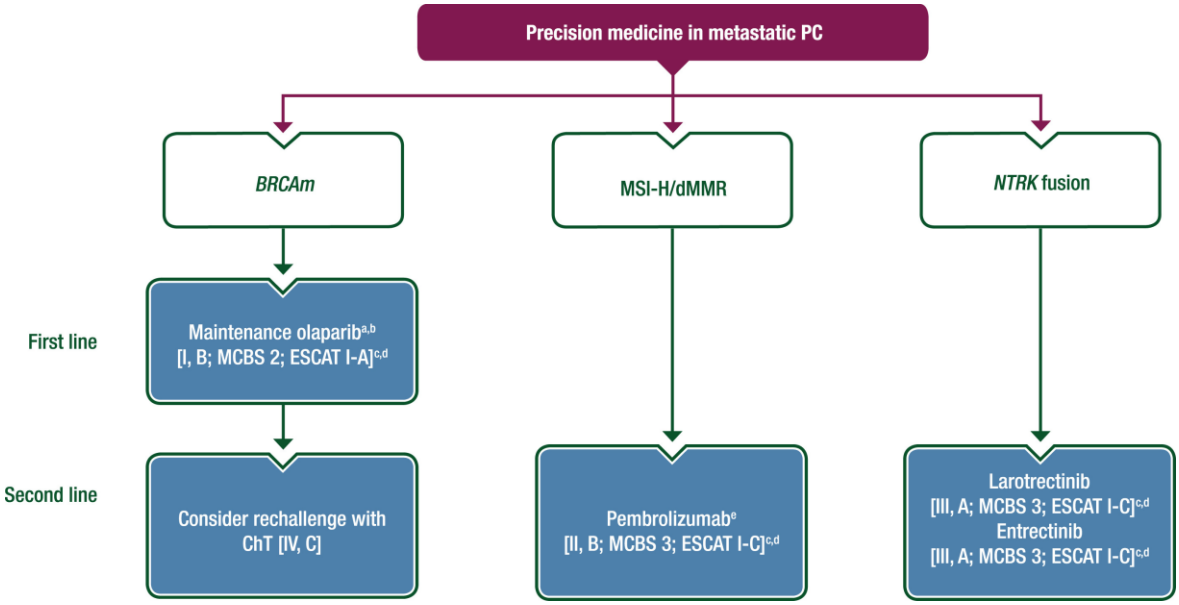

Figure 1.5 – Treatment options for pancreatic cancer patients with metastatic disease and actionable genomic alterations

Blue: systemic anticancer therapy; white: other aspects of management. ChT, chemotherapy; dMMR, mismatch repair deficient; MCBS, ESMO-Magnitude of Clinical Benefit Scale; MSI-H, microsatellite instability-high; m, mutated; PC, pancreatic cancer. Reproduced with permission from *Conroy et al., Annals of Oncology, 2023 (Figure 4) – Licence Number 6141360176423*.

Cancer vaccines represent another paradigm of immunotherapy. Akin to vaccines for infectious diseases, cancer vaccines work by specifically inducing or enhancing tumour-specific $CD8^+$ T cell responses through the presentation of antigens to the immune system (Saxena et al. 2021). Tumour antigens may be either normal peptide sequences that are abnormally expressed or overexpressed in tumours, or neoantigens, i.e., novel peptide sequences generated as a result of somatic mutations and therefore absent from normal tissues (Z. Hu et al. 2018). Vaccination relies on antigen presentation by dendritic cells, which process antigens and present antigenic peptides to naïve $CD8^+$ T cells, resulting in the formation of effector and long-lived, tumour-specific memory T cells (J. Banchereau and Steinman 1998). Vaccine strategies include peptide-based vaccines, which

deliver immunogenic peptides derived from tumour antigens (Schneble et al. 2014); nucleic acid vaccines (DNA or RNA), which encode tumour antigens for in situ expression (Weber et al. 2024); vector-based vaccines, which rely on viral delivery of tumour antigens (Gatti-Mays et al. 2020); and dendritic cell vaccines, in which patient-derived dendritic cells are loaded with tumour antigens *ex vivo* before reinfusion (Kantoff et al. 2010).

In PDAC, the GVAX therapeutic vaccine was tested, in which granulocyte-monocyte colony-stimulating factor (GM-CSF) secretion by irradiated allogeneic pancreatic cancer cells promotes recruitment of dendritic cells and $CD8^+$ T cell responses against tumour-associated antigens, including mesothelin (Jaffee et al. 2001). Whereas initial testing in the adjuvant setting in patients with resectable pancreatic cancer yielded overall survival of up to 24 months (Eric et al. 2011), subsequent trials in patients with advanced disease produced much more disappointing results (Le et al. 2019).

More recently, a much more promising individualised neoantigen vaccine with mRNA–lipoplex nanoparticles has received particular attention as, when combined with adjuvant atezolizumab and FOLFIRINOX, it was able to prevent recurrences in half of the enrolled patients at a median extended follow-up of 3.2 years after surgical resection. Importantly, in responders ($n = 8$), the expansion of neoantigen-specific $CD8^+$ T cells was observed with an average estimated lifespan of 7.7 years (range 1.5 to roughly 100 years), and some clones were predicted to have lifespans that may outlive hosts (Sethna et al. 2025).

A third immunotherapeutic strategy is adoptive cell transfer, which refers to the infusion of autologous or allogeneic effector cells after *ex vivo* expansion, activation, and, frequently, genetic manipulation to enhance functionality or overcome inhibitory signals (Rosenberg et al. 2008; Laskowski et al. 2022). The fundamental principle of adoptive cell transfer is to provide a large quantity of tumour-reactive immune cells capable of mediating tumour destruction. While this approach has been evaluated in PDAC both preclinically (S. Hu et al. 2019; Biegert et al. 2025; Dai et al. 2025) and clinically (Beatty et al. 2017; Yang Liu et al. 2020; Arya et al. 2024), the results have generally not been promising (Aznar et al. 2025), and, to the present date, no cellular immunotherapies are approved for PDAC.

There are several reasons why immunotherapy in PDAC has not gained the same momentum as in other malignancies (Hodi et al. 2010; Robert et al. 2015; Reck et al. 2016; Neelapu et al. 2017; Maude et al. 2018). Firstly, compared with cancers such as melanoma or lung cancer, which are characterised by a high tumour mutational burden and consequently produce a high number of neoantigens to elicit efficient $CD8^+$ T cell responses, the prevalence of somatic mutations in PDAC is considerably lower and comparable to that of paediatric malignancies (**Figure 1.6**).

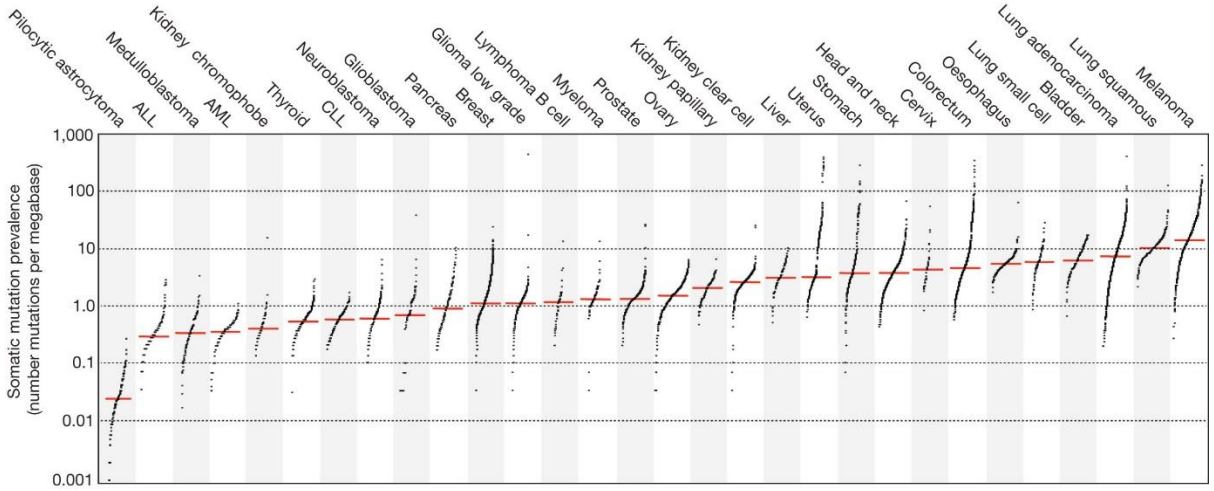

Figure 1.6 – Prevalence of somatic mutations across cancer types
Every dot represents a sample whereas the red horizontal lines are the median numbers of mutations in the respective cancer types. The vertical axis (log scaled) shows the number of mutations per megabase whereas the different cancer types are ordered on the horizontal axis based on their median numbers of somatic mutations. Reproduced with permission from *Alexandrov et al., Nature, 2013 (Figure 1) – Licence Number 6140880663561*.

Studies have consistently shown that vast majority of pancreatic tumours exhibit what can be defined as an *immune-excluded* or *immune-desert* phenotype, with only a small minority classified as *immune-inflamed* (Mi et al. 2022). This terminology refers to the framework proposed by Chen and Mellman, which links the type and spatial distribution of immune cells (and CD4/CD8$^+$ T cells in particular) within the tumour microenvironment (TME) to the probability of immunotherapy success (D. S. Chen and Mellman 2017). In a recent study, 9.9% of PDAC samples were classified as immune-inflamed, 85.2% as immune-excluded, and 4.9% as immune-desert (Kim et al. 2025). In addition to the paucity of T cells, loss of expression of MHC class I and other proteins of the antigen-presenting machinery are well-documented phenomena in PDAC (Pandha et al. 2007; Yamamoto et al. 2020), further contributing to the lack of effective immune responses.

Secondly, while effector T cells are scarce, regulatory T cells (Tregs) and myeloid-derived suppressor cells (MDSCs) are abundant, creating a profoundly immunosuppressive TME, which inhibits activation and effector functions of those few T cells that are able to infiltrate it (Hiraoka et al. 2006; Pylayeva-Gupta et al. 2012; Trovato et al. 2019). Both these subsets have been shown to negatively correlate with survival in large meta-analyses (Ai et al. 2018; Camerlingo 2022). A similar negative correlation has also been observed for immunosuppressive tumour-associated macrophages (Yu et al. 2019), whose density increases with progression to invasive cancer (Clark et al. 2007). The role of other cell types in PDAC development and resistance to immunotherapy is comparatively less well studied. B cells, for example, have only recently been shown to act as professional APCs in pancreatic cancer (Sivakumar et al. 2021), but their numbers in the TME remain generally low.

Finally, pancreatic cancer is characterised by the densest stroma of all solid cancers, with up to 90% of the tumour volume being composed of the so-called *desmoplastic reaction* (Phillips 2012): activated myofibroblasts, extracellular matrix proteins, and collagen fibres, which create a physical barrier to lymphocyte infiltration and hinder immune cell trafficking into the tumour core (Bolm et al. 2017) (**Figure 1.7**).

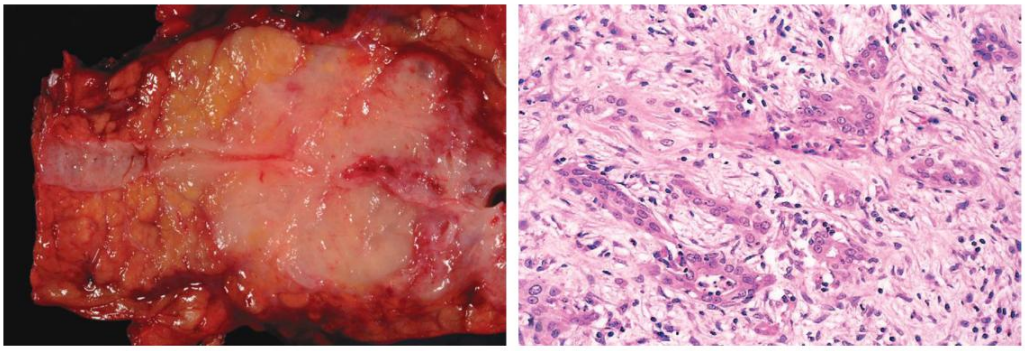

Figure 1.7 – Macroscopic and microscopic appearance of PDAC
Left: because of the high inherent invasiveness and extensive desmoplasia, adenocarcinomas of the pancreas appear macroscopically as hard, grey-white, poorly defined masses. Right: histologically, poorly-defined glandular structures can be seen embedded by the surrounding desmoplastic stroma. Reproduced with permission from *Robbins and Cotran Pathologic Basis of Disease, 9th Edition, Kumar, Abbas, Aster (Chapter 19 - The pancreas, Figure 19-13) – Licence Number 1668326-1*.

Therapeutic strategies that target the highly desmoplastic stroma can be broadly classified into two categories (Polani et al. 2021): approaches aimed at actively degrading already established stroma, such as the use of collagenases (Zinger et al. 2019) or hyaluronidases (Zhen et al. 2022b), and approaches designed to prevent the formation of new stroma, such as inhibitors of focal adhesion kinase (FAK), which prevent extracellular matrix (ECM) deposition by cancer-associated fibroblasts (CAFs) (Zaghdoudi et al. 2020). It should be noted that, given the expression of FAK on other cell types—including myeloid cells and tumour cells themselves—disruption of FAK signalling exerts multiple effects beyond ECM deposition. These broader effects are discussed in greater detail in Chapter 5.

In summary, three factors (low antigenicity, profound immunosuppression, and stromal desmoplasia) explain why immunotherapy has, so far, shown limited success in PDAC, and why novel approaches are needed.

1.2

Mouse models of Pancreatic Ductal Adenocarcinoma (PDAC)

1.2.1 Genetically engineered mouse models

Mouse models continue to be essential in immuno-oncology research for their capacity to accurately mimic the complex interplay between tumours and the immune system. Generally speaking, mouse models include chemically induced models, patient-derived xenografts (PDXs), genetically engineered mouse models (GEMMs), and syngeneic implantation models. In models of chemical induction, a carcinogen is administered to the animal to initiate tumourigenesis. While PDAC has successfully been induced in the Syrian hamster using a single administration of the mutagen N-nitrosobis(2-oxopropyl)amine (Pour et al. 1977), efforts to replicate PDAC development in mice or rats has been unsuccessful so far, likely as a result of differences in expression of drug-metabolising enzymes across the three species (Ulrich et al. 2002). PDXs, created by transplanting human tumour tissue into immunodeficient mice, preserve key genomic and structural characteristics of the original tumour, enabling investigations into patient-specific drug responses and molecular targets (Yihan Liu et al. 2023). However, the lack of an intact immune system in recipient mice enormously restricts their use for studying anti-tumour immunity (Pham et al. 2021). As a consequence, neither chemically induced models nor PDXs are widely employed for studies in immunity to pancreatic cancer.

GEMMs offer the ability to examine the interactions between immune and cancer cells all the way from tumour initiation to progression and metastasis, establishing them as a cornerstone of immuno-oncology research (Kersten et al. 2017). Amongst GEMMs that faithfully recapitulate the development of pancreatic cancer in humans, the *Pdx-1*-Cre; LSL-*Kras*$^{G12D/+}$ GEMM (Hingorani et al. 2003) exploits Cre recombinase to conditionally express *Kras*^{G12D}, found in over 90% of all pancreatic malignancies (Hilgers and Kern 1999; Almoguera et al. 1988; X. Wang et al. 2011). This model (also known as the KC model) is characterised by an age-dependent increase in lesion progression and allows the monitoring of precursor lesions, known in humans as pancreatic intraepithelial neoplasias (PanINs). The time to invasive cancer development is approximately 9-12 months, and median survival is 16 months. The two main limitations of this model are its relatively long latency for lesion development, which makes long-term studies necessary, and the fact that animals occasionally develop additional tumours, including mucocutaneous papillomas and hyperplastic polyps of the duodenum.

Two years after the description of the KC GEMM, Hingorani et al. developed a subsequent model with concomitant expression of *Trp53*^{R172H} and *Kras*^{G12D} (Hingorani et al. 2005). The generation of this model was similar to that of the KC GEMM: activation of both oncogenic Kras and Tp53 was restricted to the pancreas through cross-breeding with *Pdx-1*-Cre transgenic mice. The LSL-*Kras*$^{G12D/+}$*;*LSL-*Trp53*$^{R172H/+}$*;Pdx-1*-Cre model (also known as KPC) better recapitulates the invasive and widely metastatic phenotype of human

disease, where *TP53* mutation is a late event in tumourigenesis, found in around 75% of malignancies (**Figure 1.8**). Here, the time to tumour development is approximately 2 months, and overall survival is 5-6 months. Some KPC mice, too, can develop extra-pancreatic papillomas.

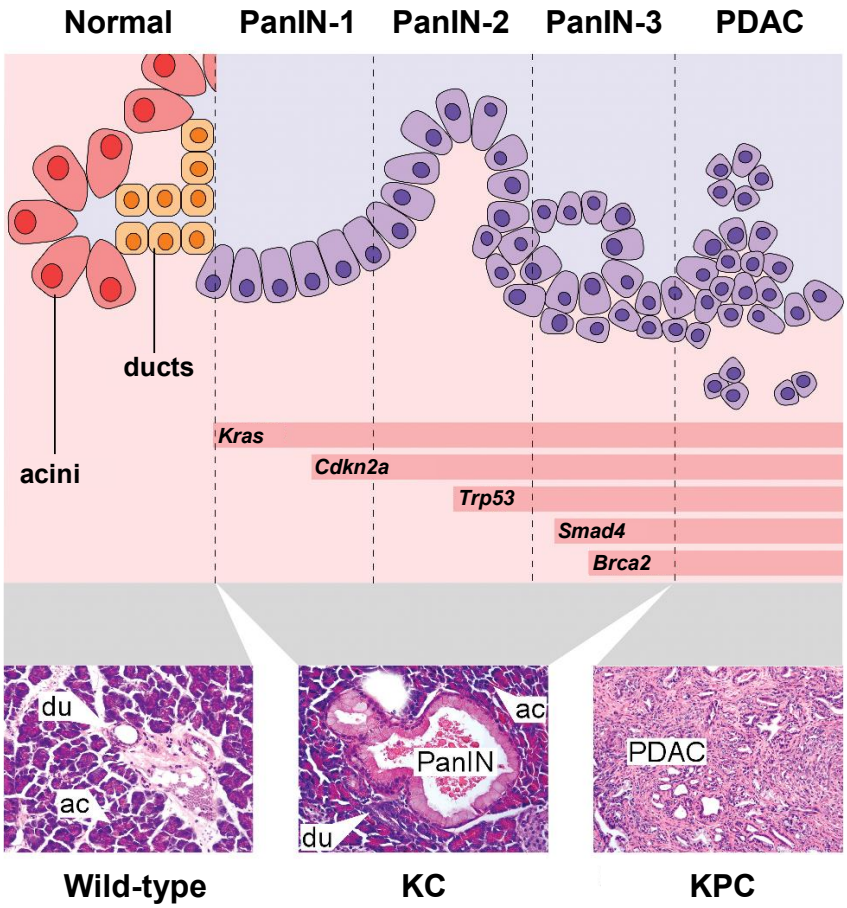

Figure 1.8 – *Kras* and *Trp53* mutations in pancreatic tumourigenesis
Top: schematic representation of normal exocrine pancreas cells, transitioning from left to right into increasingly dysplastic PanIN and PDAC. In addition to visible abnormalities including papillary morphology, loss of polarity, nuclear atypia, intraluminal budding, and stromal invasion, PanIN-to-PDAC progression in mice and humans is associated with accumulation of genetic lesions including activation of *Kras* and loss of tumour suppressor genes including *Cdkn2a*, *Trp53*, *Smad4*, and *Brca2*. Bottom: haematoxylin-and-eosin–stained sections of mouse pancreata of indicated genotypes, illustrating normal acinar (ac) and duct (du) cells as well as an early-stage PanIN lesion and advanced PDAC. PanIN: pancreatic intraepithelial neoplasia; PDAC: pancreatic ductal adenocarcinoma. Freely adapted with permission from *Murtaugh et al., Toxicology Pathology, 2013 (Figure 1) – Licence Number 6140960640309*.

1.2.2 Tumour implantation models

In contrast to GEMMs, where tumours develop spontaneously as a result of defined driver mutations, syngeneic implantation models necessitate the introduction of cancer cells into immunocompetent mice. These models present some advantages over GEMMs, providing reproducible, highly standardised platforms with a much shorter latency for tumour formation. This facilitates mechanistic studies of anti-cancer immunity and assessment of therapeutic interventions (including immunotherapeutic interventions). Their reproducibility and the possibility to interrogate anti-tumour immune responses in immunocompetent hosts have led to their widespread use in immuno-oncology research.

Tumour cells can be administered either orthotopically (i.e., into the tissue of origin of the implanted cell line), or subcutaneously, into the flank of the animal (Qiu and Su 2013). For pancreatic cancer, orthotopic implantation typically occurs in the tail of the pancreas. The procedure is technically demanding, requiring a laparotomy and fine manual technique. Potential complications include haemorrhage, infection, and unintended spread of tumour cells within the peritoneal cavity. Although rare, tumour engraftment may occasionally fail, owing to insufficient cell numbers, poor viability, or rapid immune-mediated clearance. Additionally, monitoring tumour growth is more challenging, as calliper measurements are poorly suited to the measurement of intraabdominal tumours, and serial imaging, such as ultrasound or magnetic resonance imaging, is required. Nevertheless, orthotopic models are preferred when studying the TME because they retain

the features of tumours arising in their native anatomical context, including infiltration by immune populations with tissue-specific tropism, which may be absent or reduced in subcutaneous sites (Guerin et al. 2020). Orthotopic pancreatic tumours also metastasise in a pattern resembling human disease (Killion et al., 1998), enabling the study of immune composition and response to therapy in metastatic settings (Hiroshima et al. 2016; Fernandez et al. 2023).

Subcutaneous implantation, on the other hand, involves injecting a syngeneic cancer cell line into the flank. These tumours more poorly recapitulate human disease, particularly in terms of TME composition and metastatic behaviour. However, subcutaneous models offer practical advantages: they are technically straightforward, requiring only a simple injection, and tumour growth can be monitored easily using callipers. Despite their limitations, these models are widely employed because they provide a reproducible and accessible platform for evaluating immune responses *in vivo*, complementing orthotopic and GEMM approaches.

In pancreatic cancer, orthotopic and subcutaneous tumour models exhibit different composition, growth kinetics, and response to therapy, including chemotherapy (Erstad et al. 2018), further highlighting the need to carefully select the most appropriate model for the research question to be addressed.

1.3

Natural killer (NK) cells

1.5.1 NK cells in mice and humans

NK cells were first described in 1975 as cytotoxic lymphocytes that kill tumour cells without prior sensitisation (Kiessling, Klein, and Wigzell 1975; Kiessling, Klein, Pross, et al. 1975; Herberman et al. 1975). Since their discovery, NK cells have traditionally been defined in humans as $CD3^{-}CD19^{-}CD56^{+}$ lymphocytes, with the $CD56^{dim}CD16^{+}$ subset making up 90% of circulating NK cells, and the $CD56^{bright}CD16^{-/dim}$ comprising the remaining 10% (Lanier et al. 1986). This phenotypic dichotomy was later demonstrated to reflect functional heterogeneity amongst NK cells, with $CD56^{bright}$ NK cells being more proficient producers of immunoregulatory cytokines, in contrast to the predominantly cytotoxic $CD56^{dim}$ subset (M. A. Cooper et al. 2001).

Because mouse NK cells do not express CD56, comparable murine subsets have been difficult to identify. In mice, NK cells can be detected using NK1.1, Natural Killer Protein 46 (NKp46), or CD49b (Cossarizza et al. 2021). NK1.1, encoded by *Klrb1c*, is expressed in C57BL/6J but not in BALB/c mice (Appasamy et al. 1996); its closest human ortholog, CD161 (encoded by *KLRB1*), shares 46% amino acid sequence homology with NK1.1, is only expressed on a fraction of NK cells and T cells, and, contrary to NK1.1, acts as an inhibitory receptor (Lanier et al. 1994). NKp46, encoded by *Ncr1*, is considered a better cross-species NK marker, as it is expressed in most mouse strains, in humans, and other mammals (Walzer, Bléry, et al. 2007);

however, its expression is not restricted to NK cells and subsets of NKp46^{+} T and innate lymphoid cells (ILCs) have been described in mice and humans (Walzer, Bléry, et al. 2007; Walzer, Jaeger, et al. 2007). CD49b (encoded by *Itga2*) is another suitable marker, typically used in NK1.1^{-} mouse strains (Arase et al. 2001).

1.5.2 Circulating and tissue-resident NK cells

Whereas NK cells were first described as circulating lymphocytes, tissue-resident subsets of NK cells have been described in a number of organs in both humans and mice. Tissue-resident NK (trNK) cells were first described in the mouse liver as CD49a^{+} cells (Peng et al. 2013). Liver trNK cells were proven to be tissue-resident through elegant parabiosis experiments and shown to differ phenotypically from their circulating counterparts in the liver, spleen, and bone marrow, being larger, more granular, and more immature (CD27^{+}CD11b^{low}). While conventional (circulating) NK cells at these sites expressed CD49b but lacked expression of CD49a, liver trNK cells expressed CD49a but lacked expression of CD49b. In addition, liver trNK cells expressed high levels of CD69, CXCR6, CXCR3, and LAG-3, and low levels of Eomes (Peng et al. 2013).

Similar subsets of trNK cells expressing CD49a and/or CD69 were subsequently described in the mouse skin, kidney, and uterus; these cells were also shown to be non-recirculating through parabiosis experiments (Sojka et al. 2014; Victorino et al. 2015). As a result, CD49a and CD69 have been widely used as markers of tissue residency. CD49a (also known as

integrin α1β1) binds to collagen type IV (and, to a lesser extent, collagen type I, III, and VI) in the basement membrane, providing physical anchorage to NK cells (A. I. Roberts et al. 1999). In contrast, CD69 promotes tissue retention by antagonising sphingosine-1-phosphate receptor–mediated migration towards blood or lymph. Sphingosine-1-phosphate-receptor 1 (S1PR1) is expressed on lymphocytes and promotes tissue egress following a sphingosine-1-phosphate gradient; CD69 physically associates with S1PR1 and promotes its internalisation and degradation, thereby blocking tissue egress (Shiow et al. 2006).

Around the same time that trNK cells were being characterised, tissue-resident populations of other lymphocytes, including $CD8^+$ T cells and type 1 innate lymphoid cells (ILC1s), were also described and found to express the residency marker CD103 (Gebhardt et al. 2009; Mackay et al. 2012; Fuchs et al. 2013). CD103 (also known as integrin αEβ7) binds E-cadherin at epithelial sites (Cepek et al. 1994), anchoring NK cells and other lymphocytes in place, and is preferentially expressed by intraepithelial lymphocytes in the skin and gastrointestinal tract (Pauls et al. 2001; Mueller and Mackay 2016; Hoffmann and Schön 2021). As a result, CD103 has also been widely used as a marker of tissue residency.

CD69 expression was shown to be dispensable for the establishment and maintenance of tissue residency in certain contexts, at least for $CD8^+$ T cells (Walsh et al. 2019). Moreover, CD69 is transiently upregulated on circulating T and NK cells following activation (Santis et al. 1992; Borrego et al. 1993),

which may confound its interpretation as a marker of tissue residency. This underscores the importance of distinguishing between a tissue-resident phenotype and true tissue residency: although techniques such as flow cytometry can detect surface expression of traditional tissue residency markers (e.g., CD69, CD49a, and CD103), definitive verification that these cells do not recirculate requires parabiosis studies or newer approaches, such as *in vivo* CD45 labelling (Anderson et al. 2014).

Following the initial reports in mice, NK cells expressing markers of tissue residency have been identified in multiple human solid organs, including the lung (Carrega et al. 2008; Marquardt et al. 2015; G. E. Cooper et al. 2018; Marquardt et al. 2019; Brownlie et al. 2021), skin (Torcellan et al. 2024), liver (Lunemann et al. 2017), uterus (Manaster et al. 2008), and intestine (Sagebiel et al. 2019). Certain phenotypic and transcriptional programmes appear to be conserved across tissues (Tang et al. 2023); for example, trNK cells at most human sites are predominantly $CD56^{bright}$ (Niehrs et al. 2025). However, other phenotypic and functional features are shaped by local environmental cues (**Figure 1.9**). For instance, liver trNK cells express the chemokine receptor CXCR6, which mediates migration to and retention within hepatic sinusoids in response to CXCL16 expressed by endothelial cells (Hudspeth et al. 2016), whereas CXCR6 expression is comparatively lower in trNK populations from other tissues (Dogra et al. 2020). As another example, uterine NK cells, first identified in the murine decidua (Croy et al. 1985), are distinctly cytokine-producing and uniquely participate in spiral artery remodelling and placental development (Moffett and Colucci 2014).

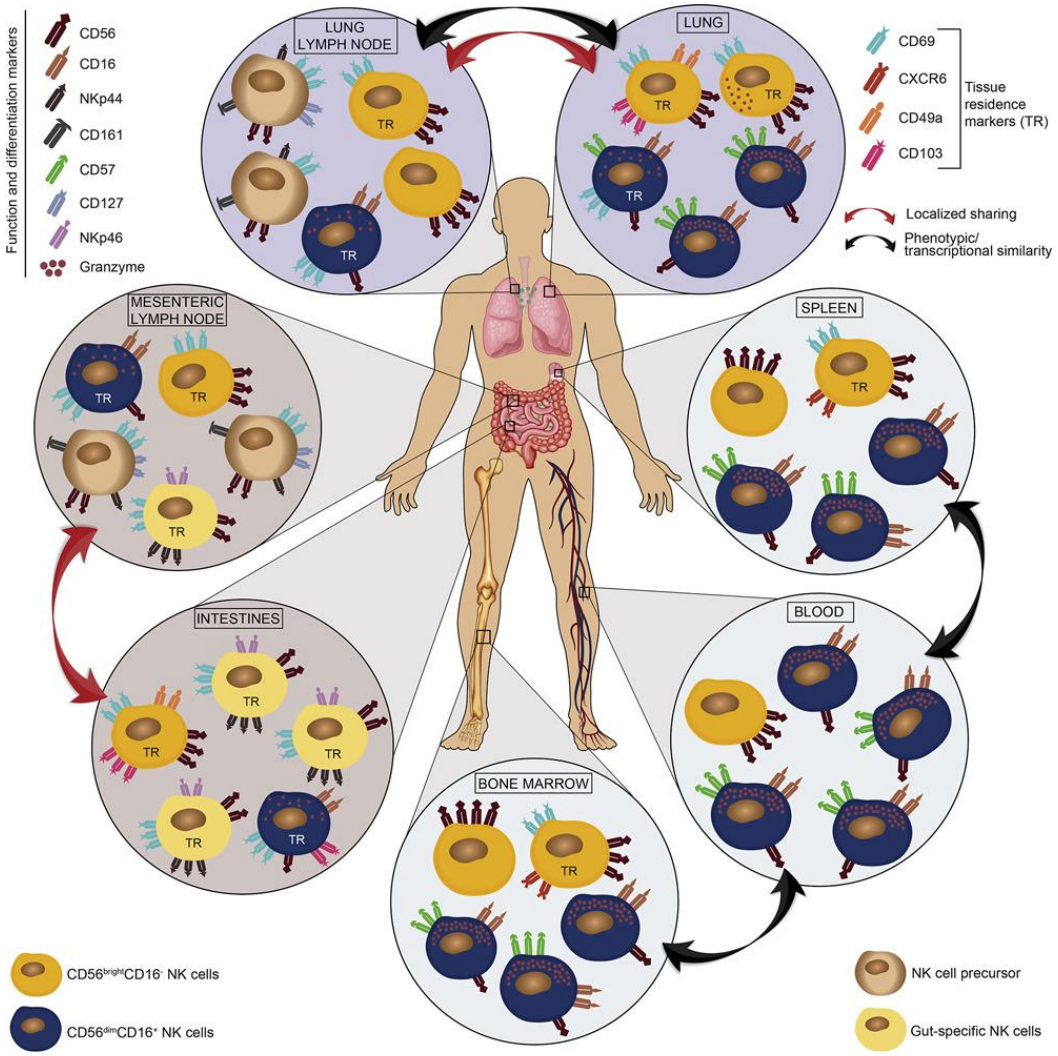

Figure 1.9 – Human NK cell phenotype across different sites
NK cells across tissues express variable levels of the lineage-defining surface markers CD56 and CD16. Within NK cells, trNK cells exhibit site-specific differences in the expression of canonical tissue-residency markers, including CD69, CD49a, CD103, and CXCR6. Reproduced with permission from *Dogra et al.*, *Cell*, *2020 (Graphical abstract) – Licence Number 6217771117860*.

1.5.3 NK cells in cancer immunity

NK cells detect and eliminate transformed cells through a balance of activating and inhibitory signals (Long 1999; Lanier 2005). Tumour cells often upregulate stress-induced ligands such as MHC class I polypeptide–related sequence A and B (MICA/B) in humans, or Retinoic acid early transcript 1 (RAE-1) in mice, which engage activating receptors on NK cells,

including NKG2D (Raulet 2003). In parallel, inhibitory receptors depend on self MHC class I (MHC-I) expression to prevent autoreactivity: in humans, KIRs (killer-cell immunoglobulin-like receptors) recognise classical Human Leukocyte Antigen (HLA) molecules (HLA-A/B/C) expressed on all nucleated cells (Vilches and Parham 2002), whereas in mice, Ly49 receptors serve a similar role (Karlhofer et al. 1992). According to the "missing-self" hypothesis (Ljunggren and Kärre 1990; Höglund et al. 1997), loss or downregulation of MHC-I on tumour cells removes inhibitory signals, tilting the balance towards activation. NK cells' unique capacity to recognise and kill tumour cells independently of classical MHC I presentation makes them an attractive therapeutic tool, especially for cancers that evade $CD8^+$ T cell surveillance by downregulating MHC-I (Morvan and Lanier 2016).

Other immune checkpoint receptors, such as T cell immunoreceptor with immunoglobulin and immunoreceptor tyrosine-based inhibitory motif domains (TIGIT), can similarly restrain NK cell function upon binding to other molecules whose expression is generally low in healthy tissues but can be upregulated by stress, DNA damage, or inflammatory cytokines, such as the poliovirus receptor (PVR, also known as CD155) (Stanietsky et al. 2009). Of note, some ligands can engage receptors with opposing functions; for example, PVR/CD155 binds both the inhibitory receptor TIGIT and the activating receptor DNAX Accessory Molecule-1 (DNAM-1, also known as CD226) (Bottino et al. 2003).

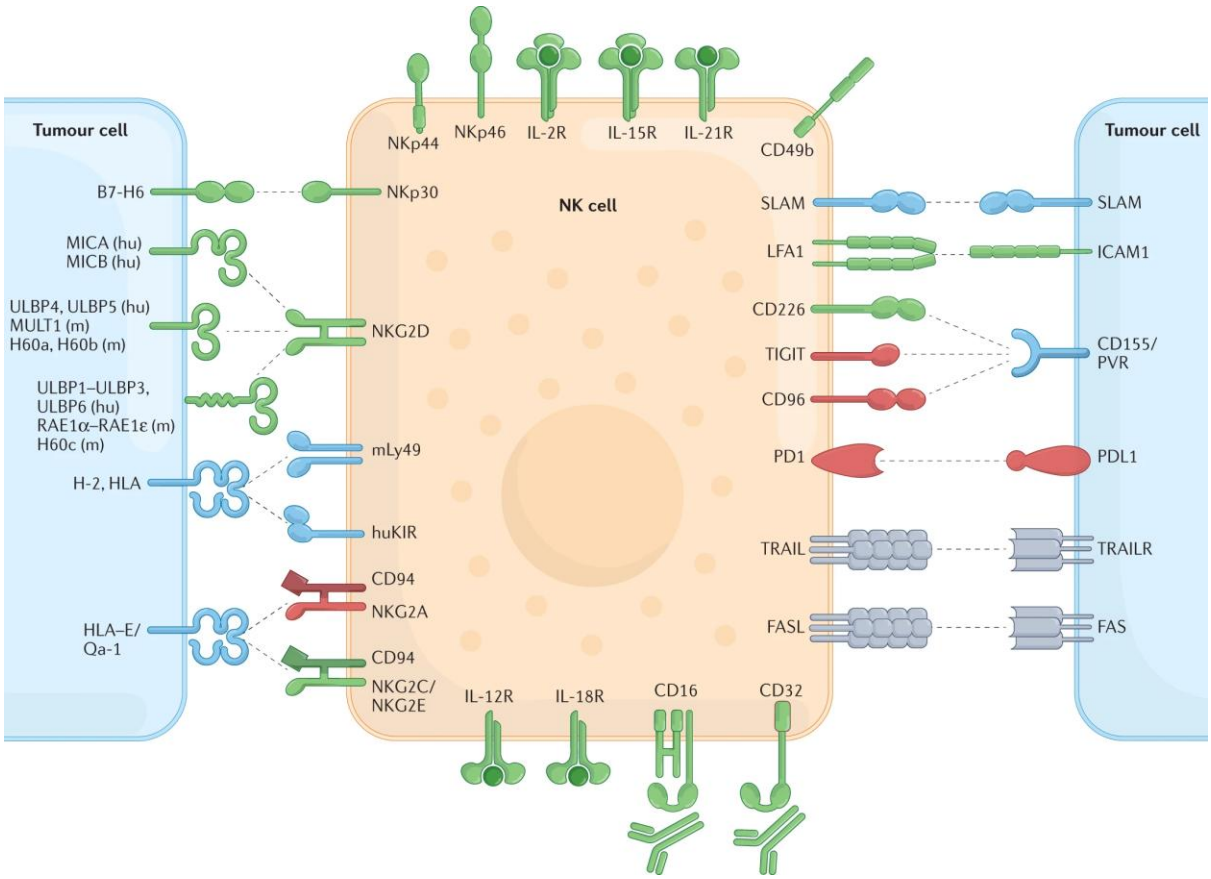

Figure 1.10 – NK cell activating and inhibitory receptors

Receptor–ligand interactions that activate (green) or inhibit (red) NK cell responses against tumour cells and other cells, or that can either activate or inhibit NK cells depending on the specific family member or the context (blue) are shown. Some ligands bind to both inhibitory and activating receptors on NK cells, as indicated. Key cytokine receptors are also depicted. The receptors for different IL-2 family cytokines consist of multiple chains, of which one (the common γ-chain) is a shared signalling component. *Hu* indicates human only and *m* indicates mouse only. KIR: killer immunoglobulin-like receptor; TIGIT: T cell immunoreceptor with immunoglobulin and immunoreceptor tyrosine-based inhibitory motif domains. Reproduced with permission from *Wolf et al.*, *Nature Reviews Immunology*, *2023 (Figure 1) – Licence Number 6220131330976*.

Once activated, NK cells kill target cells primarily through two effector molecules: perforin, which forms pores in the target cell membrane, and granzymes, serine proteases that enter through these pores to induce apoptosis (Shi et al. 1992; Nakajima et al. 1995). A specific form of granule-mediated cytotoxicity is antibody-dependent cellular cytotoxicity (ADCC).

In this process, NK cells expressing CD16 (FcγRIIIa) bind the Fc portion of naturally occurring or therapeutic IgG antibodies coating antigens on the surface of a transformed (tumour) cell, triggering NK cell activation and degranulation (Kay et al. 1977). Another, complementary mechanism by which NK cells participate in tumour surveillance is the induction of apoptosis through death receptor pathways. This is because NK cells express Fas ligand (FasL) and TNF-related apoptosis-inducing ligand (TRAIL), which bind to Fas (also known as CD95) and DR4/DR5 receptors on target cells, respectively (Medvedev et al. 1997; Smyth et al. 2001). Engagement of these receptors triggers caspase activation and programmed cell death, providing an alternative mechanism to eliminate tumour or stressed cells.

Beyond direct cytotoxicity, NK cells contribute to anti-tumour immunity through immunomodulatory cytokine and chemokine production (Wolf et al. 2023). They secrete IFN-γ, which enhances MHC expression on tumour and stromal cells, promotes type 1 immune responses, and activates macrophages and dendritic cells (Street et al. 2001; Loza et al. 2002). NK-derived tumour necrosis factor α (TNF-α) and GM-CSF can further shape myeloid cell function within the TME (Jewett et al. 1996; Smyth et al. 2001; Zhang et al. 2007; Cui et al. 2025). Chemokines such as C–C motif chemokine ligand 3 (CCL3), C–C motif chemokine ligand 4 (CCL4), CCL5, and XCL1 produced by NK cells can recruit dendritic cells and effector T cells to tumours, amplifying adaptive anti-cancer responses (Robertson 2002; Böttcher et al. 2018; K. C. Barry et al. 2018; Kirchhammer et al. 2022).

For NK cells to exert their cytotoxic or immunomodulatory functions, they must remain functionally competent within the TME. However, upon entry into the TME, NK cells progressively lose effector functions and adopt a distinct hypofunctional state and a phenotype partly associated with tissue residency (Dean et al. 2024). This functional impairment (variably referred to as NK cell exhaustion or dysfunction) has been described across multiple cancer types (Carrega et al. 2008; C. Sun et al. 2015; Mele et al. 2022; Xu et al. 2025; Slattery et al. 2025) and may result from exposure to both soluble and cell-associated suppressive factors, including TGF-β, indoleamine 2,3-dioxygenase (IDO), IL-10, prostaglandin E2, adenosine, and reactive oxygen species produced by tumour cells and stromal components, particularly myeloid cells and regulatory T cells (Jia et al. 2023).

Importantly, this dysfunctional programme has been reported to develop rapidly and to be uncoupled from the upregulation of classical checkpoint receptors (Pouxvielh et al. 2024). As disease progresses, intratumoral NK cells swiftly lose the capacity to contribute effectively to anti-tumour responses and become dispensable for tumour control; however, this impairment appears to be at least in part reversible following administration of NK-supporting cytokines such as interleukin 15 (IL-15) (Dean et al. 2024).

1.5.4 NK cells in PDAC

NK cells are typically scarce in the normal pancreas in murine models, representing approximately 2% of all lymphocytes (Brauner et al. 2010). Much of the current understanding of pancreatic NK cells derives from

studies in non-obese diabetic (NOD) mice, which are prone to develop autoimmune diabetes due to immune-mediated destruction of the islets of Langerhans (Serreze and Leiter 1994). In NOD mice, NK cells predominantly infiltrate the exocrine pancreas and can be detected in the endocrine compartment well before disease onset and prior to overt T cell infiltration of the islets (Brauner et al. 2010). NK cells may be recruited to the pancreas by chemokines such as CXC motif chemokine ligand 10 (CXCL10), a ligand for CXC motif chemokine receptor 3 (CXCR3), and C–C motif chemokine ligand 5 (CCL5), a ligand for C–C motif chemokine receptor 5 (CCR5), which can be produced by multiple cell types including pancreatic β-cells (Alba et al. 2008). Within the pancreatic microenvironment, NK cells can recognise activating ligands on β-cells via NKp46, contributing to β-cell destruction (Gur et al. 2010).

Compared with splenic NK cells, pancreatic NK cells in NOD mice exhibit a higher proliferative rate and increased expression of the activation markers CD69 and CD25, as well as the inhibitory receptors PD-1 and killer cell lectin-like receptor subfamily G member 1 (KLRG-1) (Brauner et al. 2010). However, at later stages of disease progression, these cells become hyporesponsive upon stimulation. This hyporesponsive phenotype observed during diabetes development may be at least in part driven by sustained interactions between NK cell receptors and their ligands expressed on pancreatic β-cells. For example, engagement of NKG2D by its ligands, such as Rae-1 expressed on β-cells, has been reported to induce downregulation of NKG2D and functionally dampen NK cell activity,

potentially limiting excessive autoimmunity (Ogasawara et al. 2004). Furthermore, interaction of PD-1 on pancreatic NK cells with PD-1 ligands expressed within inflamed islets may further restrain NK cell effector function (Ansari et al. 2003).

Interestingly, NK cells are present in the pancreas of C57BL/6 mice at proportions comparable to those observed in NOD mice, indicating that pancreatic recruitment can occur even in the absence of overt or sustained inflammation. However, compared with NK cells in NOD mice, pancreatic NK cells in C57BL/6 mice exhibit lower baseline proliferation and reduced expression of the activation markers NKG2D and CD69 (Brauner et al. 2010).

The role of NK cells in the development of PDAC has been comparatively understudied, with only a limited number of reports addressing this question. Peripheral blood NK cells from patients with PDAC are predominantly $CD56^{dim}CD16^{+}$ and display marked downregulation of activating receptors such as NKG2D and NKp30 compared with healthy donors (Marcon et al. 2020). In addition, these cells exhibit reduced cytotoxic activity and diminished IFN-γ production, while producing elevated levels of IL-10, an immunoregulatory cytokine that is increased in the blood of PDAC patients.

Within the PDAC TME, NK cells are largely excluded, representing approximately 3% of total cells in one study (Marcon et al. 2020) and less than 1% of all lymphocytes in another (Lim et al. 2019). Tumour-infiltrating

NK cells are predominantly $CD56^{dim}CD16^{-}$ and display marked suppression of activating receptors, including CD16, DNAM-1, and NKp30 (Marcon et al. 2020). PDAC tissues, on the other hand, display significant upregulation of ligands for NKG2D as well as the TIGIT and DNAM-1 ligand PVR, the latter increased by up to 18-fold compared with normal pancreas (Marcon et al. 2020). Notably, NK cells from patients with PDAC exhibit minimal cytotoxicity against primary PDAC cells or pancreatic cancer cell lines; however, their cytotoxic function can be restored, at least in part, following *ex vivo* expansion and stimulation (Lim et al. 2019).

1.4

Rationale for present studies

The current standard-of-care treatment for PDAC depends on both disease stage and patient fitness. In the minority of patients who present with limited tumour burden and are deemed sufficiently fit, aggressive, multi-agent chemotherapy is administered, often in combination with surgical resection. Patients with reduced fitness may receive modified or lower-intensity chemotherapy protocols tailored to balance efficacy with tolerability. However, the overwhelming majority of patients present with advanced or metastatic disease and are too frail to undergo any systemic chemotherapy. These patients are managed with best supportive care alone. The resultant prognosis in PDAC remains extremely poor, with a median overall survival of approximately 4 months from the time of diagnosis.

Given the recent surge of immunotherapeutic approaches over the past two decades and the remarkable clinical success achieved in other malignancies, it remains unclear whether such strategies can provide meaningful therapeutic benefit in PDAC, and this warrants further investigation. As PDAC is a malignancy characterised by low neoantigen production and reduced expression of MHC class I, baseline antigen-specific $CD8^+$ T cell responses are unlikely to confer substantial benefit in this context. To date, only one study aimed at enhancing antigen-specific $CD8^+$ T cell responses has reported encouraging results in humans, with unprecedented progression-free survival (PFS) and overall survival (OS) not

reached at a median follow-up of 3.2 years. However, this approach relied on an individualised neoantigen vaccine, and therefore the scalability of this and similar approaches is drastically limited by practical considerations such as cost and manufacturing complexity; moreover, only a subset of treated patients (8 individuals) demonstrated a measurable response.

In light of these considerations, NK cell–based immunotherapies represent a promising alternative as a novel immunotherapeutic strategy for PDAC. Unlike $CD8^+$ T cells, NK cells can mount anti-tumour responses independently of neoantigen burden and MHC class I expression. In addition, ligands for NK cell activating receptors are detectable within the pancreas even prior to overt tumour development, suggesting that this axis may be exploitable at relatively early stages of disease evolution. While it is well established that NK cells across a number of tumour types, including PDAC, can acquire a functionally impaired and poorly cytotoxic phenotype in the TME, these studies have primarily defined dysfunction in terms of diminished cytotoxicity, whereas other functions of NK cells (e.g., immunoregulation) have been comparatively less well explored. It is therefore plausible that, within the TME, NK cells may not simply undergo a global loss of function but rather a redirection or reprogramming of their function. Furthermore, multiple studies have demonstrated that this partial functional impairment is, at least to some extent, reversible following exposure to NK-supporting cytokines, indicating that a range of therapeutic strategies may be leveraged to restore or reinvigorate NK cell activity.

1.5

Aims and hypotheses

Aim 1

Develop a tool for analysing immune responses in murine models of PDAC, applicable at baseline or following therapeutic interventions. Underlying hypothesis**:** A comprehensive flow cytometry panel can be designed to enumerate all major immune cell populations involved in anti-tumour responses in murine models of disease, both in the TME and at distant sites, revealing that more cell types than previously recognised contribute to immunity to PDAC.

Aim 2

Use the tools developed in Aim 1, and their adaptations, to characterise the phenotype of a previously described NK cell population in the KPC orthotopic model of PDAC.

Underlying hypothesis: The NK cell subset found to correlate with survival corresponds to pancreatic tissue-resident NK cells with an immunoregulatory role; preliminary immunophenotyping will provide a foundation for future studies on their ontogeny and function.

Aim 3

Use the tools developed in Aim 1, and their adaptations, to characterise the immune response in the KPC orthotopic model of PDAC following treatment with a novel therapeutic combination including immune checkpoint inhibition and stroma-targeted therapy.

Underlying hypothesis: Disruption of physical barriers in the TME *via* FAK inhibition allows increased immune cell (including tissue-resident NK cell) infiltration; when coupled with TIGIT blockade, this can enhance anti-tumour immunity.

Aim 4

Develop and optimise a protocol for generating NK cells with a hybrid phenotype combining cytotoxicity and tissue retention, for potential translational applications.

Underlying hypothesis: *Ex vivo* exposure of donor PBMC-derived NK cells to cytokines that promote tissue retention, alongside cytokines that proliferation, activation, and cytotoxicity, can generate NK cells capable of localising to the TME and mounting effective anti-tumour responses.

Aim 5

Quantify infiltration of innate and adaptive immune cells in the pancreas during disease progression in the aging KC mouse model, reflecting immune dynamics over time.

Underlying hypothesis: Early KRAS-driven precursor lesions in the pancreas initiate antigen-specific responses by B and T cells; innate cells, including NK cells, act as first responders to malignantly transformed cells before the transition to invasive cancer.

Chapter 2

Materials and methods

2.1

Materials

All reagents used in the experiments presented in this thesis are listed in **Table 2.1** below. Methods are reported below in the order in which they appear in the main text. Unless otherwise specified, all cell lines were obtained from the laboratory of Eric O'Neill.

REAGENT	SUPPLIER	IDENTIFIER
BSA	Sigma-Aldrich	A2514
Collagen type I (human)	Sigma-Aldrich	CC050
Collagenase, type II	Gibco	17101015
Collagenase, type IV	Gibco	17104019
DMEM	Gibco	21969-035
DNase I	Roche	10104159001
EDTA	Sigma-Aldrich	E4884
FBS, heat-inactivated	Sigma-Aldrich	F9665-500ML
Ficoll-Paque PREMIUM 1.084	Cytiva	17544602
Formalin (10% neutral buffered)	Sigma-Aldrich	HT501128
HBBS	Gibco	14025092
L-Glutamine	Gibco	25030-024
Lymphoprep	STEMCELL Technologies	18060
Matrigel membrane matrix	Corning	356231
NK MACS	Miltenyi Biotec	130-114-429
PBS	Gibco	14190144
Penicillin-Streptomycin	Gibco	15140-122
Red blood cell lysis buffer	BioLegend	420301
RPMI	Gibco	21875034
Sodium azide	Sigma-Aldrich	S2002
Trypsin-EDTA	Sigma-Aldrich	T4049

IL-12 (human)	BioLegend	573004
IL-15 (human)	BioLegend	570304
IL-15 (mouse)	BioLegend	566302
IL-18 (human)	BioLegend	592104
IL-2 (human)	BioLegend	589104
IL-21 (human)	BioLegend	571206
TGF-β1 (human)	BioLegend	781802
TGF-β1 (mouse)	BioLegend	763102

CD3 EasySep selection kit	STEMCELL Technologies	17851
CD14 EasySep selection kit	STEMCELL Technologies	17858
CD19 EasySep selection kit	STEMCELL Technologies	17854
CD56 EasySep selection Kit	STEMCELL Technologies	17855
Human NK cell EasySep selection kit	STEMCELL Technologies	17955
Mouse NK cell EasySep selection kit	STEMCELL Technologies	19855

Brefeldin A	Thermo Fisher	00-4506-51
Fc block (human)	BD Biosciences	564219
Fc block (mouse)	BD Biosciences	553141
FoxP3 Fixation/Permeabilisation Buffer	Thermo Fisher	00-5523-00
LIVE/DEAD Fixable Blue	Thermo Fisher	L34962
Monensin	Thermo Fisher	00-4505-51
Super Bright Staining Buffer	Thermo Fisher	SB-4401-42
UltraComp Spectral Unmixing Beads	Thermo Fisher	U20250

CD3 BUV395	Thermo Fisher	363-0032-82
CD4 BUV496	Thermo Fisher	364-0042-82
CD8α BUV805	Thermo Fisher	368-0081-82
CD11b BUV737	Thermo Fisher	367-0112-82
CD11b BV570	BioLegend	101233
CD11c BUV615	Thermo Fisher	366-0114-82
CD19 BV750	BioLegend	115561
CD19 APC-Fire810	BioLegend	115578
CD44 BV510	BioLegend	103044
CD45 AF532	Thermo Fisher	58-0451-82
CD49a PE-Vio770	Miltenyi Biotec	130-123-892
CD62L SB702	Thermo Fisher	67-0621-82
CD69 BUV737	Thermo Fisher	367-0691-82
CD86 BV785	BioLegend	105043
CD103 SB600	Thermo Fisher	63-1031-82
CXCR3 BUV563	BD Biosciences	741438

CXCR6 APC-Cy7	BioLegend	115578
CXCR6 BV711	BioLegend	151111
DNAM-1 PE	BioLegend	128806
Eomes PE-Cy5	Thermo Fisher	15-4875-82
F4/80 BUV563	Thermo Fisher	365-4801-82
FoxP3 PE-Cy5.5	Thermo Fisher	15-4875-82
Granzyme A APC	Thermo Fisher	17-5831-82
Granzyme B VioB515	Miltenyi Biotec	130-130-543
I-A/I-E AF700	BioLegend	107622
Ki-67 BUV661	Thermo Fisher	376-5698-82
KLRG-1 PE-Fire810	BioLegend	138437
Ly6C APC-Cy7	BioLegend	128026
Ly6G PE-Cy5	BioLegend	127672
NK1.1 SB436	Thermo Fisher	62-5941-82
NKG2A PerCP-eF710	Thermo Fisher	46-5897-82
NKG2D PE-eF610	Thermo Fisher	61-5882-82
NKp46 SB645	Thermo Fisher	64-3351-82
SIRPα PE-Dazzle594	BioLegend	144015
TIM-3 BV785	BioLegend	119725
TIGIT BV480	Thermo Fisher	414-9501-82
XCR1 APC	Miltenyi Biotec	130-111-373
γδ TCR PerCP-eF710	Thermo Fisher	46-5711-82

CD3 Pacific Blue	BioLegend	300431
CD103 PE-Cy7	BioLegend	350212
CD16 BV480	Thermo Fisher	414-0168-42
CD16 FITC	BioLegend	302006
CD3 BUV563	Thermo Fisher	365-0038-42
CD49a APC	BioLegend	328314
CD56 APC-Cy7	BioLegend	318332
CD57 Pacific Blue	BioLegend	359608
CX3CR1 BV510	BioLegend	341622
CXCR3 PerCP-Fire806	BioLegend	353772
CXCR6 PE	BioLegend	356004
DNAM-1 BV785	BioLegend	338322
EOMES PE-eF610	Thermo Fisher	61-4877-42
Granzyme B VioB515	Miltenyi Biotec	130-130-543
Granzyme K PerCP-eF710	Thermo Fisher	46-8897-42
HLA-A/B/C APC	BioLegend	311410
Ki-67 BUV737	Thermo Fisher	367-5698-82
NKG2C BV421	BioLegend	375014
NKG2C PE-Vio615	Miltenyi Biotec	130-123-037

NKG2D BV605	BioLegend	320832
NKp46 PE-Cy5	BioLegend	331952
PD-1 SB702	Thermo Fisher	67-2799-42
TIGIT NovaFluor Red700	Thermo Fisher	H011T03R03A
TIM-3 SB645	Thermo Fisher	64-3109-42
CD8α unconjugated	Cell Signaling Technology	98941S
CD11c unconjugated	Abcam	ab219799
CD19 unconjugated	Cell Signaling Technology	90176T
CD103 unconjugated	Thermo Fisher	14-1031-81
E-cadherin unconjugated	Cell Signaling Technology	3195
NK1.1 unconjugated	Thermo Fisher	MA1-70100
NK1.1 unconjugated	Abcam	ab234107
Caerulein	Sigma-Aldrich	C9026
CFSE	Thermo Fisher	C34554
Defactinib	Selleckchem	PF-04554878
DMSO	Sigma-Aldrich	D4540
Enrofloxacin 2.5% oral solution	Bayer	04007221019251
IVISense680	Revvity	NEV12000
Maraviroc	Bio-Techne	3756
PEG300	Sigma-Aldrich	1546423
Protamine sulphate	Sigma-Aldrich	PP3369-10G
RetroNectin	Takara Bio	T100A
Tween80	Sigma-Aldrich	P6474
Ultra-LEAF anti–PD-1	BioLegend	135247
Ultra-LEAF anti–TIGIT	BioLegend	156108
XCL1 ELISA Kit	Thermo Fisher	EMXCL1

Table 2.1 – Reagents used in the experiments presented in this thesis

2.2

Methods

2.2.1 – Cell culture

KPC-F, MIA PaCa-2, A549 and RKO cells were cultured in DMEM supplemented with 10% foetal bovine serum (FBS), 2 mM L-glutamine, 100 U/mL penicillin, 100 µg/mL streptomycin, and maintained at 37°C, 5% CO_2.

Cells were split and medium was changed upon reaching 80-90% confluence. Primary NK cells were cultured in RPMI supplemented with 10% human AB serum, 2 mM L-glutamine, 100 U/mL penicillin, 100 µg/mL streptomycin, 1% non-essential amino acids, 1 mM sodium pyruvate, and 10 mM HEPES buffer, or in NK MACS basal medium supplemented with NK MACS supplement and 10% human AB serum, and maintained at 37°C and 5% CO_2. Cells were split and half of the medium was replenished with fresh cytokines every 2–3 days.

2.2.2 – Syngeneic cell line orthotopic implantation

Female C57BL/6J mice (8 weeks) were purchased from Charles River Laboratories and maintained in accordance with the UK Animal Law (Scientific Procedures Act 1986; PPL: PP6460882). NKPCB-NBC12.1F (KPC-F) cells, derived from a KPC mouse (LSL-*Kras*$^{G12D/+}$;LSL-*Trp53*$^{R172H/+}$;*Pdx-1*-Cre) were injected into the tail of the pancreas via laparotomy, as previously reported (Valenzano et al. 2024).

2.2.3 – *In vivo* treatments

Treatments were initiated once tumours reached predefined volumes and continued until the study endpoint, which varied between chapters. In Chapter 3, no treatment was administered; mice were culled 14 days after tumours reached 50–100 mm^3 (corresponding to a small palpable nodule by abdominal palpation). In Chapter 4, treatment began when tumours reached 50–100 mm^3 (as determined by abdominal palpation) and continued for 14 days. Mice were culled upon reaching the predefined

humane endpoint of showing obvious signs of sickness or distress. Mice were irradiated according to a fractionated protocol (3×6 Gy) using the small animal radiation research platform (SARRP). Computed tomography (CT) guidance was used to define tumour outlines prior to irradiation. Maraviroc was administered intraperitoneally (10 mg/kg in PBS) on alternate days; and Ultra-LEAF anti–PD-1 was administered intraperitoneally (5mg/kg in PBS) on alternate days. In Chapter 5, for the survival cohort, treatment started at 50–100 mm^3 (determined by abdominal palpation) and continued until the predefined humane endpoint of showing obvious signs of sickness or distress; in the immune profiling cohort, treatment began at 30–60 mm^3 (corresponding to a small palpable grain by abdominal palpation) and continued until day 14, when mice were euthanised. Defactinib was administered intraperitoneally (12.5 mg/kg in 2% DMSO + 50% PEG300 + 8% Tween80 + 40% ddH2O) on alternate days; and the Ultra-LEAF anti–TIGIT antibody was administered intraperitoneally (10 mg/kg in PBS) biweekly.

2.2.4 – Tissue collection and sample preparation

Mice were euthanised by approved Schedule 1 methods. Blood was collected via cardiac puncture under anaesthesia using EDTA-coated 25-gauge syringes. After 1:1 dilution in PBS, red blood cells (RBCs) were removed with a commercial RBC lysis buffer containing ammonium chloride. Cells were washed, counted, and stained for flow cytometric analysis. Tumours, livers, and spleens were harvested in RPMI and kept on ice. Tumours and livers were dissociated mechanically with scissors and enzymatically by incubating them in HBBS with Collagenase II 100 IU/mL

and Collagenase IV 100 IU/mL and DNase I 1 mg/mL at 37°C for 30 minutes with continuous mixing (600 rpm). The digested fraction was washed with cold RPMI supplemented with 10% FBS, filtered through 70-µm and 40-µm strainers, centrifuged at 300 × g for 5 minutes, and resuspended in PBS. The cell suspensions were then carefully overlaid onto Ficoll-Paque PREMIUM 1.084 and centrifuged at 400 × g for 30 minutes without breaks. The low-density cell fraction thus obtained was washed, counted, and stained for flow cytometric analysis. Spleens were dissociated mechanically with scissors and filtered through 70-µm and 40-µm strainers, counted, and the resultant cell suspension stained for flow cytometric analysis.

2.2.5 – Staining for flow cytometry

A detailed protocol is available elsewhere (Valenzano et al. 2024). Briefly, a single-cell suspension of murine or human cells was prepared, and up to 5×10^5 cells were seeded into a 96-well U-bottom plate. Cells were incubated with LIVE/DEAD Blue viability dye (diluted 1:1000 in PBS) for 30 minutes at 4 °C, washed (300 × g, 3 minutes), and incubated with murine or human FcR Blocking Reagent in staining buffer (PBS supplemented with 5% FBS, 0.1% w/v sodium azide, and 1 mM EDTA) for 5 minutes. Without further washing, surface antibodies and Super Bright Complete staining buffer were added and incubated for 25 minutes at 4 °C, protected from light. Cells were then washed (300 × g, 3 minutes) and fixed/permeabilised using the FOXP3 Fixation and Permeabilisation Kit prior to intracellular staining, when applicable, for 30 minutes at 4 °C, protected from light. Following incubation, cells were washed, resuspended in staining buffer, and

acquired on a Cytek Aurora 4L (UV–V–B–R) using the SpectroFlo software (v2, Cytek Biosciences). When intracellular staining for chemokines or effector molecules was performed, monensin and brefeldin A were added at each incubation step.

2.2.6 – ELISA

XCL1 ELISA was performed according to the manufacturer's instructions. Briefly, plasma was obtained from mouse blood after density gradient centrifugation and stored at -80 °C until further analysis. Upon thawing, samples were diluted 1:1 in PBS and processed: samples and standards were added to pre-coated wells, incubated with the detection antibody and streptavidin–horseradish peroxidase (HRP), washed, and developed with TMB substrate. Absorbance was read at 450 nm using a microplate reader, and XCL1 concentrations were calculated from the standard curve.

2.2.7 – *In vitro* generation of NK cells for cancer immunotherapy

Mouse splenocytes were isolated as described above, enriched for NK cells using a negative selection kit (EasySep), and cultured with IL-15 (10 ng/mL), with or without TGF-β (2 ng/mL) for 48 hours. Human peripheral blood mononuclear cells (PBMCs) were isolated from healthy donor blood cones (under ethical approvals HTA REC 19/LO/1848 and R83151/RE001) using Lymphoprep-based centrifugation. In the initial screening phase of Chapter 6, PBMCs were enriched for NK cells using a CD56 positive selection kit (EasySep), seeded at 0.5–1×10^6 cells/mL in primary NK cell culture medium, and cultured with the following cytokine combinations: IL-15 (2 ng/mL) for

7 days; TGF-β (2 ng/mL) for 7 days; IL-15 (2 ng/mL) for 5 days plus TGF-β (2 ng/mL on days 3-5, and 5 ng/mL on days 6-7); IL-15 (2 ng/mL) for 5 days plus IL-21 (50 ng/mL) on day 3 and TGF-β (5 ng/mL) on days 6-7; IL-15 (2 ng/mL for 5 days, except for 10 ng/mL on day 3) plus IL-12 (10 ng/mL) and IL-18 (50 ng/mL) on day 3, and TGF-β (5 ng/mL) on days 6-7. Cells were washed after exposure to IL-21, IL-12, and IL-18. In the optimised protocol of Chapter 6, PBMCs were enriched for NK cells either by using a CD56 negative selection kit or by sequentially removing CD3-, CD19-, and CD14-expressing cells from the PBMC mixture using dedicated positive selection kits (EasySep). The remaining NK-enriched PBMCs were seeded in gas-permeable plates at 0.5–1×10^6 cells/mL and cultured with primary NK cell culture medium supplemented with IL-2 (1000 IU/mL) for 14 days and IL-15 (2 ng/mL) added biweekly. Starting on day 15, cells were washed and cultured with IL-21 (25 ng/mL) and IL-15 (25 ng/mL) for 16 hours, washed again, and maintained in culture with IL-2 (100 IU/mL) and IL-15 (2 ng/mL) for 3 days, before repeating this cycle three times (four IL-21 pulses in total). On the final IL-21 pulse, the IL-21 concentration was increased to 50 ng/mL, with or without TGF-β (5 ng/mL). For one donor, half of the cells were cultured in a plate coated with collagen type I (20 µg/mL) starting on day 15.

2.2.8 – Cancer cell line transduction

MIA PaCa-2, A549, and RKO cells were seeded in T125 flasks and allowed to adhere. Upon reaching 60–75% confluence, mCherry-encoding lentiviral vectors were added. These vectors were packaged in HEK293T cells using the pMDG VSV-G envelope plasmid (Addgene #187440), the p8.91

packaging plasmid (Addgene #187441) and a custom-made transfer plasmid (with SFFV promoter). Lentiviral supernatant was kindly provided by Ben Futcher (Department of Oncology, University of Oxford). After an overnight incubation, cells were washed once with culture medium, and fresh lentiviral supernatant was added for an additional 24 hours. Transduced cells were then washed, harvested, and sorted for mCherry expression using a FACSAria cell sorter.

2.2.9 – Cytotoxicity assay

For the K562 cytotoxicity assay, 25,000 K562 cells were labelled with carboxyfluorescein succinimidyl ester (CFSE) and seeded into 96-well U-bottom plates, after which NK cells were added at the indicated effector-to-target (E:T) ratios and co-cultured for 4-6 hours. No additional cytokines were added during the co-culture period. For assays against solid tumour cell lines (previously transduced with mCherry), 25,000 target cells were seeded into 96-well flat-bottom plates and allowed to adhere for 16 hours before addition of NK cells at the respective E:T ratios, followed by a 6-hour co-culture. No additional cytokines were added during the co-culture period. After incubation, cells were washed, resuspended in PBS, and stained with LIVE/DEAD Blue Viability dye for 30 minutes at 4 °C. Samples were then washed and immediately acquired, unfixed, on a Cytek Aurora 4L (UV–V–B–R) flow cytometre. A separate well containing target cells only was used to determine spontaneous cell death, which was subtracted from the percentage of $CFSE^+$ or $mCherry^+$ dead cells to calculate specific lysis.

2.2.10 – MIA PaCa-2 orthotopic implantation

Female Rag2/IL2RG double-knockout (R2G2) mice (8 weeks) were purchased from Inotiv (formerly Envigo) and maintained in accordance with the UK Animal Law (Scientific Procedures Act 1986, PPL: PP6460882). 5×10^5 MIA PaCa2 cells were injected into the tail of the pancreas via laparotomy, akin to the syngeneic KPC-F cell line. Enrofloxacin oral 2.5% was added to drinking water from 2 days prior to surgery to 5 days after surgery. Mice were palpated biweekly for signs of tumour engraftment.

2.2.11 – Chronic pancreatitis induction

Caerulein was administered *via* intraperitoneal injection at 50 µg/kg hourly, for a total of eight doses per day, twice per week, for four weeks. This was followed by a single intraperitoneal administration of caerulein at 200 µg/kg, twice per week, for an additional four weeks, according to established protocols (Leal and Liby 2018; Minaga et al. 2022).

2.2.12 – Adoptive transfer *of in vitro*-generated NK cells

For initial testing of NK cell migration to epithelial sites *in vivo*, 2×10^6 NK cells obtained at the end of the optimised 28-day expansion and stimulation protocol (including IL-15, IL-21, and TGF-β exposure) were injected into a non-tumour-bearing R2G2 mouse. Complexes of recombinant human IL-15 and IL-15 receptor α–Fc, prepared by incubating equimolar amounts of both at 37 °C for 1 hour, were administered intraperitoneally at 2 µg IL-15 per mouse 30 minutes after the NK cell injection. After 48 hours, blood, spleen, lung, liver, and intestine samples were collected for flow cytometric

analyses. Blood, spleen, and liver samples were processed as described above for C57BL/6 mice. Lung and intestine samples were processed as for liver samples. Both lungs and the small and large intestines were collected and processed.

2.2.13 – Labelling *in vitro*-generated NK cells for *in vivo* tracking

For *in vivo* tracking, NK cells were pre-labelled with the IVISense680 tracker dye following the manufacturer's protocol. Briefly, cells were washed, resuspended in PBS, and incubated 1:1 with reconstituted IVISense680 for 20 minutes, followed by three washes. Labelled cells (2×10^6) were injected into one control and one caerulein-treated mouse. Complexes of recombinant human IL-15 and IL-15 receptor α–Fc were prepared and administered as above. Images were acquired using the IVIS Spectrum In Vivo Imaging System at the Oxford Centre for Advanced Preclinical Imaging.

2.2.14 – NK cell transduction

A 96-well U-bottom plate was coated overnight at 4 °C with RetroNectin (25 µg/mL). The following day, the coating solution was removed, and wells were washed once with 2% BSA in PBS. Subsequently, ZsGreen- or ZsGreen–luciferase–encoding lentiviral vectors were added at varying concentrations (% v/v in NK MACS medium). These vectors were packaged in HEK293T cells using the BaEV (baboon endogenous virus) envelope backbone previously described by others (Colamartino et al. 2019), the psPAX2 packaging plasmid (Addgene #12260), and a ZsGreen-luciferase transfer plasmid (Addgene #39196) or ZsGreen transfer plasmid (Addgene

#18121). Lentiviral supernatant was kindly provided by Berna Bou Tayeh (Ludwig Institute for Cancer Research, Oxford). Plates were centrifuged at 2000 × g for 2 hours at 37 °C to facilitate virus binding. NK cells, preactivated for 6 hours with IL-2 (1000 IU/mL) and IL-15 (10 ng/mL), were counted, resuspended at 1×10^6 cells/mL in NK MACS medium, and 100 µL were added to each well. Protamine sulphate (10 µg/mL) was added, and cells were subjected to spinoculation at 1000 × g for 90 min, with no brake, before transfer into an incubator at 37°C and 5% CO_2. After 24 hours, the medium was supplemented with fresh IL-2 (1000 IU/mL) and IL-15 (10 ng/mL), and cultures were maintained for an additional 48 hours before checking for transduction efficiency with flow cytometry.

2.2.15 – Multiplex immunofluorescence

Multiplex immunofluorescence staining was performed on 4-µm formalin-fixed, paraffin-embedded (FFPE) sections by the Translation Histopathology Laboratory (THL, Oxford Cancer Centre). Sections were stained using the OPAL protocol (AKYOA Biosciences) on a Leica BOND Auto-Stainer (Leica, Microsystems). Six consecutive staining cycles were performed using the following antibody-Opal fluorophore pairings: E-Cadherin-Opal780 (magenta), CD19-Opal520 (green), CD8α-Opal690 (red), NK1.1-Opal620 (orange), CD11c-Opal480 (cyan), CD103-Opal570 (yellow) and DAPI (blue). Batched multispectral images were fused in the HALO AI Software to produce reconstructed whole tissue images. The regions of interest within each section were outlined, annotated, and analysed.

2.2.16 – Tissue immunohistochemistry

NK1.1 staining was performed by the THL. Briefly, antigen retrieval was carried out in citrate buffer using a pressure cooker. Samples were cooled to 80 °C, then placed on ice for 1 hour before washing, blocking, and incubation with primary antibody overnight at 4 °C in a moist chamber. After washing, slides were incubated with secondary antibody for 30 minutes at room temperature. Signal was developed using DAB substrate and counterstained with Gill's haematoxylin for 20 seconds. Slides were washed, dehydrated, cleared, mounted, and scanned.

2.2.17 – Sample size determination and statistical analysis

Based on the ARRIVE 2.0 guidelines (Percie du Sert et al. 2020), 6–8 mice per group would have been required to achieve adequate statistical power in survival and immune phenotyping studies, after accounting for expected attrition (e.g., failure of orthotopic tumour engraftment). In the experiments presented in this thesis, smaller group sizes (n = 3–4 per group) were used due to logistical and resource constraints. Because underpowered studies are primarily at risk of type II error but may still detect statistically significant effects when effect sizes are large, formal statistical testing was not excluded entirely. Non-parametric tests were used, under the assumption that normality could not be reliably assessed with such small sample sizes. Statistical analyses were performed for unpaired comparisons with $n > 3$ per group, and were not conducted for unpaired comparisons with $n \leq 3$ or for paired comparisons with $n \leq 4$, as non-parametric tests cannot achieve statistical significance in these circumstances, irrespective of effect size.

2.2.18 – Data analysis

SpectroFloTM v2.2 software (Cytek Biosciences) was used for panel design. Flow cytometry data was analysed using FlowJo software v10.1. FlowSOM was run using four metaclusters, a number selected *a priori* to reflect the expected major NK cell phenotypic subgroups ($CD103^{+}CD49a^{+}$, $CD103^{+}$, $CD49a^{+}$, and $CD103^{-}CD49a^{-}$), and because higher cluster numbers did not yield additional clusters discernible by visual inspection. FlowSOM clustering was performed on concatenated samples from the same tissue type using t-SNE–reduced data generated in FlowJo with default parameters (including distance metrics). The HALO AI Software v3.6.4134.137 was used for analysis of multiplex immunofluorescence data.

Chapter 3

3. Design and optimisation of a spectral flow cytometry panel for comprehensive immune profiling in mouse models of PDAC

3.1

Introduction

Flow cytometry and immunology have developed in such close synergy that the relationship between the two has been described as a “marriage” (Cossarizza et al. 2021). This technique enables multiparametric, single-cell resolution analysis of immune cells circulating in the blood, residing in lymphoid organs, and infiltrating into tumours. Two types of flow cytometry can be employed in immunological research: conventional and spectral.

Conventional flow cytometry detects fluorescence at specific wavelengths using individual detectors, which limits the number of fluorochromes that can be used simultaneously due to the spectral overlap among similar fluorochromes (De Rosa et al. 2001). In contrast, spectral flow cytometry captures fluorescence emission across the entire spectrum using an array of detectors, which enables the simultaneous detection of up to 50 fluorochromes in a single panel (Park et al. 2024; Konecny et al. 2024).

Numerous flow cytometry panels have been developed for immuno-oncology research; however, most exhibit one or more of three key

limitations. First, the vast majority are designed for human studies, with significantly fewer tailored to characterising immune responses in murine models. While human-focussed panels are essential (e.g., for evaluating immune cell dynamics in patients before and after immunotherapy), their utility becomes limited when the goal is to investigate tumour immunity in preclinical models. Because mechanistic insights into tumour–immune interactions are still largely derived from animal studies, it is imperative that dedicated tools for immune profiling in mice are established.

Second, most panels focus on characterising specific leukocyte subsets, such as T cells (Natalini et al. 2021; Buus et al. 2019) or antigen-presenting cells (DiPiazza et al. 2019), failing to enable extensive, pan-immune profiling. These subset-specific panels are useful for researchers interested in particular aspects of the anti-tumour immune response; however, they are poorly suited to capturing the full picture of tumour immunity, which is now understood to involve a far more complex and heterogeneous interplay of immune cell populations than previously appreciated, as extensively reviewed elsewhere (de Visser and Joyce 2023).

Third, murine panels developed to date have been optimised using blood cells, splenocytes, or thymocytes (Mincham et al. 2021; Kare et al. 2023), rather than tumour-infiltrating immune cells. Whereas circulating and lymphoid-resident leukocytes are useful for assessing systemic immune responses to cancer, they should not be used as surrogates for the local immune response within the TME. This is because immune cells do not

merely transit through the TME *en route* to or from the circulation or lymphoid tissues; instead, they acquire distinct transcriptional, phenotypic, and functional states after exposure to metabolic, cellular, and molecular cues in the TME. These differences have been clearly documented in a variety of mouse and human tumours (Quinn et al. 2003; Ling et al. 2007; Chaturvedi et al. 2014; Casanova-Acebes et al. 2021). In addition, immune cell subsets capable of establishing long-term residency in peripheral tissues have been described, that differ from their circulating counterparts (D. Masopust et al. 2001; David Masopust et al. 2010; Boyman et al. 2004; Sojka et al. 2014; Mackay et al. 2012; Peng et al. 2013). Although these populations are not tumour-specific and can be found under both homeostatic and other pathological conditions, their existence further highlights the importance of analysing tissue- and tumour-specific immune cells to accurately characterise local tumour immunity.

3.2

Aims

To design and optimise a spectral flow cytometry panel that addresses three key limitations of existing panels, specifically:

I. Enables profiling of tumour immunity in murine cancer models;
II. Allows comprehensive identification of all major immune populations involved in tumour immunity, spanning both myeloid and lymphoid lineages, as well as innate and adaptive compartments;
III. Incorporates markers of tissue residency and is optimised using immune cells isolated directly from the tumour.

3.3

Results

3.3.1 Marker identification

The initial step in panel design involved identifying suitable markers to define all populations and subsets of interest. This selection was guided by an extensive review of the literature. Inclusion of a marker in the panel was contingent on meeting two criteria: its ability to define the population of interest (either alone or in combination with other markers), and its expression in the C57BL/6J mouse strain. The choice of some markers was relatively straightforward, including: CD19 for B cells (Liechti and Roederer 2019), CD3 for T cells with FoxP3 for the Treg subset and CD44/CD62L for the naïve, central memory (T_{CM}), and effector memory (T_{EM}) subsets (Natalini et al. 2021), γδ TCR for γδ T cells (Buus et al. 2019), and CD11b alongside F4/80 for macrophages (Z. Liu et al. 2020). Certain populations required more careful consideration; these are discussed below.

NK cells

As discussed in the main Introduction, NK cells are defined as $CD3^{-}CD19^{-}CD56^{+}$ lymphocytes in humans and as $NK1.1^{+}$, $NKp46^{+}$, or $CD49b^{+}$ lymphocytes in mice. To identify the most suitable NK cell lineage marker for inclusion in the panel, a pilot study was conducted in which the expression of three candidate markers—NK1.1, NKp46, and CD49b—was analysed by flow cytometry in the blood, spleen, liver, and tumours of C57BL/6J mice bearing orthotopic pancreatic tumours (**Figure 3.1A**). The degree of overlap among these markers at each anatomical site is shown in

(**Figure 3.1B**), where counts represent the number of cells expressing a given marker among 1,000 $CD3^{-}CD19^{-}$ live $CD45^{+}$ cells. Notably, expression patterns varied across tissues, and a substantial number of cells expressed only one or two of the three markers. Based on this observation, a metric of *marker specificity* was introduced, defined as the ratio between the number of triple-positive ($NK1.1^{+}NKp46^{+}CD49b^{+}$) cells and the total number of cells positive for the marker of interest at each site. This approach was based on the observation that bone marrow NK cells are more likely to co-express all three markers, whereas cells expressing only one or two markers represent other innate populations, such as NK cell progenitors or immature NK cells (Ma et al. 2022) or ILCs, as initial reports described these cells as $NKp46^{+}$ (type 3 ILCs, or ILC3s) (Sanos et al. 2009) or $NK1.1^{+}NKp46^{+}$ (ILC1s) (Fuchs et al. 2013).

Although a Friedman test would have been appropriate for comparing the three candidate markers with larger sample sizes, formal statistical analysis was not performed due to the limited sample size (n = 3), which would render such comparisons underpowered. Instead, the median marker specificity was assessed. NK1.1 displayed the higher median marker specificity across three of four tissues (liver, spleen, and blood); in the tumour, the specificity of the three selected markers was comparable (median: 72.0% for NK1.1, 74.5% for NKp46 and 73.9% for CD49b). As a result, NK1.1 was chosen as the NK-defining marker for the panel (**Figure 3.1C**).

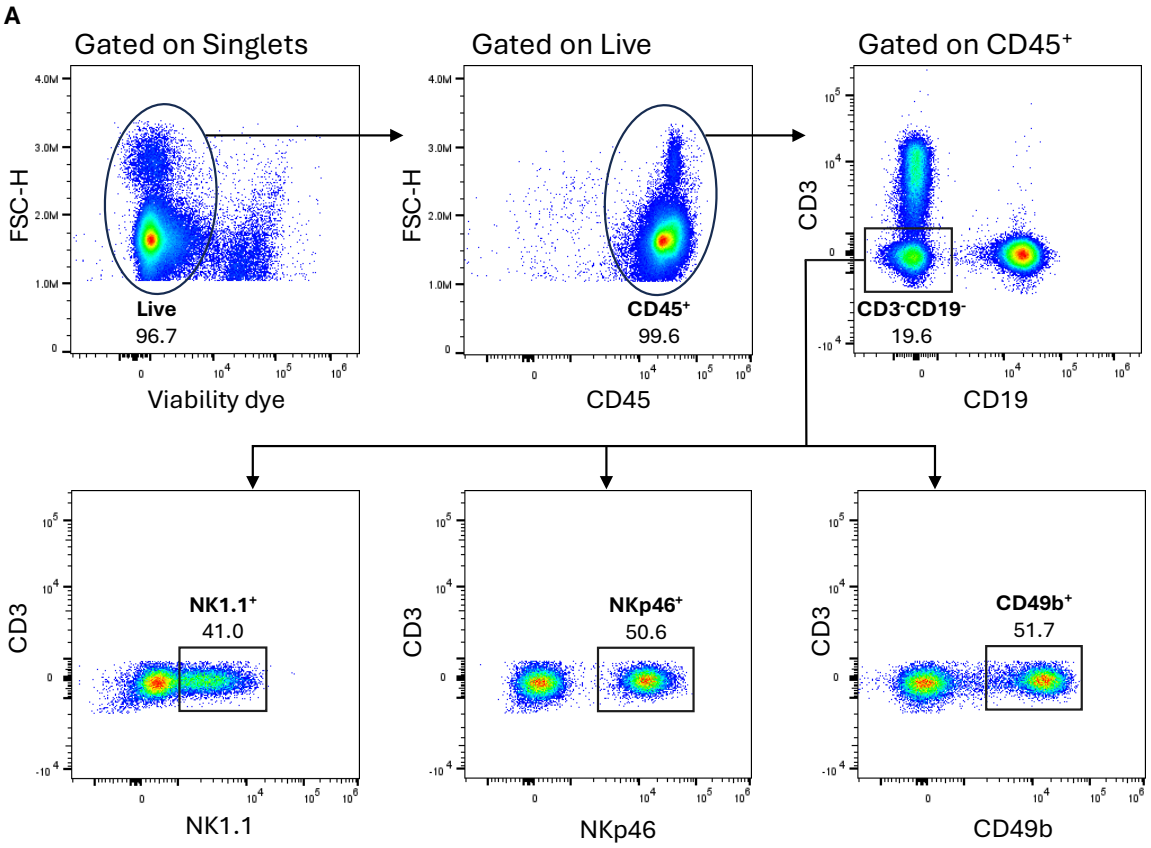
A
Gated on Singlets
Gated on Live
Gated on CD45+
FSC-H
Viability dye
Live
96.7
CD45
CD45+
99.6
CD3
CD19
CD3-CD19-
19.6
NK1.1+
41.0
NK1.1
NKp46+
50.6
NKp46
CD49b+
51.7
CD49b

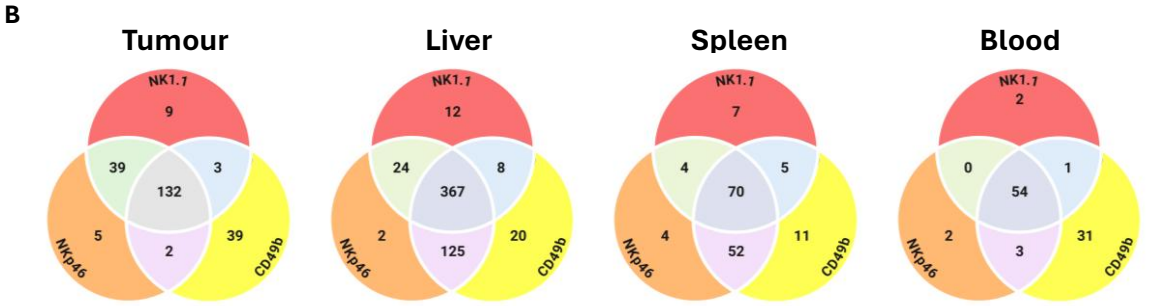
B
Tumour
Liver
Spleen
Blood
NK1.1
NKp46
CD49b
9
39
3
132
5
2
39
12
24
8
367
2
125
20
7
4
5
70
4
52
11
2
0
1
54
2
3
31

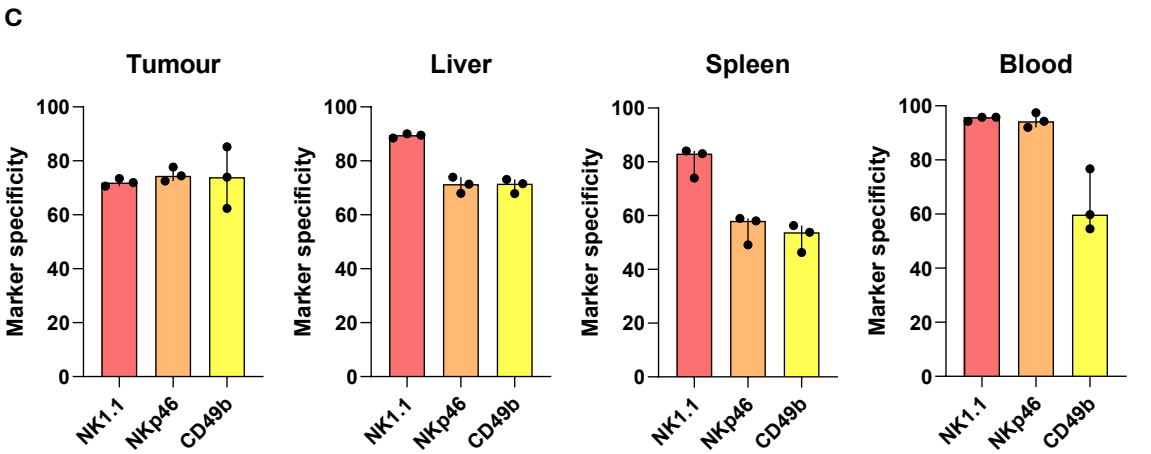
C
Tumour
Liver
Spleen
Blood
Marker specificity
100
80
60
40
20
0
NK1.1
NKp46
CD49b

Figure 3.1 – Selection of a specific NK cell lineage marker

A. Gating strategy used to quantify lineage marker expression in live $CD45^+CD3^-CD19^-$ cells from the blood, spleen, liver, and tumour of C57BL/6J mice with orthotopically implanted pancreatic tumours (KPC-F). Representative dot plots shown for one representative animal (liver).

B. Venn diagrams illustrating the overlap in expression of NK1.1, NKp46, and CD49b within each tissue. Numbers indicate the mean counts of marker-positive events among 1,000 live $CD45^+CD3^-CD19^-$ cells.

C. Relative specificity of each marker, defined as the percentage of triple-positive ($NK1.1^+NKp46^+CD49b^+$) cells among all cells positive for the marker of interest, for each anatomical compartment. Median and range shown.

Tissue resident lymphocytes

The concept of tissue residency was discussed extensively in the main Introduction relative to NK cells. The cell surface proteins that are traditionally employed as surrogates for tissue residency in NK cells can also be employed to define resident subsets of other lymphocytes. For example, human skin $CD8^+$ tissue-resident memory T cells (T_{RM}) develop in response to TGF-β and IL-15 and are $CD69^+CD103^+$, with some co-expressing CD49a (Mackay et al. 2015). Interestingly, T_{RM} cells developing independently of TGF-β and lacking CD103 expression have been reported in some tissues, including the intestine of mice (Bergsbaken and Bevan 2015). As CD69 is transiently upregulated on circulating T and NK cells following activation (Santis et al. 1992; Borrego et al. 1993), it was excluded from the panel. On the other hand, CD49a and CD103 were deemed more reliable markers of tissue residency in both $CD8^+$ T and NK cells.

ILC1s

Around the same period that trNK cells were first characterised, ILC1s were identified as a largely overlapping tissue-resident subset (Fuchs et al. 2013; Bernink et al. 2013). The nomenclature distinguishing conventional NK cells, trNK cells, and ILC1s is in constant evolution, and the overlap among these entities hard to dissect, as extensively reviewed elsewhere (Diefenbach et al. 2014; Serafini et al. 2015). However, previous studies have consistently shown that ILC1s also express NK1.1 and are inherently tissue-resident, as supported by the expression of CD49a (Bernink et al. 2013) and CD103 (Fuchs et al. 2013). Accordingly, these markers used to characterise trNK cells were also used to identify ILC1s in this panel, designating them as an overlapping rather than a distinct subset from trNK cells.

Myeloid-derived suppressor cells

Myeloid cells represent an important component of the TME, especially in solid tumours with poor lymphocytic infiltration (Engblom et al. 2016; S. T. Barry et al. 2023; Goswami et al. 2023). Within myeloid cells, neutrophils were defined in this panel as $CD3^{-}CD19^{-}Ly6G^{+}Ly6C^{+/-}$ cells and monocytes as $CD3^{-}CD19^{-}Ly6G^{-}Ly6C^{+}$ cells (Rose et al. 2012). Subsets of neutrophils and monocytes with suppressive functions (also known as polymorphonuclear- and monocytic myeloid-derived suppressor cells, PMN-MDSCs and M-MDSCs, respectively) have been described in the context of tumours, and the standardisation of their nomenclature is thoroughly discussed elsewhere (Bronte et al. 2016). According to these recommendations, functional assays are essential for the designation of

cells as MDSCs. Because this panel only identifies cells based on phenotype, cells identified using this panel should simply be termed *neutrophils* / *monocytes* (and their subsets, *cells with a PMN-MDSC* / *M-MDSC phenotype*, respectively).

Macrophage and dendritic cell subsets

Markers were included in the panel to enable the classification of conventional dendritic cell (cDC) subsets. Within cDCs ($CD11c^+$I-A/I-E^+), $XCR1^+$ type 1 cDCs (cDC1s) and $SIRP\alpha^+$ type 2 cDCs (cDC2s) were classified, following established guidelines for the flow cytometric analysis of dendritic cells from murine non-lymphoid tissues (DiPiazza et al. 2019; Probst et al. 2023). Similarly, macrophage subsets were distinguished using established polarisation markers, with classically activated M1 macrophages expressing CD86 and alternatively activated M2 macrophages expressing Arginase-1 (Liyuan Liu et al. 2022). It is important to note that these markers are not expressed in a mutually exclusive fashion; in fact, both macrophages and dendritic cells are increasingly understood as existing along a phenotypic continuum rather than discrete states. As such, while the panel supports basic characterisation of these populations, studies requiring in-depth analysis of the role of tumour-associated macrophages or dendritic cells in tumour immunity would necessitate the inclusion of additional markers. A summary of the populations of interest and corresponding markers is provided in **Table 3.1**.

POPULATIONS	IDENTIFYING MARKERS										
Live Leukocytes	DCM$^-$	CD45$^+$									
B cells	DCM$^-$	CD45$^+$	CD3$^-$	CD19$^+$							
αβ T cells	DCM$^-$	CD45$^+$	CD3$^+$	CD19$^-$	γδ TCR$^-$	NK1.1$^-$					
CD4$^+$ T	DCM$^-$	CD45$^+$	CD3$^+$	CD19$^-$	γδ TCR$^-$	NK1.1$^-$	CD4$^+$	CD8$^-$			
Tregs	DCM$^-$	CD45$^+$	CD3$^+$	CD19$^-$	γδ TCR$^-$	NK1.1$^-$	CD4$^+$	CD8$^-$	FoxP3$^+$		
CD4$^+$ $T_{naïve}$	DCM$^-$	CD45$^+$	CD3$^+$	CD19$^-$	γδ TCR$^-$	NK1.1$^-$	CD4$^+$	CD8$^-$	FoxP3$^-$	CD44$^-$	CD62L$^+$
CD4$^+$ T_{EM}	DCM$^-$	CD45$^+$	CD3$^+$	CD19$^-$	γδ TCR$^-$	NK1.1$^-$	CD4$^+$	CD8$^-$	FoxP3$^-$	CD44$^+$	CD62L$^-$
CD4$^+$ T_{CM}	DCM$^-$	CD45$^+$	CD3$^+$	CD19$^-$	γδ TCR$^-$	NK1.1$^-$	CD4$^+$	CD8$^-$	FoxP3$^-$	CD44$^+$	CD62L$^+$
CD8$^+$ T	DCM$^-$	CD45$^+$	CD3$^+$	CD19$^-$	γδ TCR$^-$	NK1.1$^-$	CD4$^-$	CD8$^+$			
CD8$^+$ $T_{naïve}$	DCM$^-$	CD45$^+$	CD3$^+$	CD19$^-$	γδ TCR$^-$	NK1.1$^-$	CD4$^-$	CD8$^+$	CD44$^-$	CD62L$^+$	
CD8$^+$ T_{EM}	DCM$^-$	CD45$^+$	CD3$^+$	CD19$^-$	γδ TCR$^-$	NK1.1$^-$	CD4$^-$	CD8$^+$	CD44$^+$	CD62L$^-$	
CD8$^+$ T_{CM}	DCM$^-$	CD45$^+$	CD3$^+$	CD19$^-$	γδ TCR$^-$	NK1.1$^-$	CD4$^-$	CD8$^+$	CD44$^+$	CD62L$^+$	
CD8$^+$ T_{RM}	DCM$^-$	CD45$^+$	CD3$^+$	CD19$^-$	γδ TCR$^-$	NK1.1$^-$	CD4$^-$	CD8$^+$	CD103$^+$	CD49a$^+$	
γδ T cells	DCM$^-$	CD45$^+$	CD3$^+$	CD19$^-$	γδ TCR$^+$	NK1.1$^-$					
NKT cells	DCM$^-$	CD45$^+$	CD3$^+$	CD19$^-$	γδ TCR$^-$	NK1.1$^+$					
Neutrophils	DCM$^-$	CD45$^+$	CD3$^-$	CD19$^-$	Ly6C$^-$	Ly6G$^+$					
Monocytes	DCM$^-$	CD45$^+$	CD3$^-$	CD19$^-$	Ly6C$^+$	Ly6G$^-$					
Macrophages	DCM$^-$	CD45$^+$	CD3$^-$	CD19$^-$	Ly6C$^-$	Ly6G$^-$	CD11b$^+$	F4/80$^+$			
M1 macrophages	DCM$^-$	CD45$^+$	CD3$^-$	CD19$^-$	Ly6C$^-$	Ly6G$^-$	CD11b$^+$	F4/80$^+$	CD86$^+$	Arg-1$^-$	
M2 macrophages	DCM$^-$	CD45$^+$	CD3$^-$	CD19$^-$	Ly6C$^-$	Ly6G$^-$	CD11b$^+$	F4/80$^+$	CD86$^{+/-}$	Arg-1$^+$	
cDCs	DCM$^-$	CD45$^+$	CD3$^-$	CD19$^-$	Ly6C$^-$	Ly6G$^-$	I/A-I/E$^+$	CD11c$^+$			
cDC1	DCM$^-$	CD45$^+$	CD3$^-$	CD19$^-$	Ly6C$^-$	Ly6G$^-$	I/A-I/E$^+$	CD11c$^+$	XCR1$^+$	SIRPα$^-$	
cDC2	DCM$^-$	CD45$^+$	CD3$^-$	CD19$^-$	Ly6C$^-$	Ly6G$^-$	I/A-I/E$^+$	CD11c$^+$	XCR1$^-$	SIRPα$^+$	
NK cells	DCM$^-$	CD45$^+$	CD3$^-$	CD19$^-$	Ly6C$^-$	Ly6G$^-$	I/A-I/E$^{+/-}$	CD11c$^{+/-}$	NK1.1$^+$		
trNK/ILC1	DCM$^-$	CD45$^+$	CD3$^-$	CD19$^-$	Ly6C$^-$	Ly6G$^-$	I/A-I/E$^{+/-}$	CD11c$^{+/-}$	NK1.1$^+$	CD103$^+$	CD49a$^+$

Table 3.1 – Cell identification table and selected markers

3.3.2 Assignment of fluorochromes to markers

The markers identified in 3.3.1 were grouped according to their expected antigen density (high, medium, low, or variable/unknown) based on a review of the relevant literature. As the primary goal of this panel was to enumerate immune cell populations rather than to characterise their function,

activation status, or migratory behaviour, markers related to those aspects were not included at this stage. Consequently, the majority of the selected markers represent lineage-defining antigens that are typically expressed at high surface densities.

A list of commercially available fluorochrome-conjugated antibodies for each marker was then compiled after interrogating the dedicated search engine *FluoroFinder*. Overall, 47 potential fluorochromes were identified and grouped into five categories using investigator-defined thresholds based on stain index data provided by the cytometre manufacturer (**Figure 3.2**). As discussed below, the stain index measures how well a dye distinguishes positive from negative populations, with higher values indicating increased brightness.

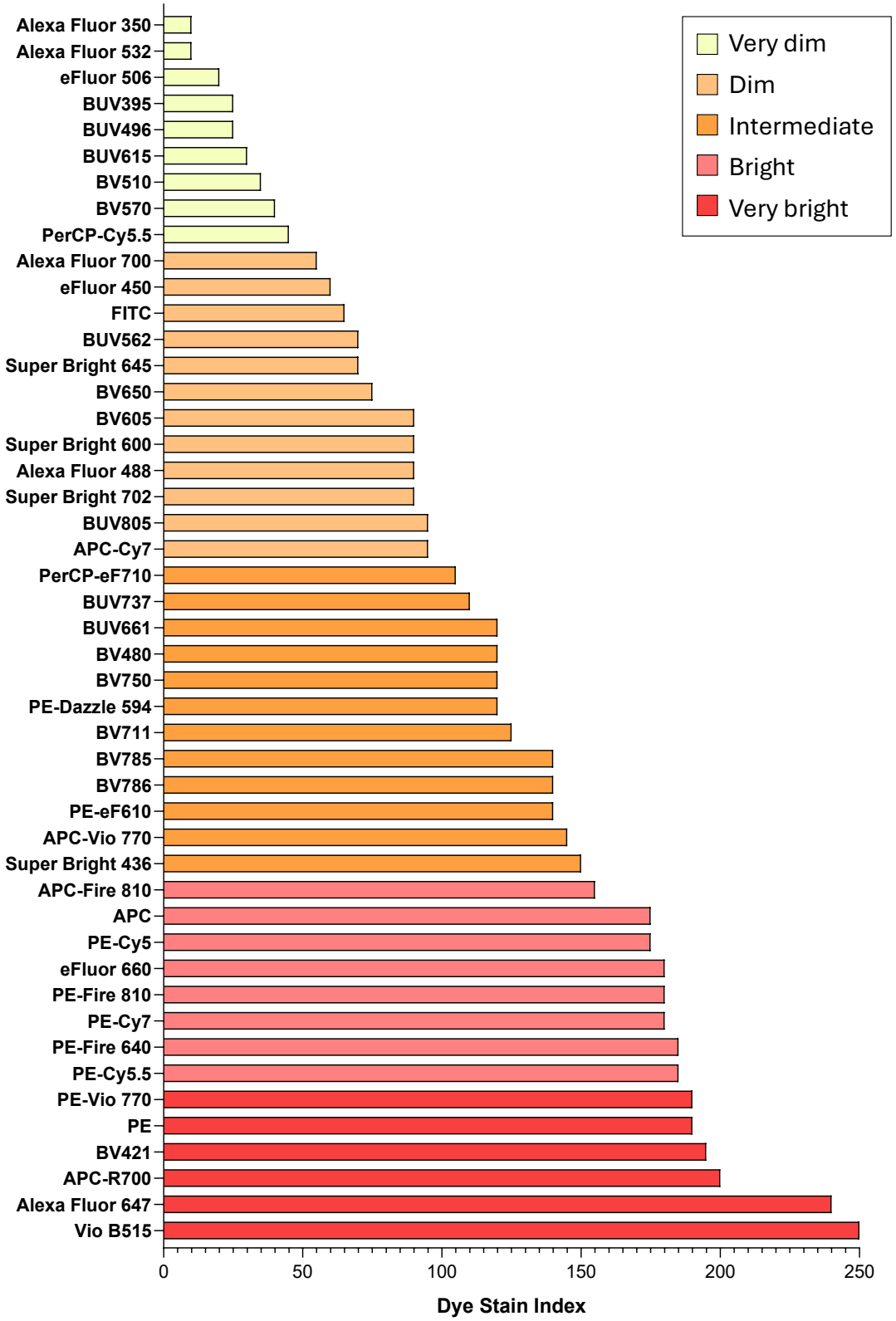

Figure 3.2 – Stain index ranking of 47 potential fluorochromes

Fluorochromes were categorised by brightness according to investigator-defined thresholds based on stain index values: very dim (0–50), dim (51–100), intermediate (101–150), bright (151–190), and very bright (191–250).

Multiple fluorochrome configurations were evaluated, and each candidate panel was assessed using two key metrics: the Similarity Index (SI) and the Complexity Index (CI). The Similarity Index quantifies spectral overlap between pairs of fluorochromes, ranging from 0 (completely distinct) to 1 (identical). The Complexity Index, instead, reflects the overall capacity of the panel to resolve multiple fluorochromes at the same time in a process known as spectral unmixing. In general, pairs with an SI exceeding 0.98 are considered difficult to distinguish reliably and are, therefore, avoided. Combinations of fluorochromes with spectral signatures as different as possible from each other were identified, so as to minimise the SI between any given pair and, as a result, reduce the overall CI of the panel. After several iterations, the combination of fluorochromes shown in **Figure 3.3A** was chosen, with an overall CI of 4.88. Other, suboptimal configurations tested displayed a CI as high as 40 (not shown).

Once a list of definitive fluorochromes was outlined, each antigen was assigned to a fluorochrome according to its expression level and the relative brightness of the fluorochrome, following two principles:

1. Antigens with limited options in terms of commercially available conjugates (such as Arginase-1 and XCR1) were prioritised in the assignment process, while those with broader fluorochrome availability (such CD4 and CD8α) were allocated later.
2. Brighter fluorochromes were preferentially reserved for the few targets with moderate or variable expression, whereas dimmer

fluorochromes were paired with highly expressed markers, following good practice in panel design (Cossarizza et al. 2021).

In addition to these rules, the Stain Index Reduction (SIR) Matrix, also known as Cross-Stain Index Matrix (**Figure 3.3B**), was used to evaluate signal spread between fluorochromes with similar emission spectra. The SIR matrix helps quantify how fluorescence spillover from one dye affects detection of another dye, thereby measuring the likelihood of spreading error. Fluorophore pairs with high SIR values were assigned to antigens that are not co-expressed or to markers used to exclude populations that were not of interest (e.g., the viability dye for dead cells), following good practice in panel design as above.

A

	BUV395	LIVE DEAD Blue	BUV496	BUV563	BUV615	BUV737	BUV805	Super Bright 436	BV510	Super Bright 600	Super Bright 702	BV785	Vio B515	Alexa Fluor 532	PE	PE-Dazzle 594	PE-Cy5	PerCP-eFluor 710	PE-Vio 770	APC	Alexa Fluor 700	APC-Cy7	APC-Fire 810
BUV395	1.00																						
LIVE DEAD Blue	0.60	1.00																					
BUV496	0.27	0.57	1.00																				
BUV563	0.09	0.15	0.39	1.00																			
BUV615	0.06	0.08	0.15	0.40	1.00																		
BUV737	0.04	0.04	0.03	0.02	0.15	1.00																	
BUV805	0.16	0.15	0.09	0.04	0.08	0.41	1.00																
Super Bright 436	0.08	0.29	0.12	0.02	0.02	0.01	0.02	1.00															
BV510	0.09	0.24	0.57	0.32	0.21	0.03	0.04	0.22	1.00														
Super Bright 600	0.02	0.05	0.09	0.16	0.44	0.06	0.03	0.13	0.44	1.00													
Super Bright 702	0.02	0.05	0.03	0.02	0.10	0.39	0.11	0.17	0.10	0.21	1.00												
BV785	0.01	0.03	0.02	0.01	0.04	0.23	0.25	0.10	0.05	0.09	0.42	1.00											
Vio B515	0.01	0.01	0.09	0.06	0.01	0.00	0.00	0.00	0.02	0.01	0.00	0.00	1.00										
Alexa Fluor 532	0.05	0.09	0.16	0.30	0.08	0.02	0.02	0.02	0.11	0.08	0.02	0.02	0.44	1.00									
PE	0.01	0.02	0.08	0.35	0.15	0.01	0.01	0.01	0.20	0.24	0.01	0.01	0.10	0.62	1.00								
PE-Dazzle 594	0.01	0.02	0.04	0.15	0.21	0.04	0.01	0.01	0.11	0.33	0.05	0.02	0.05	0.38	0.51	1.00							
PE-Cy5	0.00	0.01	0.01	0.03	0.08	0.16	0.02	0.00	0.02	0.10	0.21	0.04	0.01	0.10	0.12	0.43	1.00						
PerCP-eFluor 710	0.01	0.02	0.02	0.02	0.08	0.39	0.08	0.00	0.04	0.12	0.61	0.26	0.00	0.04	0.04	0.20	0.53	1.00					
PE-Vio 770	0.00	0.00	0.01	0.01	0.02	0.21	0.12	0.00	0.01	0.03	0.13	0.29	0.00	0.03	0.02	0.06	0.15	0.38	1.00				
APC	0.00	0.01	0.01	0.01	0.05	0.20	0.03	0.00	0.02	0.08	0.32	0.04	0.00	0.01	0.01	0.03	0.39	0.21	0.03	1.00			
Alexa Fluor 700	0.01	0.03	0.02	0.01	0.03	0.48	0.08	0.00	0.02	0.03	0.57	0.11	0.00	0.01	0.00	0.01	0.21	0.42	0.08	0.44	1.00		
APC-Cy7	0.01	0.01	0.01	0.01	0.01	0.31	0.21	0.00	0.01	0.01	0.25	0.24	0.00	0.00	0.00	0.00	0.08	0.18	0.19	0.19	0.39	1.00	
APC-Fire 810	0.01	0.02	0.02	0.01	0.02	0.21	0.27	0.00	0.02	0.02	0.18	0.22	0.00	0.01	0.00	0.01	0.08	0.15	0.15	0.18	0.27	0.68	1.00

Complexity Index: 4.88

B

	BUV395	LIVE DEAD Blue	BUV496	BUV563	BUV615	BUV737	BUV805	Super Bright 436	BV510	Super Bright 600	Super Bright 702	BV785	Vio B515	Alexa Fluor 532	PE	PE-Dazzle 594	PE-Cy5	PerCP-eFluor 710	PE-Vio 770	APC	Alexa Fluor 700	APC-Cy7	APC-Fire 810
BUV395			19	2						2	11	2		4									
LIVE DEAD Blue	84		62	22	5			84	48	5	26			38		21	7			56			10
BUV496				20					24	7	9			17									
BUV563			16		38					6	10			42	48	14							
BUV615			11	19		39	33			59	19	6		4		17		2					
BUV737	2		8				75			1	28	36		4				54	32		59	35	30
BUV805	10		14			19				4	13	14		4									30
Super Bright 436			19	1					2	6	15	4		4									
BV510			41	33	10					18	19	2		8	1								
Super Bright 600			19	15	63	8	9	7			32	12		8		10							
Super Bright 702			16		1	56	43	28		10		53		4				6			49	22	21
BV785			19			45	72	5			18			4								12	28
Vio B515			3							1				83	63	35							30
Alexa Fluor 532			19	3						1	12				14	8							
PE				36	19		10		13	7	10			33		53	19	22					2
PE-Dazzle 594			19	6	47					54	28	3		8	27		54	48	12	21			
PE-Cy5					12	30	30		7		46	18		21	5	17		69	49	73	18	19	16
PerCP-eFluor 710			16	3		52	34			7	65	43		4			30		62	6	41	20	21
PE-Vio 770						17	55				6	56		8								47	41
APC					9	18	22				11	3		21		5		5			26	23	21
Alexa Fluor 700			14				1			2	21			4								10	14
APC-Cy7			14			4	41			5	17	53											60
APC-Fire 810			16				41				11	37		4						6		28	

Figure 3.3 – Metrics for panel assessment – SI, CI, and SIR matrix
A. SI and overall CI for the fluorochromes in the definitive panel. The highest SI in the panel was 0.68, with a resultant overall CI of 4.88.
B. SIR Matrix for the definitive panel. The SIR matrix assesses the degree of spreading error (or spillover) between two dyes with similar emissions.

A few notable exceptions were made to the rules outlined above:

- APC-Fire 810, a bright fluorochrome, was assigned to CD19 despite its high antigen density on B cells, in order to achieve a balanced distribution of markers across the spectrum. Assigning all primary antigens to dim fluorochromes would have created an imbalance between channels primarily detecting dim fluorochromes (UV-V regions) and those primarily detecting brighter ones (B-R regions).
- PE-Cy5, another bright fluorochrome, was paired with Ly6G, an antigen highly expressed on neutrophils. This decision was based on the fact that PE-Cy5 introduces significant spread into PerCP-eFluor710 and APC, which were assigned to γδ TCR and XCR1, respectively. As these three markers are not co-expressed, this configuration helps preserve the resolution of low-intensity signals while minimising spillover errors, as discussed above.
- BUV737 was assigned to CD11b (Integrin alpha M), variably expressed on myeloid cells, cDC2s, and NK cells. The main spreading concerns involved BUV805 (assigned to CD8α to avoid co-expression) and Alexa Fluor 700 (assigned to I-A/I-E, the murine Major Histocompatibility Complex, MHC, Class II). Although CD11b and I-A/I-E can be co-expressed on M1 macrophages and cDC2s, initial testing of the panel showed clear separation of I-A/I-E^{+} cells from negatives (not shown).

- VioB515, the brightest fluorochrome in the panel, was assigned to FoxP3, a canonical marker of Tregs. While VioB515 can cause spillover into Alexa Fluor 532, the low abundance of Tregs within the total $CD45^+$ population rendered this spillover a largely theoretical concern.

Lastly, LIVE/DEAD Blue Fixable Viability Dye was selected as the dead cell marker because it resulted in a lower overall complexity index when compared to other alternatives (4.88 vs 9.14 for Zombie Near InfraRed and 11.65 for LIVE/DEAD Yellow) and because, when tested, provided a clear separation between positive (dead) and negative (live) cells. Throughout this thesis, LIVE DEAD Blue was used as the viability dye for the majority of experiments, and any exceptions to this are explicitly indicated.

A summary of the definitive fluorochrome-marker allocations is provided in **Table 3.2**. The distribution of fluorochromes across the spectrum is shown in **Figure 3.4**, alongside the cytometre (Cytek Aurora 4-Laser 16UV-16V-14B-8R) configuration and acquisition settings used for all runs.

Specificity	Fluorochrome	Clone	Purpose
Dead Cells	LIVE/DEAD Blue	NA	Dead cell marker
CD45	Alexa Fluor 532	30-F11	Pan-leukocyte marker
CD19	APC-Fire810	6D5	B cell lineage
CD3	BUV395	17A2	T and NKT cell lineage
CD4	BUV496	RM4-5	T cell subset
CD8α	BUV805	53-6.7	T cell subset
FoxP3	Vio B515	REA788	T cell subset
CD44	BV510	IM7	T cell subset
CD62L	Super Bright 702	MEL-14	T cell subset
γδ TCR	PerCP-eF710	eBioGL3	T cell subset
CD103	Super Bright 600	2E7	T and NK/ILC1 cell subset
CD49a	PE-Vio770	REA493	T and NK/ILC1 cell subset
NK1.1	Super Bright 436	PK136	NK and NKT cell lineage
Ly6G	PE-Cy5	1A8	Neutrophil lineage
Ly6C	APC-Cy7	HK1.4	Monocyte lineage
CD11b	BUV737	M1/70	Macrophage lineage
F4/80	BUV563	BM8	Macrophage lineage
CD86	BV785	GL-1	Macrophage subset
Arginase-1	PE	W21047I	Macrophage subset
CD11c	BUV615	N418	Conventional dendritic cell lineage
I-A/I-E	Alexa Fluor 700	M5/114.15.2	Conventional dendritic cell lineage
SIRPα	PE-Dazzle594	P84	Conventional dendritic cell subset
XCR-1	APC	REA707	Conventional dendritic cell subset

Table 3.2 – Fluorochrome-marker allocations in the definitive panel

Laser (Solid state)	Channel	Fluorochrome with peak emission	Center Wavelength (nm)	Bandwidth (nm)	Wavelength Start (nm)	Wavelength End (nm)	Detector Gain (Cytek Settings)
Ultraviolet 355 nm 20 mW	UV1	-	373	15	365	380	975
	UV2	BUV395	388	15	380	395	194
	UV3	-	428	15	420	435	400
	UV4	-	443	15	436	451	481
	UV5	-	458	15	451	466	379
	UV6	LIVE/DEAD Blue	473	15	466	481	314
	UV7	BUV496	514	28	500	528	369
	UV8	-	542	28	528	556	324
	UV9	BUV563	582	31	566	597	388
	UV10	BUV615	613	31	597	628	221
	UV11	-	664	27	651	678	339
	UV12	-	692	28	678	706	291
	UV13	-	720	29	706	735	442
	UV14	BUV737	750	30	735	765	870
	UV15	-	780	30	765	795	521
	UV16	BUV805	812	34	795	829	743
Violet 405 nm 100 mW	V1	-	428	15	420	435	205
	V2	Super Bright 436	443	15	436	451	252
	V3	-	458	15	451	466	238
	V4	-	473	15	466	481	176
	V5	-	508	20	498	518	253
	V6	-	525	17	516	533	190
	V7	BV510	542	17	533	550	285
	V8	-	581	19	571	590	379
	V9	-	598	20	588	608	360
	V10	Super Bright 600	615	20	605	625	311
	V11	-	664	27	651	678	281
	V12	-	692	28	678	706	225
	V13	Super Bright 702	720	29	706	735	256
	V14	-	750	30	735	765	301
	V15	BV785	780	30	765	795	389
	V16	-	812	34	795	829	318
Blue 488 nm 50 mW	B1	Vio B515	508	20	498	518	622
	B2	-	525	17	516	533	377
	B3	Alexa Fluor 532	542	17	533	550	340
	B4	PE	581	19	571	590	323
	B5	-	598	20	588	608	268
	B6	PE-Dazzle 594	615	20	605	625	214
	B7	-	661	17	653	670	483
	B8	PE-Cy5	679	18	670	688	327
	B9	-	697	19	688	707	501
	B10	PerCP-eFluor 710	717	20	707	727	447
	B11	-	738	21	728	479	315
	B12	-	760	23	749	772	311
	B13	PE-Vio 770	783	23	772	795	412
	B14	-	812	34	795	829	539
Red 640 nm 80 mW	R1	APC	661	17	653	670	243
	R2	-	679	18	670	688	251
	R3	-	697	19	688	707	316
	R4	Alexa Fluor 700	717	20	707	727	325
	R5	-	738	21	728	749	197
	R6	-	760	23	749	772	202
	R7	APC-Cy7	783	23	772	795	321
	R8	APC-Fire 810	812	34	795	829	208

Figure 3.4 – Configuration and settings of the Cytek Aurora 4-Laser
Lasers and filter configurations and detector gains were set according to manufacturer's standards (Cytek Assay Settings). For each laser type, the wavelength and power are shown. Fluorochromes are shown next to the channel detecting the relative peak fluorescent emission. Only the three scatter channels (FSC, SSC, and SSC-B) were adjusted at every run so as to ensure that cells were on scale, and typically as follows: FSC: 100 – SSC: 300 – SSC-B: 150.

3.3.3 Reagent titrations

Antibody titration is an absolute requirement for the development of a successful flow cytometry panel, since high titres can lead to increased background (due to non-specific binding) and issues with spillover, whereas low titres can cause under-detection (Ferrer-Font et al. 2021). Therefore, following reagent acquisition, each antibody was titrated individually to determine its optimal working concentration. Titrations were performed on live splenocytes isolated from wild-type C57BL/6J mice, with the exception of NK1.1 Super Bright 436 and γδ TCR PerCP-eFluor710, which were titrated using liver cells due to the lower expression of these markers in the spleen.

The optimal antibody concentration was determined through a combination of visual assessment (**Figure 3.5A,D**) and stain index analysis (**Figure 3.5B,C**). For each reagent, the stain index at a given concentration was calculated using FlowJo's built-in Stain Index plugin, which determines its value based on the following formula:

$$\text{Stain Index} = \frac{MFI_{positive} - MFI_{negative}}{2 \times SD_{negative}}$$

MFI: Mean fluorescence intensity; SD: Standard deviation

A *relative stain index* was then calculated for each concentration, expressed as a percentage of the maximal stain index observed across all tested concentrations. This metric was used to guide reagent selection: if a lower concentration yielded a relative stain index ≥60% and showed comparable (or superior) performance upon visual inspection, the lower concentration was selected for inclusion in the panel (**Figure 3.5E**). The 60% threshold was chosen empirically to balance signal intensity with reagent conservation.

A summary of the titrations for all reagents in the panel, including concatenated dot plots for the visual assessment of positive and negative populations at varying concentrations, along with the rationale for the selected optimal concentration, is presented in **Supplementary Figure 9.1**.

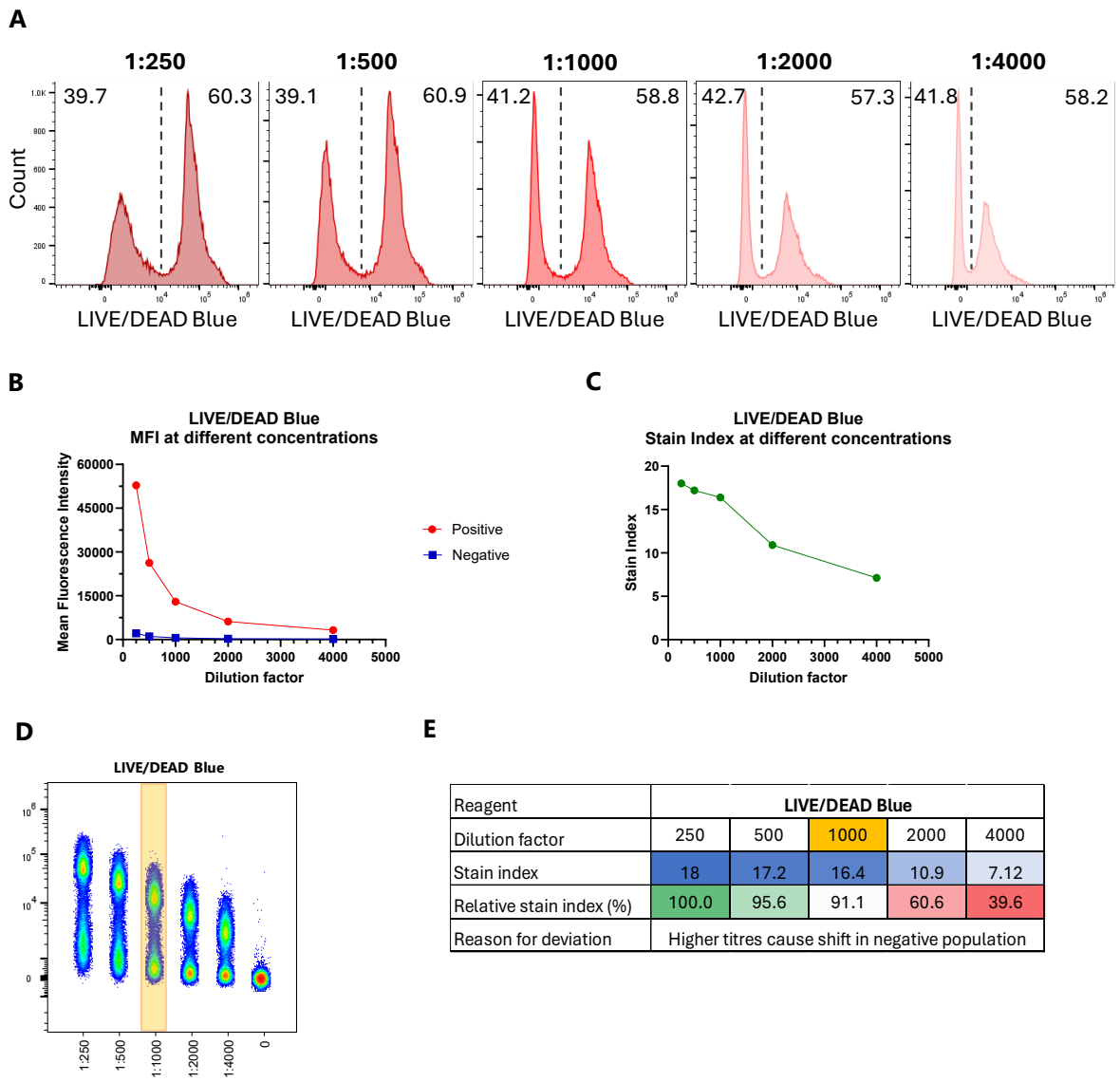

Reagent	LIVE/DEAD Blue				
Dilution factor	250	500	1000	2000	4000
Stain index	18	17.2	16.4	10.9	7.12
Relative stain index (%)	100.0	95.6	91.1	60.6	39.6
Reason for deviation	Higher titres cause shift in negative population				

Figure 3.5 – Titration of LIVE/DEAD Blue

A. Separation of positive and negative populations across a range of reagent dilutions. The fixable viability dye (LIVE/DEAD Blue) is shown as a representative example of the titration strategy applied to all reagents in the panel. Percentages of negative and positive populations are indicated in the top left and right corners, respectively.

B. Mean fluorescence intensity (MFI) of the positive (red) and negative (blue) populations across dilutions.

C. Stain index calculated at each dilution.

D. Concatenated dot plots illustrating population resolution and smearing across dilutions. The selected dilution is highlighted in yellow.

E. Relative stain index across dilutions, with rationale for the selection of a dilution yielding a stain index below the maximum stain index. The selected dilution is highlighted in yellow. Blue colour scale corresponds to stain index values (lighter: lower; darker: higher). Red-to-green colour scale corresponds to relative stain index values (red: lower; green: higher).

3.3.4 Reference controls

Good reference controls are crucial for successful unmixing. Two types of controls were used during the optimisation of the panel: unstained controls and single-colour controls.

Unstained controls were included in every run to enable autofluorescence extraction. To account for tissue-specific differences in baseline fluorescence, unstained controls were matched to the anatomical origin of the experimental samples (**Figure 3.6A**).

Single-colour controls were acquired for all reagents in the panel in order to generate the reference spectra of all fluorochromes. Best practice dictates that single-stained beads, single-stained cells, or a combination of both can be used as reference controls in a spectral flow cytometry panel but that, whenever feasible, reference controls should match the biological nature of the experimental samples, i.e., cells should be used for cell-based assays (Ferrer-Font et al. 2021; Cossarizza et al. 2021). Another essential requirement for a single-colour control to be used as reference is that it must exhibit a positive population with fluorescence intensity exceeding that of the positive population of a matched multi-colour experimental sample. Accordingly, both single-stained beads and cells were evaluated for each marker in this panel. For most markers, splenocytes from wild-type C57BL/6J mice were used, with the exception of PE-Cy5, where RBC-lysed blood cells were used, and Super Bright 436 and PerCP-eF710, where liver cells were used, due to the low frequency of $Ly6G^+$, $NK1.1^+$, and γδ TCR^+

cells in the spleen, respectively. For five markers, single-stained cells met the fluorescence intensity criterion above and were therefore used as spectral references for unmixing (**Figure 3.6B**). For all remaining markers, beads were used as reference controls.

Of note, reference controls for viability dyes are commonly prepared by staining a sample containing dead cells, under the assumption that dead cells will take up the dye and constitute the positive population, and the remaining cells will not, constituting the negative population. However, as dead and live cells exhibit distinct autofluorescence, the reference control for the LIVE/DEAD Blue viability dye was generated by heat-killing splenocytes at 70 °C for 45 minutes, dividing the cells into two aliquots (one stained with the viability dye, the other unstained) and acquiring the control in a single tube after recombining the two halves. This ensured that both positive and negative populations shared identical autofluorescence.

A

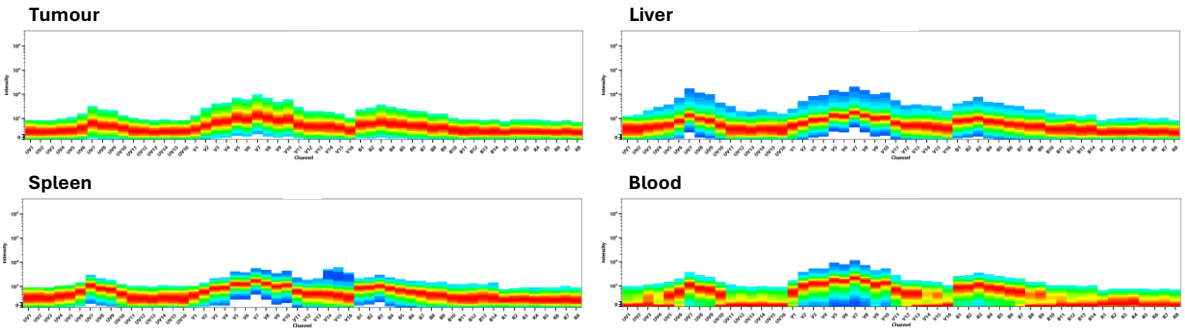
Tumour
Liver
Spleen
Blood

B

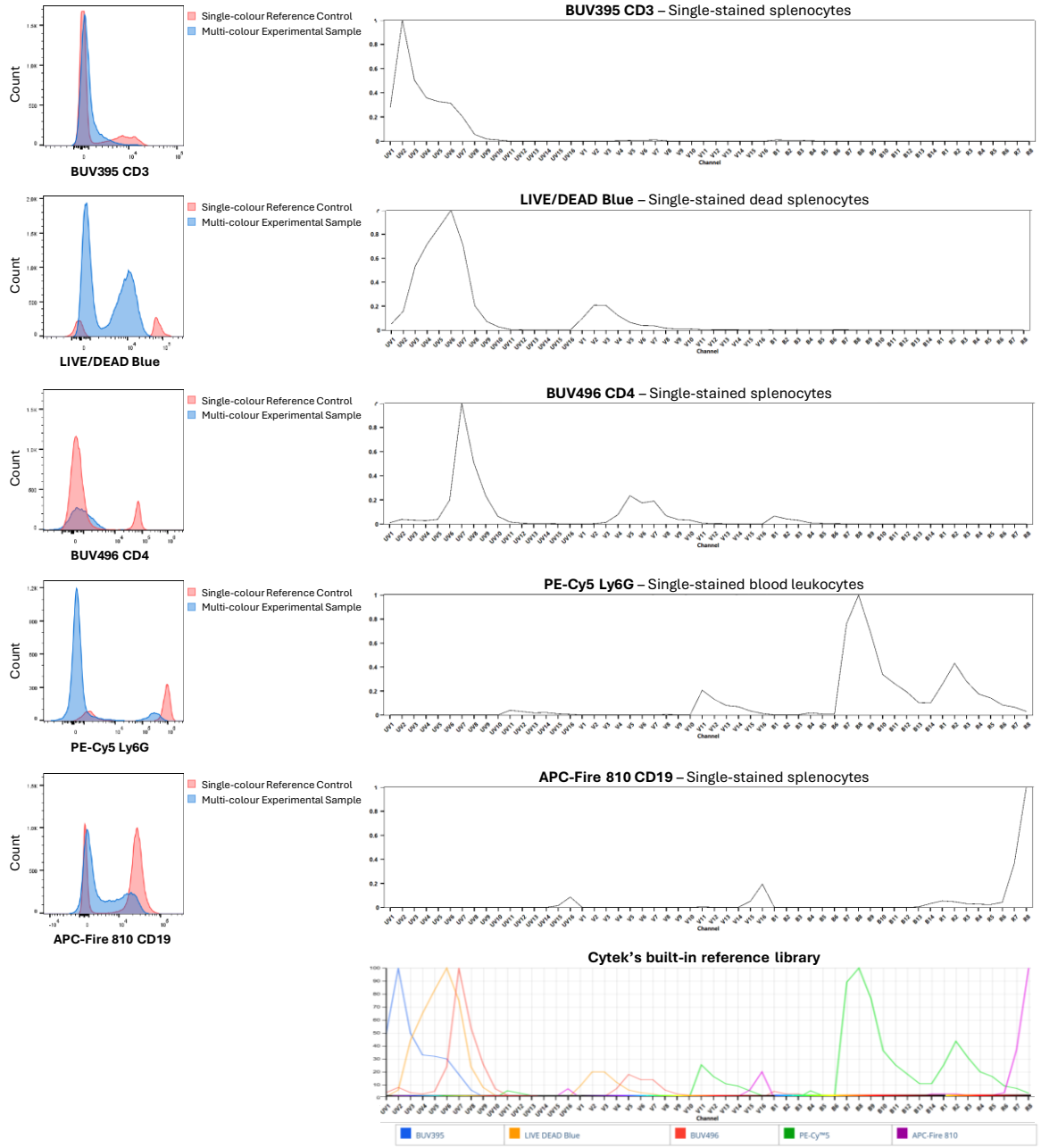
Single-colour Reference Control
Multi-colour Experimental Sample
Count
BUV395 CD3
BUV395 CD3 – Single-stained splenocytes
LIVE/DEAD Blue
LIVE/DEAD Blue – Single-stained dead splenocytes
BUV496 CD4
BUV496 CD4 – Single-stained splenocytes
PE-Cy5 Ly6G
PE-Cy5 Ly6G – Single-stained blood leukocytes
APC-Fire 810 CD19
APC-Fire 810 CD19 – Single-stained splenocytes
Cytek's built-in reference library
BUV395
LIVE DEAD Blue
BUV496
PE-Cy™5
APC-Fire 810

Figure 3.6 – Reference unstained and single-colour controls
A. Emission spectra of tissue-specific, unstained single-cell suspensions.
B. Overlay of positive and negative populations in single-colour reference controls and the matched multi-colour experimental sample for the five reagents where cell-based controls were used (left). Emission spectra of the same reagents (right), and comparison to the standard profiles provided by the cytometre manufacturer (bottom right panel).

3.3.5 Gating strategy

A gating strategy was established (**Figure 3.7**). Fluorescence Minus One (FMO) controls, typically used to define thresholds between negative and positive populations by omitting one fluorochrome-conjugated antibody at a time, were not employed, as visual inspection alone was sufficient to reliably set all gates for the populations of interest. Importantly, cells were deliberately classified based solely on marker expression rather than forward- and side-scatter properties. This approach was adopted because intratumoural leukocytes invariably displayed considerable heterogeneity in size and granularity compared with cells from the blood or spleen, and deviated from the historical classification based on FSC-A/SSC-A gating for lymphocytes, monocytes, and granulocytes (Loken et al. 1990). For example, smaller, poorly granular cells occasionally expressed neutrophil markers, whereas larger cells expressed T- or B-cell markers (data not shown). Consequently, classification based exclusively on marker expression was considered more reliable.

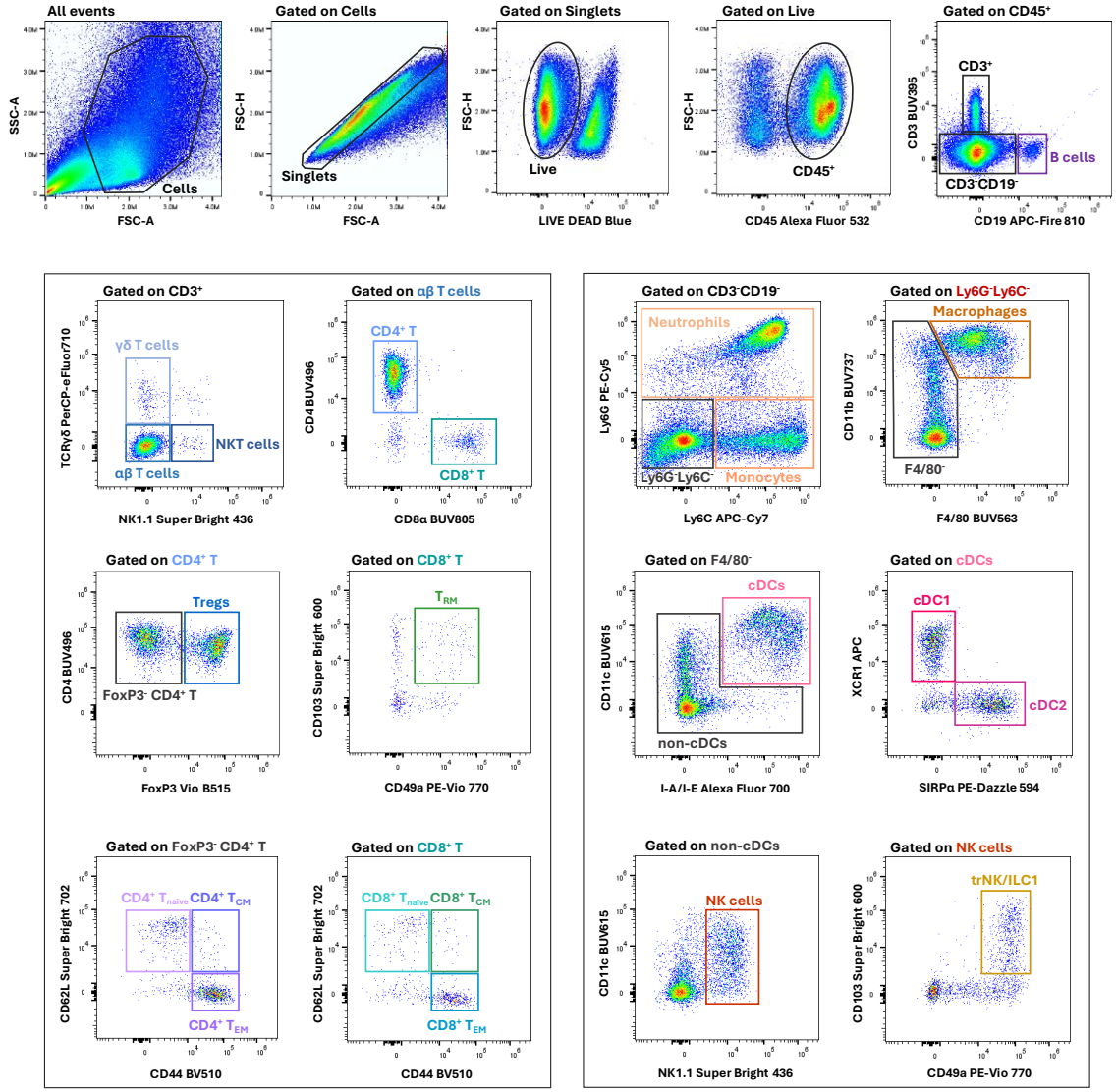

Figure 3.7 – Gating strategy

Tumour cells from a representative treatment-naïve, pancreatic tumour–bearing C57BL/6 mouse are shown. Tregs: Regulatory T cells; T_{CM}: Central memory T cells; T_{EM}: Effector memory T cells; T_{RM}: Tissue-resident memory T cells; cDCs: Conventional dendritic cells; cDC1: Type 1 conventional dendritic cells; cDC2: Type 2 conventional dendritic cells; NK: Natural killer; trNK: Tissue-resident NK cells; ILC1: Type 1 innate lymphoid cells.

3.3.6 Tissue processing protocol development

While panel design often presumes the availability of a ready-to-stain cell suspension, the preparatory steps leading to the isolation of viable, single-cell suspensions are equally critical to the success of flow cytometric analyses. While optimised protocols exist for isolating specific immune populations, such as T cells from the blood, spleen, or intestinal lamina propria (Cossarizza et al. 2021), the broad scope of this panel necessitated the development of a protocol capable of recovering a wide range of leukocyte subsets from the TME. In addition, although the primary objective was to assess local immune responses within the TME, systemic immunity was also of interest and, accordingly, site-specific adaptations of the protocol for single cell suspension preparation were developed for blood and spleen (**Figure 3.8**). The liver was also included as a site of analysis, given its role as common site of metastasis in gastrointestinal malignancies (Manfredi et al. 2006; Ryan et al. 2014) and large reservoir of NK cells in mice and humans (J. Wang et al. 2012; Sender et al. 2023).

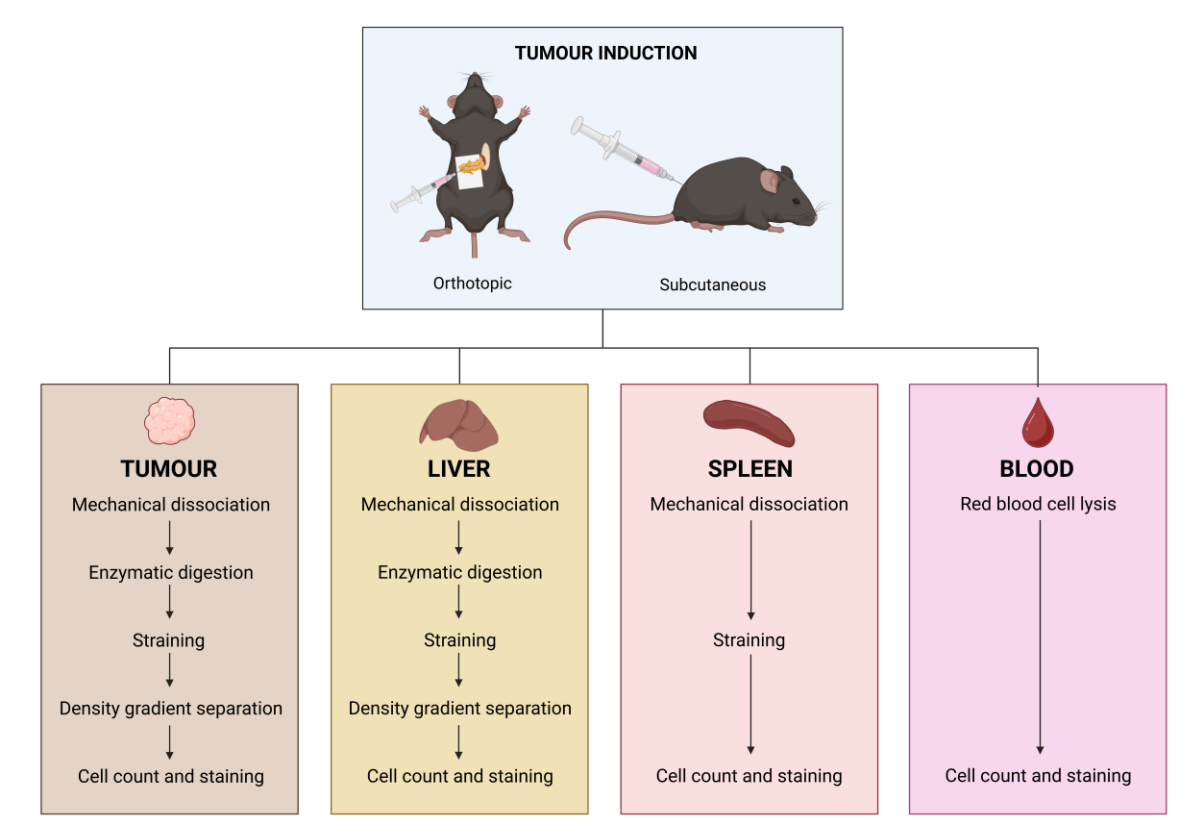

Figure 3.8 – Site-specific adaptations of the protocol

In initial protocol testing for tissue processing, tumours were harvested from C57BL/6J mice bearing orthotopic pancreatic tumours (KPC-F), mechanically dissociated with scissors, and digested with a collagenase-containing cocktail. The resulting suspensions were filtered through 70-µm and 40-µm cell strainers to remove debris and large aggregates, and then stained for flow cytometric analysis. Under these conditions, viability was consistently below 20%, largely due to enrichment of dead, $CD45^-$ non-immune cells in the suspension (**Figure 3.9A**). To address this and optimise cell recovery, a density-gradient centrifugation step was added after filtration in an exploratory pilot study (n = 3), yielding two distinct cell fractions: low-density and high-density cells. The rationale for this was the

hypothesis that dead epithelial cell fragments, debris, and small aggregates would pellet with the high-density fraction, thereby enriching for live $CD45^+$ cells in the low-density fraction. These two were stained in parallel, and the proportions of live $CD45^+$ singlets and total events were quantified by flow cytometry to evaluate whether this step could improve sample purity. An analogous protocol was applied to liver tissue from the same mice, in light of the liver's structural similarity to tumours as a solid organ with a complex epithelial and stromal architecture.

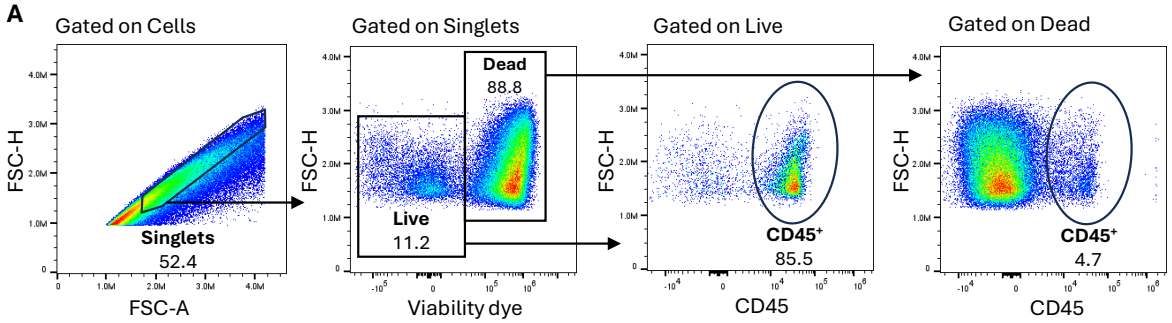
A
Gated on Cells
Gated on Singlets
Gated on Live
Gated on Dead
FSC-H
FSC-A
Singlets
52.4
Dead
88.8
Live
11.2
Viability dye
CD45+
85.5
CD45
CD45+
4.7
CD45

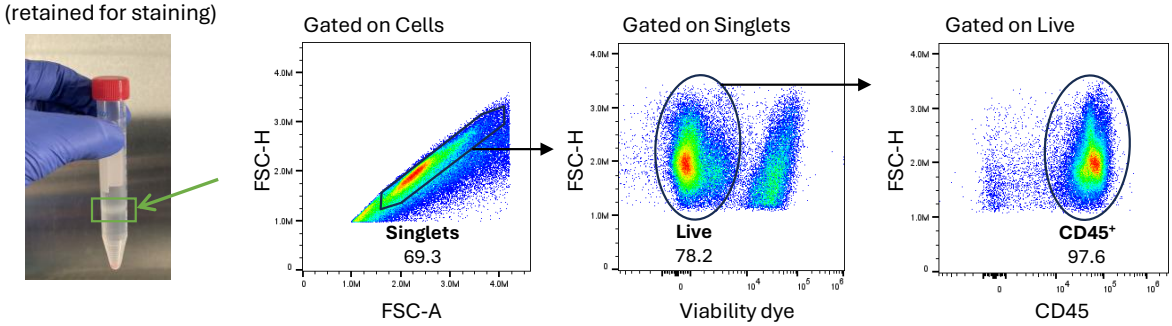
B
TUMOUR
Low-density fraction
(retained for staining)
Gated on Cells
Gated on Singlets
Gated on Live
FSC-H
FSC-A
Singlets
69.3
Live
78.2
Viability dye
CD45+
97.6
CD45

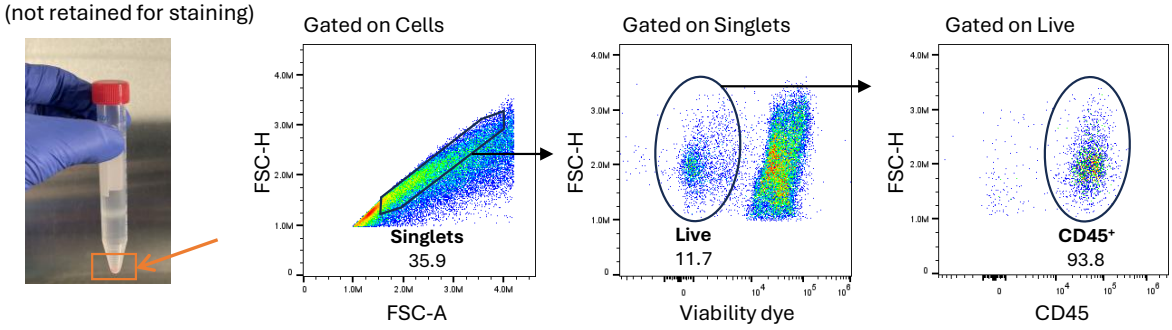
C
TUMOUR
High-density fraction
(not retained for staining)
Gated on Cells
Gated on Singlets
Gated on Live
FSC-H
FSC-A
Singlets
35.9
Live
11.7
Viability dye
CD45+
93.8
CD45

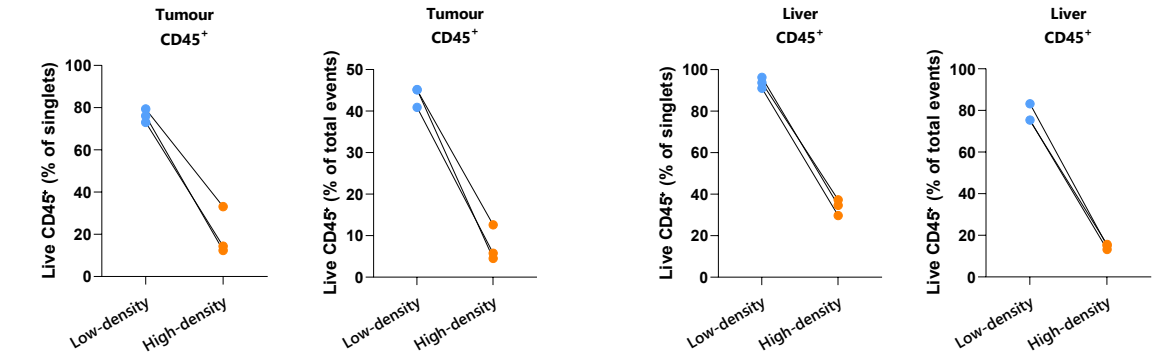
D
Tumour
CD45+
Live CD45+ (% of singlets)
Live CD45+ (% of total events)
Low-density
High-density
E
Liver
CD45+
Live CD45+ (% of singlets)
Live CD45+ (% of total events)
Low-density
High-density

Figure 3.9 – Effect of density-based centrifugation on sample purity
A. Percentage of live and dead cells, alongside CD45⁺ cell fraction, in a tumour from an early iteration of the sample processing protocol. The viability dye used in initial iterations differed from the one used in later iterations (Zombie NIR vs LIVE/DEAD Blue). Live (median, % of singlets): 14.3 (9.5 – 18.8); CD45⁺ (median, % of live): 64.9 (54.7 – 86.5)
B. Low-density cell fraction (green arrow and box) of a tumour sample after density-gradient based centrifugation of a dissociated, digested, and strained tumour cell suspension (left); examples of gating strategy for singlets, live and CD45⁺ cells (right).
C. High-density cell fraction (orange arrow and box) of a tumour sample after density-gradient centrifugation of a dissociated, digested, and strained tumour cell suspension (left); examples of gating strategy for singlets, live and CD45⁺ cells (right).
D. Percentage of live CD45⁺ singlets (left) and total events (right) in the high- and low-density cell fractions of digested tumours after density gradient-based centrifugation.
E. Percentage of live CD45⁺ singlets (left) and total events (right) in the high- and low-density cell fractions of digested livers after density gradient-based centrifugation.

While a Wilcoxon matched-pairs test would have been appropriate for comparing these two groups in case of a larger dataset, the limited sample size prevented meaningful statistical analyses. Therefore, comparisons between the two groups were made descriptively by comparing their medians. The low-density cell fraction was found to contain higher numbers of live CD45⁺ singlets than the high-density cell fraction, both in tumour (median: 76.10% vs 14.40%; **Figure 3.9B,D**) and liver samples (median: 93.70% vs 34.60%; **Figure 3.9C,E**). Based on these findings, the density-gradient centrifugation step was incorporated into the standard processing protocol of tumour and liver samples.

The incorporation of this step, along with progressive refinement of the protocol (such as minimising cellular stress by reducing enzymatic digestion times and maintaining samples on ice throughout processing)

resulted in cell viability and $CD45^+$ cell recovery rates in tumour and liver samples that were broadly similar to those observed in other anatomical sites, as determined by comparing medians of each group (*n* = 3, **Figure 3.10**). Cell viability exhibited limited variability across tissues (median: tumour 84.7%, liver 94.2%, spleen 91.1%, blood 80.2%; all within 9% of the mean across sites). Similarly, $CD45^+$ cell recovery rates were above 80% in all examined compartments.

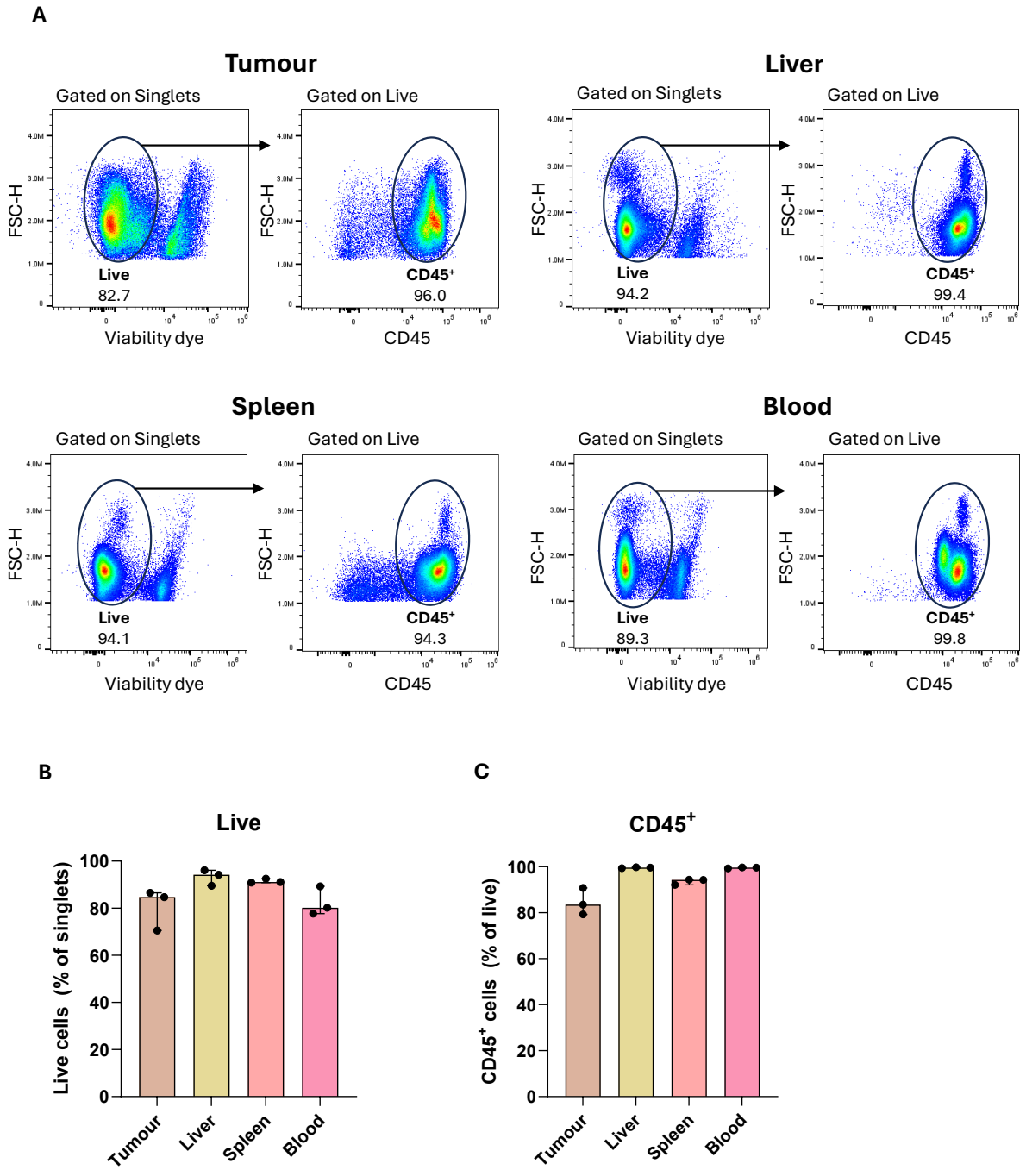

Figure 3.10 – Viability and CD45⁺ fraction following protocol refinement

A. Live and live CD45⁺ cells in tumour, liver, spleen, and blood samples of one representative animal.

B. Percentage of live cells in the four examined districts. Median and range shown.

C. Percentage of live CD45⁺ cells in the four examined districts. Median and range shown.

3.3.7 Panel application and validation

To verify the panel's efficacy in enumerating all major leukocyte populations involved in tumour immunity, these populations were quantified in the tumour, spleen, liver, and blood of a small number of mice (*n* = 3) bearing orthotopically implanted pancreatic tumours at baseline (i.e., untreated). Because the primary objective at this stage was to confirm identification of all major subsets using the gating strategy described above, no formal statistical analyses were performed; instead, data were evaluated descriptively through median values and comparisons with established ranges reported in the literature. The predominant populations within the TME of treatment-naïve mice were macrophages (median: 32.1%), neutrophils (median: 29.0%), and monocytes (median: 12.3%) (**Figure 3.11A**), consistent with the known immunosuppressive milieu of pancreatic cancer (Feig et al. 2012; Steele et al. 2020; Fernandez et al. 2023). B cells constituted the dominant cell type in the other examined tissues, and the remaining immune cell subsets aligned with published data on immune composition of mouse blood (J. Chen and Harrison 2002), spleen (Niemi et al. 2020), and liver (P. Huang et al. 2025) in the setting of cancer.

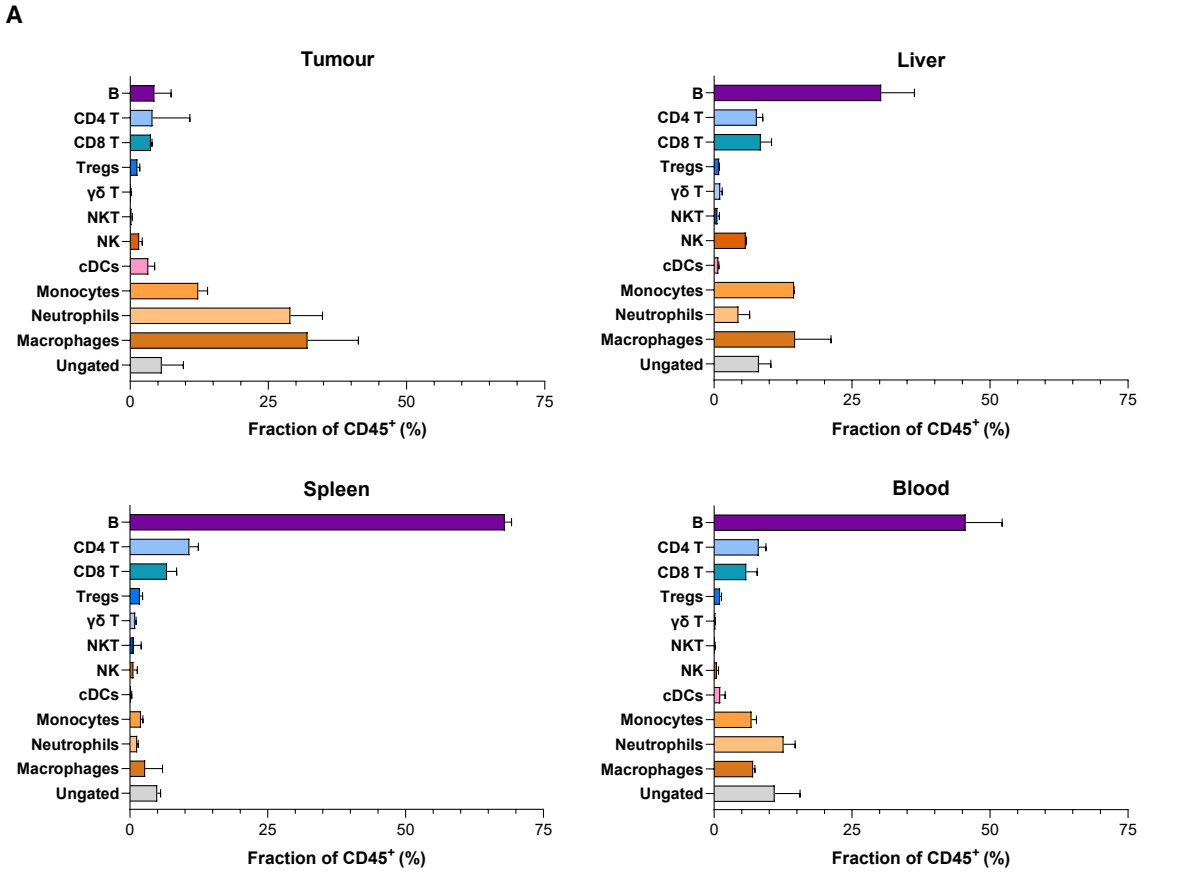
A
Tumour
Liver
Spleen
Blood
B
CD4 T
CD8 T
Tregs
γδ T
NKT
NK
cDCs
Monocytes
Neutrophils
Macrophages
Ungated
0
25
50
75
Fraction of CD45+ (%)

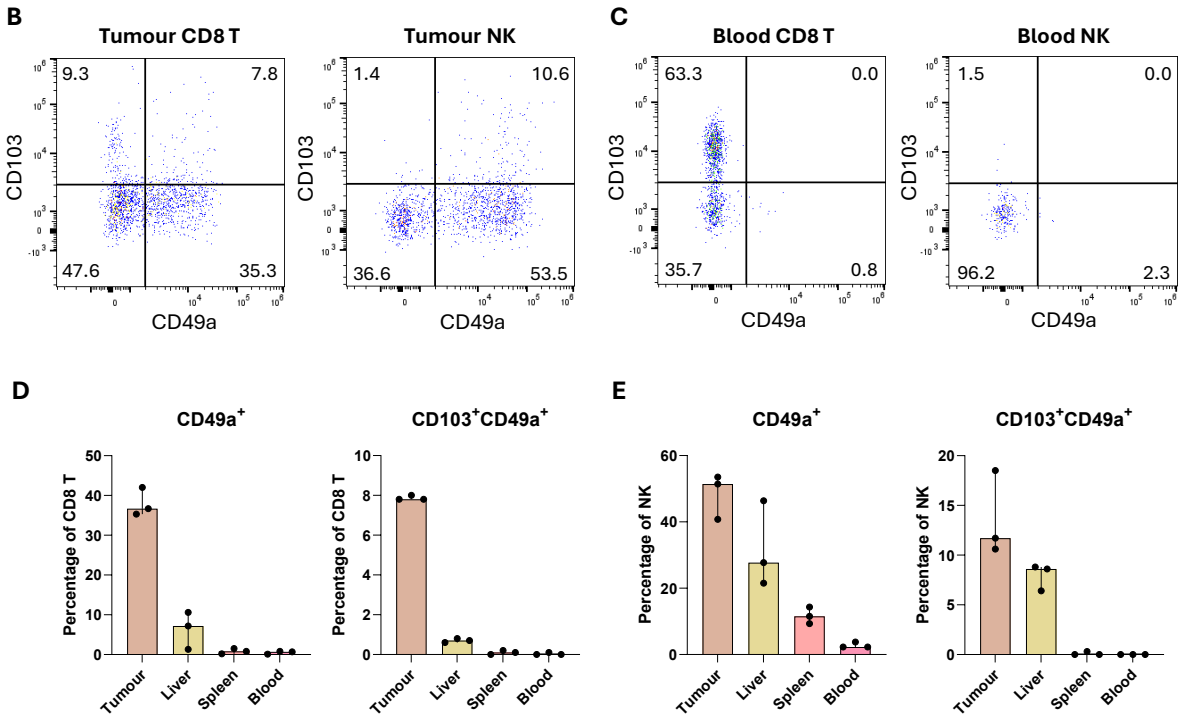
B
Tumour CD8 T
Tumour NK
C
Blood CD8 T
Blood NK
CD103
CD49a
9.3
7.8
47.6
35.3
1.4
10.6
36.6
53.5
63.3
0.0
35.7
0.8
1.5
0.0
96.2
2.3

D
E
CD49a+
CD103+CD49a+
Percentage of CD8 T
Percentage of NK
Tumour
Liver
Spleen
Blood

Figure 3.11 – Baseline immune landscape in C57BL/6J mice harbouring orthotopically implanted pancreatic tumours

A. Bar charts showing the percentage of each immune cell population in the tumour, liver, spleen, and blood of untreated C57BL/6J mice with orthotopically implanted pancreatic tumours (*n* = 3 per group). Median and range shown.

B. CD103 and CD49a expression in $CD8^+$ T cells (left) and NK cells (right) from the tumour of one representative animal.

C. CD103 and CD49a expression in $CD8^+$ T cells (left) and NK cells (right) from the blood of one representative animal.

D. CD49a (left) and dual CD49a/CD103 expression (right) in $CD8^+$ T cells from the four examined tissues (expressed as percentages of total $CD8^+$ T). Median and range shown. Median CD103 expression (% of $CD8^+$ T): tumour 9.3 (5 – 14.7), liver 52.1 (46.4 – 64.2), spleen 68.5 (65.8 – 80), blood: 63.3 (53.1 – 78.6).

E. CD49a (left) and dual CD49a/CD103 expression (right) in NK cells from the four examined tissues (expressed as percentage of total NK cells). Median and range shown.

To verify that the two markers of tissue residency identified cells within tissues, the proportions of cells expressing CD49a, CD103, or both were quantified across the four analysed compartments in $CD8^+$ T cells and NK cells. CD49a was found to be more specific for tissue localisation, being expressed on a substantial fraction of cells at epithelial sites (tumour and liver) and on a small minority of cells in non-epithelial sites (blood and spleen, **Figure 3.11B-E**). A similar pattern was observed for cells expressing both CD49a and CD103. Across all four compartments, CD49a expression was maximum in the tumour, with up to 42.0% of $CD8^+$ T cells and 53.5% of NK cells expressing this marker alone. In contrast, CD103 expression alone was detected on more than 50% of liver $CD8^+$ T cells and more than 60% of blood and spleen $CD8^+$ T cells, and approximately 10% of tumour $CD8^+$ T cells. Among NK cells, on the other hand, expression of CD103 alone was comparatively rare (median between 1% and 5% across all compartments).

3.3.8 Ungated cells

Approximately 5–10% of $CD45^+$ cells remained ungated across all tissues. To further characterise these cells, the expression of all markers included in the panel was assessed. Ungated cells were negative for all markers, with the exception of some subsets expressing CD11b or CD86 (and a minority expressing both, **Figure 3.12A**).

In the blood, over 70% of ungated cells expressed the pan-myeloid marker CD11b alone (**Figure 3.12B**). Based on this phenotype, these cells were hypothesised to represent immature myeloid precursors. To test this, CD45 expression was measured on these cells, as such precursors are known to express dimmer levels of CD45 (van Lochem et al. 2004). CD45 fluorescence intensity per ungated blood cell was the lowest, at nearly one-third of that observed in ungated tumour cells and approximately half that of ungated liver cells (**Figure 3.12D**), supporting the hypothesis that these blood cells might be immature myeloid precursors. More broadly, CD45 MFI was the lowest across the totality of blood $CD45^+$ cells, when compared to $CD45^+$ from other compartments (**Figure 3.12E**), consistent with an overall systemic shift in haematopoiesis towards immature myeloid lineages.

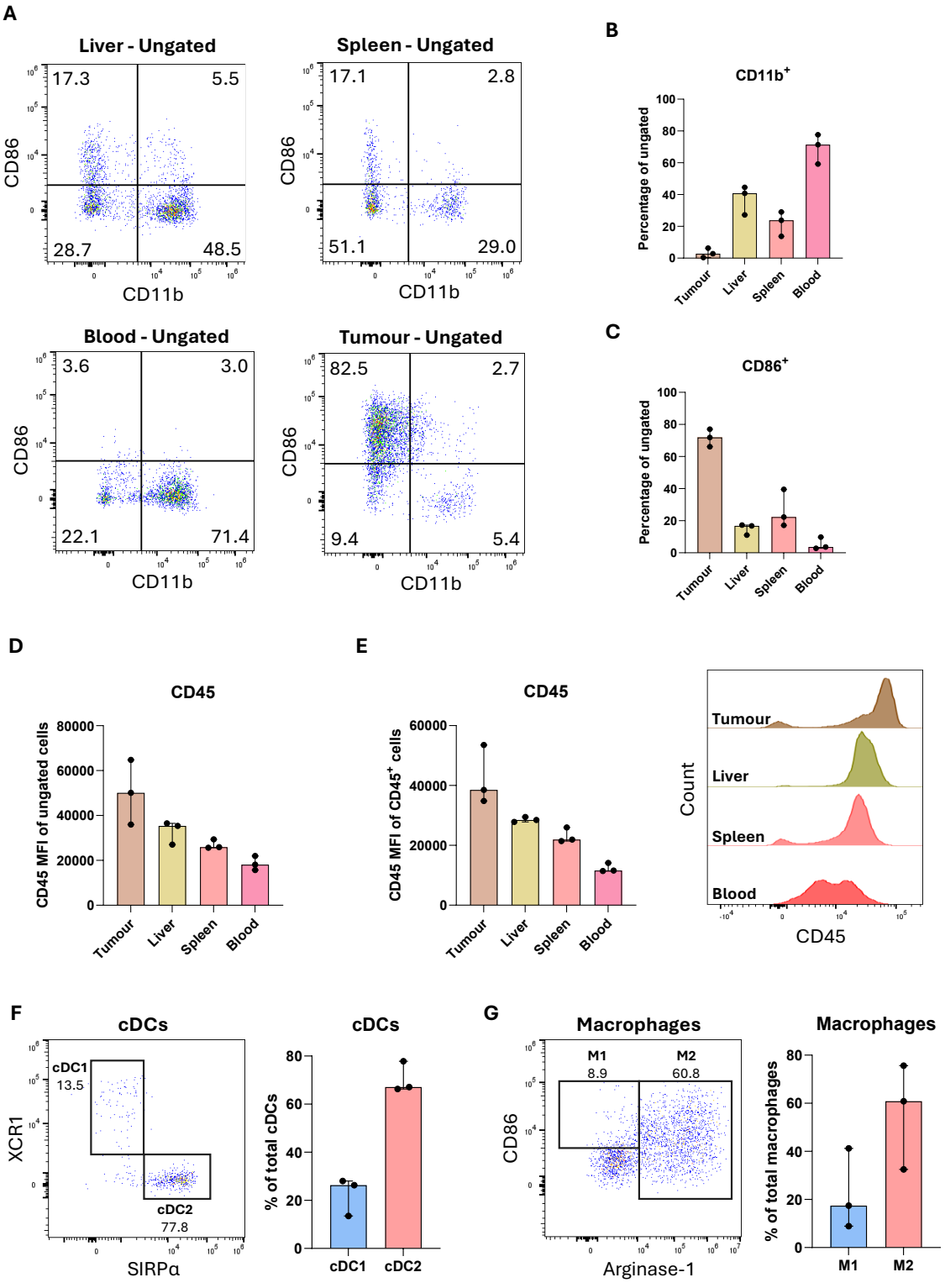
A
Liver - Ungated
17.3
5.5
28.7
48.5
CD86
CD11b
Spleen - Ungated
17.1
2.8
51.1
29.0
Blood - Ungated
3.6
3.0
22.1
71.4
Tumour - Ungated
82.5
2.7
9.4
5.4
B
CD11b+
Percentage of ungated
Tumour
Liver
Spleen
Blood
C
CD86+
D
CD45
CD45 MFI of ungated cells
E
CD45 MFI of CD45+ cells
Count
F
cDCs
cDC1
13.5
cDC2
77.8
XCR1
SIRPα
% of total cDCs
G
Macrophages
M1
8.9
M2
60.8
Arginase-1
% of total macrophages

Figure 3.12 – Characterisation of ungated cells
A. CD11b and CD86 expression in ungated cells from the liver (top left), spleen (top right), blood (bottom left), and tumour (bottom right) of one representative animal.
B. Percentage of $CD11b^{+}CD86^{-}$ ungated cells in the four examined districts (n = 3). Median and range shown.
C. Percentage of $CD11b^{-}CD86^{+}$ ungated cells in the four examined districts (n = 3). Median and range shown.
D. CD45 MFI of ungated cells. Median and range shown.
E. CD45 MFI of all $CD45^{+}$ cells (left). Median and range shown. Staggered histograms of CD45 fluorescence intensity in the four examined tissues from one representative animal (right).
F. Dot plot showing tumour cDC subsets from one representative animal (left), and percentage of cDC1s and cDC2s as a fraction of total cDCs (right, n = 3)
G. Dot plot showing tumour-associated macrophage subsets from one representative animal (left), and percentage of M1 and M2 macrophages as a fraction of total macrophages (right, n = 3).

While the phenotype of ungated cells in the blood aligned with that of immature myeloid precursors, the majority of ungated cells in the tumour were $CD11b^{-}CD86^{+}$ (**Figure 3.12C**), suggesting a lymphoid origin. This phenotype is compatible with type 2 or type 3 innate lymphoid cells (ILC2s and ILC3s, respectively), both of which are known to express CD86 in certain contexts (Oliphant et al. 2014; von Burg et al. 2014; Lehmann et al. 2020). To investigate this possibility indirectly, it was hypothesised that the presence of ILC2s would be associated with a type 2 immune response in the TME. The TME exhibited features of a type 2 immune profile, including an increased proportion of cDC2s relative to cDC1s (approximately 2:1), and a predominance of M2-polarised macrophages relative to M1 macrophages (approximately 3:1, **Figure 3.12F,G**), supporting this hypothesis.

Ungated cells in the spleen and liver were largely $CD86^{-}CD11b^{-}$ (median: 48.9% and 44.7%, respectively) and expressed intermediate levels of CD45 (**Figure 3.12E**), likely representing other mature, innate cell subsets.

3.4 Discussion

As immuno-oncology continues to advance, better tools are required to characterise the immune system's contribution to tumour initiation and progression. In this chapter, a 23-colour spectral flow cytometry panel was developed and optimised for comprehensive immune profiling in an orthotopic mouse model of PDAC, enabling parallel interrogation of the TME, blood, spleen, and liver. At the time these experiments were performed, no optimised flow cytometry panel existed to comprehensively enumerate myeloid and lymphoid, as well as circulating and resident, immune cell subsets involved in tumour immunity in murine models of cancer. Since then, a more extensive, optimised panel has been developed with a similar objective (Kare et al. 2023).

Particular attention was devoted to each stage of panel design and sample preparation, including strategic marker selection for accurate population identification, and optimisation of steps propaedeutic to and preceding single-cell suspension staining and analysis. Three candidate markers (NK1.1, CD49b, and NKp46) were evaluated for their ability to identify NK cells across the four anatomical districts of interest. Although early reports of liver-resident NK cells identified them as $CD49b^{-}$ (Peng et al. 2013), a high

proportion of $CD19^{-}CD3^{-}$ liver cells in this model expressed CD49b. The degree of overlap among NK1.1, CD49b, and NKp46 varied substantially among tissues. Consequently, marker specificity was assessed, based on existing evidence that cells co-expressing all three markers represent mature NK cells, and NK1.1 emerged a more specific NK lineage marker.

Tissue-resident subsets of $CD8^{+}$ T and NK cells have been described, with an extensive body of evidence supporting the use of CD49a and CD103 to discriminate circulating from tissue-associated subsets. Pilot testing on a small number of animals suggested that CD103 alone was insufficient to distinguish tissue-localised from circulating NK and $CD8^{+}$ T cells in this mouse model of pancreatic cancer, as high CD103 expression was also observed in non-epithelial compartments, including the blood. In contrast, CD49a, either alone or co-expressed with CD103, appeared to be a more reliable discriminator of tissue-associated lymphocytes. Whether $CD103^{+}$ blood lymphocytes represent intermediate states in the transition to a $CD49a^{+}CD103^{+}$ phenotype is difficult to determine based on flow cytometry alone and more reliable techniques (e.g., pseudotime trajectory analysis) would be better suited to infer their developmental path. However, the higher proportion of $CD49a^{+}$ cells at epithelial sites suggests that acquisition of a double-positive phenotype is more likely to occur via a $CD49a^{+}$ single-positive stage than through a $CD103^{+}$ stage. Notably, circulating $CD103^{+}$ $CD8^{+}$ T cells have been identified in multiple human cancer types in humans, and their presence has been associated with improved patient survival (Nose et al. 2023; Lian Liu et al. 2024).

While the panel is capable of identifying NK cells and *bona fide* tissue-resident NK cells, the latter designation should be used with great caution. As flow cytometry only provides a single time-point assessment, indicating the presence of cells within a tissue but not confirming long-term residency, terms such as *tissue-associated* or *tissue-localised* are preferable. Alternatively, these cells should simply be named based on phenotype (e.g., $NK1.1^{+}CD49a^{+}CD103^{+}$ cells).

Tissue-resident subsets of ILCs have also been identified and shown to display remarkable plasticity, with subsets capable of interconverting into one another (Colonna 2018). To complicate this matter further, NK cells themselves can undergo conversion into ILC1s when exposed to appropriate stimuli, such as TGF-β within the TME (V. S. Cortez et al. 2016, 2017; Gao et al. 2017). Distinguishing trNK cells from ILC1s is inherently challenging because both subsets share many surface markers, and the markers used to define them can vary with tissue context and activation state, leading to an overlap between these populations that is increasingly recognised in the field (Spits et al. 2016; Hashemi and Malarkannan 2020; Sudan et al. 2024). More in-depth techniques such as single-cell RNA sequencing and transcriptomic profiling are better suited to dissect the relationships between them (Sparano et al. 2024; Torcellan et al. 2024). In future adaptations of this flow cytometry panel where discriminating between trNK cells and ILC1s may be critical, emerging strategies rely on the inclusion of additional markers, such as CD127, Hobit, and Eomes (Gordon et al. 2012; Daussy et al. 2014; Klose et al. 2014; Allan et al. 2017).

Sample processing was optimised by incorporating a density-gradient separation step to improve cell purity. While this approach results in the loss of granulocytes from the blood of both mice and humans under physiological conditions, this was not a limitation in the present model. In the setting of cancer, neutrophils reduce their granule content, acquiring a less dense, immature phenotype (Bronte et al. 2016), and enabling their recovery in the low-density cell fraction. In fact, neutrophils were the second most abundant population in the TME, followed by monocytes. This observation is consistent with the well-established myeloid-dominated PDAC TME (Khaled et al. 2014; Trovato et al. 2019). While these populations likely correspond to PMN- and M-MDSCs, definitive classification would require functional assays to demonstrate suppressive capacity, in line with current recommendations. Further evidence of the immunosuppressive nature of the TME was provided by the predominance of M2 macrophages. In macrophages, Arginase-1 and CD86 were not expressed in a mutually exclusive fashion, resulting in a less stringent definition of M2 macrophages as macrophages expressing Arginase-1, irrespective of CD86 expression. These cells dominated the TME of our PDAC model, congruently with evidence from the literature (Zhu et al. 2014, 2017; Yang et al. 2021).

By employing the gating strategy defined during panel design, a small fraction of cells remained unclassified. The reduced CD45 fluorescence intensity observed in such unclassified cells in the blood of tumour-bearing mice is consistent with a bias in haematopoiesis towards immature myeloid populations, a pattern that has been documented in cancer for many

decades (Robinson 1974). Solid tumours secrete factors that drive myelopoiesis and contribute to the establishment of a myeloid-rich suppressive milieu (Youn et al. 2008; Casbon et al. 2015; Veglia et al. 2021). The lower CD45 expression per blood cell (including unclassified cells) may reflect immature myeloid populations newly released from the bone marrow into circulation. Within the TME, on the other hand, unclassified cells may represent ILC2s, as these cells lacked all lineage markers while expressing CD86. While there cannot be any definitive conclusion regarding the identity of these cells, the predominance of a type 2 immune profile in the TME described above is in line with an ILC2-orchestrated response. In future adaptations of this flow cytometry panel, the inclusion of the surface markers ST2 (also known as IL-33 receptor) and NKp46, and the transcription factors GATA3 and RORγt would allow the identification of ILC2s and ILC3s, too (V. Cortez et al. 2015; Mincham and Snelgrove 2023).

Overall, this panel successfully addressed the main limitations of existing panels: it was optimised using tumours and validated for the analysis of immune cells in the TME, circulation, and epithelial and lymphoid organs. It enabled comprehensive immune profiling across a wide range of leukocytes (including tissue-associated lymphocytes), leaving out only a small minority of cells, whose identity could nonetheless be hypothesised through indirect assessment. Although not discussed in this chapter, the panel was also used for subcutaneous tumours, demonstrating its versatility across different tumour models. Since its development, the panel has been made openly accessible for other researchers (Valenzano et al. 2024).

Chapter 4

Phenotypic characterisation of a novel NK cell subset emerging in the KPC orthotopic model of PDAC following combined immunotherapy and radiotherapy

4.1

Introduction

As discussed in the main introduction, the success of immunotherapy in pancreatic ductal adenocarcinoma (PDAC) has been limited. Multimodal approaches may act synergistically and offer better tumour control; for example, radiotherapy combined with PD-L1 blockade significantly enhanced tumour immunity in an orthotopic PDAC model (Azad et al. 2017).

Previous work from our laboratory tested the efficacy of combining radiotherapy, the CCR5 inhibitor Maraviroc, and an inhibitory antibody against PD-1 in promoting tumour control in the KPC orthotopic model of PDAC (Go, Demetriou, Hughes, et al. 2024). Radiotherapy was included because, as extensively reviewed elsewhere, it has the potential to reduce tumour burden and increase tumour immunogenicity (Demaria et al. 2015; Y. Wang et al. 2018; McLaughlin et al. 2020). CCR5 inhibition was selected based on a randomised phase II trial from our group and collaborators, which had identified low baseline serum levels of CCL5—the main ligand for CCR5—as an independent predictor of prolonged survival in patients with locally advanced pancreatic cancer treated with chemoradiation

(Willenbrock et al. 2021). In addition, disruption of the CCL5–CCR5 axis had been shown to impair migration and invasion of pancreatic cancer cell lines in 3D *in vitro* assays (Singh et al. 2018), substantiating this as a promising approach. Finally, PD-1 blockade was included since, despite the low T cell infiltration in PDAC (Muller et al. 2022; Goulart et al. 2021), it could release inhibitory signalling on the few tumour-infiltrating $CD8^+$ T cells (Tumeh et al. 2014).

A few key findings emerged from preliminary testing of this multimodal treatment regimen. Firstly, irradiation (hereafter: IR) was essential for tumour control: whereas single-agent therapy and the dual combination of the CCR5 inhibitor Maraviroc (hereafter: CCR5i) with anti–PD-1 (hereafter: aPD1) only achieved limited control, adding IR to any monotherapy or to the CCR5i + aPD1 combination reduced tumour volumes more markedly (**Figure 4.1A**). Secondly, the triple combination (IR + CCR5i + aPD1) produced the broadest effects on tumour control: in addition to reducing tumour volume, it also caused a significant reduction in the number of cells expressing mutant p53 (**Figure 4.1B**), a significant increase in necrotic areas (**Figure 4.1C**), and the highest rates of $CD8^+$ T cell and NK cell infiltration (**Figure 4.1D**). Thirdly, all treatment groups, including the triple combination, showed substantial inter-animal variation, with a combination of responders and non-responders; $CD8^+$ T cells and NK cells were seen in greater abundance in responders (**Figure 4.1E**).

Lastly, when animals from all treatment groups were pooled, $CD8^+$ T cells and a subset of NK cells lacking expression of Natural Killer Group 2, member D ($NKG2D^-$ NK cells) correlated negatively with E-cadherin-expressing cells (a surrogate for tumour control) (**Figure 4.1F**).

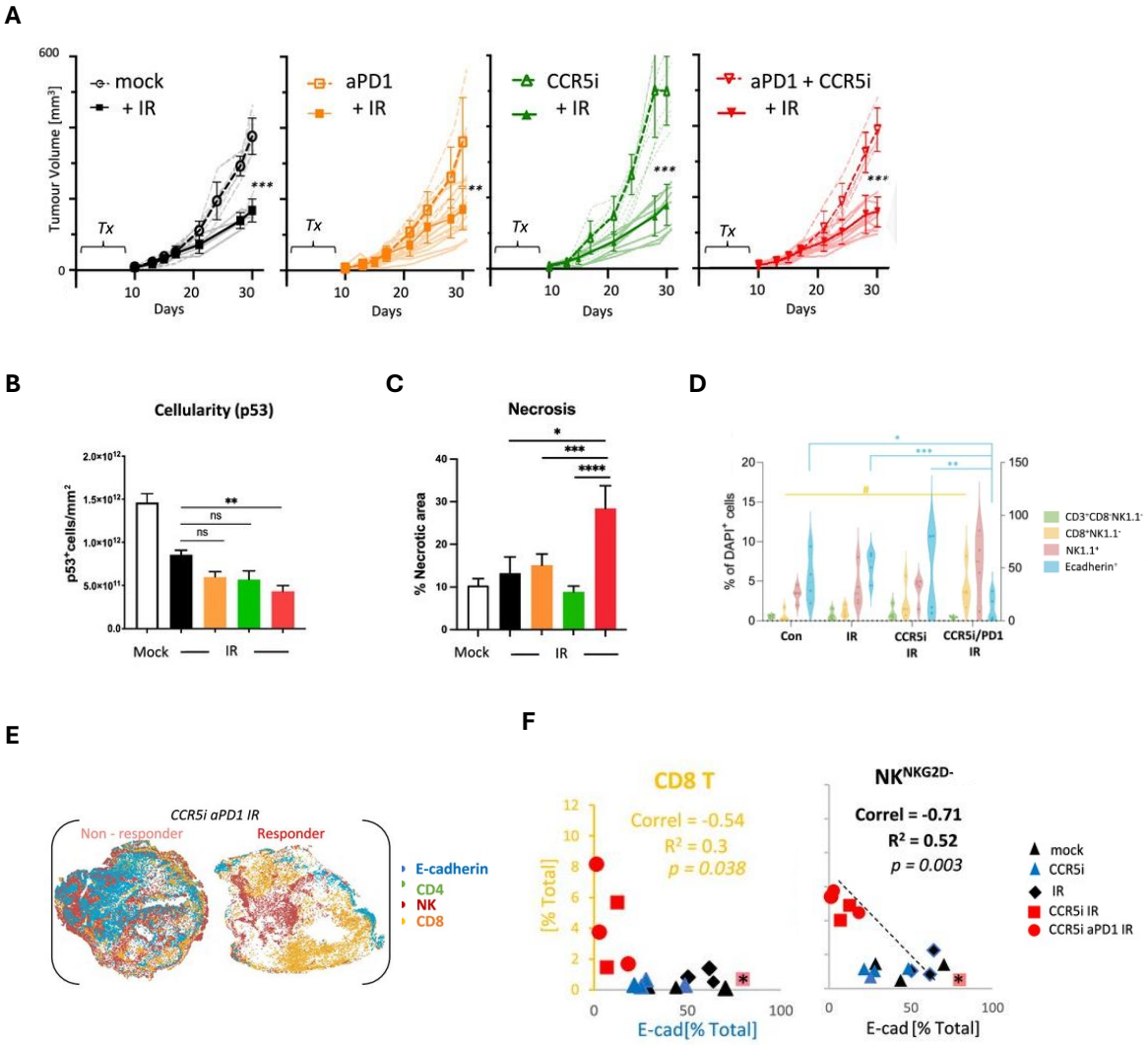

Figure 4.1 – Evidence from prior work and foundation of current study

Freely adapted from *Go, Demetriou, Valenzano, et al., eLife, 2024 (Figures 3, 4, S4) and reproduced under the terms of the Creative Commons Attribution License (CC BY)*.

A. Tumour volumes as measured by MRI and growth curves of individual treatment groups are plotted. Mean growth curves and standard deviation are depicted in bold (with IR: solid line; without IR: dashed line). Individual mice growth curves are shaded.

B. Histograms showing the number of cells expressing mutant p53 per mm^2, as determined by immunohistochemistry. Loss of mutant $p53^+$-expressing cells was used as a measure of tumour control.

C. Histograms showing the percentage of necrotic areas per tumour section, as determined by haematoxylin and eosin (H&E) staining. Extent of necrotic areas was used as a measure of tumour control.

D. Percentage of NK cells ($DAPI^+NK1.1^+$, red) and $CD8^+$ T cells ($DAPI^+NK1.1^-CD8^+$, yellow), as determined by multiplex tissue immunofluorescence of tumour slices and HALO automated image analysis and cell classifying software.

Significance was tested using two-way ANOVA with Tukey multiple comparison (blue significance lines), or one-way ANOVA with Tukey multiple comparison (yellow significance lines) using a $p<0.05$.

E. Spatial plots of individual cells produced by the HALO automated image analysis and cell classifying software for two representative tumour slices (non-responder: left; responder: right). The classification of responders and non-responders to treatment was based on loss of E-cadherin staining.

F. Correlation of $CD8^+$ T cells and $NKG2D^-$ NK cells with E-cadherin-expressing cells, after pooling animals from all groups (n = 3 per group) together (* denotes a censored non-responder).

Since only a single marker, NKG2D, was examined in prior work, the identity of the NK cell subset that correlated positively with tumour control (as per the surrogates indicated above) remained largely obscure. The only existing knowledge on this subset was that these cells, counterintuitively, lacked (rather than expressed), a key activating receptor. This intriguing observation prompted a more in-depth investigation on their phenotype, aimed at better understanding the nature of this subset seemingly driving tumour control.

Additionally, these cells were first observed in tumour samples, but no other tissues were examined. Therefore, it remained unclear whether their presence reflected a tumour-specific immune response, or a more generalised, systemic feature of tumour immunity.

4.2

Aims

To better characterise the phenotype and localisation of a novel NK cell subset that was first described in a murine orthotopic implantation model of PDAC after treatment with IR + CCR5i + aPD1.

4.3

Results

4.3.1 The IR + CCR5i + aPD1 combination causes the accumulation of tumour-infiltrating lymphocytes

A small study was conducted to replicate the emergence of the previously identified NKG2D^{-} NK cell subset. To maximise enrichment for this subset, the treatment regimen was deliberately modified from the one in the original study (Go et al. 2024). In the original study, treatment was administered over one week (including three irradiations, 3×4 Gy), followed by a prolonged wash-out period. In contrast, in this study, a 14-day treatment regimen was followed (including three irradiations, 3×6 Gy), with a shorter wash-out period, as mice were humanely culled upon showing early signs of distress. Upon culling, not only the tumour, but also the spleen, liver, and blood were collected for flow cytometric analyses. Since the emergence of this subset

had already been established in the triple combination treatment arm (IR + CCR5i + aPD1), only this group was tested, alongside a parallel control arm that received no irradiation and vehicles for the two immunotherapy drugs. As this study focussed exclusively on NK cells, a modified version of the flow cytometry panel presented in Chapter 3 was used, incorporating a small set of ten NK cell markers, and omitting markers to identify most other populations.

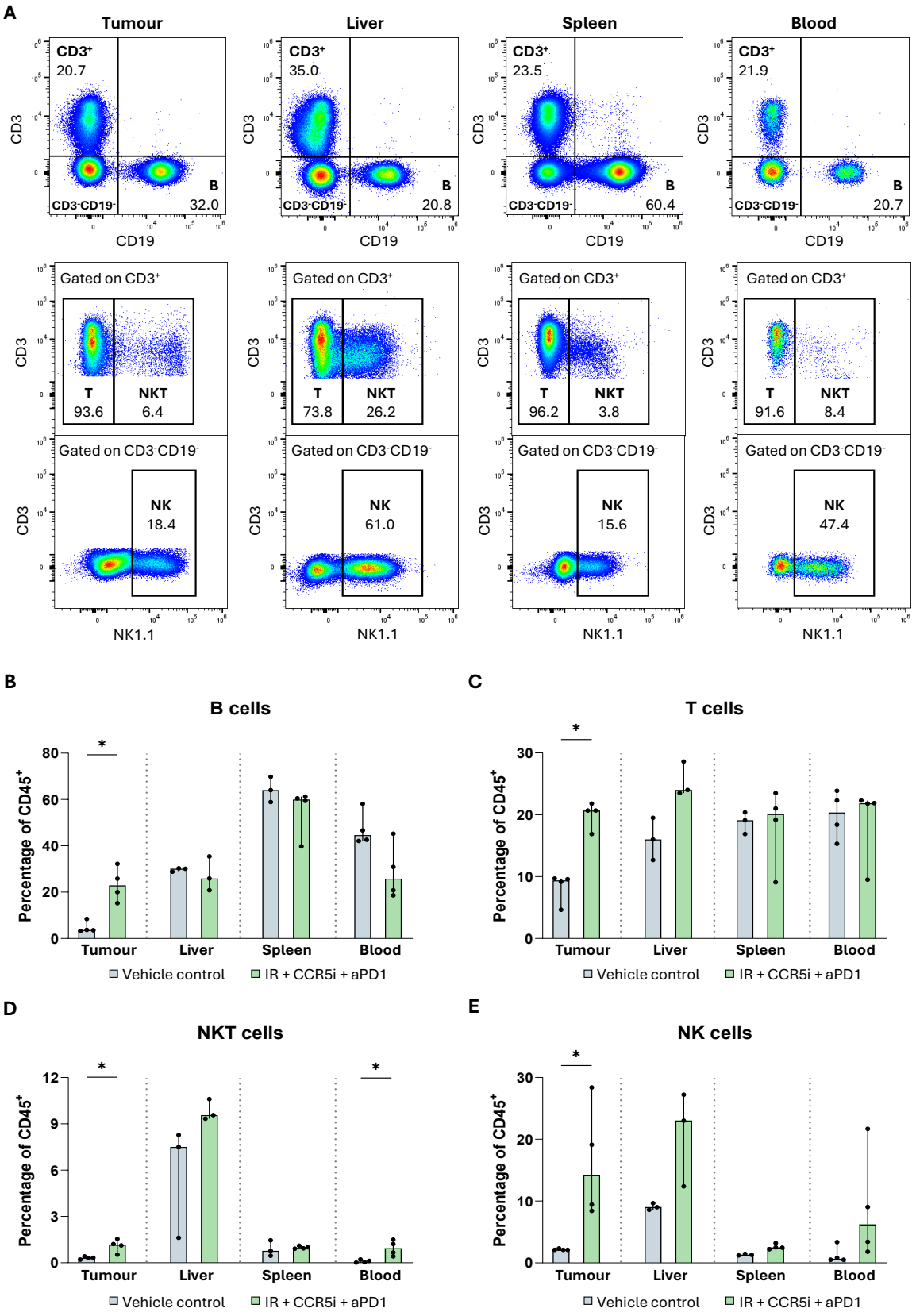
A
Tumour
Liver
Spleen
Blood
CD3⁺
20.7
35.0
23.5
21.9
B
32.0
20.8
60.4
20.7
CD3⁻CD19⁻
CD3
CD19
Gated on CD3⁺
T
93.6
73.8
96.2
91.6
NKT
6.4
26.2
3.8
8.4
Gated on CD3⁻CD19⁻
NK
18.4
61.0
15.6
47.4
NK1.1
B
B cells
C
T cells
D
NKT cells
E
NK cells
Percentage of CD45⁺
Tumour
Liver
Spleen
Blood
Vehicle control
IR + CCR5i + aPD1

Figure 4.2 – Relative abundance of major lymphocyte subsets
A. Dot plots from one representative treated mouse outlining the gating strategy used for the identification of B, T, NKT, and NK cells in the four examined compartments, arranged into columns.
B. Percentage of tumour, liver, spleen, and circulating B cells (as a fraction of live, $CD45^+$ cells). Median and range shown.
C. Percentage of tumour, liver, spleen, and circulating T cells (as a fraction of live, $CD45^+$ cells). Median and range shown.
D. Percentage of tumour, liver, spleen, and circulating NKT cells (as a fraction of live, $CD45^+$ cells). Median and range shown.
E. Percentage of tumour, liver, spleen, and circulating NK cells (as a fraction of live, $CD45^+$ cells). Median and range shown.
All comparisons for groups with $n > 3$ were performed using a two-tailed Mann–Whitney test; *$p<0.05$.

The median proportions of B, T, NKT, and NK cells isolated from tumours in the triple combination group were significantly higher than those in the control group. After treatment, a 6-fold increase in B cells could be detected (**Figure 4.2A**), alongside a 2-fold increase in T cells (**Figure 4.2B**), and a nearly 4-fold increase in NKT cells (**Figure 4.2C**). The subset that experienced the greatest increase with treatment were NK cells (median: 2.1% in controls vs 14.3% in treated mice, **Figure 4.2D**). Of note, NK cells constituted more than 20% of all circulating leukocytes ($CD45^+$ cells) in one treated animal, in stark contrast to controls, where NK cells represented a maximum of only 3.6% of circulating leukocytes. NKT cells also appeared at higher proportions in the blood of treated mice, rising from being virtually undetectable to accounting for approximately 1% of all circulating leukocytes. Substantial inter-animal variability was observed in liver and spleen samples; however, median T, NK, and NKT cell frequencies appeared numerically higher in treated mice in both compartments.

4.3.2 The IR + CCR5i + aPD1 combination alters the proportion of NK cells expressing CD103 and CD49a in the tumour and blood

Given that the population of NKG2D$^-$ cells was first observed in an epithelial solid tumour, it was hypothesised that they could represent tissue-associated NK cells. Therefore, the proportions of cells expressing CD49a, CD103, or both were analysed in the tumours of treated and control mice (**Figure 4.3A,F**). In the treatment group, a relative decrease in CD49a$^+$ NK cells was observed, paralleled by a significant increase in CD103$^+$ and CD103$^+$CD49a$^+$ NK cells (**Figure 4.3B-E**), with the latter constituting more than half of all NK cells in some mice. In control mice, blood NK cells almost invariably expressed neither of the two tissue-associated markers, whereas in treated mice, CD103$^+$, CD49a$^+$, and CD103$^+$CD49a$^+$ NK cells were all detected in the blood, with CD103$^+$CD49a$^+$ NK cells accounting for nearly half of all circulating NK cells in one animal (**Figure 4.3A,C**). In the liver and spleen, greater heterogeneity was observed in the relative proportions of the four subsets; CD103$^+$CD49a$^+$ NK cells notably made up a considerable fraction of NK cells in the spleen of treated mice (median: 1.3% in controls vs 15.0% in the treatment group).

The expression patterns of tissue-associated markers on T cells differed substantially from those described for NK cells, with a considerable fraction of T cells expressing CD103$^+$ alone in both treated mice and controls across the four examined tissues (**Supplementary Figure 9.2**). In T cells, concomitant expression of CD103 and CD49a was largely confined to cells in the TME, irrespective of treatment.

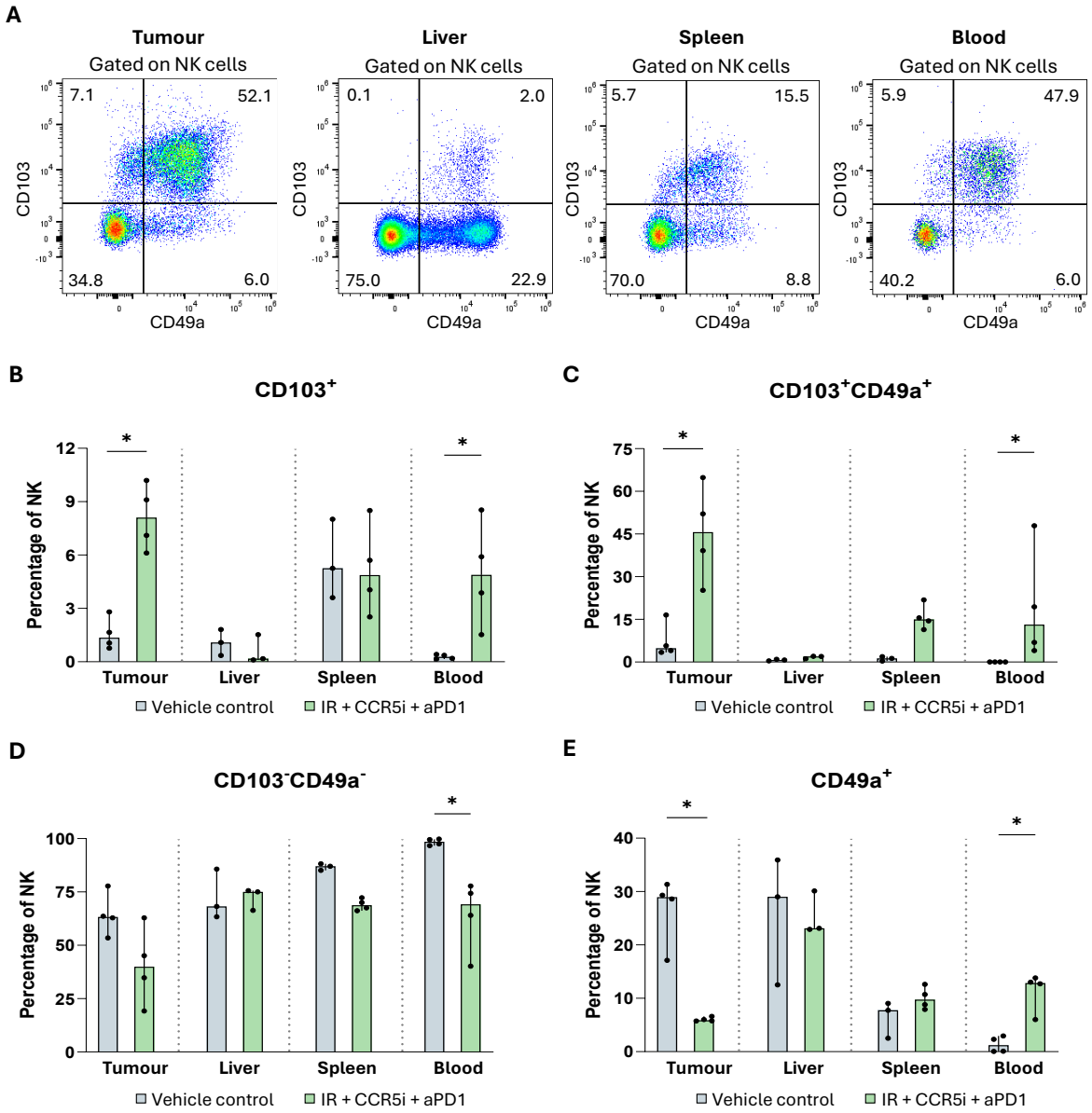
A
Tumour
Gated on NK cells
7.1
52.1
34.8
6.0
Liver
Gated on NK cells
0.1
2.0
75.0
22.9
Spleen
Gated on NK cells
5.7
15.5
70.0
8.8
Blood
Gated on NK cells
5.9
47.9
40.2
6.0
CD103
CD49a
B
CD103+
Percentage of NK
Tumour
Liver
Spleen
Blood
Vehicle control
IR + CCR5i + aPD1
C
CD103+CD49a+
D
CD103-CD49a-
E
CD49a+
F
Vehicle control
IR + CCR5i + aPD1
CD103+CD49a+
CD49a+
CD103+
CD103-CD49a-

Figure 4.3 – Expression of CD103 and CD49a on NK cells
A. Dot plots from one representative treated mouse outlining the gating strategy used to define the four subsets of NK cells in the four examined districts.
B. Percentage of tumour, liver, spleen, and circulating $CD103^+$ NK cells (as a fraction of total NK cells). Median and range shown.
C. Percentage of tumour, liver, spleen, and circulating $CD103^+CD49a^+$ NK cells (as a fraction of total NK cells). Median and range shown.
D. Percentage of tumour, liver, spleen, and circulating $CD103^-CD49a^-$ NK cells (as a fraction of total NK cells). Median and range shown.
E. Percentage of tumour, liver, spleen, and circulating $CD49a^+$ NK cells (as a fraction of total NK cells). Median and range shown.
F. Composition of the NK cell gate, based on median expression of CD103 and CD49a on NK cells, in control (upper row) or treated animals (lower row).
All comparisons for groups with n > 3 were performed using a two-tailed Mann–Whitney test; *p<0.05.

4.3.3 The IR + CCR5i + aPD1 combination expands certain NK cell subsets within the tumour and blood immune compartments

While the proportions of the four subsets within the NK cell gate are informative of their relative prevalence, they do not indicate whether the overall abundance of each subset differs between conditions. For this kind of comparison, absolute counts per unit of tumour volume (or mass) are typically employed. However, the primary aim of this study was the phenotypic characterisation of an immune population rather than the quantitative assessment of immune infiltration or treatment efficacy. As a result, tumour volume or mass measurements were not incorporated into the experimental design, and the proportion of each subset relative to the total immune compartment ($CD45^+$ cells) was used as a surrogate measure of relative abundance (**Figure 4.4**).

In the tumour immune microenvironment, the proportions of $CD103^+$, double-positive, and double-negative NK cells rose significantly with treatment, with double-positive NK cells exhibiting the most pronounced increase, from being nearly absent in untreated mice to accounting for 6% of all immune cells in treated mice. The abundance of $CD49a^+$ NK cells was approximately the same in both groups (median: 0.7% of $CD45^+$ cells in the control group vs 0.9% of $CD45^+$ cells in the treatment group).

In the blood of treated mice, the $CD49a^+$ and $CD103^+CD49a^+$ NK cell fractions emerged after treatment, being virtually undetectable in controls. An apparent increase in $CD49a^+$, double-positive, and double-negative NK cells was noted in the immune cellularity of liver and spleen in treated mice.

The expression patterns observed for NK cells within the totality of immune cells in the TME were mirrored by T cells, with the proportions of $CD103^+$, double-positive, and double-negative T cells rising significantly following treatment, and the proportion of $CD49a^+$ T cells remaining comparable between treatment and control groups. For T cells, however, the $CD103^-CD49a^-$ subset was the most abundant across all four tissues (**Supplementary Figure 9.3**).

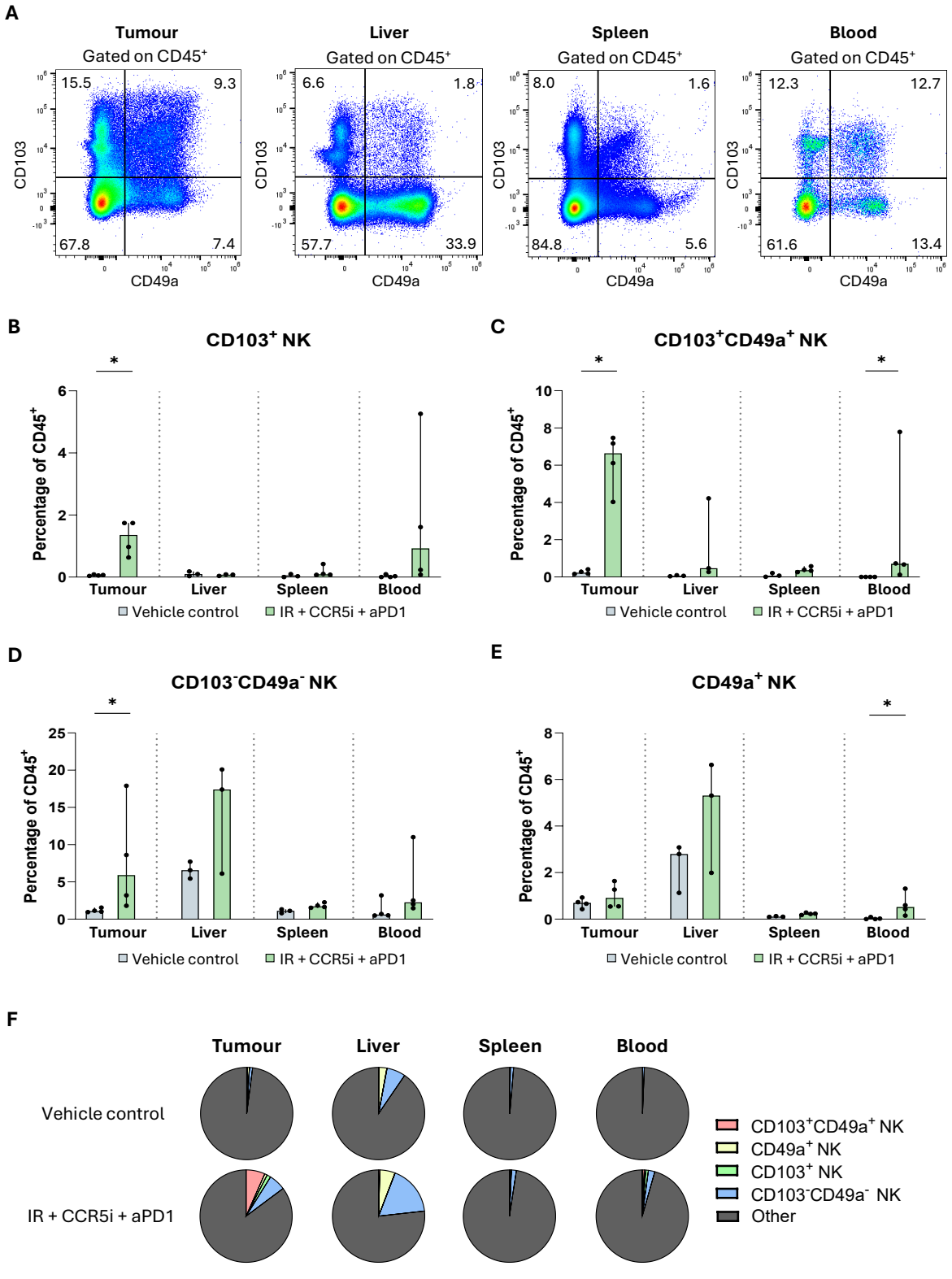
A
Tumour
Gated on CD45+
15.5
9.3
67.8
7.4
Liver
Gated on CD45+
6.6
1.8
57.7
33.9
Spleen
Gated on CD45+
8.0
1.6
84.8
5.6
Blood
Gated on CD45+
12.3
12.7
61.6
13.4
CD103
CD49a
B
CD103+ NK
Percentage of CD45+
Tumour
Liver
Spleen
Blood
Vehicle control
IR + CCR5i + aPD1
C
CD103+CD49a+ NK
D
CD103-CD49a- NK
E
CD49a+ NK
F
Vehicle control
IR + CCR5i + aPD1
CD103+CD49a+ NK
CD49a+ NK
CD103+ NK
CD103-CD49a- NK
Other

Figure 4.4 – Expression of CD103 and CD49a on $CD45^+$ cells

A. Percentage of $CD103^+$ cells, $CD49a^+$ cells, and $CD103^+CD49a^+$ cells (including both NK and T cells) within the totality of $CD45^+$ cells in one representative animal. To calculate the percentage of each NK cell subset specifically, the gating strategy presented in Figures 4.2 and 4.3 was used.

B. Percentage of tumour, liver, spleen, and circulating $CD103^+$ NK cells (as a fraction of $CD45^+$ cells). Median and range shown.

C. Percentage of tumour, liver, spleen, and circulating $CD103^+CD49a^+$ NK cells (as a fraction of $CD45^+$ cells). Median and range shown.

D. Percentage of tumour, liver, spleen, and circulating $CD103^-CD49a^-$ NK cells (as a fraction of $CD45^+$ cells). Median and range shown.

E. Percentage of tumour, liver, spleen, and circulating $CD49a^+$ NK cells (as a fraction of $CD45^+$ cells). Median and range shown.

F. Composition of the $CD45^+$ gate, based on median expression of CD103 and CD49a on NK cells, in control (upper row) or treated animals (lower row).

All comparisons for groups with n > 3 were performed using a two-tailed Mann–Whitney test; *p<0.05.

4.3.4 Tumour NK cells in treated mice can be classified into two clusters, one expressing CD103 and CD49a, and the other expressing NKp46 and NKG2D

Based on the above findings, it was hypothesised that the $CD103^+CD49a^+$ NK subset could correspond to the $NKG2D^-$ NK population in the original study, since both were preferentially expanded following treatment with IR + CCR5i + aPD1. To test this, FlowSOM clustering (Van Gassen et al. 2015) was applied as an unsupervised approach to classify NK cells from tumours of treated mice using eight additional markers, including NKG2D (**Figure 4.5A,B**). This analysis provided two crucial insights: first, the near totality of NK cells in the TME of treated mice segregated into two dominant clusters: Cluster 1 (comprising 70.4% of all NK cells and 97.8% of double positives) and Cluster 3 (comprising 28.3% of all NK cells and 99.3% of double

negatives). The other two minor clusters collectively comprised the remaining 1.3% of all NK cells (**Figure 4.5C,D**). Second, the dichotomy between these two dominant clusters was dependent not only on the expression of the tissue-localisation markers CD103 and CD49a, but also on broader phenotypic differences. On this basis, further phenotypic characterisation and comparisons were restricted to these two biologically distinct populations. Of note, NK cells identified by manual gating as $CD103^+$ mapped almost exclusively to FlowSOM Cluster 1. In contrast, $CD49a^+$ NK cells were distributed across the two major clusters, with over 70% falling within Cluster 1 and the remainder predominantly assigned to Cluster 3.

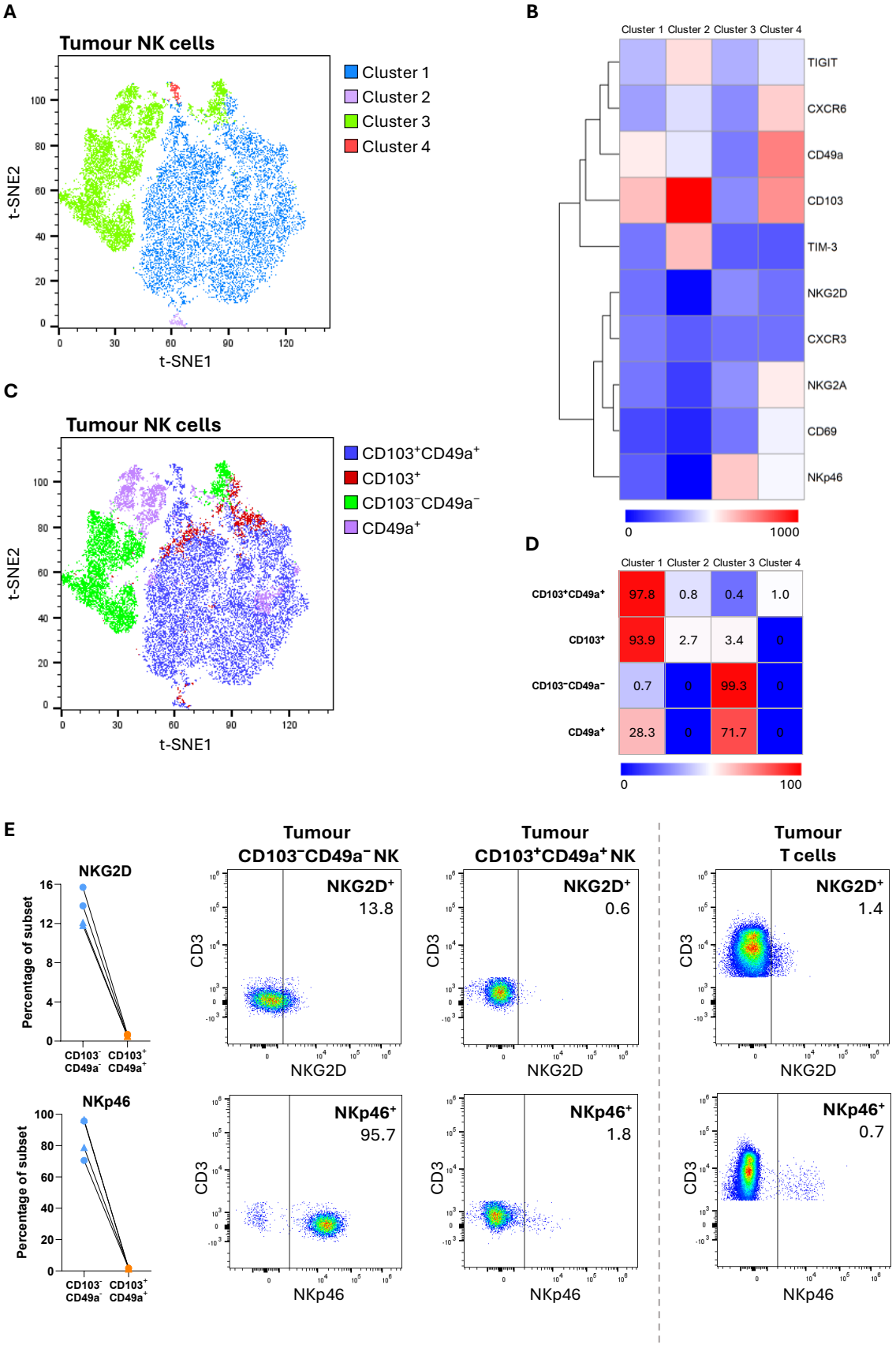
A
Tumour NK cells
Cluster 1
Cluster 2
Cluster 3
Cluster 4
t-SNE2
t-SNE1
B
Cluster 1 Cluster 2 Cluster 3 Cluster 4
TIGIT
CXCR6
CD49a
CD103
TIM-3
NKG2D
CXCR3
NKG2A
CD69
NKp46
0
1000
C
Tumour NK cells
CD103+CD49a+
CD103+
CD103−CD49a−
CD49a+
t-SNE2
t-SNE1
D
Cluster 1 Cluster 2 Cluster 3 Cluster 4
CD103+CD49a+ 97.8 0.8 0.4 1.0
CD103+ 93.9 2.7 3.4 0
CD103−CD49a− 0.7 0 99.3 0
CD49a+ 28.3 0 71.7 0
0
100
E
NKG2D
Percentage of subset
CD103− CD49a−
CD103+ CD49a+
NKp46
Tumour CD103−CD49a− NK
Tumour CD103+CD49a+ NK
Tumour T cells
NKG2D+ 13.8
NKG2D+ 0.6
NKG2D+ 1.4
NKp46+ 95.7
NKp46+ 1.8
NKp46+ 0.7
CD3
NKG2D
NKp46

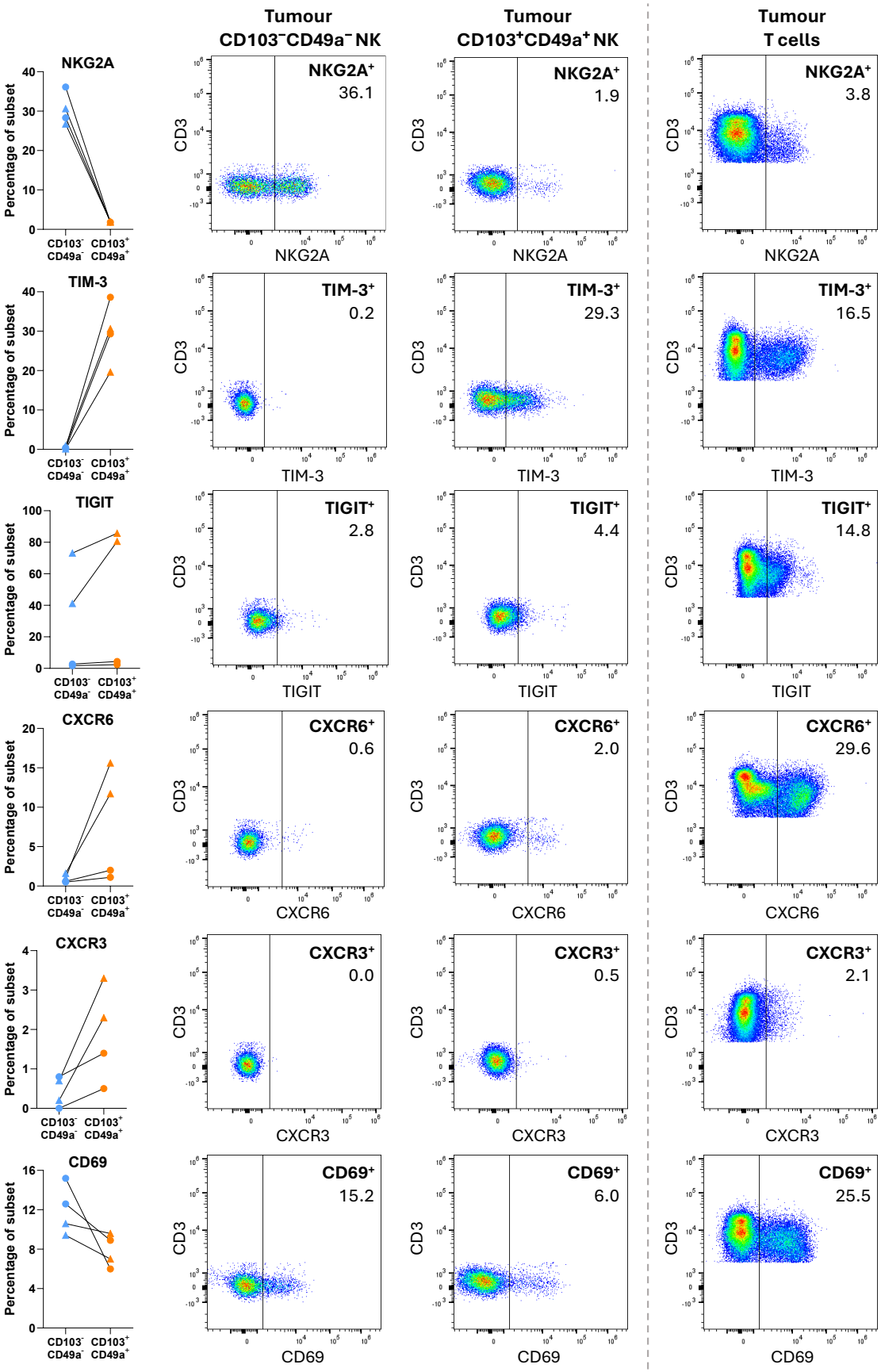
Tumour
CD103⁻CD49a⁻ NK
Tumour
CD103⁺CD49a⁺ NK
Tumour
T cells
NKG2A
Percentage of subset
CD103⁻ CD49a⁻
CD103⁺ CD49a⁺
NKG2A⁺ 36.1
NKG2A⁺ 1.9
NKG2A⁺ 3.8
CD3
NKG2A
TIM-3
TIM-3⁺ 0.2
TIM-3⁺ 29.3
TIM-3⁺ 16.5
TIM-3
TIGIT
TIGIT⁺ 2.8
TIGIT⁺ 4.4
TIGIT⁺ 14.8
TIGIT
CXCR6
CXCR6⁺ 0.6
CXCR6⁺ 2.0
CXCR6⁺ 29.6
CXCR6
CXCR3
CXCR3⁺ 0.0
CXCR3⁺ 0.5
CXCR3⁺ 2.1
CXCR3
CD69
CD69⁺ 15.2
CD69⁺ 6.0
CD69⁺ 25.5
CD69

Figure 4.5 – NK cell characterisation in the tumour of treated mice
A. t-SNE dimensionality reduction of concatenated NK cells from tumours of mice in the IR + CCR5i + aPD1 group (*n* = 4, total 40,000 cells). Four self-organising clusters were identified using the FlowSOM plugin in FlowJo.
B. Heatmap of relative scaled marker expression in the four FlowSOM clusters identified in A. The dendrogram on the side indicates similarity between clusters.
C. Overlay of the four NK cell subsets defined by manual CD103/CD49a gating onto the same t-SNE map shown in A.
D. Degree of overlap between FlowSOM clusters and the four manually gated subsets. The table is read by rows: of the cells in the indicated subset, the percentage that falls into each FlowSOM cluster is shown.
E. Expression of NKG2D, NKp46, NKG2A, TIM-3, TIGIT, CXCR6, CXCR3, and CD69 on $CD103^{-}CD49a^{-}$ and $CD103^{+}CD49a^{+}$ tumour NK cells. Expression on tumour T cells is shown for comparison to the right of the dashed line and was used to assist in gate definition. All markers are plotted against CD3 (Y axis). ▲: culled 1-2 days post-treatment; ●: culled 5-6 days post-treatment.

Due to the small sample size (*n* = 4) and the limited power of a Wilcoxon matched-pairs test for very small datasets, formal statistical comparisons were not performed. Comparisons between $CD103^{+}CD49a^{+}$ and $CD103^{-}CD49a^{-}$ NK cells are therefore presented descriptively using medians (**Figure 4.5E**). $CD103^{+}CD49a^{+}$ NK cells were largely negative for NKG2D (median: 0.6% vs 13.0% of double-negatives) and NKp46 (median: 1.9% vs 87.3% of double-negatives) and expressed higher levels of the inhibitory receptor T cell immunoglobulin and mucin-domain containing-3, TIM-3 (median: 30.0% vs 0.3% of double-negatives), suggesting an overall more inhibited phenotype. The slightly lower CD69 expression by the same cells (median: 7.9% vs 11.6% of double-negatives) partly supports this interpretation. An exception, however, was Natural Killer Group 2, member A (NKG2A), which was expressed at lower levels in double positives than in double negatives (median: 1.9% vs 29.5%).

Considerable inter-animal variability was observed for the inhibitory receptor T cell immunoreceptor with Ig and ITIM domains (TIGIT) and the chemokine receptor CXC motif chemokine receptor 6 (CXCR6). To investigate the reason for this heterogeneity, the washout period for each mouse was examined. The two mice with lower TIGIT and CXCR6 expression had a longer washout (culled 5–6 days post-treatment), whereas the two mice with higher expression were culled 1–2 days post-treatment. This expression pattern was also mirrored in tumour T cells for the same markers (data not shown). CXC motif chemokine receptor 3 (CXCR3) was expressed at low levels by all NK cells and seemed unaffected by washout duration.

4.3.5 Blood and splenic NK cells recapitulate tumour NK cell clusters, while liver NK cells form a distinct CD49a$^+$ subset

Having established that the intratumoural NKG2D$^-$ NK cell subset induced by the IR + CCR5i + aPD1 combination in prior work likely corresponded to CD103$^+$CD49a$^+$ cells with reduced expression of NKG2D and NKp46, it remained to be determined whether CD103$^+$CD49a$^+$ NK cells detected at other sites represented the same subset. As a distinct CD103$^+$CD49a$^+$ population was detected in the circulation of treated mice but not controls, FlowSOM clustering was applied to blood NK cells from treated animals (**Figure 4.6A,B**). As in the tumour, the vast majority of circulating NK cells segregated into two dominant clusters: Cluster 1 (48.8% of NK cells, including 99.7% of double-positive cells), and Cluster 4 (51.9% of NK cells, including 89.5% of double-negative cells). The remaining two clusters collectively accounted for only 1.3% of NK cells (**Figure 4.6C,D**).

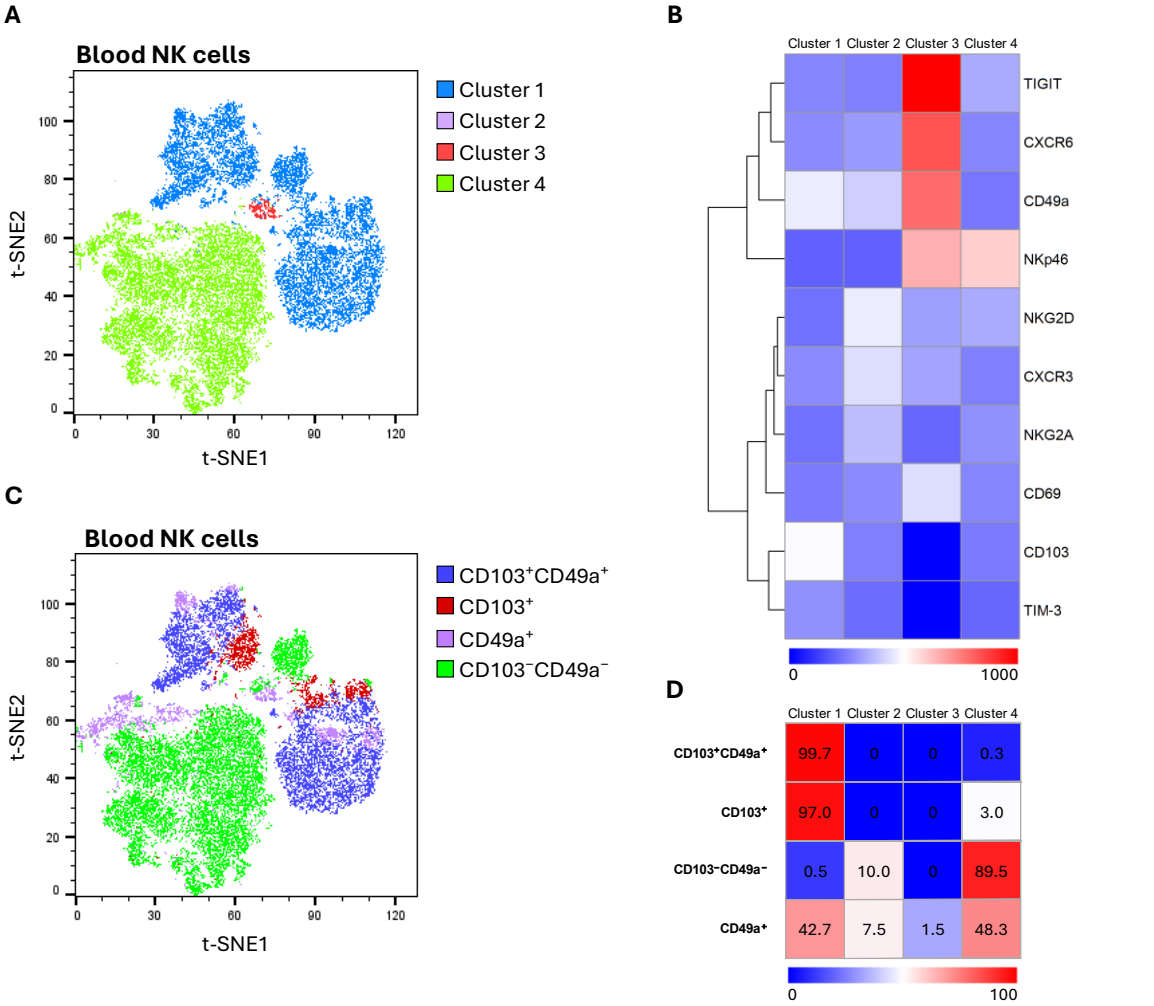
A
Blood NK cells
Cluster 1
Cluster 2
Cluster 3
Cluster 4
t-SNE2
t-SNE1
B
Cluster 1 Cluster 2 Cluster 3 Cluster 4
TIGIT
CXCR6
CD49a
NKp46
NKG2D
CXCR3
NKG2A
CD69
CD103
TIM-3
0
1000
C
Blood NK cells
CD103+CD49a+
CD103+
CD49a+
CD103−CD49a−
t-SNE2
t-SNE1
D
Cluster 1 Cluster 2 Cluster 3 Cluster 4
CD103+CD49a+ 99.7 0 0 0.3
CD103+ 97.0 0 0 3.0
CD103−CD49a− 0.5 10.0 0 89.5
CD49a+ 42.7 7.5 1.5 48.3
0
100
E
NKG2D
Percentage of subset
CD103− CD49a−
CD103+ CD49a+
Blood CD103−CD49a− NK
Blood CD103+CD49a+ NK
Blood T cells
NKG2D+ 41.2
NKG2D+ 0.3
NKG2D+ 3.4
CD3
NKG2D
NKp46
NKp46+ 92.7
NKp46+ 0.4
NKp46+ 0.0

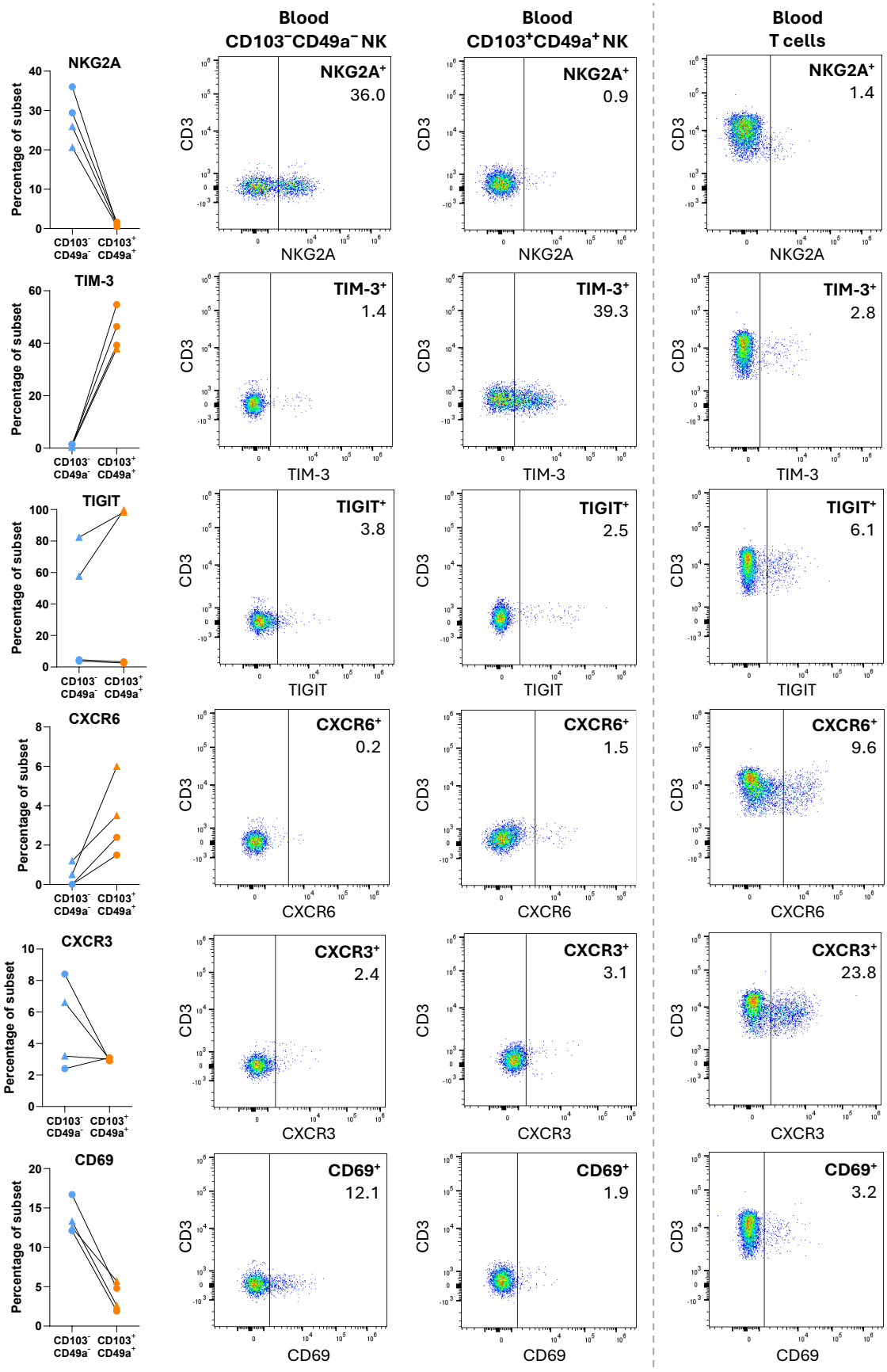
Blood
CD103⁻CD49a⁻ NK
Blood
CD103⁺CD49a⁺ NK
Blood
T cells
NKG2A
Percentage of subset
CD103⁻ CD49a⁻
CD103⁺ CD49a⁺
CD3
NKG2A
NKG2A⁺
36.0
NKG2A⁺
0.9
NKG2A⁺
1.4
TIM-3
TIM-3
TIM-3⁺
1.4
TIM-3⁺
39.3
TIM-3⁺
2.8
TIGIT
TIGIT
TIGIT⁺
3.8
TIGIT⁺
2.5
TIGIT⁺
6.1
CXCR6
CXCR6
CXCR6⁺
0.2
CXCR6⁺
1.5
CXCR6⁺
9.6
CXCR3
CXCR3
CXCR3⁺
2.4
CXCR3⁺
3.1
CXCR3⁺
23.8
CD69
CD69
CD69⁺
12.1
CD69⁺
1.9
CD69⁺
3.2

Figure 4.6 – NK cell characterisation in the blood of treated mice
A. t-SNE dimensionality reduction of concatenated NK cells from blood of mice in the IR + CCR5i + aPD1 group (*n* = 4, total 27,496 cells). Four self-organising clusters were identified using the FlowSOM plugin in FlowJo.
B. Heatmap of relative scaled marker expression in the four FlowSOM clusters identified in A. The dendrogram on the side indicates similarity between clusters.
C. Overlay of the four NK cell subsets defined by manual CD103/CD49a gating onto the same t-SNE map shown in A.
D. Degree of overlap between FlowSOM clusters and the four manually gated subsets. The table is read by rows: of the cells in the indicated subset, the percentage that falls into each FlowSOM cluster is shown.
E. Expression of NKG2D, NKp46, NKG2A, TIM-3, TIGIT, CXCR6, CXCR3, and CD69 on $CD103^{-}CD49a^{-}$ and $CD103^{+}CD49a^{+}$ blood NK cells. Expression on blood T cells is shown for comparison to the right of the dashed line and was used to assist in gate definition. All markers are plotted against CD3. ▲: culled 1-2 days post-treatment; ●: culled 5-6 days post-treatment.

Single-positive subsets defined by manual gating were again distributed across the two dominant clusters in the same pattern as in the tumour: $CD103^{+}$ cells mapping almost entirely to Cluster 1, and $CD49a^{+}$ cells split between Clusters 1 and 4, with a predominance in the latter. Because these two clusters together encompassed virtually all circulating NK cells and largely corresponded to the double-positive and double-negative subsets, phenotypic analyses were restricted to these two biologically distinct populations, as above.

No formal statistical analyses were performed and comparisons between $CD103^{+}CD49a^{+}$ and $CD103^{-}CD49a^{-}$ NK cells are presented descriptively, with medians, as above. Overall, double positive cells largely recapitulated the phenotype of double positive cells in the tumour, with lack of expression of the activating receptors NKG2D and NKp46, and the inhibitory receptor

NKG2A (**Figure 4.6E**). NKG2D, however, was expressed by a higher number of double-negative cells in the blood than in the tumour (median: 43.0% of blood NK cells vs 13.0% of tumour NK cells). As in the tumour, double-positive NK cells in the blood appeared less likely to be activated overall (median CD69 expression: 3.7% vs 12.9% double-negative cells), possibly also as a result of higher TIM-3 expression (median: 42.85% vs 1.2% double-negative cells). As in the tumour, TIGIT and CXCR6 expression was variable, and higher on the two mice culled immediately after treatment (a trend observed on blood T cells, too). Whereas CXCR3 was expressed only by a minority of NK cells in both blood and tumour, a median of over 20% of circulating T cells expressed this chemokine receptor in treated mice.

The same analysis was performed on splenic and hepatic NK cells from treated animals. In the spleen, FlowSOM identified two dominant clusters that together encompassed nearly all NK cells: one largely corresponding to $CD103^{+}CD49a^{+}$ cells and the other to $CD103^{-}CD49a^{-}$ cells (**Figure 4.7A-D**).

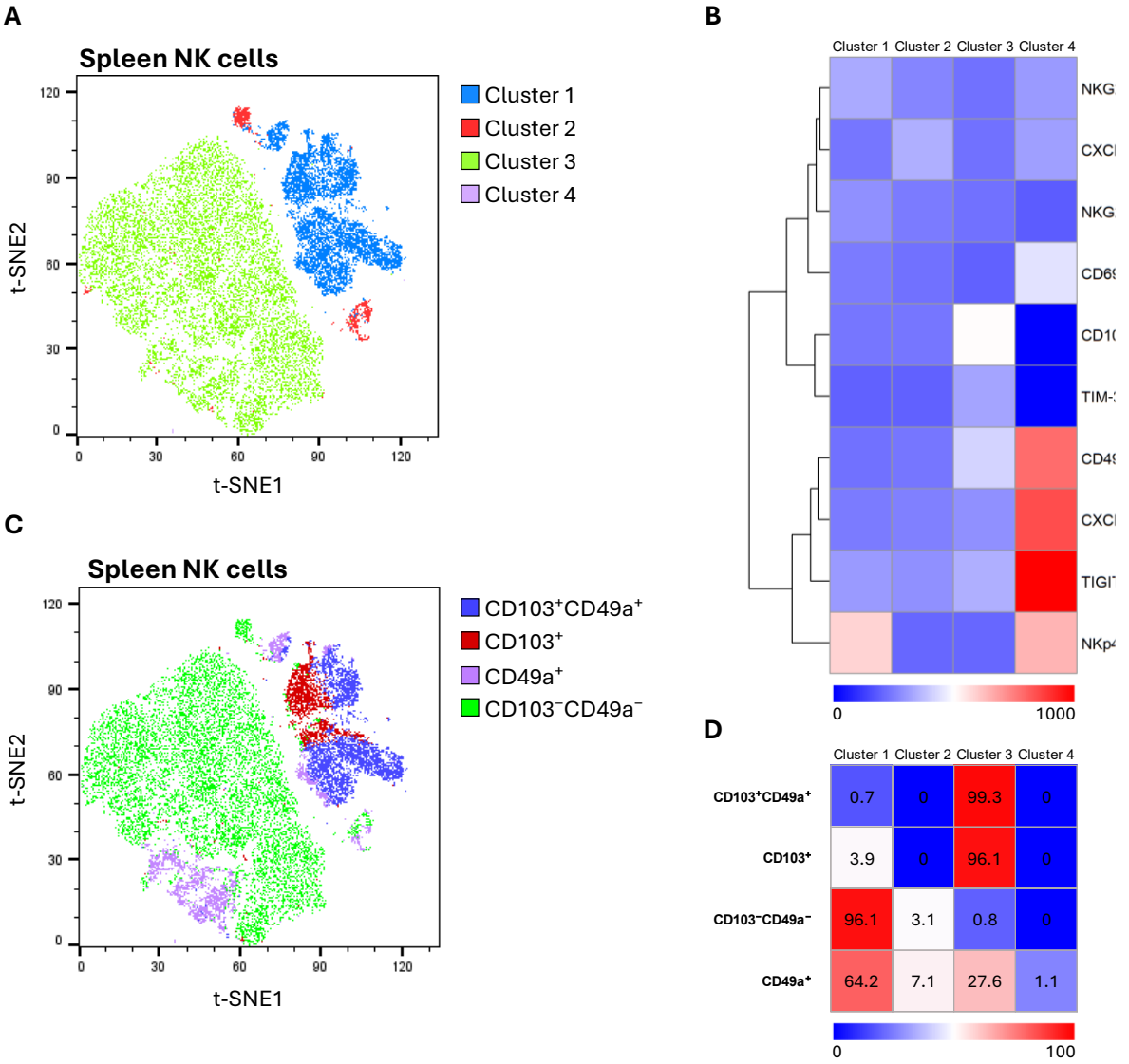
A
Spleen NK cells
Cluster 1
Cluster 2
Cluster 3
Cluster 4
t-SNE2
t-SNE1
B
Cluster 1 Cluster 2 Cluster 3 Cluster 4
0
1000
C
Spleen NK cells
CD103⁺CD49a⁺
CD103⁺
CD49a⁺
CD103⁻CD49a⁻
t-SNE2
t-SNE1
D
Cluster 1 Cluster 2 Cluster 3 Cluster 4
CD103⁺CD49a⁺ 0.7 0 99.3 0
CD103⁺ 3.9 0 96.1 0
CD103⁻CD49a⁻ 96.1 3.1 0.8 0
CD49a⁺ 64.2 7.1 27.6 1.1
0
100
E
NKG2D
NKp46
NKG2A
TIM-3
TIGIT
CXCR6
CXCR3
CD69
Percentage of subset
CD103⁻ CD49a⁻
CD103⁺ CD49a⁺

Figure 4.7 – NK cell characterisation in the spleen of treated mice
A. t-SNE dimensionality reduction of concatenated NK cells from spleens of mice in the IR + CCR5i + aPD1 group (*n* = 4, total 37,000 cells). Four self-organising clusters were identified using the FlowSOM plugin in FlowJo.
B. Heatmap of relative scaled marker expression in the four FlowSOM clusters identified in A. The dendrogram on the side indicates similarity between clusters.
C. Overlay of the four NK cell subsets defined by manual CD103/CD49a gating onto the same t-SNE map shown in A.
D. Degree of overlap between FlowSOM clusters and the four manually gated subsets. The table is read by rows: of the cells in the indicated subset, the percentage that falls into each FlowSOM cluster is shown.
E. Expression of NKG2D, NKp46, NKG2A, TIM-3, TIGIT, CXCR6, CXCR3, and CD69 on $CD103^{-}CD49a^{-}$ and $CD103^{+}CD49a^{+}$ spleen NK cells. ▲: culled 1-2 days post-treatment; ●: culled 5-6 days post-treatment.

As observed in blood and tumour samples, $CD103^{+}$ NK cells were almost exclusively assigned to the double-positive cluster, whereas $CD49a^{+}$ NK cells preferentially segregated with the double-negative cluster. The phenotypic profile closely mirrored that of tumour-infiltrating and circulating $CD103^{+}CD49a^{+}$ NK cells, characterised by absence of NKG2D, NKp46, and NKG2A, reduced CD69 expression, and increased TIGIT and TIM-3 expression (**Figure 4.7E**). Few NK cells expressed CXCR3 or CXCR6 (median <5% in both double-positive and double-negative subsets for both markers). By contrast, nearly 25% of T cells expressed CXCR3, consistent with findings in blood (not shown).

The liver represented an exception. As anticipated from the quantitative shifts described in **Figure 4.3**, the dominant FlowSOM clusters consisted of double-negative and $CD49a^{+}$ single-positive NK cells, rather than double-positive cells (**Figure 4.8A-D**).

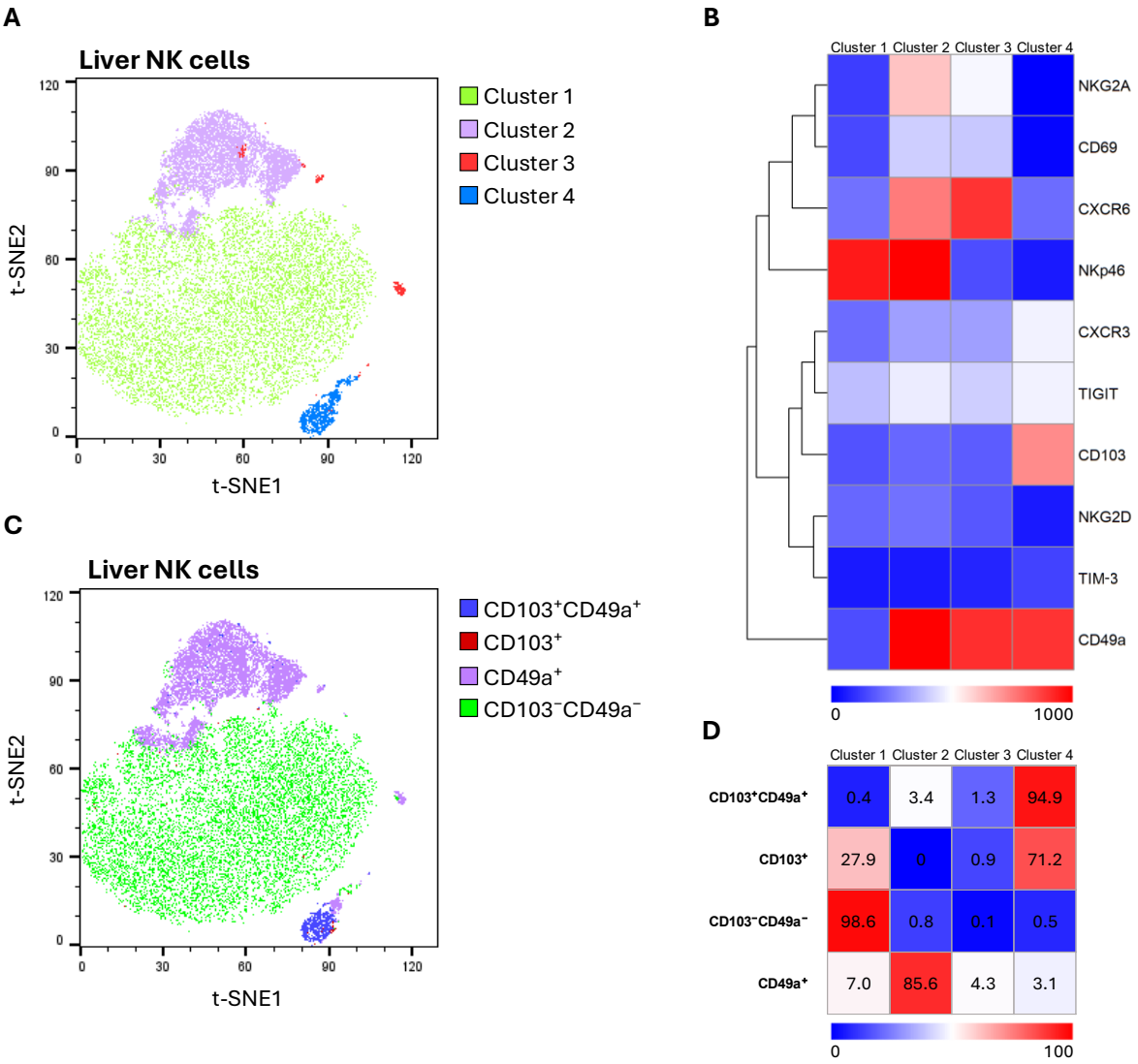
A
Liver NK cells
Cluster 1
Cluster 2
Cluster 3
Cluster 4
t-SNE2
t-SNE1
B
Cluster 1 Cluster 2 Cluster 3 Cluster 4
NKG2A
CD69
CXCR6
NKp46
CXCR3
TIGIT
CD103
NKG2D
TIM-3
CD49a
0
1000
C
Liver NK cells
CD103+CD49a+
CD103+
CD49a+
CD103-CD49a-
t-SNE2
t-SNE1
D
Cluster 1 Cluster 2 Cluster 3 Cluster 4
CD103+CD49a+ 0.4 3.4 1.3 94.9
CD103+ 27.9 0 0.9 71.2
CD103-CD49a- 98.6 0.8 0.1 0.5
CD49a+ 7.0 85.6 4.3 3.1
0
100

E

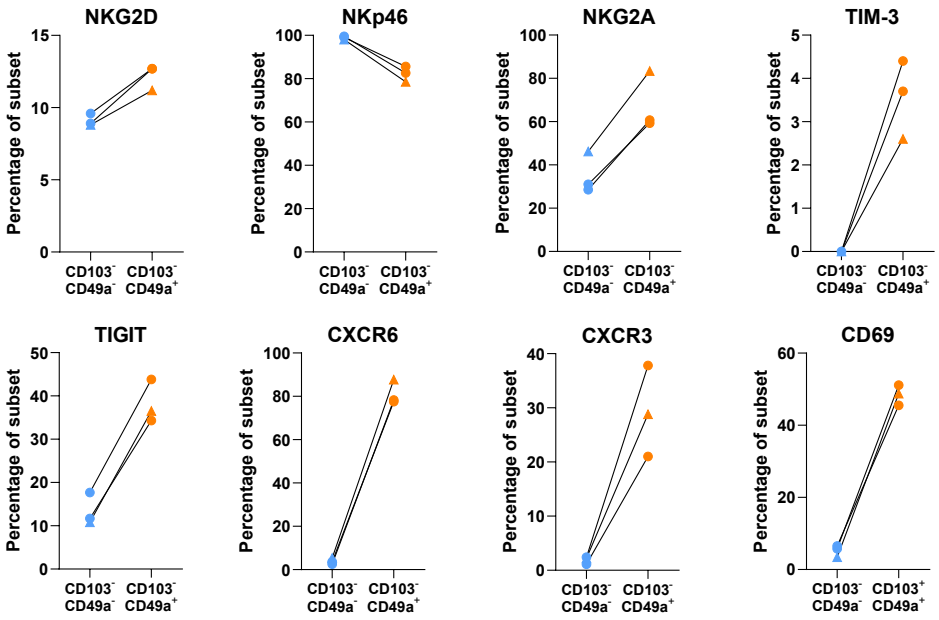
NKG2D
NKp46
NKG2A
TIM-3
TIGIT
CXCR6
CXCR3
CD69
Percentage of subset
CD103- CD49a-
CD103- CD49a+
CD103+ CD49a+

Figure 4.8 – NK cell characterisation in the liver of treated mice
A. t-SNE dimensionality reduction of concatenated NK cells from livers of mice in the IR + CCR5i + aPD1 group (*n* = 3, total 55,778 cells). Four self-organising clusters were identified using the FlowSOM plugin in FlowJo.
B. Heatmap of relative scaled marker expression in the four FlowSOM clusters identified in A. The dendrogram on the side indicates similarity between clusters.
C. Overlay of the four NK cell subsets defined by manual CD103/CD49a gating onto the same t-SNE map shown in A.
D. Degree of overlap between FlowSOM clusters and the four manually gated subsets. The table is read by rows: of the cells in the indicated subset, the percentage that falls into each FlowSOM cluster is shown.
E. Expression of NKG2D, NKp46, NKG2A, TIM-3, TIGIT, CXCR6, CXCR3, and CD69 on $CD103^{-}CD49a^{-}$ and $CD49a^{+}$ liver NK cells. ▲: culled 1-2 days post-treatment; ●: culled 5-6 days post-treatment.

Liver $CD103^{+}$ NK cells predominantly co-clustered with double-positive cells within a minor, separate population (3.0% of hepatic NK cells). Given that $CD49a^{+}$ cells in the liver formed a major distinct cluster, subsequent analyses focussed on comparisons between this subset and the double-negative population. $CD49a^{+}$ NK cells (as well as $CD49a^{+}$ T cells, not shown) displayed markedly elevated expression of CD69 and CXCR6, and up to 40% also expressed CXCR3, a marker not expressed by NK cells with tissue-localisation markers at other sites (**Figure 4.8E**). Both $CD49a^{+}$ and double-negative NK cells expressed NKp46 at high levels, although expression was greater among double negatives (median: 99.0% vs. 82.6% of double-negative cells). By contrast, inhibitory receptors including NKG2A, TIM-3, and TIGIT were more abundantly expressed on $CD49a^{+}$ NK cells.

4.3.6 The presence of CD103$^+$CD49a$^+$NKG2D$^-$ NK cells in tumours may correlate with tumour control through an NK–cDC1–CD8$^+$ T cell axis

The previously described NK cell subset correlating with better tumour control matches NK cells with reduced expression of activating receptors (NKG2D, NKp46), increased expression of inhibitory receptors (TIM-3, TIGIT), and a less activated phenotype overall. In an attempt to gain clarity on this seemingly paradoxical correlation, two publicly available single-cell RNA sequencing (scRNA-seq) datasets of NK cells from human pancreatic cancer (Peng et al. 2019; Steele et al. 2020) were examined by other members of the research group. In the Steele dataset (51,561 cells), three NK subpopulations were identified (**Figure 4.9A**): a tissue-associated, exhausted cluster (Cluster 1) and two non-tissue-associated, cytotoxic clusters (Clusters 2 and 3). The transcriptomic profile of Cluster 1 closely matched the murine CD103$^+$CD49a$^+$ NK subset, and additionally included XCL1 and XCL2 expression, chemokines known to attract cDC1s, which present antigens to CD8$^+$ T cells (Go et al. 2024).

In the original study by Go et al., correlation analyses showed that the abundance of the NKG2D$^-$ NK subset was associated with CD8$^+$ T cell frequencies in tumours of mice (**Figure 4.9B**), and that its human counterpart associated with CD8$^+$ T cells in human pancreatic tumours only when a high cDC1 signature was present (**Figure 4.9C**). A working model was therefore proposed in which CD103$^+$CD49a$^+$NKG2D$^-$ NK cells act in an immunoregulatory capacity, promoting CD8$^+$ T cell responses indirectly via

XCL1/2-mediated recruitment of cDC1s (**Figure 4.9E**). This model would explain, at least in part, the improved tumour control observed in the original study, and the prolonged survival in patients with pancreatic cancer exhibiting a high NK–Cluster 1 signature (**Figure 4.9D**).

As a preliminary and purely exploratory assessment of the proposed model, XCL1 concentrations were measured in the plasma from mice in the study presented in this chapter. XCL1 was detectable in 75% of treated animals and undetectable in all untreated controls (n = 4 for both groups, **Figure 4.9F**).

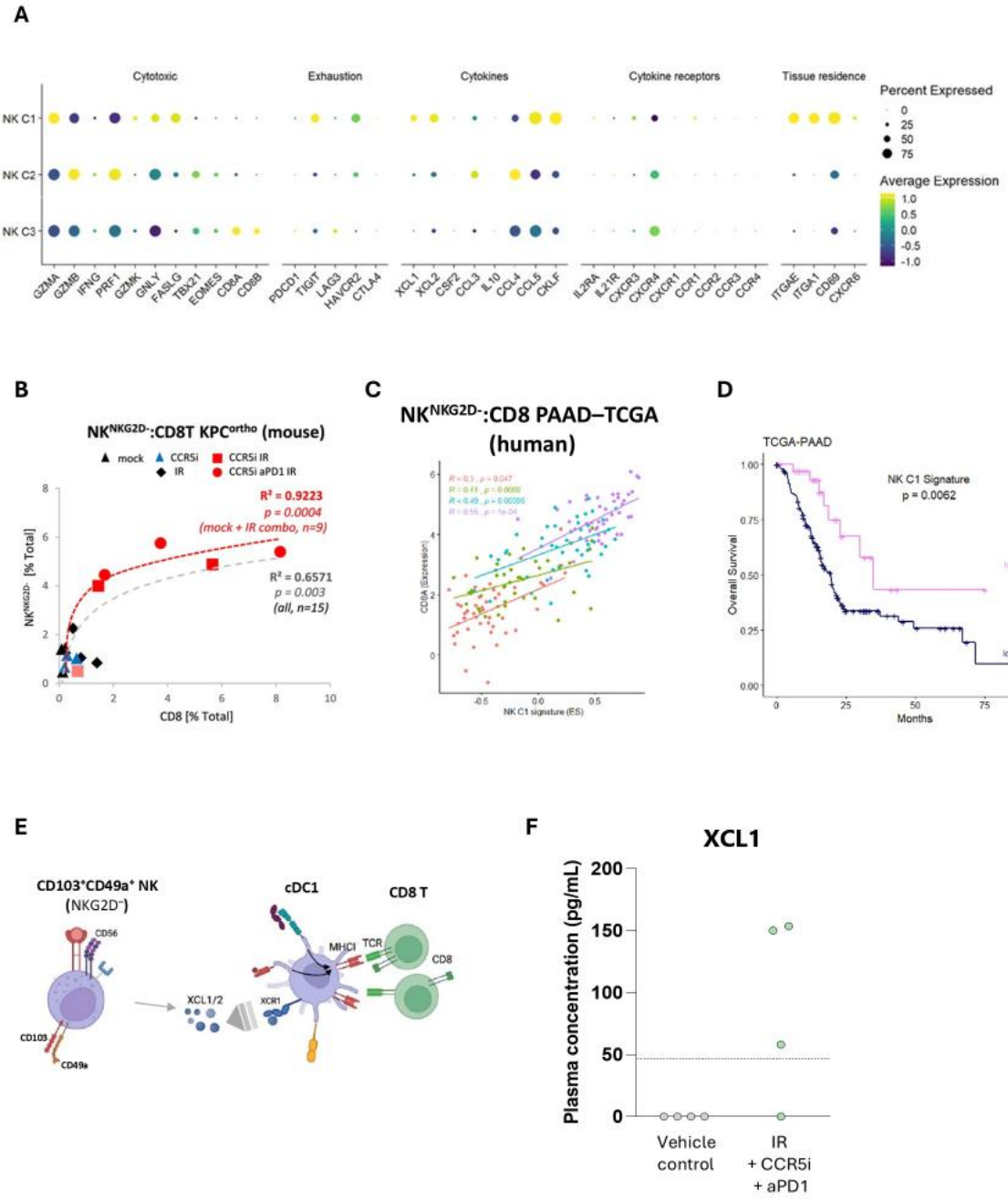
A
Cytotoxic
Exhaustion
Cytokines
Cytokine receptors
Tissue residence
NK C1
NK C2
NK C3
GZMA GZMB IFNG PRF1 GZMK GNLY FASLG TBX21 EOMES CD8A CD8B
PDCD1 TIGIT LAG3 HAVCR2 CTLA4
XCL1 XCL2 CSF2 CCL3 IL10 CCL4 CCL5 CKLF
IL2RA IL21R CXCR3 CXCR4 CXCR1 CCR1 CCR2 CCR3 CCR4
ITGAE ITGA1 CD69 CXCR6
Percent Expressed
0
25
50
75
Average Expression
1.0
0.5
0.0
-0.5
-1.0
B
NK^NKG2D-:CD8T KPC^ortho (mouse)
mock
CCR5i
CCR5i IR
IR
CCR5i aPD1 IR
R² = 0.9223
p = 0.0004
(mock + IR combo, n=9)
R² = 0.6571
p = 0.003
(all, n=15)
NK^NKG2D- [% Total]
CD8 [% Total]
C
NK^NKG2D-:CD8 PAAD–TCGA (human)
CD8A (Expression)
NK C1 signature (ES)
D
TCGA-PAAD
NK C1 Signature
p = 0.0062
high (n=34)
low (n=142)
Overall Survival
Months
E
CD103+CD49a+ NK
(NKG2D-)
CD56
CD103
CD49a
XCL1/2
cDC1
MHCI
TCR
XCR1
CD8 T
CD8
F
XCL1
Plasma concentration (pg/mL)
200
150
100
50
0
Vehicle control
IR + CCR5i + aPD1

Figure 4.9 – Proposed working model: CD103$^+$CD49a$^+$ NK cells as immune regulators
(A-E) Freely adapted from *Go, Demetriou, Valenzano, et al., eLife, 2024 (Figures 5-7) and reproduced under the terms of the Creative Commons Attribution License (CC BY)*.
(F) Generated from data produced in this study.
A. Dot plot (scaled) showing the different gene expression programmes across the three NK clusters in the Steele dataset.
B. Correlation of NKG2D$^-$ NK cells (CD3$^-$NK1.1$^+$NKG2D$^-$) with CD8$^+$ T cells (CD3$^+$CD8$^+$) calculated on sections of tumours from treated mice in the original study by Go et al., as determined by the HALO automated image analysis and cell classifying software. R^2 and p-values indicate positive correlation across all tumours (grey, *n* = 15) or samples limited to mock, IR+CCR5i, and IR+CCR5i+αPD1 combinations (red, *n* = 9).
C. Correlation of NKG2D$^-$ NK (NK Cluster 1) signature with CD8A in bulk RNA-sequencing data from the pancreatic adenocarcinoma (PAAD) cohort of the TCGA (The Cancer Genome Atlas) based on strength of cDC1 signature stratified by quartiles.
D. Kaplan-Meier survival curves of patients in the PAAD-TCGA cohort, stratified based on expression of the NK Cluster 1 signature.
E. Proposed working model in which CD103$^+$CD49a$^+$ NK cells attract cDC1s to tumours, thereby facilitating tumour-specific CD8$^+$ T cell responses.
F. XCL1 plasma concentration (measured by ELISA) in control and treated mice from the study presented in this chapter. Dashed line: detection threshold (40 pg/mL). Samples for which concentrations fell below the detection threshold were plotted at 0.

4.4

Discussion

The work presented in this chapter aimed to characterise a novel NK cell subset that accumulated in pancreatic tumours of mice treated with a multimodal regimen comprising radiotherapy and dual immunotherapy. This subset had been identified in previous work from our laboratory and shown to correlate with tumour control.

Before delving into the interpretation of the data presented in this chapter, four key limitations must be acknowledged. Firstly, the experiments in this chapter were underpowered to reliably detect treatment effects, and formal

statistical analyses could only be conducted for some comparisons (see Methods for more details). Consequently, results should be interpreted with great caution, as indicative of trends, and further validation is required before any definitive conclusions may be drawn. Secondly, treatment initiation was based on tumour palpation, using established tumour size ranges from prior experience with this model. However, because exact tumour volumes were not measured, some inter-mouse variability in size at treatment onset cannot be excluded. Thirdly, the treatment schedule differed slightly from that described in the original study, limiting direct comparisons. Specifically, a higher fractionated irradiation dose was administered with the expectation that it might improve survival, and a shorter washout period was used prior to culling to facilitate detection of treatment-induced immune alterations. Lastly, because the study endpoint was defined by the humane endpoint (signs of sickness or distress), mice were culled at variable times following treatment. This variability complicates data interpretation, and repeating the study with a predefined culling time would improve consistency and facilitate comparison across samples.

With these caveats in mind, a population of NK cells co-expressing two key markers of tissue localisation (CD103 and CD49a) was observed in the tumours of treated mice. This is the first report of NK cells bearing markers typically associated with tissue residency in pancreatic tumours. Although absolute counts per gram of tissue were not measured, the relative abundance of these cells increased in treated tumours both within NK cells

(at the expense of NK subsets expressing either marker alone or neither), and within the total leukocyte pool. The effects of treatment were broader than simply promoting intratumoural accumulation of the double positive NK cell population. In fact, $CD103^+$ and $CD103^-CD49a^-$ NK cells, as well as B, T, and NKT cells all rose significantly with treatment, resulting in the lymphocyte fraction (the sum of the B, T, NK, and NKT cells) rising 4-fold. While originally described in the tumours of treated mice, NK cells expressing both markers of tissue localisation were also detected in the blood of treated mice. This demonstrates that, although expressing markers of tissue localisation (and, therefore, in spite of their capacity and propensity to localise to sites rich in E-cadherin and collagen IV), these cells leave their homing tissues, at least transiently, to recirculate in the blood. This further reinforces the notion that phenotype alone is insufficient to label a cell as tissue-resident, as presented in main Introduction.

Unsupervised clustering of NK cells in treated mice revealed several crucial insights. Irrespective of the abundance of $CD103^+CD49a^+$ NK cells in a given tissue, this subset (found to varying degrees in the tumour, blood, and spleen of treated animals) seemed to represent the same cellular identity. This suggests that the development and/or maintenance of this subset is only in part dependent on tissue-specific cues, as the overall phenotype was largely maintained across the three tissues. At these three sites, this phenotype was characterised by lack of expression of NKG2D, NKp46, and NKG2A, and moderate expression of TIM-3.

CXCR6 and TIGIT showed time-dependent expression on CD103$^+$CD49a$^+$ NK cells after treatment. Both markers were highest in animals culled soon after treatment, with CXCR6 detected at lower levels in mice with a longer washout likely due to downregulation upon entry into the TME. A high TIGIT expression was expected on double-positive NK cells in tumours irrespective of washout, in line with a recent study elegantly demonstrating that NK cells upregulate genes leading to suppression within 24 hours from ingress into tumours (Dean et al. 2024). However, surprisingly, this this was not the case in this study, highlighting the need for more detailed analyses (e.g., pseudotime trajectory) to resolve the dynamics of marker regulation. Interestingly, CXCR3 was expressed on very few circulating and splenic NK cells, but on approximately 25% of circulating and splenic T cells, suggesting a different role for this chemokine receptor in innate and adaptive lymphocytes.

The liver of treated mice was virtually devoid of CD103$^+$CD49a$^+$ NK cells. Instead, two NK cell subsets were found: double-negative NK cells and CD49a$^+$ NK cells. The CD49a$^+$ population displayed a phenotype largely distinct from the double-positive population observed at other sites, and instead resembling liver-resident NK cells described in the literature (Peng et al. 2013). This subset was characterised by high expression of CD69, CXCR6, and NKp46, and moderate expression of TIGIT, CXCR3, and NKG2A. The high expression of CD69 on liver CD49a$^+$ NK cells, compared with its near absence on double-positive cells in the tumour, supports the fact that markers used to define tissue localisation vary across tissues. Liver CD49a$^+$

NK cells appeared largely unaffected by the duration of washout, as their phenotype was consistent across all examined mice, suggesting a relatively stable population. Indeed, the population most substantially enriched after treatment in the liver was the double-negative NK cell subset, rather than the CD49a$^+$ subset.

In Chapter 3, it was speculated that CD103$^+$ NK cells were unlikely to represent a transitional state towards the acquisition of a double-positive state by conventional (double-negative) NK cells, in light of the observation that many tissue NK cells expressed CD49a, whereas CD103$^+$ cells were also found at high proportions in non-epithelial sites, including the blood. Interestingly, unsupervised clustering provided evidence to the contrary, as it consistently assigned the vast majority of manually defined CD103$^+$ cells to the same cluster as CD103$^+$CD49a$^+$ NK cells, suggesting that these two populations are in fact more similar than previously presumed. On the other hand, CD49a$^+$ were invariably distributed between double-positive and double-negative clusters, with a preference for the latter (except for the liver, as already discussed), suggesting a closer resemblance to circulating NK cells.

Because the aim of this chapter was to merely characterise this novel subset in terms of phenotype, the questions as to how CD103$^+$CD49a$^+$ NK cells accumulate in tumours and correlate with positive outcomes despite their inhibited phenotype remain largely unresolved. Go et al. have proposed a model in which these cells recruit cDC1 to tumours, thereby

promoting antigen-specific T cell responses. However, this hypothesis was primarily based on correlations from human data and has not yet been mechanistically demonstrated in the context of pancreatic cancer. An NK–cDC1 axis has been proven to exist in other cancers (Böttcher et al. 2018; Kirchhammer et al. 2022), supporting the plausibility of such a model.

Providing evidence for the proposed NK–cDC1–$CD8^+$ T cell axis would require extensive *in vivo* validation and a considerably more comprehensive investigation, which was beyond the scope of this chapter (and of this DPhil thesis altogether). First, because XCL1 can be produced not only by NK cells but also by other lymphocyte populations—including activated $CD8^+$ T cells and $CD4^+$ T cells (Dorner et al. 2002; Kroczek and Henn 2012)—, it would be essential to demonstrate that NK cells represent a major source of XCL1 in this setting. This could be achieved by detecting XCL1 production at the protein level in NK cells by intracellular flow cytometry, or by assessing *Xcl1* transcript expression in sorted NK cells using RNA sequencing or quantitative PCR. Second, as XCL1 is proposed to recruit cDC1s through XCR1 signalling, the accumulation of NK cells with immunoregulatory features should be accompanied by enhanced $XCR1^+$ cDC1 accumulation in the tumour and/or tumour-draining lymph nodes. This could be evaluated, for example, by measuring absolute numbers of $XCR1^+$ cDC1s using flow cytometry or immunohistochemistry. Third, because cDC1s are specialised in cross-presentation of exogenous antigens to $CD8^+$ T cells, recruitment of this subset would be expected to promote the priming and activation of tumour-specific $CD8^+$ T cells. This could be assessed by

quantifying $CD8^+$ T cells expressing markers of activation or effector differentiation in tumours or tumour-draining lymph nodes. Antigen-specific priming could also be tested more directly using the OT-I TCR transgenic mouse model (Clarke et al. 2000). If all of the above were demonstrated to be true, then the abundance of $XCL1^+$ NK cells, $XCR1^+$ cDC1s, and activated $CD8^+$ T cells would be expected to correlate positively with direct measures of tumour control, such as tumour volume reduction or improved survival, rather than with indirect surrogates alone. A stronger demonstration of causality would then require perturbation of individual components of the axis. For example, selective depletion (Yamazaki et al. 2013) or constitutive loss (Hildner et al. 2008) of cDC1s would be expected to impair tumour control if the pathway were functionally relevant. Similarly, depletion of $CD8^+$ T cells (Kruisbeek 2001) should attenuate any survival or tumour growth benefit mediated by the proposed axis. Complementary mechanistic insight could also be obtained from *in vitro* co-culture systems involving sorted tissue-resident NK cells, cDC1s, and antigen-specific $CD8^+$ T cells, or from cytotoxicity assays involving $CD8^+$ T cells and tumour cells. Given the complexity of the proposed model, XCL1 concentrations in plasma cannot provide adequate mechanistic insight into this axis. Such measurements do not identify the cellular source of the chemokine, its site of production, or whether its presence is linked to cDC1 recruitment or $CD8^+$ T cell activation. Consequently, the plasma XCL1 data presented above should be interpreted as exploratory and, at best, hypothesis-generating observations rather than evidence for the proposed axis.

Lastly, it should be reiterated that, both in the original study by Go et al. and in the present work, NK cells were defined solely on the basis of NK1.1 expression. As already discussed extensively in the main Introduction, murine NK cells, and the tissue-associated/resident subsets in particular, share several features with ILC1s, making the distinction between the two blurred. The salivary glands provide an exemplar of this concept, as they are the closest embryological, histological, and functional homologue of the exocrine pancreas. Salivary gland NK cells were initially described in mice as a hyporesponsive $CD69^+$ subset, with lower NKp46 expression than splenic NK cells, and simply termed *salivary gland NK cells* (Tessmer et al. 2011). This subset was shown to develop independently of Nfil3, a transcription factor required for conventional (circulating) NK cell development (Cortez et al. 2014). The same group subsequently demonstrated that cells in this subset depended on TGF-β signalling (which downregulates Eomes and induces CD103 and CD49a expression), leading to their reclassification as a distinct ILC subset with features intermediate between ILC1s and NK cells (Cortez et al. 2016). Notably, these salivary gland ILCs expressed both T-bet and Eomes, like conventional NK cells; however, unlike NK cells or ILC1s, they were able to develop in the absence of both transcription factors. Parabiosis experiments further established that they were largely tissue-resident and not replenished from the circulation. More recently, the same group reclassified this subset once again as trNK cells and, rather confusingly, went on to show that their maintenance depends on TGF-β produced by $NKp46^+$ ILC1s (Sparano et al. 2025). Thus, the very same population, described by the same group, has

undergone continuous redefinition over time. Importantly, the authors describe an Eomes$^+$CD49a$^+$ population in the pancreas with similar traits to salivary gland trNK cells. However, while salivary glands trNK cells express CD69 (Cortez 2014, 2016), the tumour subset described in this chapter mostly lacked CD69 expression. Moreover, trNK cells can be detected in salivary glands as early as 1.5 weeks of age (Sparano et al. 2025), clearly a different context to an implanted tumour.

Whereas distinguishing trNK cells from ILC1s remains challenging in mice, XCL1-secreting subsets have been clearly identified in humans within CD56$^+$ NK cells, by us (Go et al. 2024) and others (Rebuffet et al. 2024). Because the proposed mechanism for the contribution of NK1.1$^+$CD103$^+$CD49a$^+$ cells to tumour control was the secretion of XCL1, these cells were designated as NK cells in the present study. Existing literature in mice, too, supports a role for NK cells (not ILC1s) in cDC1 recruitment to tumours and promotion of cDC1-CD8 interactions (Böttcher et al. 2018; K. C. Barry et al. 2018; Kirchhammer et al. 2022). In contrast to some of these studies, cells in this study were not termed “trNK”, but more cautiously “CD103$^+$CD49a$^+$ NK cells”, as they were also observed in the circulation.

Chapter 5

Preliminary evaluation of a novel combination of FAK and TIGIT inhibition in the KPC orthotopic model of PDAC

Introduction

Chapter 4 described a treatment regimen that promotes adaptive anti-tumour responses by expanding an NK cell population with tissue-associated markers and potential immunoregulatory features. While certainly a promising approach, the fact that radiotherapy is currently indicated for only a minority of pancreatic cancer patients (Conroy et al. 2023) limits its translational potential.

Although the triple combination of radiotherapy, CCR5 inhibition, and PD-1 blockade expanded $CD103^{+}CD49a^{+}$ NK cells, similar tissue-associated NK populations have been reported in multiple cancer types even in the absence of therapy (H. Sun et al. 2019; Moreno-Nieves et al. 2021; Brownlie et al. 2021), suggesting that this subset is not uniquely induced by this regimen. These observations imply that alternative strategies could be used to facilitate lymphocyte (including $CD103^{+}CD49a^{+}$ NK cell) infiltration into pancreatic tumours, without relying on radiotherapy.

Given several reports that focal adhesion kinase (FAK) inhibition could enhance lymphocyte infiltration in mouse models of cancer (Serrels et al. 2015; Jiang et al. 2016a), the FAK inhibitor Defactinib (hereafter: FAKi) was

chosen as a promising candidate. FAK is expressed by tumour cells (and is overexpressed in human PDAC) (Jiang et al. 2016a), as well as stromal cells, including myeloid suppressor cells (Davidson et al. 2022) and Tregs (Serrels et al. 2015). Importantly, FAK is also expressed by cancer-associated fibroblasts (CAFs) in pancreatic cancer, where it mediates a positive feedback loop: increased extracellular matrix (ECM) deposition by CAFs causes desmoplasia, which in turn promotes FAK activation in CAFs and tumour cells (via integrin engagement), enhancing proliferation and invasion (Zaghdoudi et al. 2020) (**Figure 5.1**). Pharmacological blockade of FAK has, therefore, the potential to: (I) limit tumour cell survival, proliferation and invasion, (II) reduce fibrosis and desmoplastic barriers that impede immune cell access, and (III) relieve immune suppression to permit greater effector cell function.

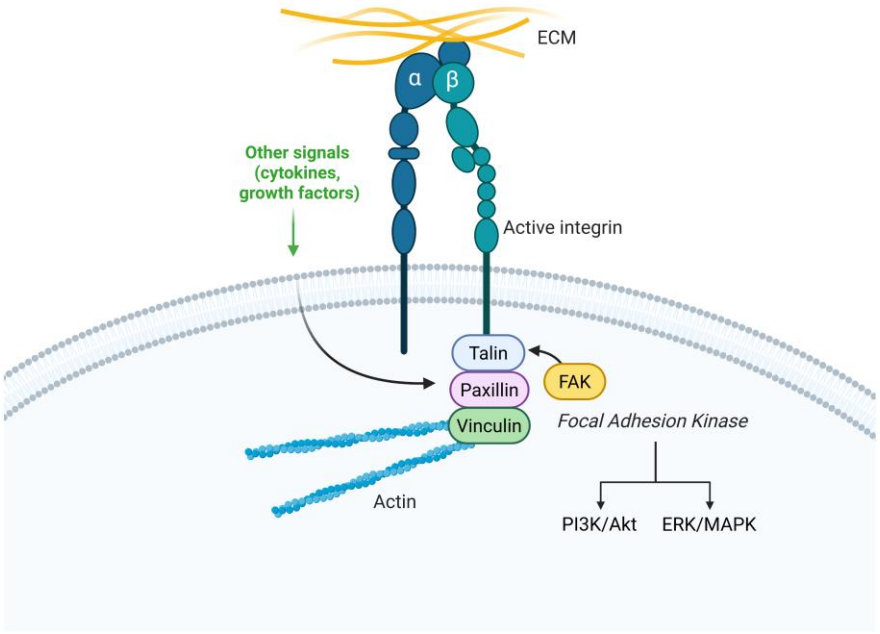

Figure 5.1 – Schematic of FAK signalling
Binding of integrins to proteins in the ECM promotes FAK activation, which triggers downstream pathways involved in cell proliferation, invasion, and migration. For simplicity, direct translocation of FAK to the nucleus is not depicted. PI3K: phosphatidylinositol 3-kinase; Akt: protein kinase B; ERK: extracellular signal-regulated kinase; MAPK: mitogen-activated protein kinase. Created with BioRender.

To augment the potential efficacy of FAK inhibition, this was tested in combination with a blocking antibody targeting TIGIT (hereafter: aTIGIT), as this checkpoint receptor (rather than PD-1) was shown to define exhaustion in $CD8^+$ T cells in patients with PDAC (Steele et al. 2020), and its expression was detected on a broad array of lymphocytes in both humans and mice (Freed-Pastor et al. 2021; Peng et al. 2022; Heiduk et al. 2023).

5.2
Aims

To test the efficacy of a novel combination of FAK and TIGIT blockade in the KPC orthotopic model of PDAC.

5.3
Results

5.3.1 An increase in median survival and immune cell density is observed in mice treated with FAKi and FAKi + aTIGIT

A study was conducted to determine how effective the combination of FAK and TIGIT inhibition was with respect to FAKi alone or no treatment (n = 5 per group). Mice were randomised into three groups upon detection of a palpable tumour, which corresponds to an estimated volume of approximately 50–100 mm^3 based on prior experience and published

measurements from our laboratory. The endpoint for this cohort was survival. Median survival differed among the three groups (15 days in controls vs 19 days in the FAKi group, and 22 days in the FAKi + aTIGIT group); however, the overall comparison among survival curves did not reach statistical significance (p = 0.08) (**Figure 5.2A**).

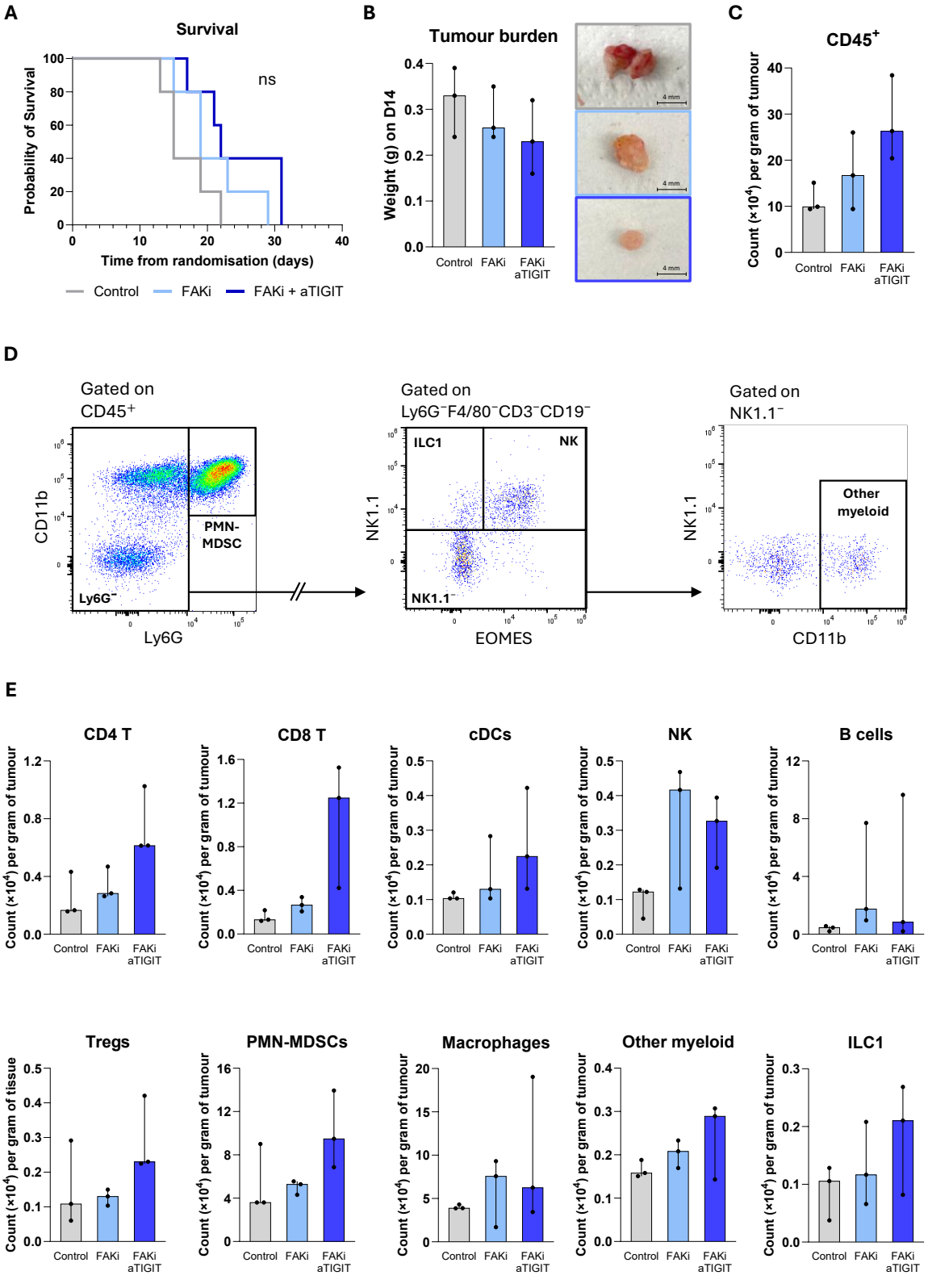
A
Survival
Probability of Survival
ns
Time from randomisation (days)
Control
FAKi
FAKi + aTIGIT
B
Tumour burden
Weight (g) on D14
Control
FAKi
FAKi aTIGIT
C
CD45+
Count (×10⁴) per gram of tumour
D
Gated on CD45+
CD11b
Ly6G
PMN-MDSC
Ly6G⁻
Gated on Ly6G⁻F4/80⁻CD3⁻CD19⁻
NK1.1
EOMES
ILC1
NK
NK1.1⁻
Gated on NK1.1⁻
CD11b
Other myeloid
E
CD4 T
CD8 T
cDCs
NK
B cells
Tregs
Count (×10⁴) per gram of tissue
PMN-MDSCs
Macrophages
Other myeloid
ILC1

Figure 5.2 – Survival, tumour burden, and immune cell infiltration
A. Kaplan-Meier survival curves of mice in the survival cohort (*n* = 5 per group). Overall and pairwise comparisons were non-significant (log-rank test).
B. Left: tumour weight of mice in the immune profiling cohort (*n* = 3 per group) on the day of culling (D14). Right: representative images of tumours harvested on D14. Image outlines match the colour scheme used throughout the chapter.
C. Immune (live $CD45^+$) cell infiltration into tumours of mice in the immune profiling cohort. Figures refer to counts ($\times 10^4$) per gram of tumour.
D. Updates in gating strategy from the strategy presented in Chapter 3. PMN: polymorphonuclear myeloid-derived suppressor cells; ILC1: type 1 innate lymphoid cells; NK: natural killer cells.
E. Cell density of each immune cell subset for mice in the immune profiling cohort. Figures refer to counts ($\times 10^4$) per gram of tumour. Throughout this chapter, $CD4^+$ T cells are defined as $CD4^+FoxP3^-$ T cells; Tregs are instead defined as $CD4^+FoxP3^+$ T cells.

Because treatment was based on immunotherapy and another drug known to promote, amongst other effects, immune cell infiltration, a second small study was conducted (*n* = 3 per group). In this experiment, treatment was initiated earlier (30–60 mm^3), and all mice were culled at day 14 (D14) from the start of treatment to assess the local and systemic immune responses (i.e., tumour and blood immune composition). Mice in the two studies are hereafter referred to as the survival cohort and the immune profiling cohort. This second, immune-focussed study was necessary because survival studies capture mice at various and often advanced disease stages, whereas performing immune profiling at a fixed timepoint avoids confounding from variable tumour burden and late-stage systemic immune perturbations (e.g., the left skew in myelopoiesis), thereby allowing clearer interpretation of treatment-induced immune effects.

As the small sample size in the immune profiling cohort prevented formal statistical analyses, medians were used for all comparisons, as in the previous chapters. Whereas considerable variation was observed, tumours were largest in controls and smallest in the combination group, suggestive of better local tumour control with treatment (median tumour weight: 0.33 g in controls vs 0.26 g in the FAKi group, and 0.23 g in the FAKi + aTIGIT group) (**Figure 5.2B**). In mice from the immune profiling cohort, more immune cells infiltrated tumours with treatment, peaking in the combined blockade group (median $CD45^+$ cell count $\times 10^4$/g tumour: 9.9 in controls vs 16.7 in the FAKi group, and 30.7 in the FAKi + aTIGIT group) (**Figure 5.2C**).

In order to understand which immune populations were contributing to the longer median survival and reduction in median tumour size, the absolute counts of all major immune cell populations per gram of tumour were analysed. This metric was prioritised because absolute cell numbers more directly reflect the magnitude of immune infiltration and, as a consequence, are more likely to correlate with treatment-induced changes in tumour control. Relative changes (i.e., the frequency of each subset within $CD45^+$ cells) are shown in **Supplementary Figure 9.4**, as they were not the primary endpoint for the immune profiling cohort but could nonetheless provide complementary information on composition shifts in the immune infiltrate. In addition, relative changes occurring within each subset (e.g., the fraction of $CD8^+$ T cells expressing a given marker) are discussed below when relevant to the interpretation of treatment effects.

An updated flow cytometry panel with a revised gating strategy was used for immune cell enumeration (**Figure 5.2D**). While still acknowledging that functional assays remain the gold standard for their classification, the $CD11b^+$ subset of neutrophils was classified as PMN-MDSCs, as the simple designation as *neutrophils* was thought to overlook their suppressive potential. $NK1.1^+$ cells were separated into NK cells ($Eomes^+$) and ILC1s ($Eomes^-$). Most cells left ungated expressed CD11b, likely comprising monocytes (including M-MDSCs) and immature myeloid precursors. However, since Ly6C was not included in the panel, these cells were collectively classified as *other myeloid*.

Dual treatment increased the absolute abundance of key anti-tumour subsets, with median $CD8^+$ T cell counts per unit weight rising nearly 10-fold, $CD4^+$ T (i.e., $CD4^+FoxP3^-$) cells 4-fold, and dendritic cell counts doubling with respect to controls (**Figure 5.2E**). However, treatment effects were not limited to tumour-controlling populations: median counts of tumour-promoting subsets such as Tregs and PMN-MDSCs more than doubled in the combination group relative to controls. For NK cells, B cells, and macrophages, the addition of TIGIT blockade did not seem to benefit tumour infiltration; in fact, the median cell counts per tumour weight were lower than in the FAKi monotherapy group.

5.3.2 Tumour control in the FAKi and FAKi + aTIGIT groups may be driven, at least in part, by $CD8^+$ T cell responses

Absolute cell counts alone could not fully explain the apparent improvement in tumour control observed with treatment, because increases were observed not only in tumour-countering subsets but also in immunosuppressive populations, such as Tregs. To assess the net balance between tumour-promoting and tumour-suppressing T cells in the TME, the tumour T_{eff}/T_{reg} ratio was analysed. This ratio, widely used as a measure of the balance between tumour suppression and promotion within the T cell compartment (Roychoudhuri et al. 2015), increased with treatment and was highest in the combination group, with approximately 6 effector T cells per Treg (as opposed to approximately 3 in the control group) (**Figure 5.3A**).

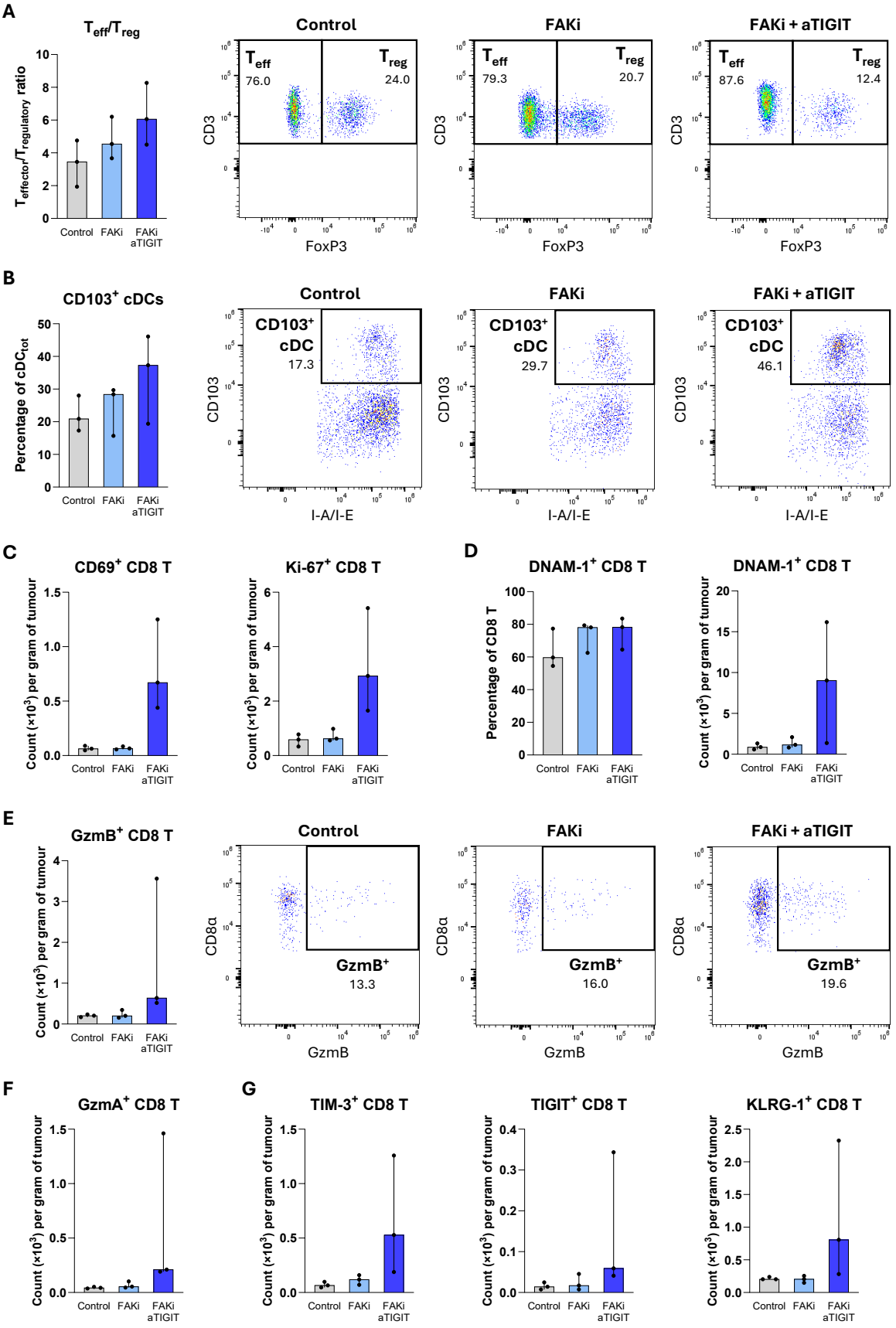
A
Teff/Treg
Control
FAKi
FAKi + aTIGIT
Teffector/Tregulatory ratio
Control FAKi FAKi aTIGIT
Teff 76.0
Treg 24.0
Teff 79.3
Treg 20.7
Teff 87.6
Treg 12.4
CD3
FoxP3
B
CD103+ cDCs
Percentage of cDCtot
CD103+ cDC 17.3
CD103+ cDC 29.7
CD103+ cDC 46.1
CD103
I-A/I-E
C
CD69+ CD8 T
Ki-67+ CD8 T
Count (×10³) per gram of tumour
D
DNAM-1+ CD8 T
Percentage of CD8 T
E
GzmB+ CD8 T
GzmB+ 13.3
GzmB+ 16.0
GzmB+ 19.6
CD8α
GzmB
F
GzmA+ CD8 T
G
TIM-3+ CD8 T
TIGIT+ CD8 T
KLRG-1+ CD8 T

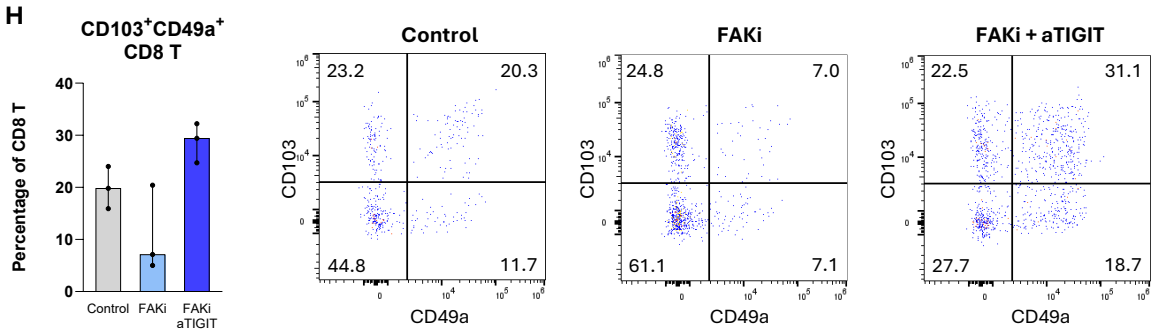

Figure 5.3 – CD8⁺ T cells may play a role in local tumour immunity

A. Left: T_{eff}:T_{reg} ratio in the immune profiling cohort (*n* = 3 per group). T_{eff} corresponds to the sum of CD4⁺ T (i.e., CD4⁺FoxP3⁻) and CD8⁺ T cells. Right: representative dot plots showing the percentage of Tregs within total T cells in the TME.

B. Left: percentage of intratumoural CD103⁺ cDCs. Right: representative dot plots showing the percentage of CD103⁺ cDCs within total tumour cDCs.

C. Cell density of CD69⁺ (left) and Ki-67⁺ (right) CD8⁺ T cells in the tumour.

D. Percentage (left) and absolute density (right) of DNAM-1⁺ CD8⁺ T cells in the tumour.

E. Left: cell density of tumour GzmB⁺ CD8 T cells. Right: representative dot plots showing the highest fraction of GzmB⁺ CD8⁺ T cells in the three groups.

F. Cell density of GzmA⁺ CD8⁺ T cells in the tumour.

G. Cell density of intratumoural CD8⁺ T cells expressing the inhibitory receptors TIM-3 (left), KLRG-1 (middle), and TIGIT (right).

H. Left: percentage of tumour CD103⁺CD49a⁺ CD8 T cells. Right: representative dot plots showing the percentage of CD103⁺CD49a⁺ CD8⁺ T cells in the three groups.

Density figures refer to counts (×10³) per gram of tumour.

Similarly, the proportion of CD103⁺ cDCs (that is, the subset specialised in cross-presenting antigens to CD8⁺ T cells), was also increased by treatment, being highest in the combination group. In the FAKi + aTIGIT group, up to 46.8% of cDCs in the tumour and 36.4% of cDCs in the blood were capable of antigen cross-presentation, compared with a maximum of 28.0% of tumour cDCs and 19.3% of blood cDCs in controls (**Figure 5.3B**, **Supplementary Figure 9.5A**).

To provide indirect support for the hypothesis that FAKi facilitated $CD8^+$ T cell ingress into the tumour and TIGIT blockade further unleashed anti-tumour T cell activity, counts of recently activated ($CD69^+$) and actively proliferating ($Ki\text{-}67^+$) $CD8^+$ T cells were used as indirect proxies of T cell disinhibition. These counts reached their highest levels in the combination group (**Figure 5.3C**). Furthermore, the highest counts of $CD8^+$ T cells expressing the effector molecules granzyme A (GzmA, **Figure 5.3F**) and granzyme B (GzmB, **Figure 5.3E**) were observed in mice receiving dual treatment (median $GzmB^+$ $CD8^+$ T cell count $\times 10^3$/g tumour: 0.2 in controls vs 0.3 in the FAKi group, and 0.6 in the FAKi + aTIGIT group), consistent with higher cytotoxic capacity. $CD8^+$ T cells expressing the costimulatory receptor DNAM-1 (Gilfillan et al. 2008) and the exhaustion markers TIM-3, TIGIT, and KLRG-1, were also more numerous in mice treated with the combination regimen (**Figure 5.3D,G**). Overall, these data suggest that $CD8^+$ T cells may be implicated in tumour control by direct cytotoxicity, especially in the FAKi + aTIGIT treatment arm.

It should be noted that, for the majority of the above markers, there was little variation in the proportion of marker-positive $CD8^+$ T cells across the three groups, and increases in absolute counts were largely a consequence of the absolute increase in $CD8^+$ T cell influx into the tumour. For example, the median CD69 expression was 11.7% in controls vs 12.1% in the FAKi + aTIGIT group, and the median Ki-67 expression 41.6% in controls vs 39.1% in the FAKi + aTIGIT group. For other markers, such as DNAM-1, the increase in absolute counts reflected a parallel increase in proportion of marker-

positive cells (median: 59.7% of $CD8^+$ T cells in controls vs 78.1% in the FAKi group, and 78.3% in the FAKi + aTIGIT group). For yet other markers, such as KLRG-1, an overall increase in absolute count was observed despite a reduction in proportion of marker-positive cells (median: 16.9% of $CD8^+$ T cells in controls vs 7.2% in the FAKi group, and 6.7% in the FAKi + aTIGIT group). Of note, while a considerable fraction of $CD8^+$ T cells expressed the exhaustion marker TIM-3 (with a median expression of approximately 50% across all three groups), only an inconspicuous minority of $CD8^+$ T cells expressed TIGIT (median: 1.0% of $CD8^+$ T cells in controls vs 0.6% in the FAKi group, and 1.4% in the FAKi + aTIGIT group). Lastly, the fraction of $CD8^+$ T cells expressing both markers of tissue retention (CD103 and CD49a) was higher in the FAKi + aTIGIT group than in the FAKi and control groups (**Figure 5.3H**).

6 $CD4^+$ T cells and B cells may also participate in tumour control in the FAKi and FAKi + aTIGIT groups

To determine whether $CD8^+$ T cells were acting alone or in concert with other lymphocytes, $CD4^+$ T cells and B cells were analysed next. Analogously to $CD8^+$ T cells, the density of Ki-67^+ $CD4^+$ T cells in the tumour increased with treatment, and was greatest for mice receiving combination therapy (median Ki-67^+ $CD4^+$ T cell count $\times 10^3$/g tumour: 0.5 in controls vs 0.7 in the FAKi group, and 2.1 in the FAKi + aTIGIT group) (**Figure 5.4A**). Median counts of $CD69^+$, TIM-3^+, $TIGIT^+$, and KLRG-1^+ $CD4^+$ T cells were also highest in the same group (**Figure 5.4B,C**). As for $CD8^+$ T cells, the fraction of $CD4^+$ T cells expressing activation and exhaustion markers did not differ dramatically

among the three groups and the increase in density for each marker stemmed from the absolute increase in $CD4^+$ T cells per gram of tumour. Only a minority of $CD4^+$ T cells expressed the exhaustion marker TIGIT, detected on a median of 3.7% of cells in controls vs 4.1% in the FAKi group, and 2.5% in the FAKi + aTIGIT group. The expression of TIM-3 and KLRG-1 was comparably higher, at approximately 5-10% across the three groups.

As both cDC2s (here defined as $CD11b^+CD103^-$ cDCs) and M1 macrophages (here defined loosely as I-A/I-E^+ macrophages) can present antigens to $CD4^+$ T cells, resulting in their activation and proliferation, the density of these two cell types in the tumour was evaluated. Both cell types were more prevalent in the tumours of treated mice (**Figure 5.4D,E**), with the count of cDC2s only exhibiting a marginal rise (median $\times 10^3$/g tumour: 0.8 in controls vs 0.9 in the FAKi group, and 1.0 in the FAKi + aTIGIT group), and the count of M1 macrophages more than doubling with dual treatment (median $\times 10^4$/g tumour: 1.7 in controls vs 3.5 in the FAKi group, and 4.1 in the FAKi + aTIGIT group).

The proportion of proliferating (Ki-67^+) B cells also increased with treatment, showing a 50% rise in FAKi-treated mice and a 2-fold increase in mice receiving combination therapy (**Figure 5.4F**). On the other hand, only a small fraction of B cells expressed the activation marker CD69 (median: 4.0% of B cells in controls vs 1.6% in the FAKi group, and 5.1% in the FAKi + aTIGIT group).

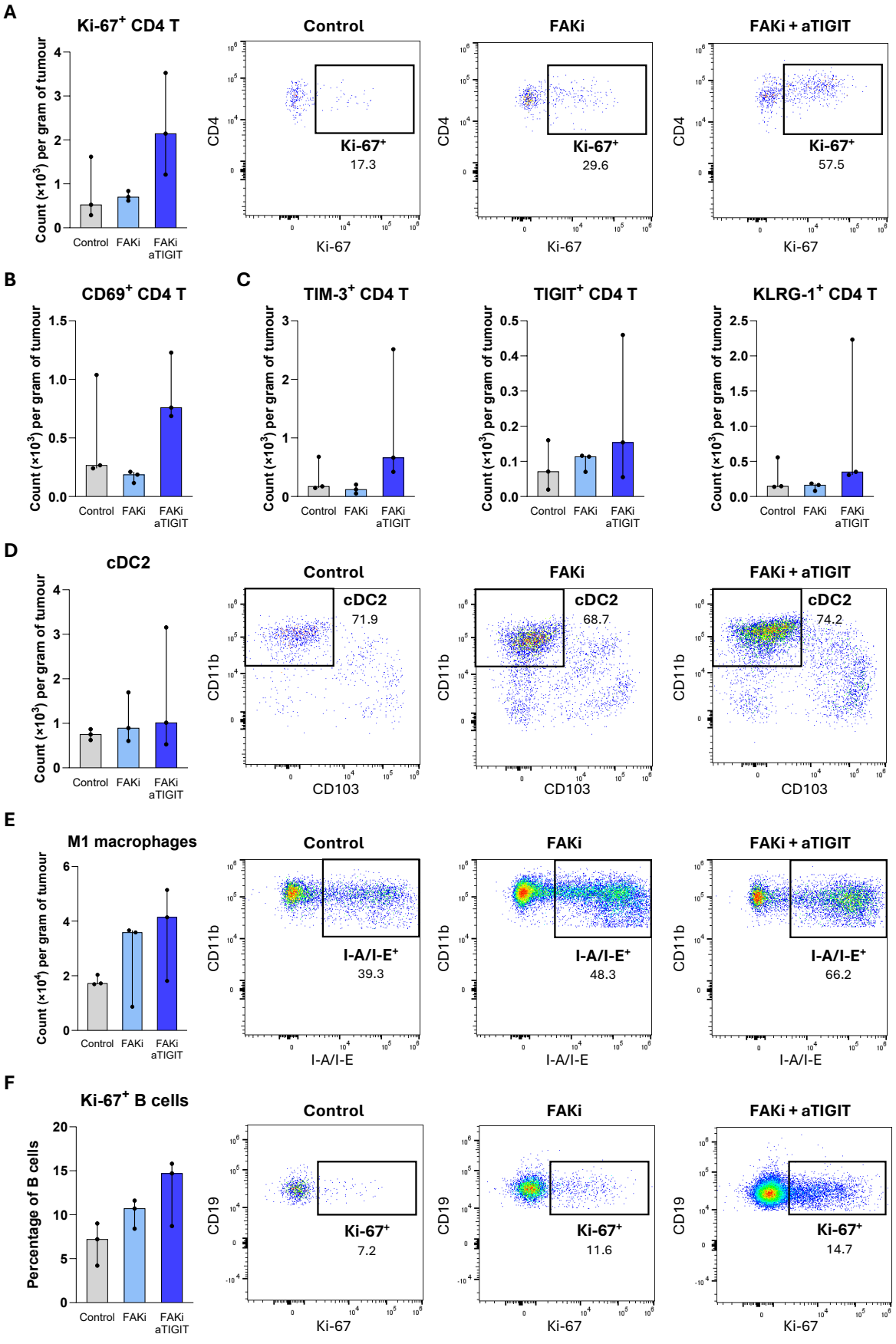
A
Ki-67+ CD4 T
Count (×10³) per gram of tumour
Control
FAKi
FAKi aTIGIT
Control
FAKi
FAKi + aTIGIT
CD4
Ki-67
Ki-67+
17.3
29.6
57.5
B
CD69+ CD4 T
C
TIM-3+ CD4 T
TIGIT+ CD4 T
KLRG-1+ CD4 T
D
cDC2
CD11b
CD103
71.9
68.7
74.2
E
M1 macrophages
Count (×10⁴) per gram of tumour
I-A/I-E
I-A/I-E+
39.3
48.3
66.2
F
Ki-67+ B cells
Percentage of B cells
CD19
7.2
11.6
14.7

Figure 5.4 – $CD4^+$ T and B cells may play a role in local tumour immunity
A. Left: cell density of Ki-67^+ (right) $CD4^+$ T cells in the tumour. Right: representative plots showing the percentage of Ki-67^+ $CD4^+$ T cells within $CD4^+$ T cells in the three groups.
B. Cell density of $CD69^+$ $CD4^+$ T cells in the tumour.
C. Cell density of intratumoural $CD4^+$ T cells expressing the inhibitory receptors TIM-3 (left), TIGIT (middle), and KLRG-1 (right).
D. Left: cell density of cDC2s ($CD11b^+CD103^-$ cDCs) in the tumour. Right: representative dot plots showing the percentage of cDC2s within cDCs in the three groups.
E. Left: cell density of M1 (I-A/I-E^+) macrophages in the tumour. Right: representative dot plots showing the percentage of M1 macrophages within macrophages.
F. Left: percentage of intratumoural Ki-67^+ B cells. Right: representative dot plots showing the percentage of Ki-67^+ B cells within B cells.

7 Dual treatment led to the accumulation of recently activated, proliferating Tregs with a terminally differentiated phenotype

Having established that $FoxP3^-$ $CD4^+$ T and $CD8^+$ T cells collectively outnumbered Tregs, the analysis next focussed on whether, despite their lower abundance, the activation profile of Tregs changed with treatment.

Tumours from mice in the FAKi + aTIGIT arm exhibited the highest density of recently activated ($CD69^+$) and proliferating (Ki-67^+) Tregs (**Figure 5.5A,B**). FAKi monotherapy reduced the proportion of activated Tregs relative to controls, whereas the addition of aTIGIT appeared to bring this proportion back to values near those observed in controls (median CD69 expression: 38.7% of Tregs in controls, 24.7% in the FAKi group, and 32.4% in the FAKi + aTIGIT group). The median expression of Ki-67 was instead comparable across the three groups, with approximately 45% of Tregs actively proliferating.

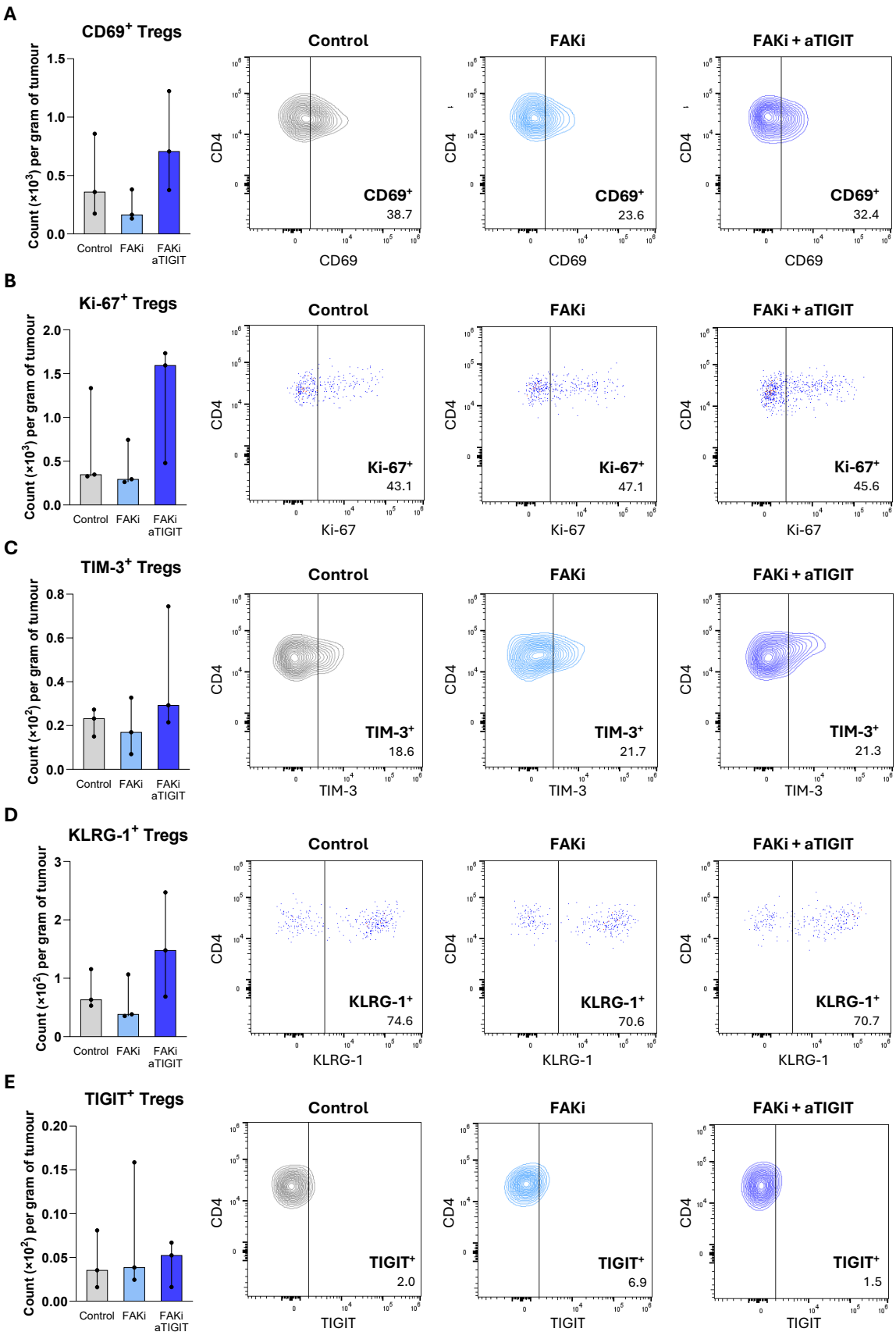
A
CD69+ Tregs
Count (×10³) per gram of tumour
1.5
1.0
0.5
0.0
Control
FAKi
FAKi aTIGIT
Control
FAKi
FAKi + aTIGIT
CD4
CD69
CD69+
38.7
CD69+
23.6
CD69+
32.4
B
Ki-67+ Tregs
Count (×10³) per gram of tumour
2.0
1.5
1.0
0.5
0.0
Control
FAKi
FAKi aTIGIT
Control
FAKi
FAKi + aTIGIT
CD4
Ki-67
Ki-67+
43.1
Ki-67+
47.1
Ki-67+
45.6
C
TIM-3+ Tregs
Count (×10²) per gram of tumour
0.8
0.6
0.4
0.2
0.0
Control
FAKi
FAKi aTIGIT
Control
FAKi
FAKi + aTIGIT
CD4
TIM-3
TIM-3+
18.6
TIM-3+
21.7
TIM-3+
21.3
D
KLRG-1+ Tregs
Count (×10²) per gram of tumour
3
2
1
0
Control
FAKi
FAKi aTIGIT
Control
FAKi
FAKi + aTIGIT
CD4
KLRG-1
KLRG-1+
74.6
KLRG-1+
70.6
KLRG-1+
70.7
E
TIGIT+ Tregs
Count (×10²) per gram of tumour
0.20
0.15
0.10
0.05
0.00
Control
FAKi
FAKi aTIGIT
Control
FAKi
FAKi + aTIGIT
CD4
TIGIT
TIGIT+
2.0
TIGIT+
6.9
TIGIT+
1.5

Figure 5.5 – Tregs characterisation in tumours
A. Left: cell density of $CD69^+$ Tregs in the tumour. Right: representative contour plots showing the percentage of Tregs expressing CD69.
B. Left: cell density of $Ki\text{-}67^+$ Tregs in the tumour. Right: representative dot plots showing the percentage of Tregs expressing Ki-67.
C. Left: cell density of $TIM\text{-}3^+$ Tregs in the tumour. Right: representative contour plots showing the percentage of Tregs expressing TIM-3.
D. Left: cell density of $KLRG\text{-}1^+$ Tregs in the tumour. Right: representative dot plots showing the percentage of Tregs expressing KLRG-1.
E. Left: cell density of $TIGIT^+$ Tregs in the tumour. Right: representative contour plots showing the percentage of Tregs expressing TIGIT.

Across all treatment groups, approximately 20% and 70% of Tregs expressed the terminal differentiation markers TIM-3 and KLRG1, respectively (**Figure 5.5C,D**). In contrast, TIGIT expression was comparatively low (median TIGIT expression: 2.0% of Tregs in controls vs 6.9% in the FAKi group, and 1.5% in the FAKi + aTIGIT group, **Figure 5.5E**).

8 $CD103^-CD49a^-$ NK cells predominate in tumours, with treatment-dependent differences in the densities of NK cells expressing activating and inhibitory receptors, and effector markers

NK cells are also potential targets of aTIGIT, as they, too, express this receptor. While treatment with FAKi resulted in increased NK cell infiltration compared to controls (median $\times 10^4$/g tumour: 0.1 in controls vs 0.4 in the FAKi group), the addition of aTIGIT to FAKi led to a slight reduction in NK cell abundance in the TME, both in terms of relative frequency (**Supplementary Figure 9.4B**) and absolute cell density (**Figure 5.2E**).

To determine whether tumour-infiltrating NK cells had a tissue-associated phenotype, the expression of CD103 and CD49a was assessed. Most NK cells across all three groups were conventional ($CD103^{-}CD49a^{-}$) NK cells (**Figure 5.6B**, top panel). The higher NK cell density observed with FAKi therapy was primarily due to the accumulation of double negative NK cells (**Figure 5.6A**), whereas the addition of aTIGIT led to a relative enrichment for $CD49a^{+}$ cells (median: 25.2% of total NK cells in controls vs 26.2% in the FAKi group, and 40.2% in the FAKi + aTIGIT group). While dual treatment was associated with the highest density of double positive cells (**Figure 5.6C**), the latter only accounted for about 0.1% of all immune cells in the TME (median: 0.05% of $CD45^{+}$ cells in controls vs 0.07% in the FAKi group, and 0.11% in the FAKi + aTIGIT group, **Figure 5.6B**, bottom).

A similar pattern was also observed in the blood. The vast majority of circulating NK cells displayed a $CD103^{-}CD49a^{-}$ phenotype in both treated and control mice, with treatment leading to a modest increase in the fraction of $CD49a^{+}$ cells (median: 1.0% of total NK cells in controls vs 8.3% in the FAKi group, and 12.6% in the FAKi + aTIGIT group). Double positive NK cells remained an inconspicuous minority. These data are summarised in **Supplementary Figure 9.5B**, which also captures the relative changes observed in the blood for all the remaining major immune cell subsets.

To evaluate whether NK cell activity was unleashed by TIGIT blockade, overall NK cell phenotype was examined in the three groups. As some markers were expressed at low levels on NK cells, fluorescence minus one (FMO) controls were used to assist threshold definition, as shown in **Supplementary Figure 9.6**.

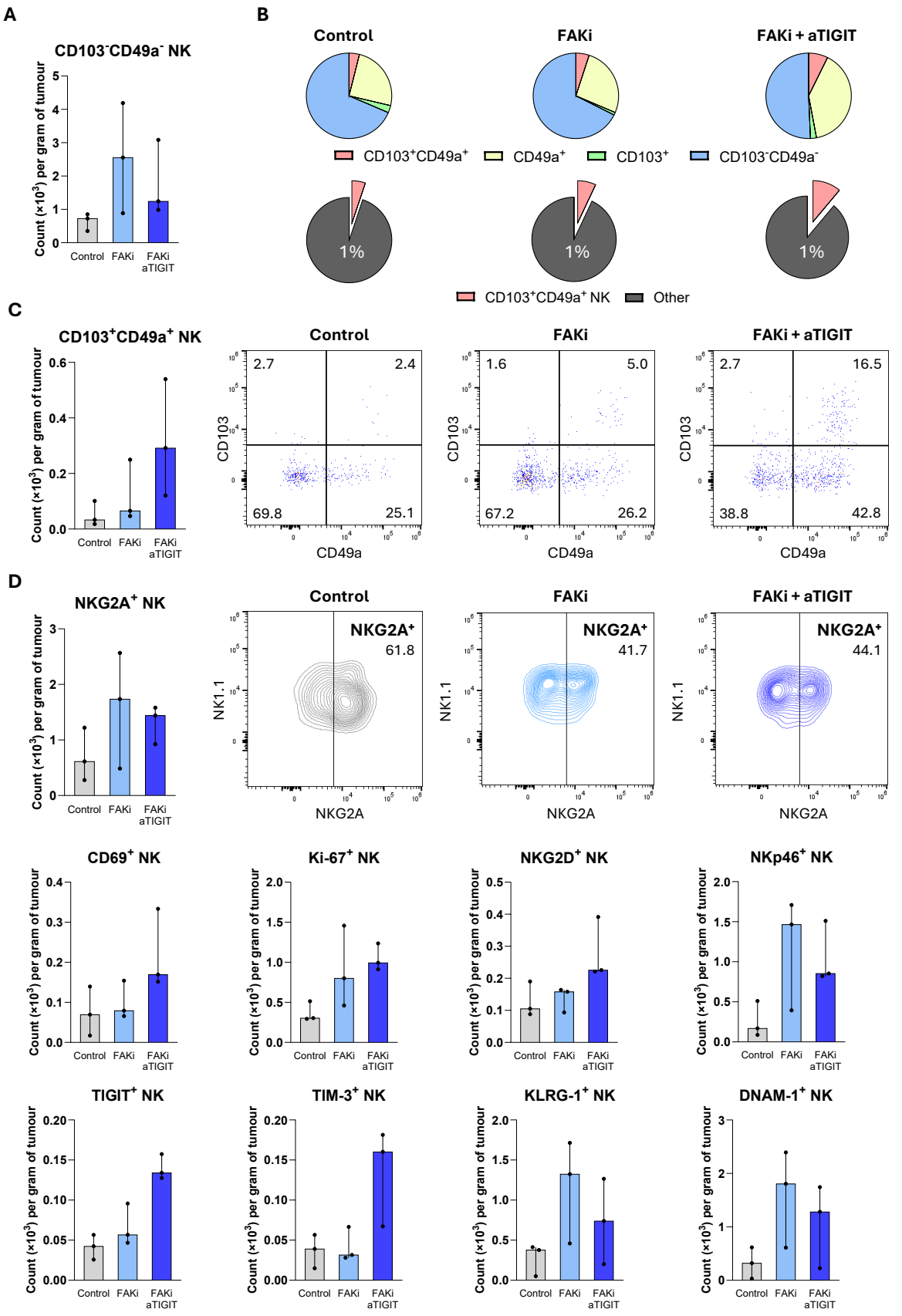
A
CD103⁻CD49a⁻ NK
Count (×10³) per gram of tumour
Control
FAKi
FAKi aTIGIT
B
Control
FAKi
FAKi + aTIGIT
CD103⁺CD49a⁺
CD49a⁺
CD103⁺
CD103⁻CD49a⁻
1%
CD103⁺CD49a⁺ NK
Other
C
CD103⁺CD49a⁺ NK
Control
FAKi
FAKi + aTIGIT
2.7
2.4
69.8
25.1
1.6
5.0
67.2
26.2
2.7
16.5
38.8
42.8
CD103
CD49a
D
NKG2A⁺ NK
NKG2A⁺
61.8
41.7
44.1
NK1.1
NKG2A
CD69⁺ NK
Ki-67⁺ NK
NKG2D⁺ NK
NKp46⁺ NK
TIGIT⁺ NK
TIM-3⁺ NK
KLRG-1⁺ NK
DNAM-1⁺ NK

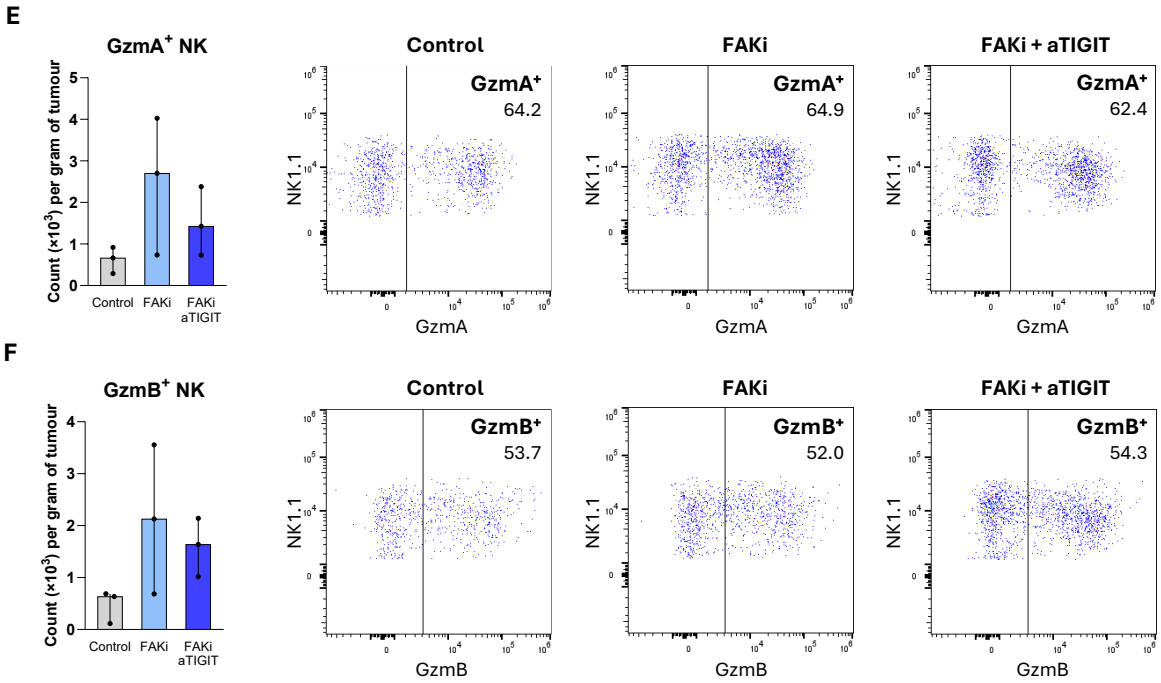

Figure 5.6 – NK cells may play a role in local tumour immunity

A. Cell density of CD103⁻CD49a⁻ NK cells in the tumour.

B. Top row: pie charts showing the composition of the NK cell gate, based on median expression of CD103 and CD49a. Bottom row: composition of the CD45⁺ cell gate, based on median expression of CD103 and CD49a on NK cells. For the bottom panel, one pie chart represents 1% of intratumoural CD45⁺ cells.

C. Left: cell density of CD103⁺CD49a⁺ NK cells in the tumour. Right: representative dot plots showing the percentage of NK cells expressing CD103 and/or CD49a.

D. Cell density of intratumoural NK cells expressing CD69, Ki-67, the activating receptors NKG2D and NKp46, the inhibitory receptors NKG2A, TIGIT, TIM-3, and KLRG-1, and the chemokine receptor CXCR6. NKG2A is shown at the top alongside representative contour plots as an example of threshold definition.

E. Left: cell density of GzmA⁺ NK cells in the tumour. Right: representative dot plots showing the percentage of NK cells expressing GzmA.

F. Left: cell density of GzmB⁺ NK cells in the tumour. Right: representative dot plots showing the percentage of NK cells expressing GzmB.

Overall, dual treatment resulted in the highest density of recently activated (CD69⁺) and proliferating (Ki-67⁺) NK cells (**Figure 5.6D**). The highest counts of NK cells expressing the activating receptor NKG2D as well as the inhibitory receptors TIM-3 and TIGIT were also identified in the same group. FAKi monotherapy, on the other hand, was associated with the highest

counts of NK cells expressing the activating receptors NKp46 and DNAM-1, the inhibitory receptors KLRG-1 and NKG2A, as well as GzmA and GzmB. These two effector molecules were expressed by approximately half of all NK cells across the three groups (**Figure 5.6E,F**), suggesting that, irrespective of treatment, NK cells may contribute to tumour control at least in part through direct cytotoxicity.

Only two markers showed substantial differences in median expression across the three groups when comparing medians: NKG2A, which appeared to be reduced by treatment (median: 61.8% of NK cells in controls vs 41.7% in the FAKi group, and 44.1% in the FAKi + aTIGIT group), and DNAM-1, which conversely appeared to be augmented by treatment (median: 26.1% of NK cells in controls vs 46.3% in the FAKi group, and 39.2% in the FAKi + aTIGIT group). The relative expression of the other markers was comparable across treated mice and controls.

As with $CD4^+$ T cells, $CD8^+$ T cells, and Tregs, only a minority of NK cells expressed TIGIT (median: 3.3% of NK cells in controls vs 2.3% in the FAKi group, and 3.9% in the FAKi + aTIGIT group). Expression of TIM-3 was also in the same range, whereas expression of KLRG-1 was comparably higher and above 30%.

5.4

Discussion

In this chapter, a novel drug combination was tested in the KPC orthotopic mouse model of pancreatic cancer. The combination of FAKi inhibition and TIGIT blockade has previously been tested only once, in an immunodeficient mouse model of human high-grade serous ovarian cancer (Ozmadenci et al. 2022); however, a different inhibitor, dosage, and administration route were employed, limiting the possibility of direct comparisons.

Two chief limitations of the present study must be acknowledged. Firstly, the small sample sizes prevented formal statistical analyses; therefore, the presented data can only be interpreted as indicative of patterns or trends, with further validation needed to draw conclusions. Secondly, treatment initiation in both the survival and immune profiling cohorts was standardised according to tumour palpation criteria, informed by prior experience with the same model. Because individual tumour volumes were not quantified, some variability in tumour size at the time of treatment initiation may have been present.

With these limitations in mind, treatment was associated with a trend towards prolonged survival, with a median survival for mice treated with FAKi alone nearly 30% higher than that of control mice, and a median survival for mice treated with both FAKi and aTIGIT nearly 50% higher. Treatment appeared to improve local tumour control, as median tumour size decreased with FAKi monotherapy, and reached the lowest value in the

dual treatment arm. While survival and tumour size were recorded in separate cohorts, these findings are consistent with the idea that survival in control mice may have been poorer due to larger primary tumours, whereas treated mice may have survived longer due to reduced tumour burden.

In an attempt to identify immune populations potentially contributing to tumour control, the density of all major subsets was calculated as the number of cells per gram of tumour. The rationale for this approach was that populations likely responsible for the treatment effects should vary with treatment (e.g., tumour-promoting populations would be expected to decrease, whereas tumour-suppressing populations would be expected to expand). Functional validation through larger mechanistic studies would be required to establish a causal link between a given subset and the effects of treatment; however, as this was an exploratory study, quantitative changes in cell density provided useful exploratory insights as a starting point.

It is important to note that for some populations (e.g., $CD8^+$ T cells), increases in cell density within the tumour reflected proportional enrichment within $CD45^+$ cells (in other words, the subset was both more abundant in absolute terms, and more represented within the tumour immune infiltrate). For others (e.g., PMN-MDSCs), the absolute count per gram only increased because overall $CD45^+$ infiltration increased, while the relative abundance within $CD45^+$ cells remained unchanged or even decreased. This highlights the importance of considering absolute numbers alongside relative frequencies when interpreting immune infiltration data.

Previous studies have suggested that FAK inhibition may enhance immune cell infiltration through extracellular matrix remodelling. Consistent with this notion, tumours from Defactinib-treated mice exhibited a higher overall density of immune cell than controls. In line with previous reports describing a decrease in the myeloid component of the immune infiltrate in pancreatic cancer models after FAKi (Stokes et al. 2011; Jiang et al. 2016; Canel et al. 2020), the relative abundance of PMN-MDSCs, macrophages, and other myeloid cells within $CD45^+$ cells all decreased with FAKi monotherapy. However, whereas previous studies reported decreases of up to 50%, only a 10% reduction was observed for each subset in the present study. This difference in the magnitude of effect may be related to the use of different models (KPC orthotopic in the present study vs KPC genetically engineered, other orthotopic lines, and subcutaneous models in the other studies) and to the use of different inhibitors (Defactinib in the present study vs VS-4718, PF-562271, and BI-853520 in the other studies), which vary in potency, binding affinity, and relative selectivity for the FAK1 and FAK2 kinases.

Similarly, while some reports have indicated that FAK inhibition alone markedly increases intratumoural T cell infiltration, those studies relied on genetic ablation (Serrels et al. 2015) or gene silencing through shRNA (Jiang et al. 2016). In contrast, in the present study, pharmacological inhibition with a small-molecule FAK inhibitor only resulted in a modest rise in the median proportion of intratumoural CD4 and $CD8^+$ T cells among $CD45^+$ cells (by approximately 12% and 14%, respectively), consistent with another report employing small-molecule inhibition (Canel et al. 2020). This

discrepancy likely reflects differences between sustained protein loss and partial, reversible enzymatic inhibition.

Coupling FAK inhibition with TIGIT blockade affected immune cell infiltration in a number of ways. CD4 and $CD8^+$ T cells exhibited the most pronounced changes in tumour infiltration, with their cell density rising nearly 4-fold and 10-fold, respectively, with dual treatment compared with controls. In both cases, the absolute increase mirrored an increase in relative proportions among $CD45^+$ cells. For both subsets, TIGIT blockade was essential for the enrichment, as absolute counts in the FAKi monotherapy group were only marginally different from those in controls. While the addition of TIGIT blockade seemed to be critical for CD4 and $CD8^+$ T cell accumulation, it did not seem to impact their activation or proliferation: the median fractions of CD4 and $CD8^+$ T cells expressing markers of recent activation or active proliferation were comparable among mice in the three groups. Nevertheless, the highest density of recently activated and actively proliferating CD4 and $CD8^+$ T cells was observed in the FAKi + aTIGIT group, suggesting that a higher number of effector T cells may be actively engaging in anti-tumour responses in this group.

The reason behind the higher abundance of effector T cells observed in tumours from mice treated with FAKi + aTIGIT despite similar proliferation and activation rates to the FAKi and control groups remains unclear, especially in light of the very low TIGIT expression (less than 5% of CD4 and $CD8^+$ T cells). Factors such as prolonged survival, enhanced recruitment, or

increased retention (or a combination of these mechanisms) might explain the observed phenomenon. Although neither of these mechanisms was investigated in depth, a larger fraction of $CD8^+$ T cells in the FAKi + aTIGIT group co-expressed markers of tissue retention (CD49a and CD103). Whereas a direct role for TIGIT in regulating tissue migration or retention has not been established in the literature, TIGIT blockade might have plausibly prolonged $CD8^+$ T cell survival, allowing sufficient time for the upregulation of retention markers and accumulation within the TME.

Whereas only a small fraction of $CD8^+$ T cells expressed TIGIT, more than half of $CD8^+$ T cells in control mice expressed DNAM-1 (a co-stimulatory receptor that binds to the same ligand, PVR), with the proportion rising to nearly 80% in both the FAKi and FAKi + aTIGIT groups. In the dual treatment arm, the density of $DNAM^+$ $CD8^+$ T cells was approximately 10-fold higher than in controls and FAKi-treated mice, suggesting that this subset might have specifically contributed to tumour control.

$CD4^+$ T cells mount antigen-specific responses to peptides presented on MHC class II molecules and provide critical help for multiple aspects of $CD8^+$ T cell immunity (Speiser et al. 2023). Conversely, $CD8^+$ T cells mount antigen specific responses to peptides presented on MHC class I molecules (Giles et al. 2023). Dendritic cells are the most efficient APCs; they prime naïve T cells resulting in the formation of effector and memory T cells (Banchereau and Steinman 1998; Banchereau et al. 2000). Amongst dendritic cells, cDC2s predominantly present exogenous antigens on MHC

class II molecules, priming $CD4^+$ T cells, and cDC1s predominantly present endogenous antigens on MHC class I molecules, priming $CD8^+$ T cells (Guermonprez et al. 2002). Exogenous antigens (e.g., tumour antigens derived from apoptotic cells) may also be internalised by cDC1s and presented on MHC class I molecules, in a process known as antigen cross-presentation (Joffre et al. 2012; Luri-Rey et al. 2025). In mice, $CD103^+$ cDC1s have been identified as the most efficient subset capable of antigen cross-presentation to $CD8^+$ T cells and are required for effective $CD8^+$ T-cell responses in both infection and tumour settings (del Rio et al. 2007; Bedoui et al. 2009; Jelinek et al. 2011; Salmon et al. 2016; E. W. Roberts et al. 2016). The fraction $CD103^+$ cDC1s increased with treatment, reaching a maximum in the dual treatment arm (both in the tumour and the blood), and resulting in the highest density of intratumoural $CD103^+$ cDCs in the same group. Although the relative fraction of the near-specular cDC2 subset inevitably decreased with treatment, the absolute number of cDC2s increased slightly, with negligible difference between the FAKi and FAKi + aTIGIT arms.

While cDCs efficiently prime naïve T cells, macrophages can serve as APCs for activated or memory $CD4^+$ T cells in peripheral tissues due to their expression of MHC class II (Roche and Furuta 2015; DeNardo and Ruffell 2019). Both the relative fraction and the absolute density of I-A/I-E^+ macrophages rose with treatment, peaking in the dual treatment group. This indicates that not only effector T cells but also cDCs and macrophages increased with treatment, providing a mechanistic foundation for the high counts of activated and proliferating cells described above.

After antigen presentation and activation, $CD8^+$ T cells kill tumour cells by releasing granzymes, serine proteases that cause apoptosis upon internalisation by the target cell (Jenne and Tschopp 1988). Across all treatment groups, a median of approximately 4-5% of $CD8^+$ T cells expressed GzmA, and 15-20% expressed GzmB. The density of $GzmA^+$ and $GzmB^+$ $CD8^+$ T cells was higher in treated mice than in controls, peaking in the combination treatment arm, further supporting the notion that $CD8^+$ T cells in the tumour may be engaging in cytotoxic anti-tumour responses.

Importantly, a considerable fraction of $CD8^+$ T cells expressed TIM-3 and KLRG-1, suggesting that although these cells may actively participate in anti-tumour responses, they also exhibit features of terminal differentiation and/or functional exhaustion (Joshi et al. 2007; Sakuishi et al. 2010; Dolina et al. 2021). This is a common occurrence in the TME and typically a response to chronic stimulation (Sakuishi et al. 2010; Zeng et al. 2024).

Tregs express both FAK1/2 (Serrels et al. 2015) and TIGIT (Joller et al. 2011; Steele et al. 2020); therefore, FAKi and aTIGIT can have opposing effects: while FAKi can reduce Treg activity and survival, aTIGIT may enhance their immunosuppressive potential. As expected, FAKi alone produced a 20% reduction in the relative abundance of Tregs among $CD45^+$ cells compared to controls, accompanied by a considerable reduction in activation, as measured by CD69 expression. Despite the low expression of TIGIT on Tregs, the addition of aTIGIT to FAKi reverted these changes, with the median fraction of Tregs amongst $CD45^+$ cells returning to control levels, and the

fraction of $CD69^+$ Tregs remaining similar (38% in controls vs 35% in the FAKi + aTIGIT group). The majority of Tregs in all groups expressed KLRG-1, a marker previously associated with high immunosuppressive capacity (Adeegbe et al. 2018), with the highest density of $KLRG1^+$ Tregs observed in the dual treatment arm. However, as the ratio of effector T cells to Tregs in this group was very skewed towards effector T cells, it is likely that Tregs, albeit highly immunosuppressive, did not prevent effective antitumour immunity.

Previous studies on FAK inhibition focussed on immunosuppressive cells (as they express FAK at high levels), and on how reducing their numbers or function could enhance $CD8^+$ T cell activity. However, little was known about the effects of FAK inhibition on NK cells. Surprisingly, the density of intratumoural NK cells nearly quadrupled with FAKi monotherapy. Perhaps even more surprisingly, the addition of TIGIT blockade did not further increase NK cell numbers; instead, it reduced the median fraction of NK cells among $CD45^+$ cells in the TME, and consequently, the overall intratumoural NK cell density. As discussed for T cells above, activation and proliferation rates remained nearly identical across the three groups, suggesting that the accumulation seen with treatment (particularly with FAKi monotherapy) may result from other factors. For example, NK cells in the FAKi monotherapy group exhibited the highest expression of the activating receptor DNAM-1 and the lowest expression of the inhibitory receptor NKG2A. Thus, even if differences in activation or proliferation were not detected, NK cells may have maintained a less exhausted/dysfunctional

phenotype, allowing greater persistence in the tumour. Neither treatment appeared to affect the production of cytotoxic effector molecules, as the fractions of $GzmA^+$ and $GzmB^+$ NK cells remained comparable across all groups.

To summarise, this chapter examined a combination of TIGIT blockade and FAK inhibition. TIGIT was selected as a checkpoint inhibitor because of its reported expression in PDAC (Steele et al. 2020; Heiduk et al. 2023) and because of studies showing that TIGIT inhibition can promote tumour control (Freed-Pastor et al. 2021; Peng et al. 2022). Based on the experiments presented in this chapter, this combination appeared to provide a survival advantage and enhance tumour control, primarily through greater immune cell infiltration. An apparent paradox of this study is that TIGIT blockade was associated with measurable changes despite very low baseline TIGIT expression (1–5% of $CD4^+$ and $CD8^+$ T cells, Tregs, and NK cells across all experimental groups). As neither activation nor proliferation differed substantially across treatment groups in these populations, it is difficult to speculate what might have contributed to the observed effects, apart from the potential explanations discussed above for T cells (prolonged survival, enhanced recruitment, or increased retention).

Future studies investigating this regimen as a potential therapeutic strategy for PDAC would benefit from the following crucial refinements: (I) sufficiently large sample sizes to enable formal statistical analyses and generate robust evidence; (II) assessment of tumour-intrinsic and stromal

FAK levels, since low expression can result in low treatment efficacy; (III) comprehensive assessment of baseline expression of immune checkpoint receptors (e.g., PD-1, CTLA-4, TIGIT, TIM-3) and their corresponding ligands (e.g., PD-L1, PD-L2, CD80, CD86, PVR, galectin-9) on tumour, immune, and other stromal cells, to inform the selection of the immune checkpoint strategy most likely to produce clinical benefit; (IV) the design of combination strategies that more selectively target tumour-controlling populations, without simultaneously expanding tumour-promoting immune subsets.

Although the present regimen was hypothesised to enrich for tissue-associated NK cells expressing CD103 and CD49a, this subset was largely absent from the TME of treated mice, suggesting that alternative approaches (such as the modality described in Chapter 4) may be more effective for promoting this population.

Chapter 6

In vitro generation of cytotoxic NK cells expressing tissue-retention markers for cancer immunotherapy

6.1

Introduction

Chapter 4 demonstrated that a multimodal therapeutic regimen comprising radiotherapy, CCR5 antagonism, and PD-1 blockade led to the accumulation of a subset of NK cells expressing markers typically associated with tissue localisation/retention in a mouse PDAC model. This subset was particularly enriched in responders to therapy. Even more notably, compiling a corresponding human tissue-associated NK cell gene signature and subsequently interrogating the Cancer Genome Atlas (TCGA) cohort revealed a significant positive association between this signature and survival across multiple cancer types (**Figure 6.1**). These observations suggest that tissue-associated NK cells may represent a promising foundation for the development of next-generation immunotherapies.

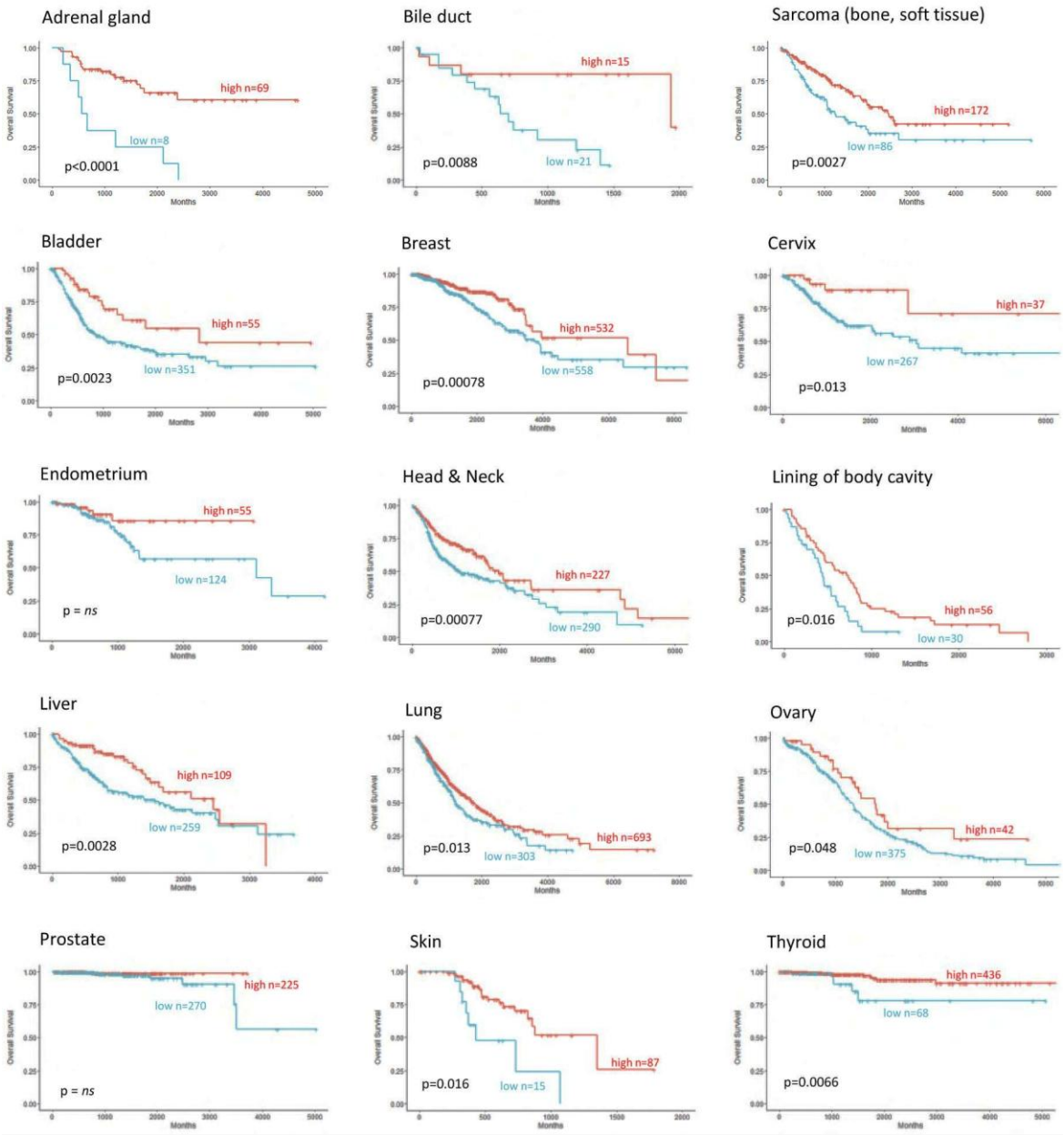

Figure 6.1 - Correlation between human tissue-associated NK cell gene signature and survival in a variety of solid cancers

Reproduced with permission from *Go, Demetriou, Valenzano, et al., eLife, 2024 (Figure 8) under the terms of the Creative Commons Attribution License (CC BY)*.

An enrichment score of the signature was first calculated per patient sample in the TCGA RNA-sequencing dataset using the Gene Set Variation Analysis (GSVA) method. A cut-off value was then determined using the maximally selected rank statistics (max-stat R package) method to divide patients into “high” and “low”.

Chapter 5 examined whether modulation of tumour–stroma interactions through pharmacological inhibition of FAK could enhance the infiltration of this and other lymphocyte subsets into tumours and thereby potentiate anti-cancer immune responses. FAK inhibition resulted in an increased abundance of several immune cell populations within the tumour microenvironment; however, this did not extend specifically to the tissue-associated ($CD103^+CD49a^+$) NK cell subset.

In pursuit of a therapeutic strategy capable of promoting tumour infiltration by tissue-associated NK cells, an alternative approach is explored in this chapter, whereby peripheral blood NK cells are isolated and induced to acquire a tissue-associated ($CD103^+CD49a^+$) phenotype *in vitro* prior to adoptive transfer into mice. Given that intratumoural NK cells often display reduced cytotoxicity or functionality (Carrega et al. 2008; Marcon et al. 2020; Zecca et al. 2021; Go et al. 2024), efforts were directed towards generating a hybrid NK cell phenotype that maintained cytotoxic capacity while expressing markers of tissue localisation.

6.2

Aims

To establish an *in vitro* approach for the generation of NK cells displaying both cytotoxic activity and a tissue-associated phenotype, enabling tumour localisation and retention for application in cancer immunotherapy.

6.3 Results

6.3.1 IL-15 and TGF-β cooperate to induce expression of CD103 and CD49a on NK1.1$^+$ splenocytes from C57BL/6J mice

As a proof-of-concept experiment to test whether a tissue-resident (or tissue-associated) phenotype could be induced *in vitro*, splenocytes from non-tumour-bearing C57BL/6J mice were enriched for NK1.1$^+$ cells by magnetic-bead positive selection and cultured for 48 hours with either IL-15 alone or IL-15 plus TGF-β (**Figure 6.2A**). These cytokines were selected because of their known role in promoting CD103 and CD49a expression, as extensively discussed in Chapter 3. Freshly isolated, NK1.1-enriched splenocytes were included as unstimulated, negative controls.

The vast majority of unstimulated NK cells expressed neither marker of tissue retention, with approximately 10% expressing either CD49a or CD103 and a median of less than 1% co-expressing both (**Figure 6.2B**). Culture with IL-15 alone led to a 4-fold increase in the CD49a$^+$ fraction, with the remaining cells being almost exclusively double negatives. In contrast, combined stimulation with IL-15 and TGF-β resulted in a dominant CD49a$^+$ subset (median: 67.3% of total NK cells) and a marked expansion of the CD103$^+$CD49a$^+$ population (median: 0.8% in unstimulated, 0.6% in IL-15, and 6.4% in IL-15 + TGF-β). The CD103$^+$CD49a$^-$ subset was present to varying degrees in unstimulated NK cells, but nearly absent in both culture conditions (**Figure 6.2C**).

To assess whether the different culture conditions impacted cell viability, the viability of the enriched cell culture was analysed next. Median overall viability decreased slightly upon IL-15 stimulation and further with the addition of TGF-β (by approximately 6% and 17%, respectively, compared with unstimulated controls); however, these differences were not statistically significant (**Figure 6.2D**).

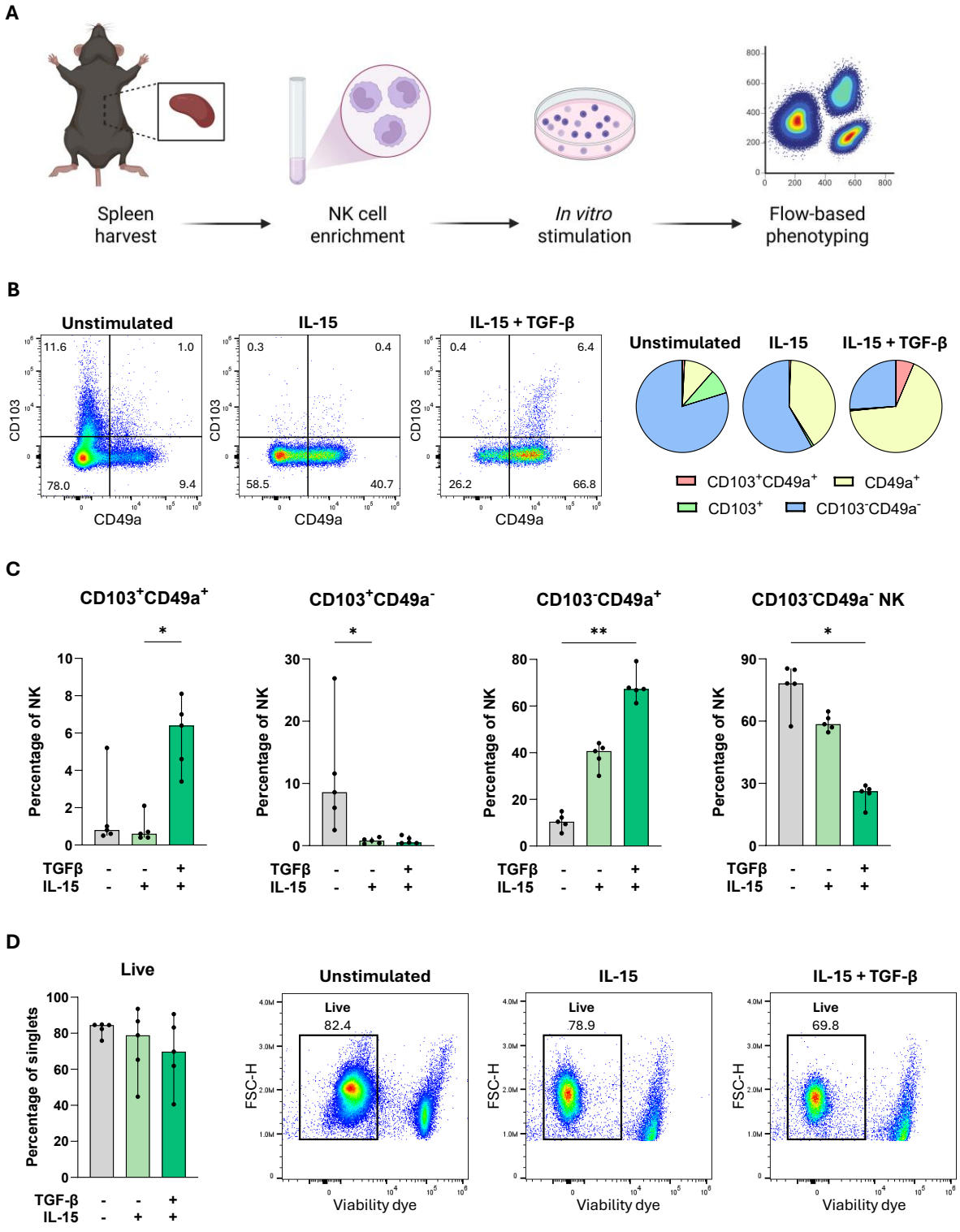
A
Spleen harvest
NK cell enrichment
In vitro stimulation
Flow-based phenotyping
B
Unstimulated
IL-15
IL-15 + TGF-β
CD103
CD49a
11.6
1.0
78.0
9.4
0.3
0.4
58.5
40.7
0.4
6.4
26.2
66.8
CD103+CD49a+
CD49a+
CD103+
CD103-CD49a-
C
CD103+CD49a+
CD103+CD49a-
CD103-CD49a+
CD103-CD49a- NK
Percentage of NK
TGFβ
IL-15
D
Live
Percentage of singlets
TGF-β
IL-15
Unstimulated
IL-15
IL-15 + TGF-β
Live
82.4
78.9
69.8
FSC-H
Viability dye

Figure 6.2 – Effect of IL-15 and TGF-β on mouse splenocytes
A. Schematic of the experimental workflow. Splenocytes isolated from C57BL/6J mice underwent magnetic-bead negative selection to enrich for NK cells and were cultured for 48 hours under different conditions prior to flow cytometric analysis.
B. Left: representative dot plots showing the percentage of NK cells (live NK1.1$^+$ cells) expressing CD103 and CD49a. Right: pie charts showing the composition of the NK cell gate, based on median expression of CD103 and CD49a.
C. Percentage of NK cells expressing each of the four subsets shown in (B) after CD103/CD49a biaxial gating.
D. Left: percentage of live cells. Right: representative dot plots showing the percentage of live cells within singlets.
All comparisons were performed using a Friedman test; *p<0.05; **p<0.01.

6.3.2 A cytokine cocktail containing TGF-β, IL-15, and IL-21 promotes expansion of CD103$^+$CD49a$^+$ NK cells from healthy donor peripheral blood mononuclear cells (PBMCs)

The proof-of-concept study with mouse splenocytes demonstrated that the combination of IL-15 and TGF-β could, albeit modestly, promote the expansion of the double-positive (CD103$^+$CD49a$^+$) NK cell subset in mice. As the overarching aim of the experiments presented in this chapter was to design a novel immunotherapy approach with potential translational relevance to humans, a similar proof-of-concept study was performed using human samples.

PBMCs from healthy donors were isolated by density-gradient centrifugation, and CD56$^+$ cells were enriched through magnetic bead-based negative selection (**Figure 6.3A**). A range of cytokine cocktails was tested in an initial screening with a small number of donors (n = 3). A detailed description of the stimulation protocol is provided in the Methods section. Briefly, for conditions including TGF-β, cells were exposed to TGF-β during

the final 48 hours of a 7-day culture period, except for the TGF-β-alone control, in which cells were cultured with TGF-β for the entire duration. Interleukin 21 (IL-21) was included due to its well-established role in enhancing NK cell cytotoxicity (Skak et al. 2008), while interleukin 12 (IL-12) and interleukin 18 (IL-18) were tested in combination with IL-15 because of their ability to cooperatively drive a cytokine-induced memory-like (CIML) NK cell phenotype (M. A. Cooper et al. 2009). In line with previous studies on *in vitro* NK cell polarisation, exposure to IL-21 and to IL-12/IL-18 occurred as a short pulse of 16–24 hours, preceding the final exposure to TGF-β.

Culturing NK cells with TGF-β alone or IL-15 alone led to a moderate expansion of the tissue-associated (i.e., $CD103^{+}CD49a^{+}$) subset, with median frequencies of approximately 20% and 30%, respectively (**Figure 6.3C**). The combination of TGF-β and IL-15 markedly increased the expansion, reaching a median of approximately 70% double-positive NK cells. Adding IL-21 further increased the median proportion to 75.1%, whereas stimulation with a CIML-based cocktail slightly reduced it to 65.2%. Double-negative NK cells remained a minority across all conditions, except for TGF-β alone, where over one third lacked both tissue-retention markers (**Figure 6.3B**). The largest fraction of $CD49a^{+}$ NK cells was observed with IL-15 stimulation, while $CD103^{+}CD49a^{-}$ NK cells remained negligible in most conditions, except for TGF-β alone, where they reached a median of 7.5% of total NK cells.

In addition to promoting the biggest enrichment for double positives, IL-21 also produced the strongest per-cell expression of both tissue-retention markers on these cells, as indicated by highest median MFI among the conditions tested (**Figure 6.3D,E**).

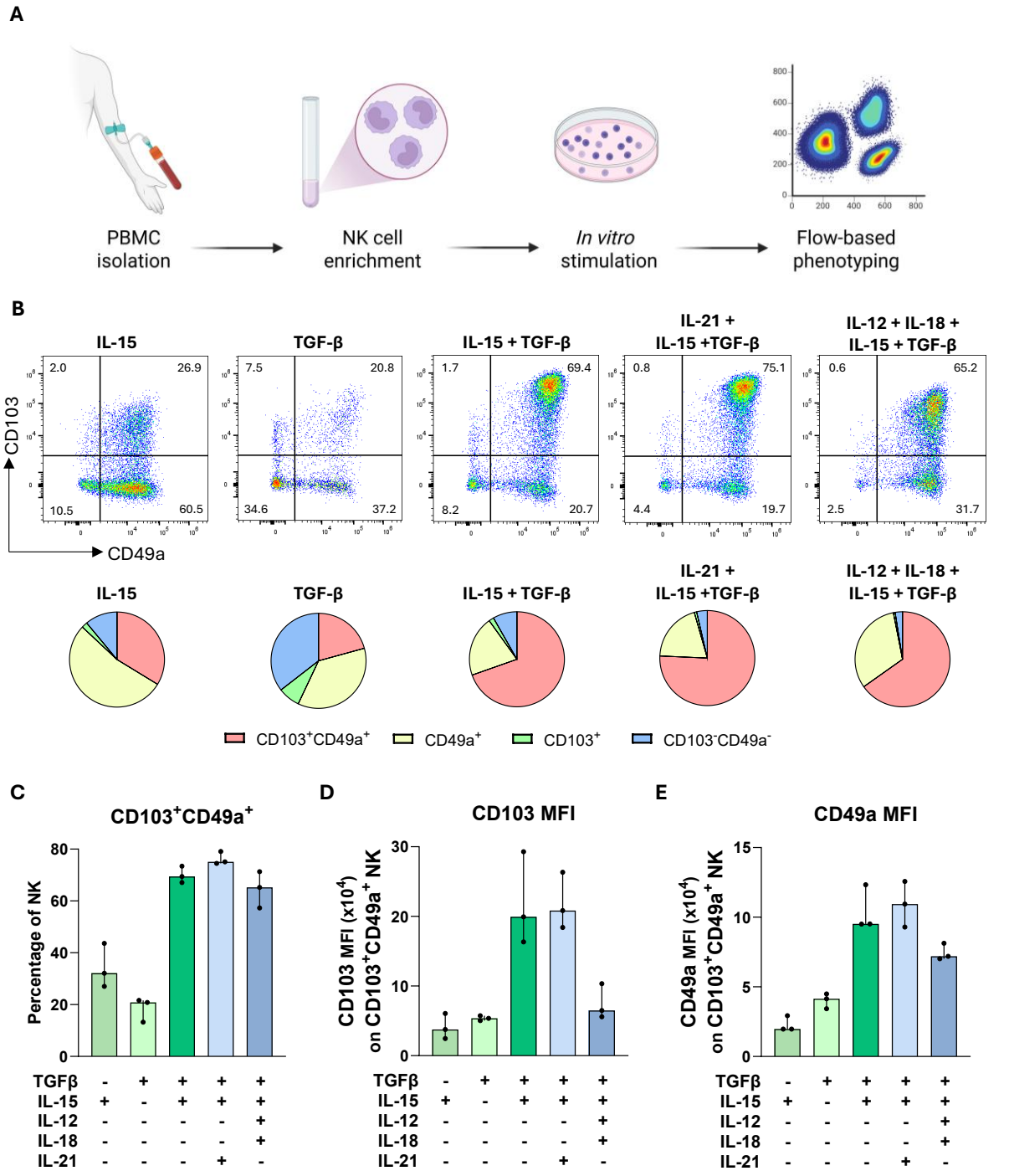

Figure 6.3 – Generating $CD103^+CD49a^+$ NK cells from PBMCs *in vitro*: original protocol overview

A. Schematic of the experimental workflow. PBMCs isolated from healthy donors underwent magnetic-bead positive selection to enrich for $CD56^+$ cells, and then cultured for 7 days under different cytokine conditions prior to flow cytometric analysis.

B. Top: representative dot plots showing the percentage of NK cells ($CD56^+CD3^-$ live cells) expressing CD103 and/or CD49a. Bottom: composition of the NK cell gate, based on median expression of CD103 and CD49a.

C. Percentage of $CD103^+CD49a^+$ NK cells.

D. CD103 MFI on $CD103^+CD49a^+$ NK cells.

E. CD49a MFI on $CD103^+CD49a^+$ NK cells.

6.3.3 Different stimulation conditions differentially affect the viability and NK cell proportion of the enriched cell culture

The proportion of live cells in the enriched NK cell culture was next evaluated to determine how each condition affected viability. Continuous exposure to TGF-β alone was most detrimental, with only approximately half of the cells remaining viable after 7 days (**Figure 6.4A,C**). The use of IL-15 markedly improved viability, peaking in the IL-15 + TGF-β condition (median: 80.0%). Among IL-15 –containing stimulations, the CIML-inspired cocktail supported viability least effectively, with a median live cell fraction of only 57.2%.

The different stimulations also influenced the overall NK cell yield. Magnetic bead-based enrichment did not completely remove non-NK populations; as a result, some contaminating cells remained and expanded during the 7-day culture period. Variable proportions of T cells ($CD3^+CD56^-$) and NKT cells ($CD3^+CD56^+$) were detected at the end (**Figure 6.4B**). In all conditions except TGF-β alone, NK cells ($CD56^+CD3^-$) remained the predominant

population, whereas contaminating subsets represented only a minority (**Figure 6.4D**). In contrast, continuous exposure to TGF-β appeared to favour the expansion of T and NKT cells (median: 40.2% and 7.9% of live cells, respectively), with substantial inter-donor variability. TGF-β not only resulted in the lowest proportion of NK cells but was also associated with reduced CD56 expression on these cells (**Figure 6.4E**).

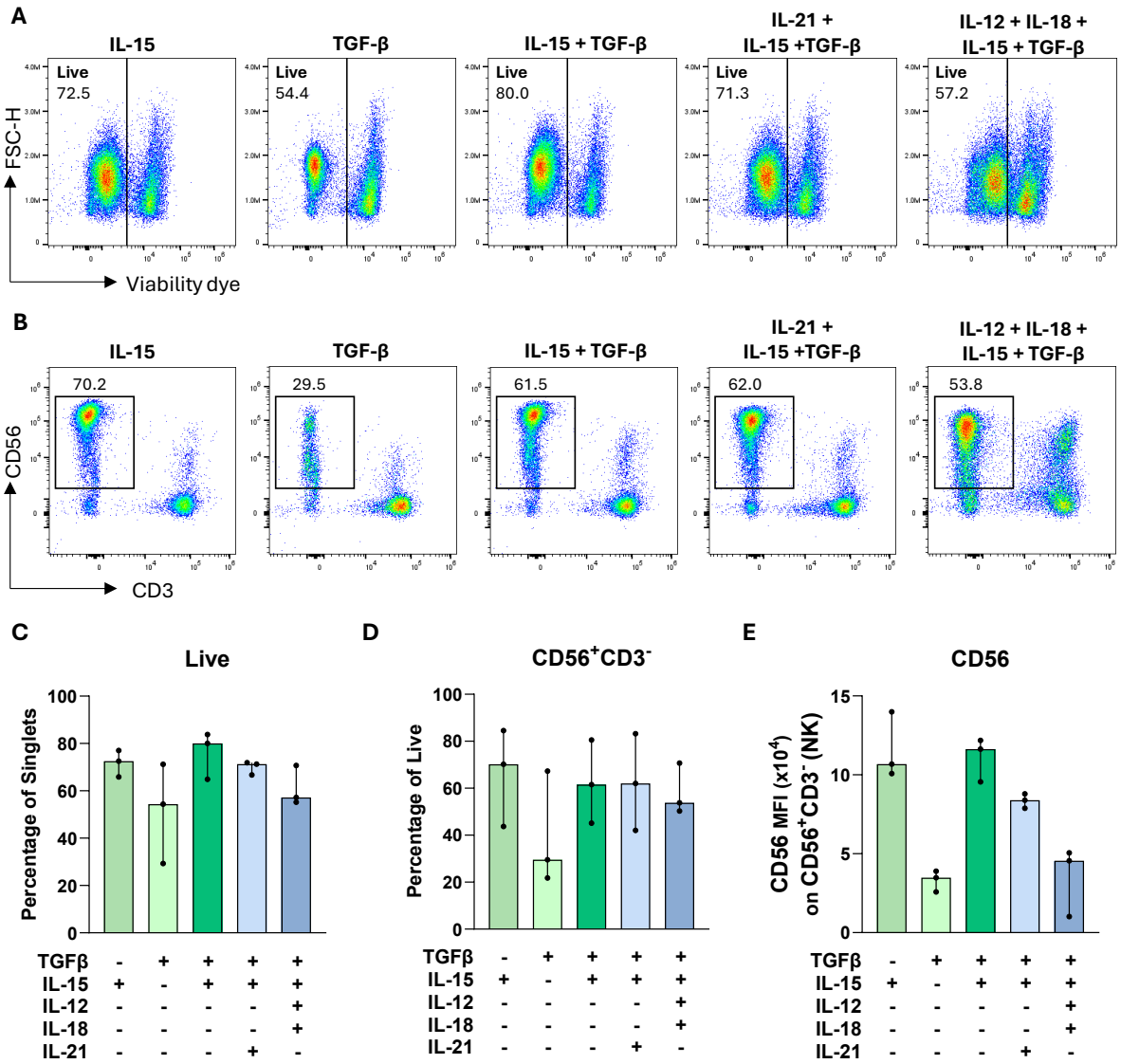

Figure 6.4 – Original protocol: viability and NK cell yield
A. Representative dot plots showing the percentage of live cells (as a fraction of singlets).
B. Representative dot plots showing the percentage of NK cells ($CD56^{+}CD3^{-}$) as a fraction of live cells.
Bottom: pie charts showing the composition of the NK cell gate, based on median expression of CD103 and CD49a.
C. Percentage of live cells (as a fraction of singlets) after the 7-day culture period.
D. Percentage of NK cells ($CD56^{+}CD3^{-}$) as a fraction of live cells.
E. CD56 MFI on NK cells.

6.3.4 Different stimulation conditions differentially affect the phenotype and cytotoxic capacity of NK cells

After being stimulated, NK cells did not neatly segregate into the canonical peripheral blood subsets (immunoregulatory $CD56^{bright}CD16^{-}$ and cytotoxic $CD56^{dim}CD16^{+}$) described by Lanier *et al.* in 1986. Instead, populations with intermediate phenotypes emerged, to varying degrees. In most conditions, the majority of NK cells were $CD56^{bright}CD16^{-}$ (**Figure 6.5A**). The only exception was continuous TGF-β exposure, which preferentially expanded the $CD56^{dim}CD16^{+}$ subset. A considerable fraction of cells cultured with IL-15 expressed both high levels of CD56 and CD16 (median $CD56^{bright}CD16^{+}$ fraction: 18.6%).

Although the expression of CD56 and/or CD16 can be suggestive of cytotoxic potential, accurate assessment of NK cell killing capacity requires functional cytotoxicity assays. To evaluate whether different stimulation conditions conferred cytotoxic capacity alongside the acquisition of a tissue-associated phenotype, pre-stimulated, NK-enriched PBMCs were co-cultured with K562 target cells. Cells stimulated with IL-15 alone exhibited the highest killing efficiency across all effector-to-target (E:T)

ratios tested. The presence of TGF-β markedly reduced cytotoxicity in all other conditions, with continuous exposure to TGF-β resulting in nearly absent target cell death. However, inclusion of IL-21 restored killing capacity to levels comparable to those observed with IL-15 alone, particularly at higher E:T ratios (**Figure 6.5B,D**). CIML-stimulated cells displayed comparatively low killing activity, and, although a greater fraction expressed Natural Killer Group 2, member C (NKG2C), the overall frequency remained low, representing less than 5% of total NK cells (**Figure 6.5C,E**).

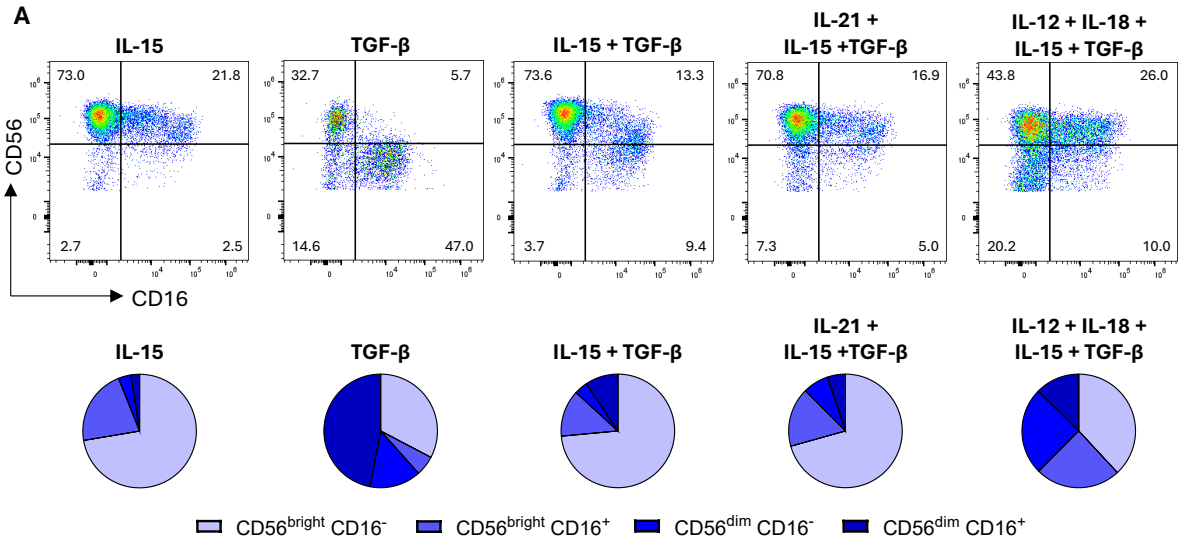
A
IL-15
TGF-β
IL-15 + TGF-β
IL-21 +
IL-15 +TGF-β
IL-12 + IL-18 +
IL-15 + TGF-β
CD56
CD16
73.0
21.8
2.7
2.5
32.7
5.7
14.6
47.0
73.6
13.3
3.7
9.4
70.8
16.9
7.3
5.0
43.8
26.0
20.2
10.0
CD56bright CD16-
CD56bright CD16+
CD56dim CD16-
CD56dim CD16+

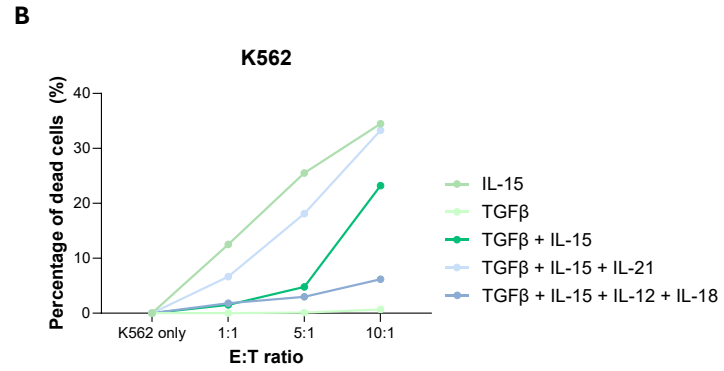
B
K562
Percentage of dead cells (%)
E:T ratio
K562 only
1:1
5:1
10:1
IL-15
TGFβ
TGFβ + IL-15
TGFβ + IL-15 + IL-21
TGFβ + IL-15 + IL-12 + IL-18

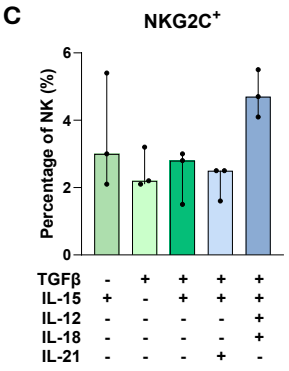
C
NKG2C+
Percentage of NK (%)
TGFβ
IL-15
IL-12
IL-18
IL-21

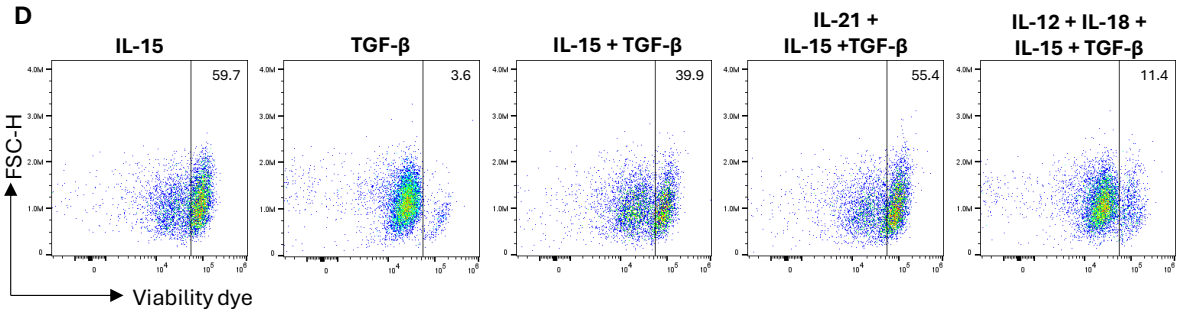
D
IL-15
TGF-β
IL-15 + TGF-β
IL-21 +
IL-15 +TGF-β
IL-12 + IL-18 +
IL-15 + TGF-β
FSC-H
Viability dye
59.7
3.6
39.9
55.4
11.4

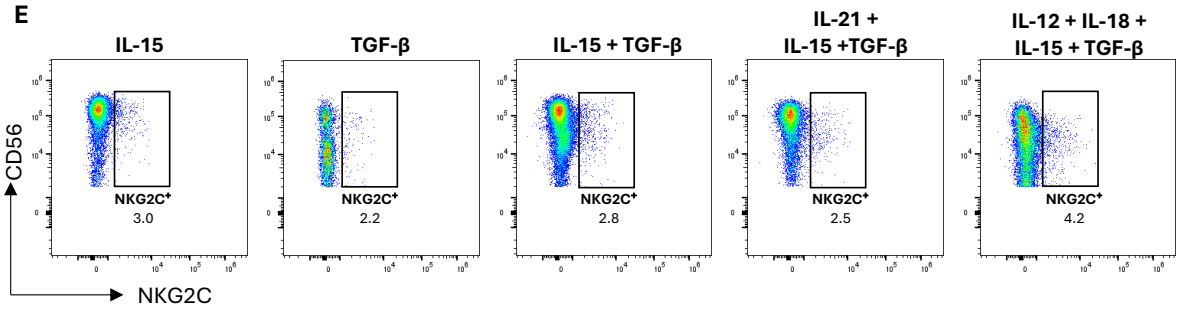
E
IL-15
TGF-β
IL-15 + TGF-β
IL-21 +
IL-15 +TGF-β
IL-12 + IL-18 +
IL-15 + TGF-β
CD56
NKG2C
NKG2C+
3.0
2.2
2.8
2.5
4.2

Figure 6.5 – Original protocol: phenotype and cytotoxicity

A. Top: representative dot plots showing the percentage of NK cells expressing CD16 and high or low-to-intermediate levels of CD56 ($CD56^{bright}$ and $CD56^{dim}$, respectively). Bottom: composition of the NK cell gate, based on median expression of CD56 and CD16.

B. Percentage of dead (viability dye^+) K562 cells after 4 hours of co-culture with NK-enriched PBMCs stimulated with the indicated conditions and at the specified E:T ratios. NK-enriched PBMCs were used without further purification, thus including non-NK cell contaminants. Cell death was quantified by flow cytometry and normalised to spontaneous cell death in a well containing target cells alone (not shown). For all E:T ratios except 10:1, $n = 3$; for 10:1, $n = 2$. Median shown, with no error bars.

C. Percentage of $NKG2C^+$ NK cells (as a fraction of total NK cells).

D. Representative dot plots showing the percentage of dead (viability dye^+) K562. K562 were labelled with CFSE prior to the co-culture, and only $CFSE^+$ cells (K562) are shown.

E. Representative dot plots showing the percentage of $NKG2C^+$ NK cells.

6.3.5 Protocol optimisation results in greater viability, NK cell yield, and $CD103^+CD49a^+$ subset expansion

As the IL-21–containing cocktail produced the greatest expansion of tissue-associated NK cells while maintaining cytotoxicity rates comparable to those observed in the absence of TGF-β, it was selected for further optimisation. The stimulation protocol was refined so as to increase viability, NK cell yield, and cytotoxic capacity with a view to subsequent adoptive transfer experiments. A final protocol was developed, comprising an initial 14-day expansion phase with high-dose IL-2, followed by a 14-day stimulation period including IL-15 and multiple IL-21 short pulses, with or without a final exposure to TGF-β (see **Figure 6.6A** and Methods for more details). In remainder of this chapter, the conditions with and without TGF-β are compared, using the post-expansion but pre-stimulation (i.e., IL-2 only) condition as a control. As only a small number of samples ($n = 3$) were tested due to resource availability, comparisons are made using medians.

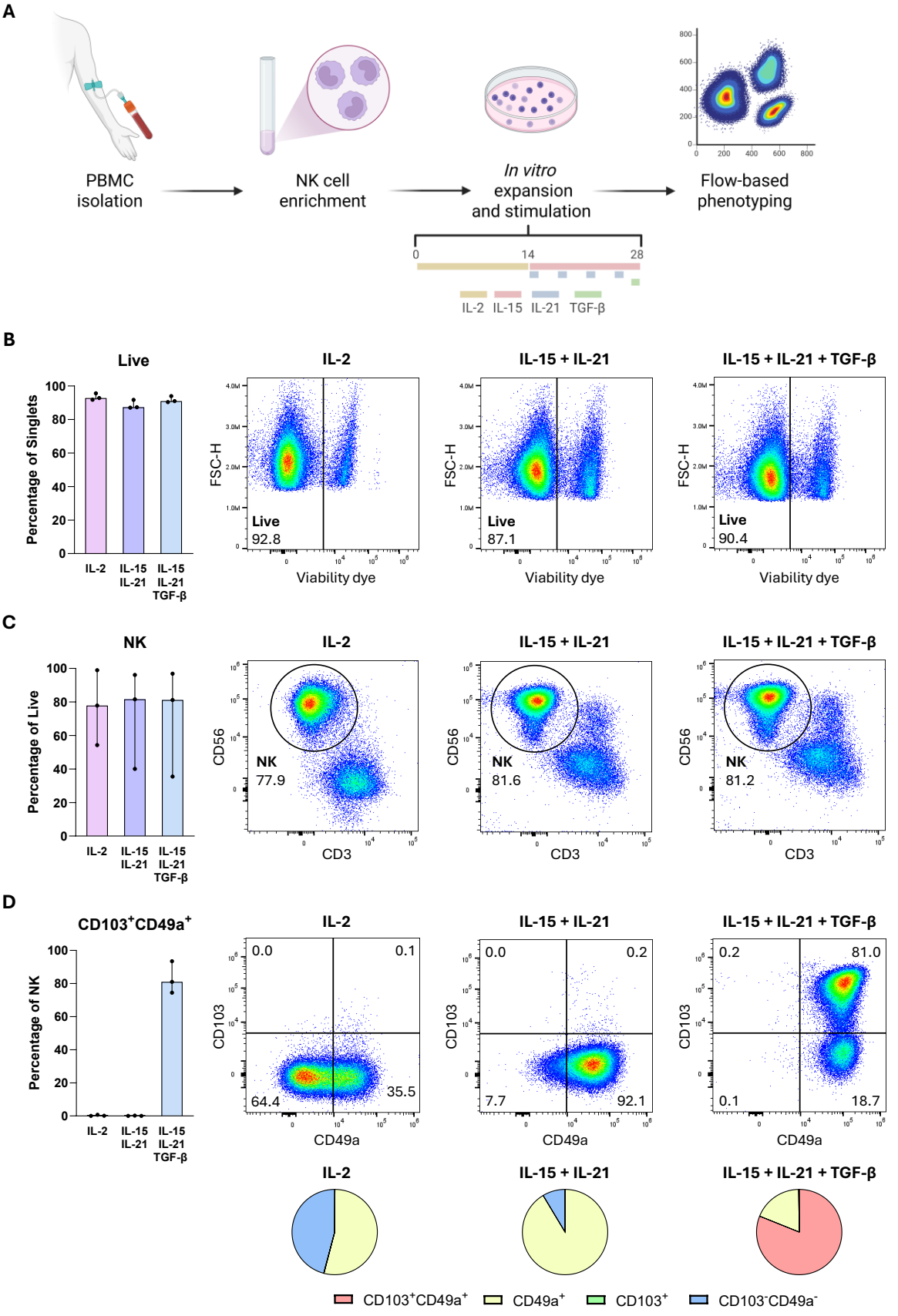
A
PBMC isolation
NK cell enrichment
In vitro expansion and stimulation
Flow-based phenotyping
0
14
28
IL-2
IL-15
IL-21
TGF-β
B
Live
Percentage of Singlets
IL-2
IL-15 IL-21
IL-15 IL-21 TGF-β
IL-2
IL-15 + IL-21
IL-15 + IL-21 + TGF-β
FSC-H
Live
92.8
87.1
90.4
Viability dye
C
NK
Percentage of Live
CD56
CD3
77.9
81.6
81.2
D
CD103+CD49a+
Percentage of NK
CD103
CD49a
0.0
0.1
64.4
35.5
0.0
0.2
7.7
92.1
0.2
81.0
0.1
18.7
CD103+CD49a+
CD49a+
CD103+
CD103-CD49a-

Figure 6.6 – Optimised protocol: viability and NK cell yield
A. Schematic of the experimental workflow. Following PBMC isolation from *n* = 3 healthy donors, $CD56^+$ cells were enriched using a negative selection kit or removing $CD3^+$, $CD19^+$, and $CD14^+$ cells using positive selection kits. The resultant cell mixture was then cultured for 28 days prior to flow cytometric analysis, with an initial 14-day expansion phase with high-dose IL-2 followed by a stimulation phase with IL-15 and pulses of IL-21.
B. Left: percentage of live cells (as a fraction of singlets). Right: representative dot plots showing the percentage of live cells.
C. Left: percentage of NK cells ($CD56^+CD3^-$) as a fraction of live cells. Right: representative dot plots showing the percentage of NK cells.
D. Top: percentage of $CD103^+CD49a^+$ NK cells and representative dot plots showing the percentage of NK cells expressing CD103 and CD49a. Bottom: composition of the NK cell gate, based on median expression of CD103 and CD49a.

The stimulation phase of the protocol, with or without brief exposure to TGF-β, did not appear to affect cell viability, as the median percentage of live cells at the end of the 14-day (IL-2 only) or 28-day period was close to 90% across all three groups. In fact, median viability was higher in TGF-β–exposed cells than in those cultured without it, although the difference was only a few percentage points (**Figure 6.6B**). NK cell yield (the fraction of $CD56^+CD3^-$ cells) varied substantially among donors (**Supplementary Figure 9.7B**). Nonetheless, the median NK cell fraction was comparable across all three conditions, at approximately 80% (**Figure 6.6C**).

Regarding the expression of the tissue retention markers CD103 and CD49a, the NK cell gate composition was virtually dichotomous across all three conditions (**Figure 6.6D**). IL-2–expanded NK cells were either double negatives or $CD49a^+$ (medians: 45.9% and 54.0%, respectively); NK cells stimulated with IL-21 but without TGF-β were predominantly $CD49a^+$, with a minority of double negatives (medians: 91.4% and 8.6%, respectively); and

NK cells stimulated with IL-21 and TGF-β were mainly double positives, with a smaller CD49a$^+$ fraction (medians: 81.0% and 18.7%, respectively). For one donor, cells were cultured in parallel with and without collagen I (a ligand for CD49a); however, this did not appear to influence the distribution of subsets within the CD103 vs CD49a gate (**Supplementary Figure 9.7A**).

6.3.6 The addition of TGF-β only affects expression of a few activating or inhibitory receptors, whereas others remain unaffected

To evaluate how stimulation with or without TGF-β influenced NK cell phenotype, a focussed analysis using a dedicated 16-marker panel was conducted. Most markers showed a clear separation between positive and negative populations. For markers where separation was less obvious by visual inspection, positivity thresholds were defined using either fluorescence minus one (FMO) controls (**Figure 6.7A**) or internal controls, such as the T cell gate representing marker-negative cells (**Figure 6.7B**).

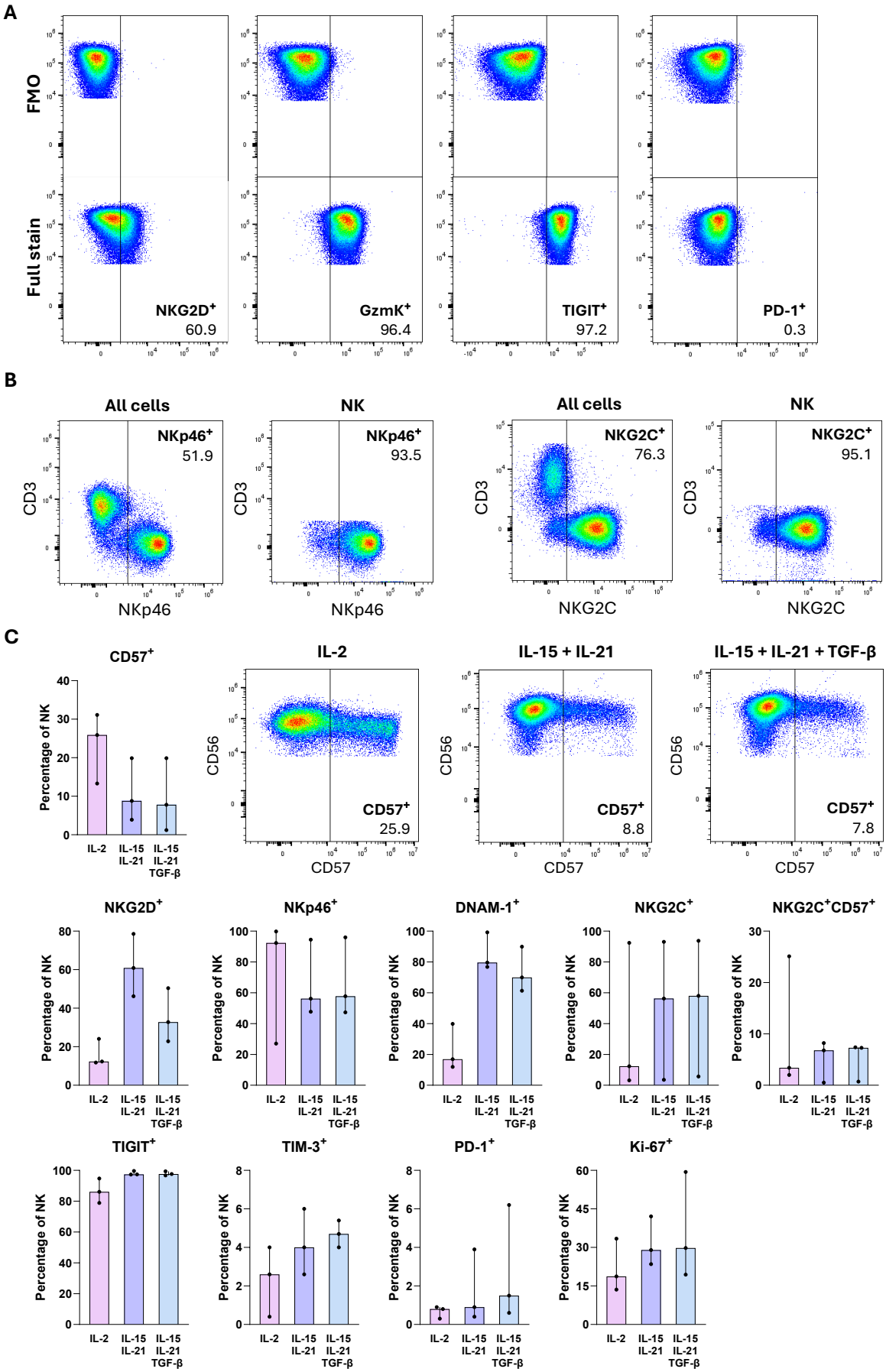
A
FMO
Full stain
NKG2D+
60.9
GzmK+
96.4
TIGIT+
97.2
PD-1+
0.3
B
All cells
NK
All cells
NK
NKp46+
51.9
NKp46+
93.5
NKG2C+
76.3
NKG2C+
95.1
CD3
NKp46
NKG2C
C
CD57+
IL-2
IL-15 + IL-21
IL-15 + IL-21 + TGF-β
Percentage of NK
CD56
CD57
CD57+
25.9
CD57+
8.8
CD57+
7.8
IL-2
IL-15 IL-21
IL-15 IL-21 TGF-β
NKG2D+
NKp46+
DNAM-1+
NKG2C+
NKG2C+CD57+
TIGIT+
TIM-3+
PD-1+
Ki-67+

Figure 6.7 – Optimised protocol: activating and inhibitory receptors
A. Representative dot plots of markers for which FMO controls (top row) were used to set a positivity threshold. The corresponding full stain samples are shown in the bottom row.
B. Representative dot plots of markers for which T cells ($CD3^+CD56^-$) were used as internal controls to define positive thresholds. For the two markers shown, expression is displayed after gating on all cells (including T cells; left) or on NK cells only (right).
C. Percentage of NK cells expressing the activating receptors NKG2D, NKp46, DNAM-1, and NKG2C, the inhibitory receptors TIGIT, TIM-3, and PD-1, and Ki-67. CD57 is shown at the top alongside representative dot plots as an example of threshold definition.

Amongst activating receptors, only NKG2D expression was considerably affected by the inclusion of TGF-β in the stimulation protocol (**Figure 6.7C**), as the median fraction of NK cells expressing this marker was approximately half in the TGF-β condition compared with the condition without TGF-β (medians: 32.8% and 60.9%, respectively). Nevertheless, the proportion of $NKG2D^+$ cells remained higher than in IL-2-expanded cells (median: 12.3%). For DNAM-1, a slight reduction was observed with TGF-β, although expression levels were still substantially higher than in IL-2–expanded cells across both conditions (medians: 16.9% for IL-2, 79.6% for IL-15 + IL-21, and 70.1% for IL-15 + IL-21 + TGF-β). For NKp46 and NKG2C, hardly any difference was detected in marker expression with or without TGF-β. At the end of the 14/28-day protocol, one donor displayed over 90% $NKG2C^+$ NK cells (a proportion unaffected by stimulation condition). Of these, up to 25.1% co-expressed CD57. The median proportion of proliferating NK cells also remained unaffected by TGF-β addition, and was 50% higher in both IL-21-contatining conditions than in IL-2–expanded cells.

As for inhibitory receptors, expression of both PD-1 and TIM-3 was slightly higher with the addition of TGF-β, although the median fraction of NK cells expressing these markers remained below 5% of the total in both conditions. Nearly all NK cells stimulated with IL-21 (with or without TGF-β) upregulated TIGIT, and the proportion of $TIGIT^+$ cells also approached 90% in IL-2–expanded NK cells.

6.3.7 The addition of TGF-β has minimal impact on the cytotoxic and migratory capacity of stimulated NK cells

To assess whether stimulated NK cells could potentially be recruited to the tumour site in subsequent adoptive transfer experiments, the chemokine receptor profile of stimulated cells was examined. Both IL-21-containing stimulation conditions increased the median proportion of cells expressing the three chemokine receptors analysed (CXCR3, CXCR6, and CX3C motif chemokine receptor 1, CX3CR1). CXCR6 was the only receptor whose expression was marginally reduced by TGF-β exposure (**Figure 6.8A**); the fraction of $CXCR6^+$ cells remained, however, substantially higher than in IL-2-expanded cells, where CXCR6 expression was virtually absent (median: 0.9% for IL-2 vs 37.7% for IL-15 + IL-21, and 33.0% for IL-15 + IL-21 + TGF-β). TGF-β seemed to have no effect on CXCR3 or CX3CR1, with the stimulation protocol producing approximately 90% positive cells for both receptors.

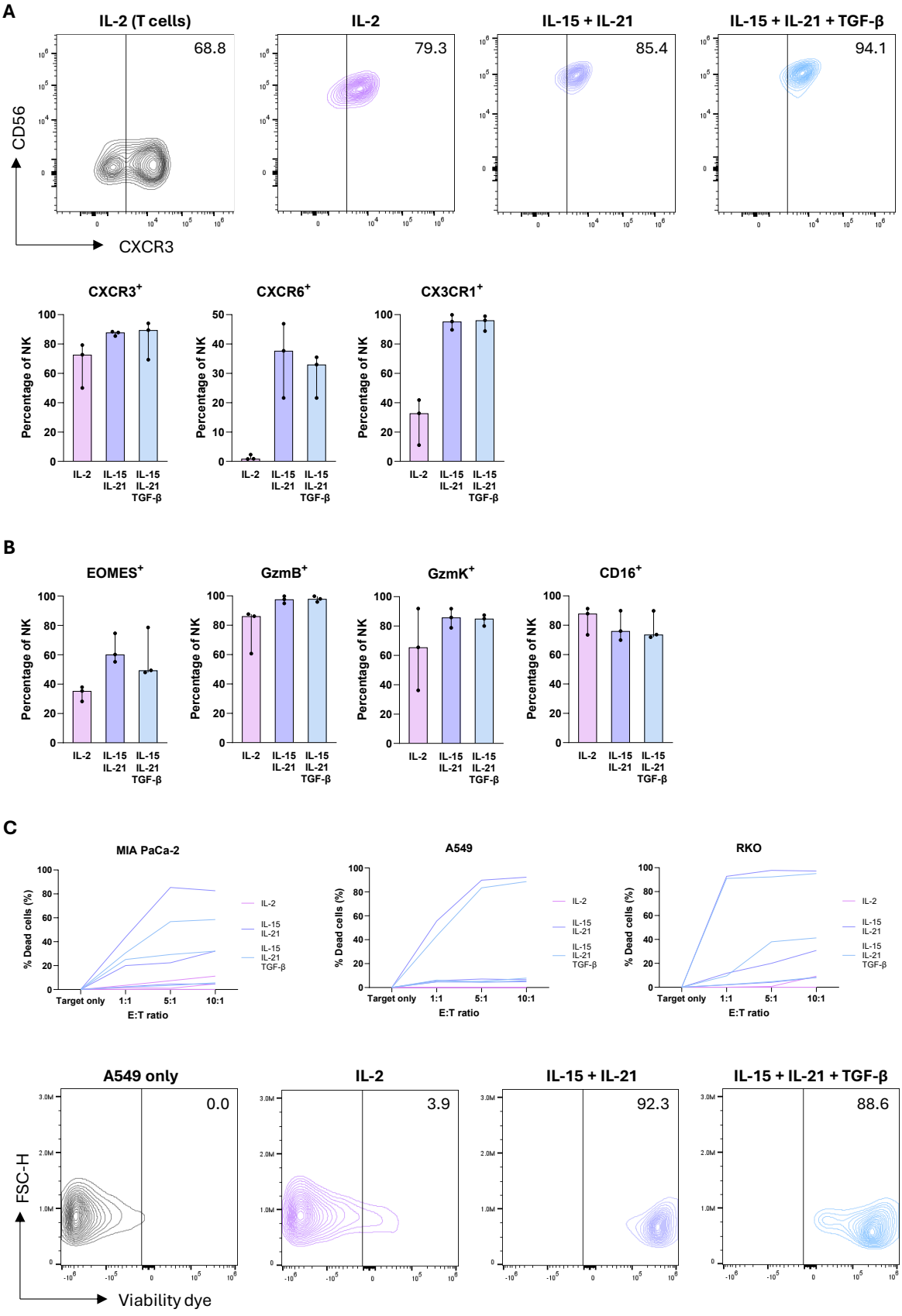
A
IL-2 (T cells)
IL-2
IL-15 + IL-21
IL-15 + IL-21 + TGF-β
68.8
79.3
85.4
94.1
CD56
CXCR3
CXCR3+
CXCR6+
CX3CR1+
Percentage of NK
IL-2
IL-15 IL-21
IL-15 IL-21 TGF-β
B
EOMES+
GzmB+
GzmK+
CD16+
C
MIA PaCa-2
A549
RKO
% Dead cells (%)
Target only
1:1
5:1
10:1
E:T ratio
A549 only
0.0
3.9
92.3
88.6
FSC-H
Viability dye

Figure 6.8 – Optimised protocol: migration capacity and cytotoxicity
A. Top: representative contour plots showing the percentage of CXCR3$^+$ NK cells among total NK cells. The plot on the left (grey outline) shows how the T cell gate was used to assist in threshold definition. Bottom: percentage of NK cells expressing the chemokine receptors CXCR3, CXCR6, and CX3CR1.
B. Percentage of NK cells expressing key molecules involved in cytotoxic activity.
C. Top: percentage of dead (viability dye$^+$) MIA PaCa-2, A549, and RKO cells after 6 hours of co-culture with NK-enriched PBMCs stimulated with the indicated conditions and at the specified effector-to-target (E:T) ratios. NK-enriched PBMCs were used without further purification, i.e., including non-NK contaminants. Each line represents an individual biological replicate ($n = 3$). Bottom: cell death was quantified by flow cytometry and normalised to spontaneous cell death in target cells alone (left, grey outline). Target cells were transduced with mCherry prior to the co-culture; only mCherry$^+$ cells are shown.

Cytotoxic function was next evaluated to determine whether, upon recruitment to the tumour site, NK cells would effectively kill tumour cells. Cells stimulated with IL-21 expressed high levels of GzmB and granzyme K (GzmK), with median fractions of positive cells approaching 100% and 90%, respectively, irrespective of TGF-β exposure (**Figure 6.8B**). Similarly, CD16 expression was observed in approximately 75% of cells irrespective of TGF-β treatment, although IL-2-expanded cells displayed an even higher proportion of CD16$^+$ cells (median: 87.9%). In contrast, expression of the transcription factor EOMES declined with TGF-β, but remained higher than in IL-2–expanded cells (median: 35.3% for IL-2 vs 60.2% for IL-15 + IL-21, and 49.4% for IL-15 + IL-21 + TGF-β).

As this protocol was developed with a view to using NK cells for solid cancer immunotherapy, cytotoxicity was tested *in vitro* against pancreas (MIA PaCa-2), lung (A549), and colon (RKO) cancer cell lines, rather than K562. Unlike K562, these lines express high levels of HLA class I

(**Supplementary Figure 9.7D**) , which can engage inhibitory KIRs on NK cells and generally renders them less susceptible to NK cell-mediated killing, although the degree of inhibition depends on the specific KIR–HLA ligand interactions present in both the NK cell population and the target cell line (Purdy and Campbell 2009; Yokoyama et al. 2010).

Remarkable heterogeneity was observed in the rates of killing both across cell lines and, for each cell line, amongst donors (**Figure 6.8C**). When comparing median killing rates, TGF-β–exposed NK cells outperformed non-exposed cells at two of three E:T ratios across all three cell lines, although in some cases the difference was less than 1%. For the donor who exhibited the highest killing rates across all three cell lines, the difference between TGF-β–exposed and non-exposed NK cells was negligible for RKO and A549 (only a few percentage points at all E:T ratios), but more pronounced for MIA PaCa-2 (up to 30% lower in TGF-β–exposed cells).

To investigate why one donor showed efficient killing whereas the other two did not, the hypothesis that a high fraction of non-NK contaminants reduced target cell killing was assessed. The NK cell fraction ($CD56^{+}CD3^{-}$), shown in **Figure 6.6C**, correlated with killing rates. Pooling data from all donors and all E:T ratios, the NK cell fraction at the end of the 28-day protocol correlated with the proportion of killed target cells (**Supplementary Figure 9.7C**). This was true for all three target cell lines, suggesting that the considerably lower killing observed in two of the three donors might be, at least in part, due to the presence of non-NK cells in the co-cultures.

6.3.8 *In vitro* generated, tissue-associated NK cells may localise to the pancreas of mice with cancer-predisposing conditions

Having established that the 28-day stimulation protocol expands human blood NK cells and induces a tissue-associated phenotype ($CD103^+CD49a^+$) while preserving cytotoxic and migratory capacity *in vitro*, the next step was to assess whether these cells maintained these properties *in vivo*. As an initial proof-of-concept to determine whether TGF-β–exposed NK cells were capable of trafficking to, and being retained within, non-lymphoid tissues (an essential prerequisite for their prospective use in cancer immunotherapy), they were intravenously administered to an immunodeficient, non-tumour-bearing Rag2/IL2RG double-knockout (hereafter: R2G2) mouse (n = 1). At 48 hours post-injection, donor cells were detected in epithelial tissues and in the spleen but were absent from blood (**Figure 6.9A**), indicating efficient extravasation and tissue retention *in vivo*.

To test the anti-tumour activity of these cells against pancreatic cancer, MIA PaCa-2 cells were injected orthotopically in a small cohort (n = 6) of R2G2 mice, with the aim of adoptively transferring *in-vitro*–generated NK cells upon tumour development. Orthotopic engraftment, however, failed, and tumours did not develop.

As preliminary observations from one mouse had indicated that NK cells could home to epithelial tissues even in the absence of a tumour (**Figure 6.9A**), the question then arose as to whether this property could be exploited for cancer immunotherapy in a preventative or precancerous setting. To

explore this possibility, caerulein was repeatedly administered to one R2G2 mouse over 8 weeks, following established protocols for chemical induction of chronic pancreatitis in mice (Leal and Liby 2018; Minaga et al. 2022). A second animal received vehicle (PBS) as a control (*n* = 1 per group). Chronic pancreatitis is the main predisposing condition for pancreatic cancer (Lowenfels et al. 1993; Malka et al. 2002). At the end of the induction period, donor NK cells, expanded and stimulated for 28 days with a terminal TGF-β pulse to induce CD103 and CD49a expression, were labelled with a commercially available tracker dye (IVISense680) (Peterson 2023) (**Supplementary Figure 9.7E**) and injected intravenously into both mice.

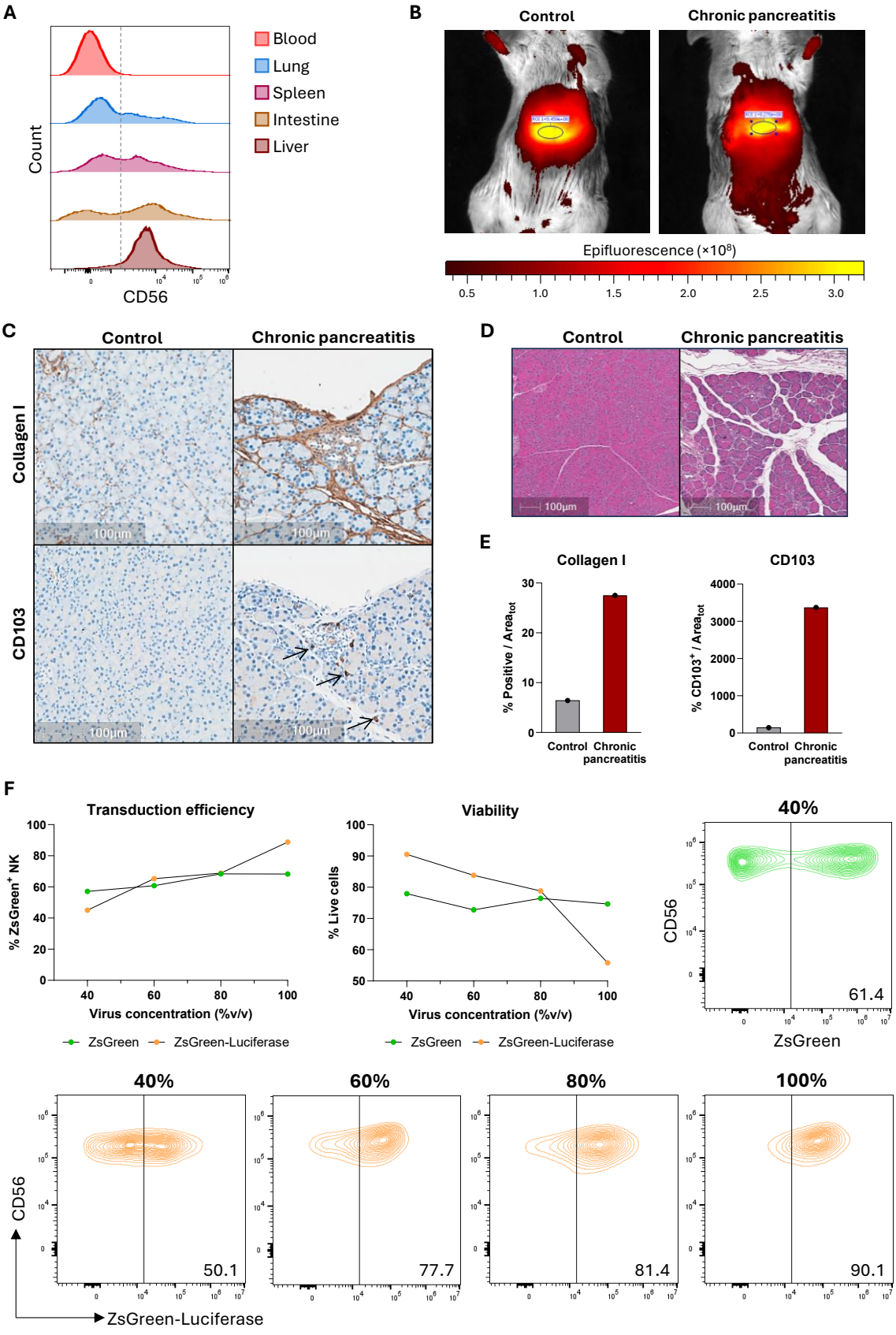
A
Blood
Lung
Spleen
Intestine
Liver
Count
CD56
B
Control
Chronic pancreatitis
Epifluorescence (×10⁸)
0.5
1.0
1.5
2.0
2.5
3.0
C
Control
Chronic pancreatitis
Collagen I
CD103
100µm
D
Control
Chronic pancreatitis
100µm
E
Collagen I
% Positive / Area tot
Control
Chronic pancreatitis
CD103
% CD103+ / Area tot
F
Transduction efficiency
% ZsGreen+ NK
Virus concentration (%v/v)
ZsGreen
ZsGreen-Luciferase
Viability
% Live cells
40%
CD56
61.4
ZsGreen
60%
80%
100%
50.1
77.7
81.4
90.1
ZsGreen-Luciferase

Figure 6.9 – Optimised protocol: *in vivo* localisation and monitoring
A. CD56 expression in the blood, lung, intestine, spleen, and liver of *n* = 1 R2G2 mouse, after excluding cell debris and aggregates with forward and side scatter (FSC and SSC). The Y axis was set to unit area to account for differences in cell number among samples. Dotted line indicates threshold for positivity.
B. Quantification of fluorescence in a region of interest (ROI) drawn onto the pancreas of a mouse treated with caerulein and a control mouse (*n* = 1 per group) 48 hours post-injection of *in vitro*–generated NK cells. Signal was recorded in the near-infrared channel, compatible with IVISense680.
C. Immunohistochemical staining of pancreatic sections from the mice shown in (B). Top row: collagen I; bottom row: CD103. Arrow indicates $CD103^+$ cells.
D. Haematoxylin and eosin staining of pancreatic sections from the mice shown in (B).
E. Percentage of $marker^+$ area in the pancreatic sections in shown in (C).
F. Transduction efficiency and viability of IL-2–expanded NK cells transduced with a luciferase-containing viral vector (*n* = 3 per group). Median is shown, with no error bars. The X axis indicates the concentration of viral particles relative to NK cells (% v/v). Positivity threshold was set using ZsGreen-transduced cells as a reference as better separation was observed for these cells (top right, in green).

Epifluorescence in the pancreas region from the pancreatitis mouse was 50% higher than in the control mouse 48 hours post-injection, suggestive of increased NK cell localisation (**Figure 6.9B**). However, as epifluorescence imaging is only semi-quantitative and some background signal was observed in both mice, definitive assessment was performed by post-mortem histological analysis. Examination of pancreatic sections revealed that a greater area of pancreas was occupied by stroma/extracellular matrix, which was observed both in standard haematoxylin and eosin staining (**Figure 6.9D**) and immunohistochemistry for collagen I (**Figure 6.9C**, top row). In the inflamed pancreas, not only could a higher number of $CD103^+$ cells be detected compared with the healthy control (**Figure 6.9E**), but they seemed to co-localise with collagen-dense regions by visual inspection (**Figure 6.9C**, bottom row).

The limitations of short-term, semi-quantitative fluorescence imaging were apparent in this small experiment, highlighting the need for improved *in vivo* monitoring methods that allow assessment of NK cell localisation without animal sacrifice in future studies of adoptive cancer immunotherapy. In a final, small proof-of-concept experiment (n = 3), IL-2–expanded NK cells were transduced to stably express luciferase. Among the virus concentrations tested (**Figure 6.9F**), 60% v/v provided the optimal compromise between transduction efficiency (median: 65.3%) and cell viability (median: 83.8%). At higher virus concentrations, efficiency as high as 90% could be achieved, although at the cost of reduced viability.

6.4

Discussion

Current evidence supports both a positive association between tissue-associated NK cells and tumour control and their functional impairment within the tumour microenvironment. In this chapter, a protocol was established for generating NK cells expressing key tissue-retention markers while preserving functionality and cytotoxicity, with potential application in cancer immunotherapy. Except for the initial mouse experiments, very small sample sizes were used. Therefore, the findings presented should be considered exploratory, and any inferences should be made with caution.

After demonstrating that conventional $CD103^{-}CD49a^{-}$ NK cells could be induced to express one or both tissue-retention markers in mice, several cytokine combinations were screened for their ability to promote expansion

of the corresponding subset starting from human PBMCs. Initial screening indicated that IL-15 + IL-21 with a terminal brief exposure to TGF-β produced the largest proportion of $CD103^+CD49a^+$ NK cells (approaching 80% of total NK cells) while maintaining cytotoxicity comparable to that of NK cells cultured with IL-15 alone. Because viability, NK cell yield, and cytotoxic capacity at the end of the 7-day stimulation were only modest, the protocol for generation of tissue-associated NK cells was further optimised.

The initial, shorter protocol was adapted to include a 14-day expansion phase with high-dose IL-2 and maintenance-dose IL-15, and a 14-day stimulation phase with high-dose IL-15 and IL-21 (with or without a brief final exposure to TGF-β). Despite the inclusion of TGF-β, NK cell viability remained above 90% for all three donors tested, indicating that short-term TGF-β exposure does not compromise viability. Continuous TGF-β exposure for one week in the original screening, instead, had reduced viability to approximately 50%. The addition of TGF-β also resulted in a $CD103^+CD49a^+$ fraction of up to 93.5% of total NK cells, suggesting that nearly all NK cells generated using this protocol could potentially be retained in tissues.

The median NK cell yield showed marked interindividual variability. This was irrespective of TGF-β, and most likely stemmed from a combination of several factors, including a lower NK cell percentage in the blood of donors or occasional deviations from the manufacturer's instructions due to limited reagent availability. The degree of sample purity appeared to influence the cytotoxic capacity of NK cells in an *in vitro* assay against three

solid cancer cell lines. The lower cytotoxicity observed in cultures of cells from the two donors with suboptimal NK cell enrichment was, at least in part, attributable to a lower proportion of NK cells (or rather, a higher proportion of contaminating T/NKT cells). It is plausible that T cell contaminants were not only acting as inert bystanders in the culture (as T cells require antigen presentation and co-stimulation for activation and killing), but may have competed with NK cells for cytokines in the stimulation phase of the protocol, thereby further reducing the cytotoxic potential of those NK cells that survived to the end of the protocol. This underscores the importance of employing high-standard, GMP-compliant isolation platforms such as the CliniMACS (Miltenyi Biotec) or equivalent magnetic separation systems in potential future translational applications. Despite this, the cytotoxicity observed in the donor samples with near exclusive NK cell presence remained notable, and was comparable to, and in fact higher than, that achieved in other well-established NK cell stimulation protocols (Tarannum et al. 2024). It should be noted that other factors may have significantly influenced cytotoxicity in these experiments, and may impact the efficacy of NK cell–based therapies in future applications. For example, NK cell donors express diverse KIR repertoires and tumour cell lines express distinct KIR ligands, reflecting differences in both KIR gene content and HLA class I expression (Parham and Moffett 2013), which can influence the balance of inhibitory and activating signals and ultimately affect NK cell cytotoxicity (Purdy and Campbell 2009).

Most markers exhibited comparable expression between TGF-β–exposed and non-exposed NK cells, indicating that a brief terminal incubation is sufficient to induce a $CD103^{+}CD49a^{+}$ phenotype with minimal impact on activation status, checkpoint receptor and chemokine receptor profiles, proliferation, or cytotoxicity. Expression of only a few markers, including the transcription factor EOMES (which governs NK cell differentiation and effector function) and the activating receptor NKG2D, was moderately reduced following TGF-β incubation. Apart from these, moderate-to-high expression of key receptors and effector molecules involved in activation and cytotoxicity was observed (e.g., DNAM-1, NKp46, NKG2C, CD16, GzmB, and GzmK), indicating that, despite TGF-β exposure, these NK cells retained strong functional capacity. Notably, while CXCR6 is the chemokine receptor most frequently implicated in gastrointestinal malignancies such as pancreatic and hepatic cancer (Hudspeth et al. 2016; Lesch et al. 2021), the concomitant expression of additional chemokine receptors suggests that NK cells generated using this protocol may also be suitable for immunotherapy of other solid tumours.

The key experiment needed to assess the *in vivo* anti-tumour efficacy of the *in vitro*–generated NK cells could not be completed as MIA PaCa-2 cells failed to engraft after orthotopic implantation into n = 6 R2G2 mice. Importantly, subcutaneous implantation of the same cell line in the same mice was successful, suggesting that the failure was related to the orthotopic implantation procedure itself rather than to the host or the cell line. This undoubtedly represents the major limitation of the present study:

while the phenotype and *in vitro* activity of the generated NK cells provide some indication of their potential performance *in vivo*, several factors are known to limit the effectiveness of adoptive cell therapies. These include efficient migration to the tumour site, retention within the TME, and avoidance of inhibitory signals (Laskowski et al. 2022). Therefore, future experiments to determine whether these challenges can be overcome and whether the NK cells can achieve tumour control *in vivo* are essential.

Almost serendipitously, the failure of tumour engraftment in the current study redirected the focus towards a perhaps more intriguing possibility. The findings presented above raise the question of whether NK cells could home to, and populate, sites of potential tumour formation even before tumourigenesis occurs, as observed here, albeit for only one mouse, in the context of chronic pancreatitis. If future studies confirmed that *in vitro*–generated NK cells can (I) home to tissues, (II) persist long-term, and (III) retain functionality *in vivo*, a new paradigm for cancer prevention would be conceivable whereby (repeated) NK cell administration could pre-emptively arm tissues with a first line of defence against developing tumours. It should be emphasised again that the little evidence gathered in the present study is, at best, hypothesis-generating, and any suggestion of a paradigm shift toward NK cell adoptive transfer in a preventative setting remains highly speculative. Validating all three parts of this potential paradigm shift (homing, persistence, and functionality) will require much more extensive and rigorous testing in models of cancer predisposing conditions (such as chronic pancreatitis) or precancerous conditions (such as the KC model).

Non-invasive methods for tracking adoptively transferred NK cells *in vivo* are essential for such future studies. The feasibility of transducing NK cells with luciferase was evaluated here as a method that enables long-term monitoring and is compatible with bioluminescence imaging systems. Transduction was performed after the IL-2 expansion phase, as NK cells are more susceptible to viral uptake during active proliferation (Allan et al. 2021). This would allow the 14-day cytokine stimulation phase (as configured in the present study or with further adaptations in future studies) to occur on already transduced cells.

Further adaptations of the protocol described in this chapter could be introduced depending on specific research objectives and questions. For example, NK cells could be virally transduced with genes in addition to or in place of luciferase to modulate phenotype and/or function, drastically expanding the applicability of this immunotherapy approach.

Chapter 7

Longitudinal profiling of innate and adaptive immune cells during pancreatic tumourigenesis in the KC model of PDAC

7.1

Introduction

Building on the hypothesis that NK cells may populate sites of incipient tumourigenesis even before the development of overt cancer, the next logical step was to investigate whether the frequency of these cells (and other immune populations) change during the earliest stages of pancreatic tumour development. To this end, the well-established *Pdx-1*-Cre;LSL-*Kras*$^{G12D/+}$ (KC) mouse model was employed, because, as discussed in the main Introduction, it accurately recapitulates the sequential progression from low- to high-grade PanINs and ultimately to invasive PDAC over the course of 12 months. This model therefore provides an appropriate system to examine the dynamics of NK cell abundance across evolving disease stages, alongside broader changes in the immune landscape accompanying the PanIN-to-PDAC transition.

7.2

Aims

To determine whether the abundance of key players in anti-tumour immunity changes with the transition from precursor lesions (PanINs) to overt cancer (PDAC) in the KC mouse model of pancreatic tumourigenesis.

7.3

Results

7.3.1 – NK cells

Formalin-fixed, paraffin-embedded slices of pancreata from wild-type C57BL/6J (control) and KC mice were kindly donated by Paul Miller (Ludwig Institute for Cancer Research, Oxford), and stained by the Translational Histopathology Laboratory (THL, Oxford Cancer Centre, Oxford). Initially, a six-colour immunofluorescence panel was designed in collaboration with the THL to identify innate and adaptive lymphocytes, and in particular NK cells expressing the tissue-retention marker CD103 ($NK1.1^+CD103^+$ cells). This would have enabled assessment of whether these cells act as early responders at sites of PanIN formation. However, a number of technical issues prevented this. A first NK1.1 antibody failed to bind cells and precipitated as amorphous extracellular aggregates (not shown). A second NK1.1 antibody consistently detected *bona fide* NK cells by immunohistochemistry (IHC) in pancreatic and control spleen sections, but failed to do so when adjacent sections from the same samples were stained with all antibodies of the multiplex immunofluorescence panel (not shown). It is unclear whether steric hindrance prevented binding in the context of multiplex immunofluorescence, as changing the staining order (Syed et al. 2019) did not yield satisfactory staining (not shown). Consequently, NK1.1 was excluded from the multiplex panel, and $NK1.1^+$ cells were analysed independently on adjacent sections by IHC alone, precluding assessment as to whether they exhibited a tissue-associated ($CD103^+$) phenotype.

Despite numerous rounds of optimisation, some non-specific NK1.1 background staining was observed (especially, but not exclusively, in the islets of Langerhans, which are known to show marked artefactual positivity in IHC due to strong nonspecific IgG binding) (Baskin 2015). As a result, *bona fide* NK cells ($NK1.1^+$) were identified by setting a very high threshold for positivity in the cell-identification software (HALO) and, among highly positive cells, further confirmed based on a combination of morphology and location (**Figure 7.1A**).

NK cells were completely absent from the pancreas of control mice at 3 and 6 months of age, and only appeared in negligible proportions in the pancreas of control mice at 9 months of age. In KC mice, on the other hand, NK cells could be detected starting at 6 months of age, and, at 9 months, were found at significantly higher proportions than in controls (**Figure 7.1B**). Apart from very rare exceptions, NK cells localised to the stroma between glands, rather than as intraepithelial lymphocytes.

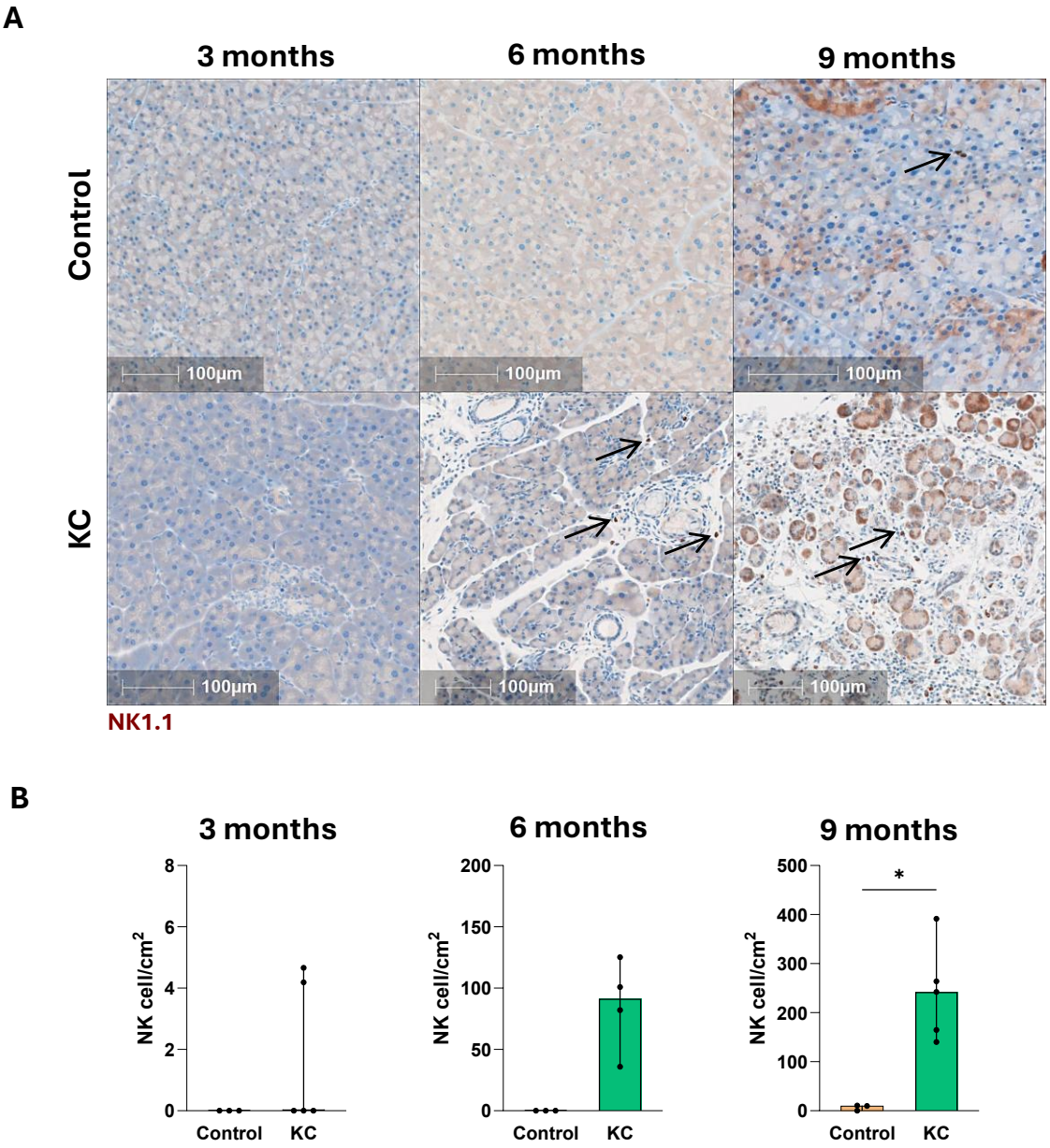

Figure 7.1 – NK cells in the pancreas of ageing KC mice

A. Representative NK1.1 IHC staining in control and KC mice at 3, 6, and 9 months of age. Black arrows indicate NK cells (NK1.1$^+$).

B. Counts of NK cells (NK1.1$^+$) in control and KC mice at 3, 6, and 9 months. Statistical significance was assessed using a two-tailed Mann–Whitney U test.

7.3.2 – $CD8^+$ T cells

To determine whether only innate or adaptive lymphocytes, too, accumulate in the pancreas of KC mice during disease progression, the proportion of $CD8^+$ T cells and B cells was analysed next. In control mice, *bona fide* $CD8^+$ T cell ($DAPI^+CD8\alpha^+$) counts remained modest (<100 cells/cm^2) throughout the observation period, and even appeared to show a slight decline over time (median in controls: 92.6 cells/cm^2 at 3 months, 77.4 cells/cm^2 at 6, and 74.2 cells/cm^2 at 9). In contrast, KC mice displayed a marked and progressive increase in $CD8^+$ T cell density in the pancreas, with values consistently and substantially higher than those observed in controls at all three timepoints (**Figure 7.2**).

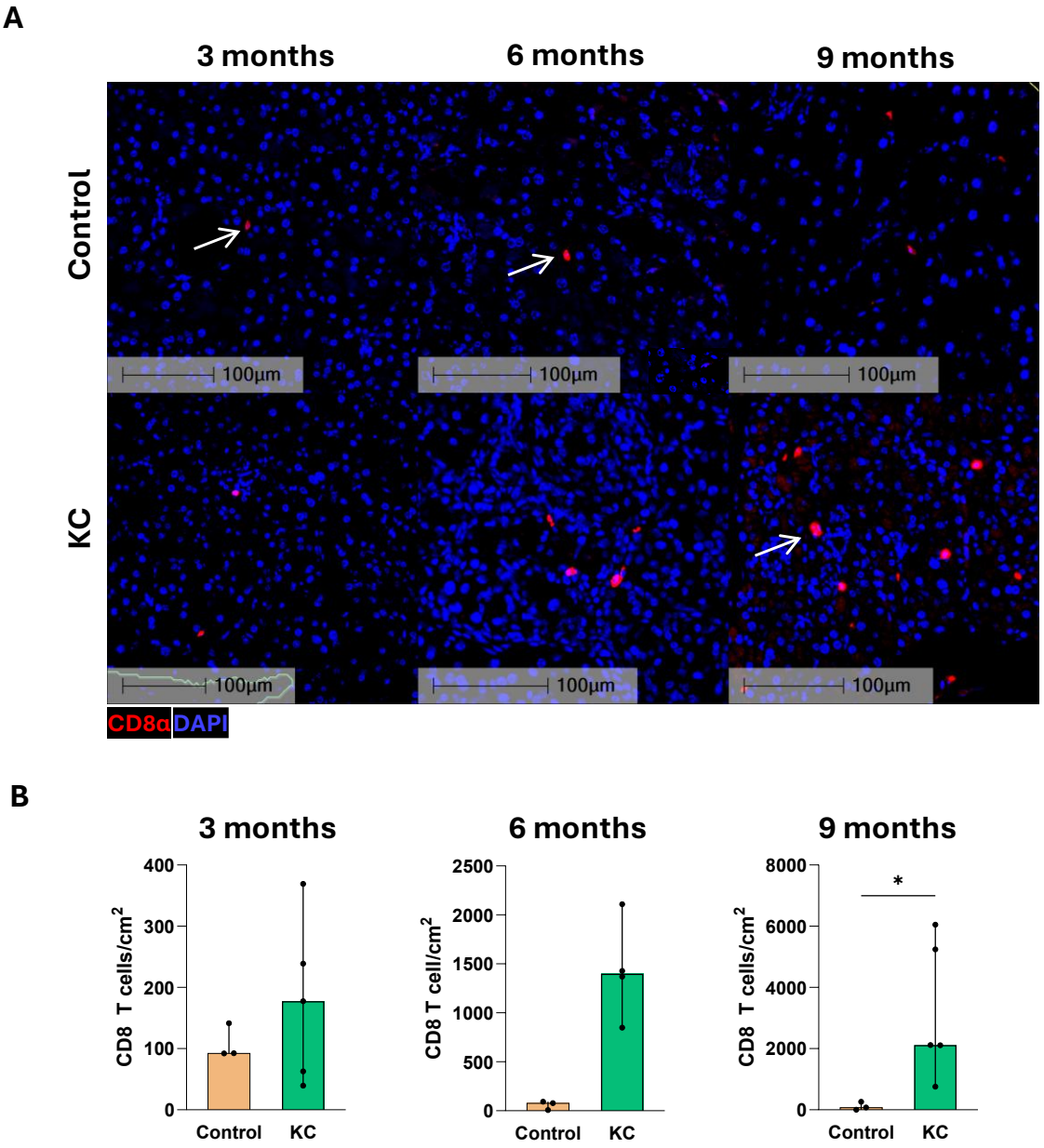

Figure 7.2 – CD8⁺ T cells in the pancreas of ageing KC mice

A. Representative CD8α immunofluorescence staining in control and KC mice at 3, 6, and 9 months of age. Blue: DAPI. Red: CD8α. White arrows indicate $CD8^+$ T cells ($DAPI^+CD8\alpha^+$).

B. Counts of $CD8^+$ T cells ($DAPI^+CD8\alpha^+$) in control and KC mice at 3, 6, and 9 months. Statistical significance was assessed using a two-tailed Mann–Whitney U test.

7.3.3 – B cells

The proportion of *bona fide* B cells ($DAPI^+CD19^+$) remained relatively stable over time in control mice (median between 140 and 240 cells/cm^2 across the three timepoints). In KC mice, instead, while B cell counts were comparable to controls at 3 months, their number increased markedly with disease progression, reaching levels approximately 5-fold higher than in controls at 9 months (**Figure 7.3**).

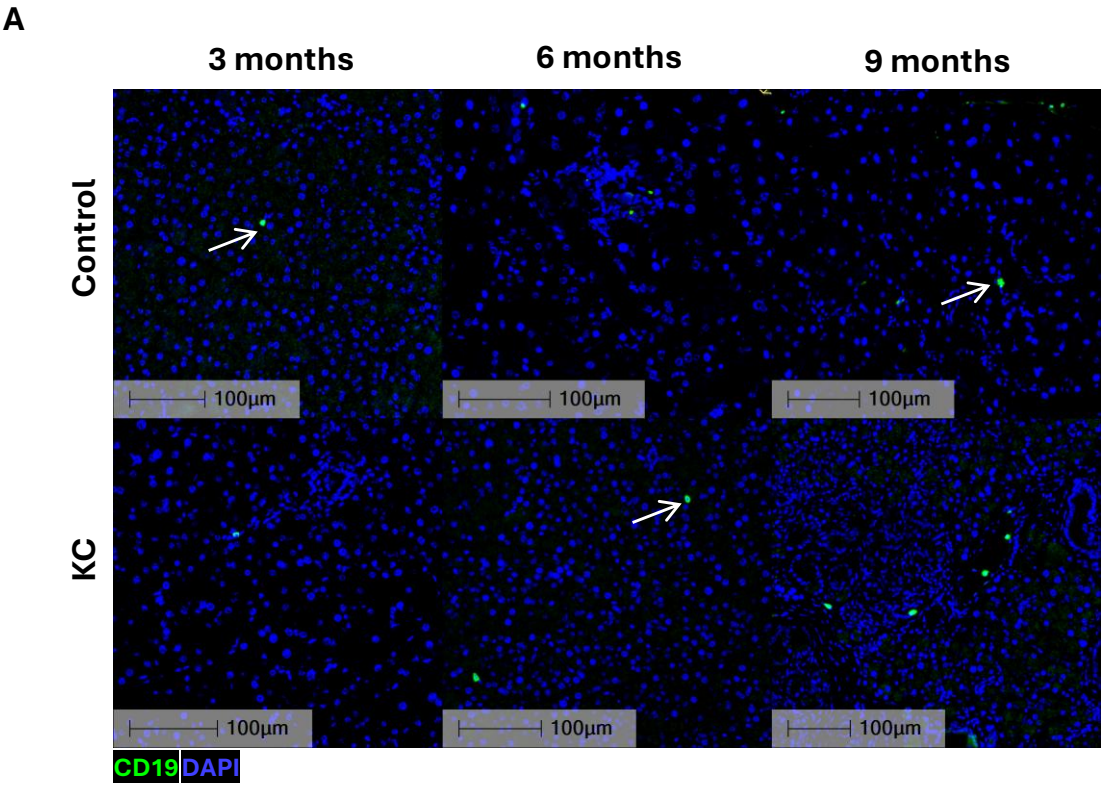

Figure 7.3 – B cells in the pancreas of ageing KC mice
A. Representative CD19 immunofluorescence staining in control and KC mice at 3, 6, and 9 months of age. Blue: DAPI. Green: CD19. White arrows indicate B cells ($DAPI^+CD19^+$). B. Counts of B cells ($DAPI^+CD19^+$) in control and KC mice at 3, 6, and 9 months. Statistical significance was assessed using a two-tailed Mann–Whitney U test.

7.3.4 – Type 1 conventional dendritic cells

As $CD8^+$ T cells showed both the most pronounced increase over time and the greatest difference compared with controls, it was hypothesised that they might be responding to tumour neoantigens arising before development of overt PDAC. Supporting this hypothesis, *bona fide* cDC1s ($DAPI^+CD11c^+CD103^+$) were detected at very low proportions in control mice, with their numbers increasing markedly over time in KC mice (**Figure 7.4**).

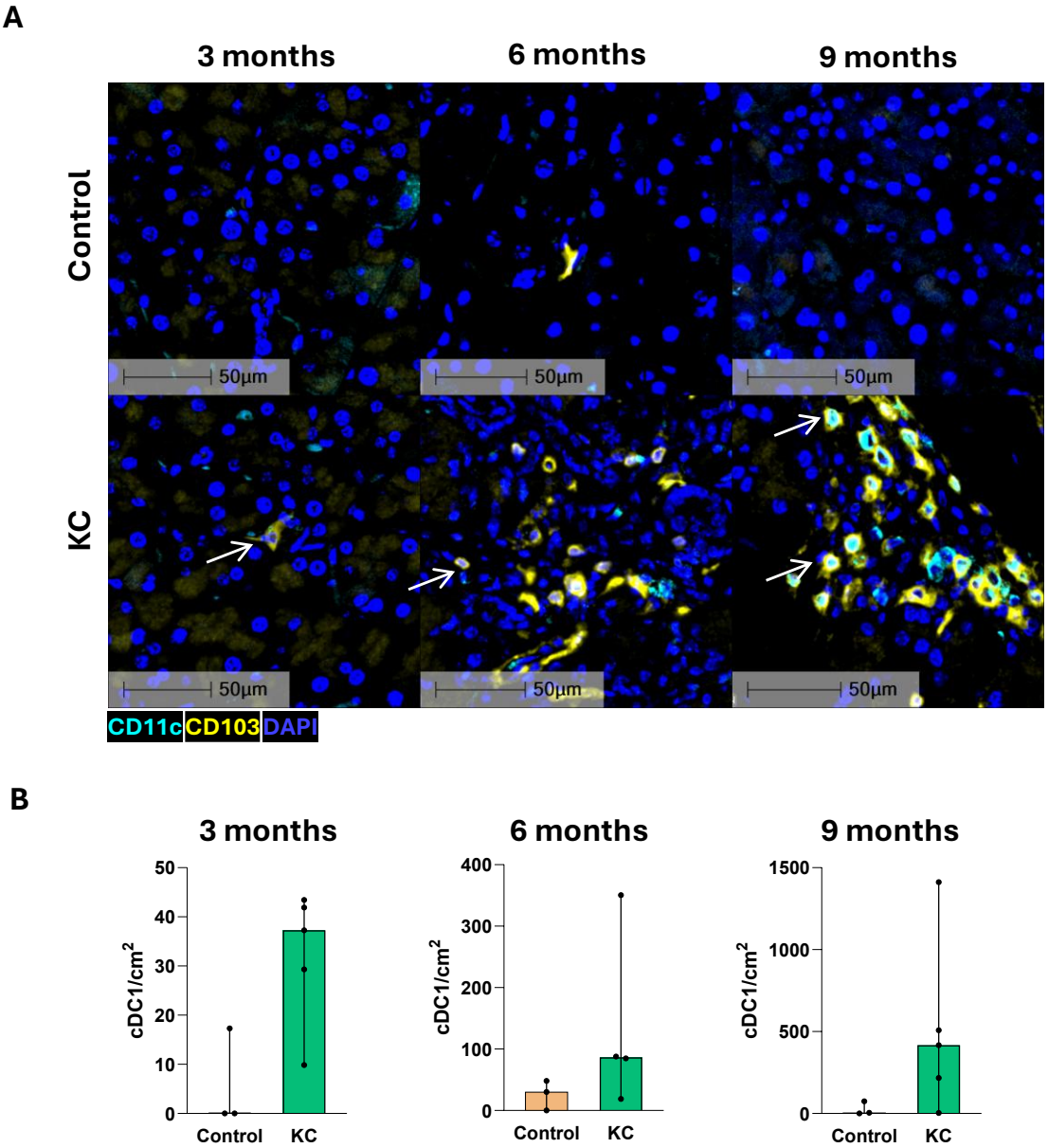

Figure 7.4 – cDC1s in the pancreas of ageing KC mice

A. Representative CD11c/CD103 immunofluorescence staining in control and KC mice at 3, 6, and 9 months of age. Blue: DAPI. Cyan: CD11c. Yellow: CD103. White arrows indicate cDC1s ($DAPI^+CD11c^+CD103^+$).

B. Counts of cDC1s ($DAPI^+CD11c^+CD103^+$) in control and KC mice at 3, 6, and 9 months. Statistical significance was assessed using a two-tailed Mann–Whitney U test.

7.3.5 – Overall immune infiltrate

Having established that all immune cell subsets analysed increased in density with age (and thus with disease progression), a qualitative assessment was next performed to evaluate potential localisation patterns within the pancreas. Although not formally quantified, visual inspection revealed three recurring features: (I) immune cells, irrespective of subtype, predominantly occupied stromal-rich areas between glands; (II) clusters of immune cells were occasionally observed in proximity to large blood vessels; and (III) most notably, immune cells were frequently located near PanINs (**Figure 7.5**).

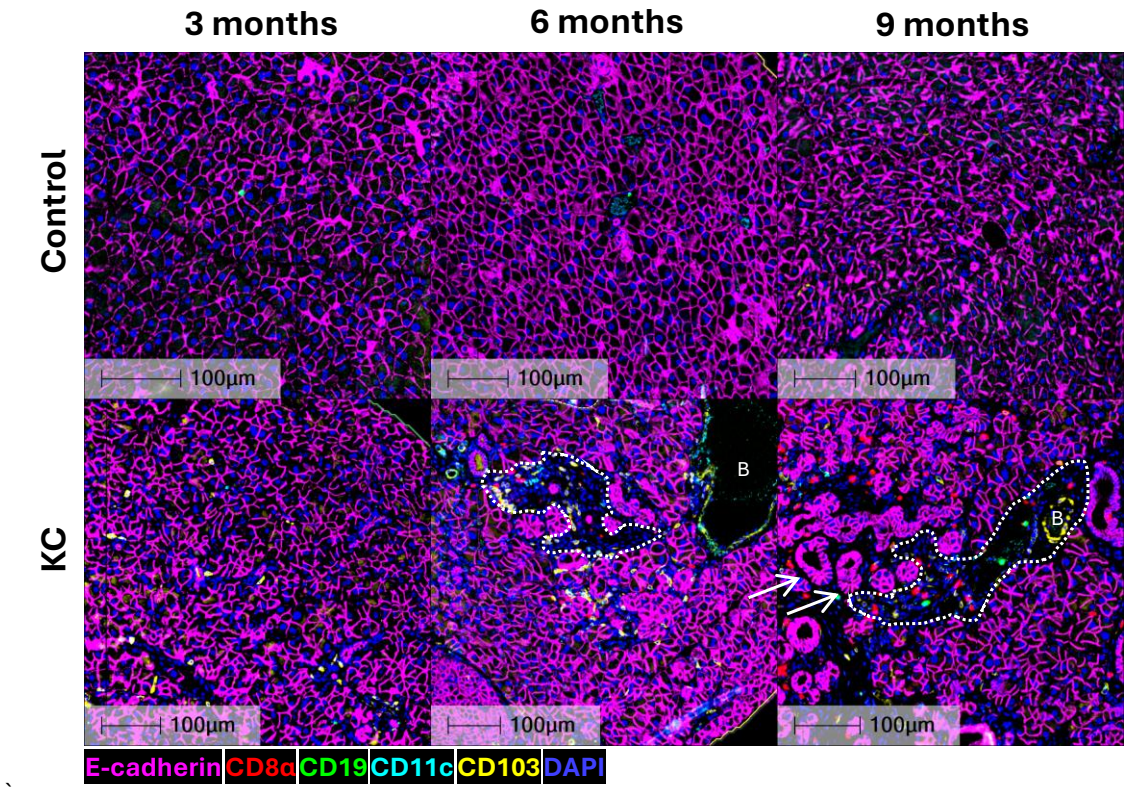

Figure 7.5 – Overall infiltration in the pancreas of ageing KC mice
Based on visual inspection, immune cells predominantly localise within the stroma, close to PanINs or blood vessels in the pancreas of KC mice. Representative multiplex immunofluorescence staining in control and KC mice at 3, 6, and 9 months of age. Blue: DAPI. Red: CD8α. Green: CD19. Cyan: CD11c. Yellow: CD103. Magenta: E-cadherin. White arrows indicate PanINs. White dashed outline indicate stroma amidst glands.

7.4

Discussion

While the immune landscape of PDAC has been extensively characterised, very little is known about the immune context of PanINs and how it evolves during the transition from preinvasive lesions to overt adenocarcinoma. Most studies have focussed on the TME at the end stage, whereas early events shaping immune infiltration remain poorly defined. At the time the analyses presented in this chapter were performed, evidence existed for both humans and mice that immune infiltration in the pancreas begins at the PanIN stage (Hiraoka et al. 2006; Clark et al. 2007; McAllister et al. 2014; Liou et al. 2017). These previous reports described early infiltration of these lesions by Tregs and MDSCs accompanied by effector T cell exclusion.

In line with these reports, the present data suggest that multiple immune populations (namely, NK cells, B cells, $CD8^+$ T cells, and cDC1s) may accumulate progressively in the pancreas of KC mice as PanINs develop and expand. This would imply that immune recruitment accompanies, rather than follows, neoplastic transformation. Importantly, when assessed descriptively by inspection, immune cells appeared to localise to stromal-rich regions and in proximity to PanINs or blood vessels, in agreement with previous reports (Clark et al. 2007; Kiemen et al. 2024), suggesting that the immune compartment may become spatially organised even before invasive disease emerges.

Unlike previous reports, $CD8^+$ T cell counts were found to increase over time. In fact, amongst the populations analysed, $CD8^+$ T cells displayed the most pronounced increase with disease progression. One possible explanation is that previous analyses compared immune infiltrates (including $CD8^+$ T cells) between healthy tissue, PanINs, and PDAC within the same pancreas of KC mice, whereas the present study quantified immune cells across entire pancreatic sections from control and KC mice at different stages of development, providing a more global estimate. Moreover, a recent preprint reported that immune infiltration around PanINs is highly heterogeneous, featuring alternating immune "hot" and "cold" regions that can vary over tens of micrometres, which could also account for differences in observed cell densities (Kiemen et al. 2024).

The co-occurrence of $CD103^+CD11c^+$ cells (here classified as type 1, cross-presenting dendritic cells) and $CD8^+$ T cells in KC pancreata could be weakly suggestive of early immune engagement at sites of neoplasia, although it does not necessarily imply productive antigen-specific priming or activation, and may very well represent coincidental, nonspecific accumulation. Further characterisation of T cell activation states and/or analysis of pancreatic-draining lymph nodes would be required to add clarity on this point.

To the best of current knowledge, this is the first time NK cells are reported to increase in abundance over the course of PanIN progression. It must be acknowledged that, although great attention was devoted to correctly

identifying NK cells, the analysis of NK cell frequencies should nevertheless be interpreted with caution. Because of the very high background staining across the near totality of sections, the automated cell identification software was less reliable at discriminating *bona fide* NK cells from noise; therefore, NK1.1^{+} cells were identified manually by visually inspecting entire sections—a process that is highly investigator-dependent and potentially subject to bias. Analyses repeated using larger sample sizes, better sample quality, and improved staining technique would help provide more definitive insights. Based on the current data, NK cells were largely absent in wild-type pancreata and appeared only at later stages in KC mice, suggesting that innate lymphocyte recruitment may occur later than the recruitment of cytotoxic T cells. What exactly would promote NK cell recruitment in the pancreas of KC mice remains an open (and highly compelling) question. NK cell counts remained the least conspicuous across the examined immune populations, consistent with previous reports indicating that NK cells are often excluded from, or functionally impaired within, pancreatic neoplasias (Marcon et al. 2020).

At 3 months, there was no statistically significant difference between the B cell content of pancreata from control and KC mice, consistent with previous reports describing comparable B cell frequencies between PanINs and healthy pancreas (Clark et al. 2007). Although data on B cell clustering were not formally quantified and therefore not shown in the Results section, B cells were occasionally found in small clusters, suggestive of very primordial tertiary lymphoid structure (TLS) formation, which has been

documented both in PDAC (Spear et al. 2019) and, more recently, even at pre-invasive stages (Lyman et al. 2025). In the present analysis, B cell density in KC mice increased at 6 and 9 months (and was greater than in controls). Although it could be intuitive to interpret this as an anti-tumour response, the functional significance of this increase is impossible to determine with these data alone, and B cells may in fact be bystanders, participating in non-specific inflammatory responses, as discussed for $CD8^+$ T cells above. Interestingly, while some reports linked B cells and TLS to improved immune surveillance in PDAC (Kinker et al. 2023), others have shown that B cells can themselves promote pancreatic tumourigenesis (Pylayeva-Gupta et al. 2012).

Overall, these data suggest that the immune microenvironment of the pancreas in the KC mouse model evolves dynamically during PanIN development, featuring a progressive enrichment of both innate and adaptive populations and a defined spatial distribution surrounding stromal-rich and perivascular regions. Although this infiltration could indicate early immune responses to neoplastic cells, the ultimate failure to prevent tumour progression implies that such responses are either insufficient or rapidly suppressed by the prominent immunosuppressive TME. Further characterisation of all immune cell phenotypes and functions and a more precise assessment of the relationship between cell types and evolving PanIN stages will be critical to understanding how early immune surveillance is subverted during pancreatic tumourigenesis.

Chapter 8

General discussion and future directions

The overarching goal of the work presented in this thesis was the development of novel immunotherapeutic strategies for PDAC, as this remains a major unmet clinical need. Despite decades of research, PDAC still carries an extremely poor prognosis. Current first-line therapies are still long-standing regimens, such as gemcitabine (first introduced in 1997) (Burris et al. 1997) or FOLFIRINOX (introduced in 2011) (Conroy et al. 2011), and have only marginally improved survival, highlighting the urgent need for innovative approaches.

Recent evidence has shown that, even in the context of PDAC's low inherent immunogenicity, it is possible to harness the immune system (and, specifically, $CD8^+$ T cell responses) to achieve durable anti-tumour responses (Sethna et al. 2025). This suggests that a paradigm shift towards immunotherapy-based treatments may be feasible, possibly in combination with conventional cytotoxic regimens that remain the current standard of care.

Given the lack of alternative platforms that faithfully recapitulate the complex interplay between tumour development and anti-tumour immunity, *in vivo* mouse models continue to represent an indispensable tool in immuno-oncology research, including for PDAC. For this reason, in Chapter 3, a multiparametric flow cytometry panel was designed for the

comprehensive analysis of immune alterations occurring both in pancreatic tumours and in systemic compartments. The rationale was that the design of novel therapies requires a deep understanding of the immune landscape of pancreatic cancer, both in baseline conditions and under therapeutic perturbations. While this panel filled some important gaps, for the sake of transparency, it should be acknowledged that another, more extensive flow cytometry panel has been made publicly available around the same time, with a similar aim of investigating anti-tumour responses both locally and systemically in mouse models of cancer (Kare et al. 2023). The two can be regarded as complementary tools: the panel by Kare et al. may be employed when detailed subset-level information across all or nearly all immune populations is required, whereas the smaller panel presented in Chapter 3 is more suitable when a cytometre with fewer detection channels is available, or when flexibility is needed to add additional fluorochromes to investigate additional parameters beyond the core set.

In Chapter 4, one such panel adaptation was employed to characterise an NK cell subset identified in a preclinical study combining the CCR5 inhibitor Maraviroc, an anti–PD-1 antibody, and radiotherapy. These NK cells expressed canonical markers of tissue residency yet were also detectable in circulation (and in one mouse, at high frequency). This is in stark contrast to the initial descriptions of tissue-resident cells as non-recirculating in parabiosis experiments (Peng et al. 2013), and highlights how, phenotypic analyses (e.g., flow cytometry) and cell behaviour assessments (e.g., parabiosis experiments) should be used as complementary, rather than alternative, approaches to demonstrate tissue residency. Integrating mouse and human data led to the hypothesis that this NK subset may act as

an immunoregulatory population, indirectly supporting anti-tumour immunity by enhancing antigen-specific T cell responses rather than through direct cytotoxicity. Although definitive validation of this model through large-scale preclinical studies is still required, the finding that a tissue-resident NK cell signature in human PDAC correlates with improved survival suggests that immunotherapeutic strategies that promote responses by NK cells (and not necessarily $CD8^+$ T cells only), may represent a promising avenue for future research.

In Chapter 5, a different combination therapy was investigated, comprising the FAK inhibitor Defactinib, aimed at modulating the dense PDAC stroma, and an anti–TIGIT antibody, expected to unleash both T and NK cell activity. In light of the limited sample size, no conclusive evidence on therapeutic efficacy could be drawn, but the data indicated improved tumour control and survival trends, as well as enhanced immune cell infiltration. In line with previous reports, Defactinib alone sufficed to enhance immune cell influx into tumours. Rather surprisingly, however, the addition of TIGIT blockade further increased overall immune infiltration and density, despite a low baseline expression of TIGIT among T and NK cells, and despite activation, proliferation, and effector function markers being largely comparable between treatments. As already discussed above, TIGIT blockade may have acted in more subtle, circuitous ways, likely skewing survival, retention, and potentially even recruitment of various immune cell subsets into tumours.

In Chapter 6, an alternative strategy was explored to increase the density of tissue-resident–like NK cells within tumours. A protocol for *in vitro* stimulation and polarisation was developed to generate NK cells that

retained cytotoxic potential while acquiring tissue localisation markers, thus aiming to avoid the inhibitory phenotype typically induced by TGF-β in the tumour microenvironment (Lee et al. 2004; Viel et al. 2016; Zhao et al. 2019). The rationale for this line of work was that NK cells capable of localising to the tumour while maintaining cytotoxic function could be particularly valuable in pancreatic cancer immunotherapy, given the very low neoantigen load and the resultant limited and often ineffective T cell infiltration observed in PDAC. The protocol successfully generated cytotoxic NK cells co-expressing CD103 and CD49a. Upon *in vivo* transfer, these cells were found at epithelial sites, and notably within the pancreas of a mouse with chemically induced chronic pancreatitis—the most common predisposing condition for PDAC. Although these observations are based on a single mouse, and therefore provide extremely limited (if any) evidence, they raise the question of whether adoptive transfer of cytotoxic NK cells with tissue-resident traits might be considered in pre-invasive or early cancer settings, an approach that remains highly speculative and requires rigorous validation. Autologous NK cell adoptive transfer after *in vitro* expansion and stimulation has shown therapeutic potential in haematological malignancies (Torelli et al. 2022), but application to solid tumours in an advanced disease setting have proven no clinical benefit (Sakamoto et al. 2015).

Finally, in Chapter 7, following this conceptual shift from overt disease to pre-invasive stages, the role of NK and other immune populations was investigated in the early phases of pancreatic tumourigenesis using a genetically engineered mouse model. Both innate and adaptive lymphocytes were found to progressively accumulate in the pancreas of KC,

but not control, mice as disease developed. Although preliminary, these findings highlight the potential for immune surveillance even at pre-invasive stages, suggesting that immunotherapeutic interventions might also be effective before full tumour establishment.

Overall, while still acknowledging the many limitations of the studies presented in this thesis, the data presented here provide hypothesis-generating evidence supporting two important conceptual shifts for pancreatic cancer immunotherapy: (I) a shift from leveraging exclusively on $CD8^+$ T cells to potentially exploiting innate lymphocytes such as NK cells; and (II) a shift from targeting exclusively advanced disease to emphasising the importance of preventative, early-stage interventions. Future work aimed at translating these strategies into clinically applicable protocols, particularly in pre-invasive or high-risk individuals, may offer a novel avenue to improve outcomes in a malignancy whose outlook remains dismal.

SUPPLEMENTARY FIGURES

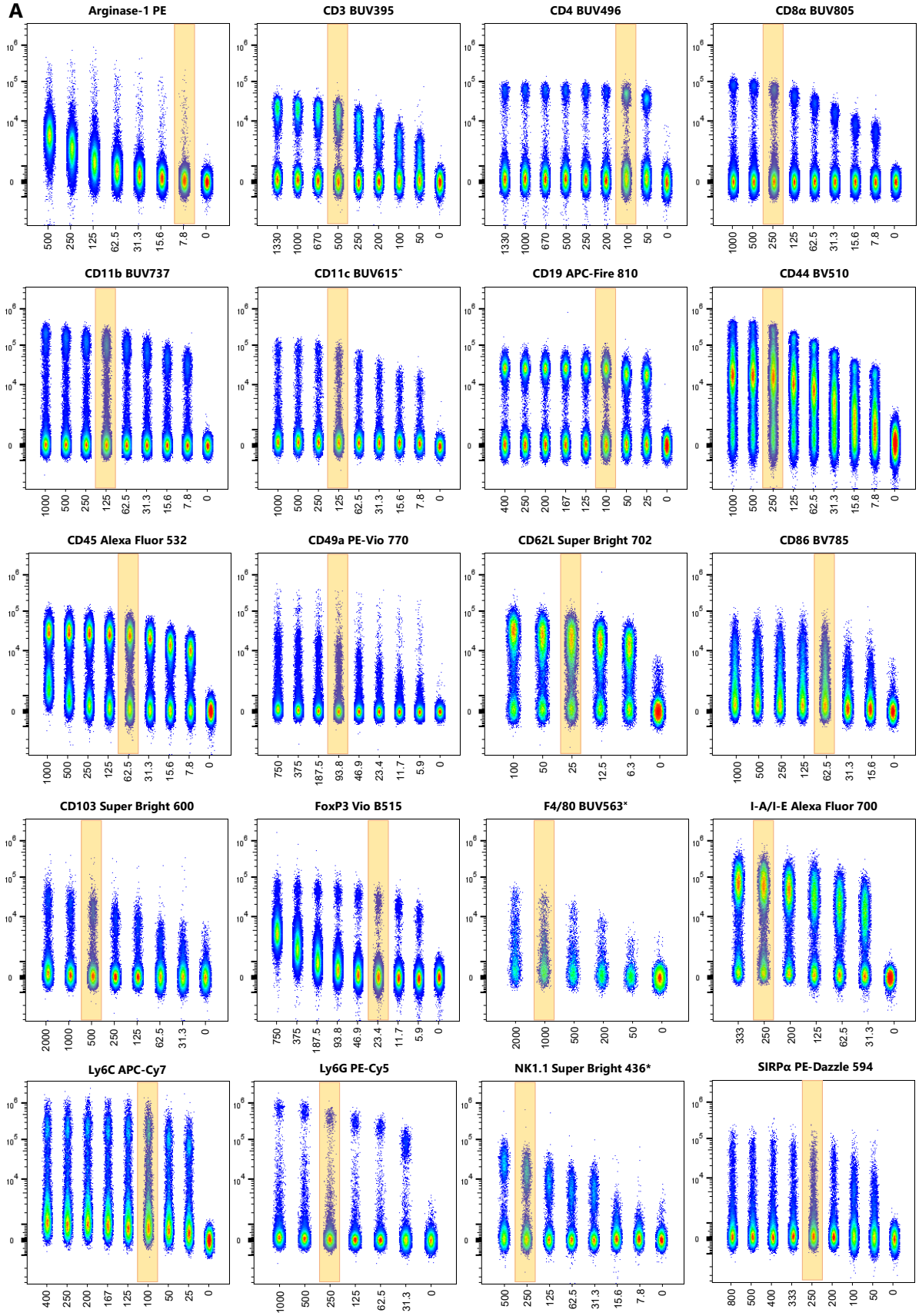

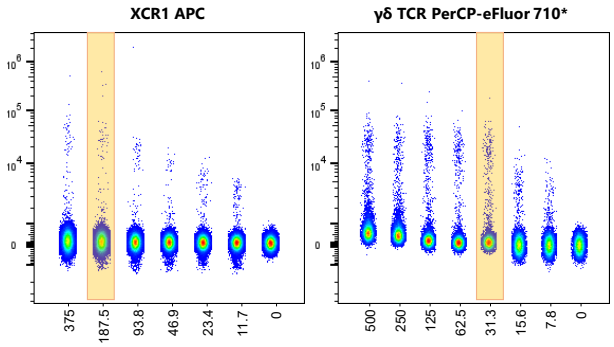

B

Reagent	Arginase-1 PE						
Concentration (ng/test)	500	250	125	62.5	31.3	15.6	7.8
Stain index	9.6	7.2	6.1	4.8	4.2	4.9	6.3
Relative stain index (%)	100.0	75.5	63.5	49.7	44.1	51.4	66.3
Reason for deviation	Higher titres cause smearing of the negative population						

Reagent	CD4 BUV496							
Concentration (ng/test)	1330	1000	670	500	250	200	100	50
Stain index	64.1	65.9	65.9	65.5	65.1	60.9	48.1	35.8
Relative stain index (%)	97.3	100.0	100.0	99.4	98.8	92.4	73.0	54.3
Reason for deviation	Comparable resolution to concentration with highest stain index							

Reagent	CD11b BUV737							
Concentration (ng/test)	1000	500	250	125	62.5	31.3	15.6	7.8
Stain index	196	181	152	134	117	86.8	57.1	41.8
Relative stain index (%)	100.0	92.3	77.6	68.4	59.7	44.3	29.1	21.3
Reason for deviation	Comparable results with 1/8 reagent							

Reagent	CD19 APC-Fire 810							
Concentration (ng/test)	400	250	200	167	125	100	50	25
Stain index	31.7	30.8	30.7	30.6	30.2	30.5	21.1	19.6
Relative stain index (%)	100.0	97.2	96.8	96.5	95.3	96.2	66.6	61.8
Reason for deviation	Nearly identical performance with 1/4 reagent							

Reagent	CD45 Alexa Fluor 532							
Concentration (ng/test)	1000	500	250	125	62.5	31.3	15.6	7.8
Stain index	12.9	19.7	24.6	26.3	26.1	22.4	16.3	12.1
Relative stain index (%)	49.0	74.9	93.5	100.0	99.2	85.2	62.0	46.0
Reason for deviation	Identical resolution compared to concentration with highest stain index							

Reagent	CD62L Super Bright 702				
Concentration (ng/test)	100	50	25.0	12.5	6.3
Stain index	27.5	21.1	17	15.1	11.6
Relative stain index (%)	100.0	76.7	61.8	54.9	42.2
Reason for deviation	Comparable results attained with lower titre				

Reagent	CD103 Super Bright 600						
Concentrations tested (ng/t	2000	1000	500	250	125	62.5	31.3
Stain index	23.5	21.4	18.5	12.9	9.4	3.6	2.6
Relative stain index (%)	100.0	91.1	78.7	54.9	40.0	15.3	11.2
Reason for deviation	Comparable results attained with lower titre						

Reagent	F4/80 BUV563				
Concentration (ng/test)	2000	1000	500	200	50
Stain index	6.23	6.81	5.68	5.36	2.68
Relative stain index (%)	91.5	100.0	83.4	78.7	39.4
Reason for deviation	NA				

Reagent	Ly6C APC-Cy7							
Concentration (ng/test)	400	250	200	166.7	125	100	50	25
Stain index	116	123	122	118	120	118	79.7	61.3
Relative stain index (%)	94.3	100.0	99.2	95.9	97.6	95.9	64.8	49.8
Reason for deviation	Identical resolution compared to concentration with highest stain index							

Reagent	NK1.1 Super Bright 436						
Concentration (ng/test)	500	250	125	62.5	31.3	15.6	7.8
Stain index	28.5	19.8	13.7	9.4	9.1	3.3	2.5
Relative stain index (%)	100.0	69.5	48.1	32.8	31.9	11.7	8.7
Reason for deviation	Lower titre provides sufficient separation						

Reagent	XCR1 APC					
Concentration (ng/test)	375	187.5	93.8	46.9	23.4	11.7
Stain index	25.6	17.4	13.4	7.04	4.3	3.5
Relative stain index (%)	100.0	68	52.3	27.5	16.7	13.8
Reason for deviation	Comparable results attained with lower titre					

Reagent	CD3 BUV395							
Concentration (ng/test)	1330	1000	670	500	250	200	100	50
Stain index	25.3	23.8	20.6	17.9	10.5	8.9	3.9	2.6
Relative stain index (%)	100.0	94.1	81.4	70.8	41.5	35.1	15.2	10.1
Reason for deviation	Identical resolution compared to concentration with highest stain index							

Reagent	CD8α BUV805							
Concentration (ng/test)	1000	500	250	125	62.5	31.3	15.6	7.8
Stain index	106	99.4	79.7	56.3	36.5	21.3	11.2	7.6
Relative stain index (%)	100.0	93.8	75.2	53.1	34.4	20.1	10.6	7.2
Reason for deviation	Comparable results with 1/4 reagent							

Reagent	CD11c BUV615							
Concentration (ng/test)	1000	500	250	125	62.5	31.3	15.6	7.8
Stain index	22.3	24.1	27.3	24.2	18.3	14.8	10.8	10.4
Relative stain index (%)	81.7	88.3	100.0	88.6	67.0	54.2	39.6	38.1
Reason for deviation	Identical resolution compared to concentration with highest stain index							

Reagent	CD44 BV510							
Concentration (ng/test)	1000	500	250	125	62.5	31.3	15.6	7.8
Stain index	8.4	8.1	7.3	5.1	3.3	2.3	2.6	3.3
Relative stain index (%)	100.0	97.3	87.5	60.3	39.8	27.6	30.7	39.9
Reason for deviation	Lower concentrations cause loss of distinction between CD44$^+$ / CD44^{lo}							

Reagent	CD49a PE-Vio770							
Concentration (ng/test)	750	375	187.5	93.8	46.9	23.4	11.7	5.9
Stain index	7.17	9.27	10.3	11.2	9.4	6.9	5.2	4.7
Relative stain index (%)	64.0	82.8	92.0	100.0	84.2	61.2	46.3	42.0
Reason for deviation	NA							

Reagent	CD86 BV785						
Concentration (ng/test)	1000	500	250	125	62.5	31.3	15.6
Stain index	5.2	5.3	5.3	5.5	5.3	4.8	4.8
Relative stain index (%)	96.1	97.8	97.8	100.0	96.5	87.5	88.6
Reason for deviation	NA						

Reagent	FoxP3 Vio B515							
Concentration (ng/test)	750	375	187.5	93.8	46.9	23.4	11.7	5.9
Stain index	11.5	18.6	27.4	35.8	36.5	31.3	22.3	14.4
Relative stain index (%)	31.5	51.0	75.1	98.1	100.0	85.8	61.1	39.5
Reason for deviation	Comparable results attained with lower titre							

Reagent	I-A/I-E Alexa Fluor 700					
Concentration (ng/test)	333	250	200	125	62.5	31.3
Stain index	52.8	47.6	39.2	33	22.5	15.8
Relative stain index (%)	100.0	90.2	74.2	62.5	42.6	29.9
Reason for deviation	Comparable results attained with lower titre					

Reagent	Ly6G PE-Cy5					
Concentration (ng/test)	1000	500	250	125	62.5	31.3
Stain index	1045	996	716	585	418	113
Relative stain index (%)	100.0	95.3	68.5	56.0	40.0	10.8
Reason for deviation	Comparable results attained with lower titre					

Reagent	SIRPα PE-Dazzle 594							
Concentration (ng/test)	800	500	400	333	250	200	100	50
Stain index	26.4	25.6	26.6	26.2	24.4	22.6	6.2	4.45
Relative stain index (%)	99.2	96.2	100.0	98.5	91.7	85.0	23.3	16.7
Reason for deviation	Identical resolution compared to concentration with highest stain index							

Reagent	γδ TCR PerCP-eFluor 710						
Concentration (ng/test)	500	250	125	62.5	31.3	15.6	7.8
Stain index	45.5	38.8	59.9	53.5	49.9	7	4.2
Relative stain index (%)	76.0	64.8	100	89.3	83.3	11.7	7.0
Reason for deviation	Comparable results attained with lower titre						

Supplementary Figure 9.1 – Reagent titration

All reagents used in the definitive panel are shown in alphanumerical order. Titrations were performed on live singlets after splenocytes from wild type C57BL/6J mice were Fc-blocked, fixed, and permeabilised, unless stated otherwise.

A. Concatenated dot plots for the visual assessment of the positive and negative populations at different concentrations are shown for each reagent. Y axis: fluorescence intensity; X axis: nanograms of reagents used to stain 10^6 cells in 100 µL of staining buffer; yellow highlight: selected concentration.

B. For each reagent, the stain index for each tested concentration is shown, alongside the relative stain index (i.e., the ratio of stain index to maximal stain index, expressed as a percentage). When a different concentration was chosen to the one resulting in the highest stain index, the reason is clarified. Selected dilution is highlighted in yellow. Blue colour scale corresponds to stain index values (lighter: lower; darker: higher). Red-to-green colour scale corresponds to relative stain index values (red: lower; green: higher).

*Titration performed on live, Fc-blocked, fixed and permeabilised liver low-density cell fraction from wild type C57BL/6J mice

ˣTitration performed on live, Fc-blocked, fixed and permeabilised splenocytes from wild type C57BL/6J mice, after pre-gating on $CD11b^+$ cells.

^Titration performed on live, Fc-blocked, fixed and permeabilised splenocytes from wild type C57BL/6J mice, after pre-gating on $I\text{-}A/I\text{-}E^+$ cells.

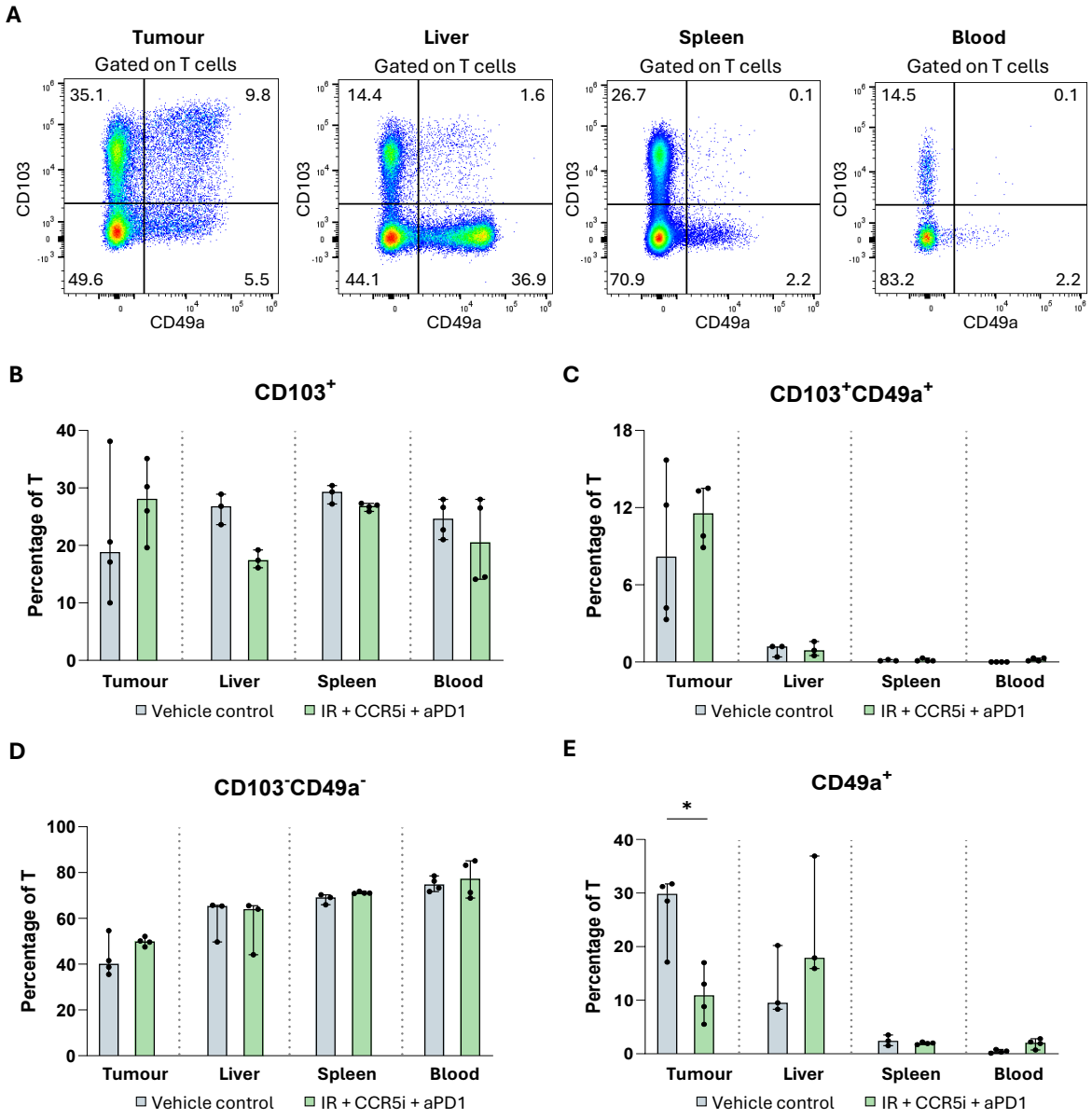
A
Tumour
Gated on T cells
35.1
9.8
49.6
5.5
Liver
Gated on T cells
14.4
1.6
44.1
36.9
Spleen
Gated on T cells
26.7
0.1
70.9
2.2
Blood
Gated on T cells
14.5
0.1
83.2
2.2
CD103
CD49a
B
CD103+
Percentage of T
Tumour
Liver
Spleen
Blood
Vehicle control
IR + CCR5i + aPD1
C
CD103+CD49a+
Percentage of T
Tumour
Liver
Spleen
Blood
Vehicle control
IR + CCR5i + aPD1
D
CD103-CD49a-
Percentage of T
Tumour
Liver
Spleen
Blood
Vehicle control
IR + CCR5i + aPD1
E
CD49a+
*
Percentage of T
Tumour
Liver
Spleen
Blood
Vehicle control
IR + CCR5i + aPD1
F
Tumour
Liver
Spleen
Blood
Vehicle control
IR + CCR5i + aPD1
CD103+CD49a+
CD49a+
CD103+
CD103-CD49a-

Supplementary Figure 9.2 – CD103 and CD49a expression on T cells

A. Dot plots from one representative treated mouse outlining the gating strategy used to define the four subsets of T cells ($CD3^+NK1.1^-$) in the four examined districts.

B. Percentage of tumour, liver, spleen, and circulating $CD103^+$ T cells (as a fraction of total T cells). Median and range shown.

C. Percentage of tumour, liver, spleen, and circulating $CD103^+CD49a^+$ T cells (as a fraction of total T cells). Median and range shown.

D. Percentage of tumour, liver, spleen, and circulating $CD103^-CD49a^-$ T cells (as a fraction of total T cells). Median and range shown.

E. Percentage of tumour, liver, spleen, and circulating $CD49a^+$ T cells (as a fraction of total T cells). Median and range shown.

F. Composition of the T cell gate, based on median expression of CD103 and CD49a in control (upper row) or treated animals (lower row).

All comparisons for groups with $n > 3$ were performed using a two-tailed Mann–Whitney test; *$p<0.05$.

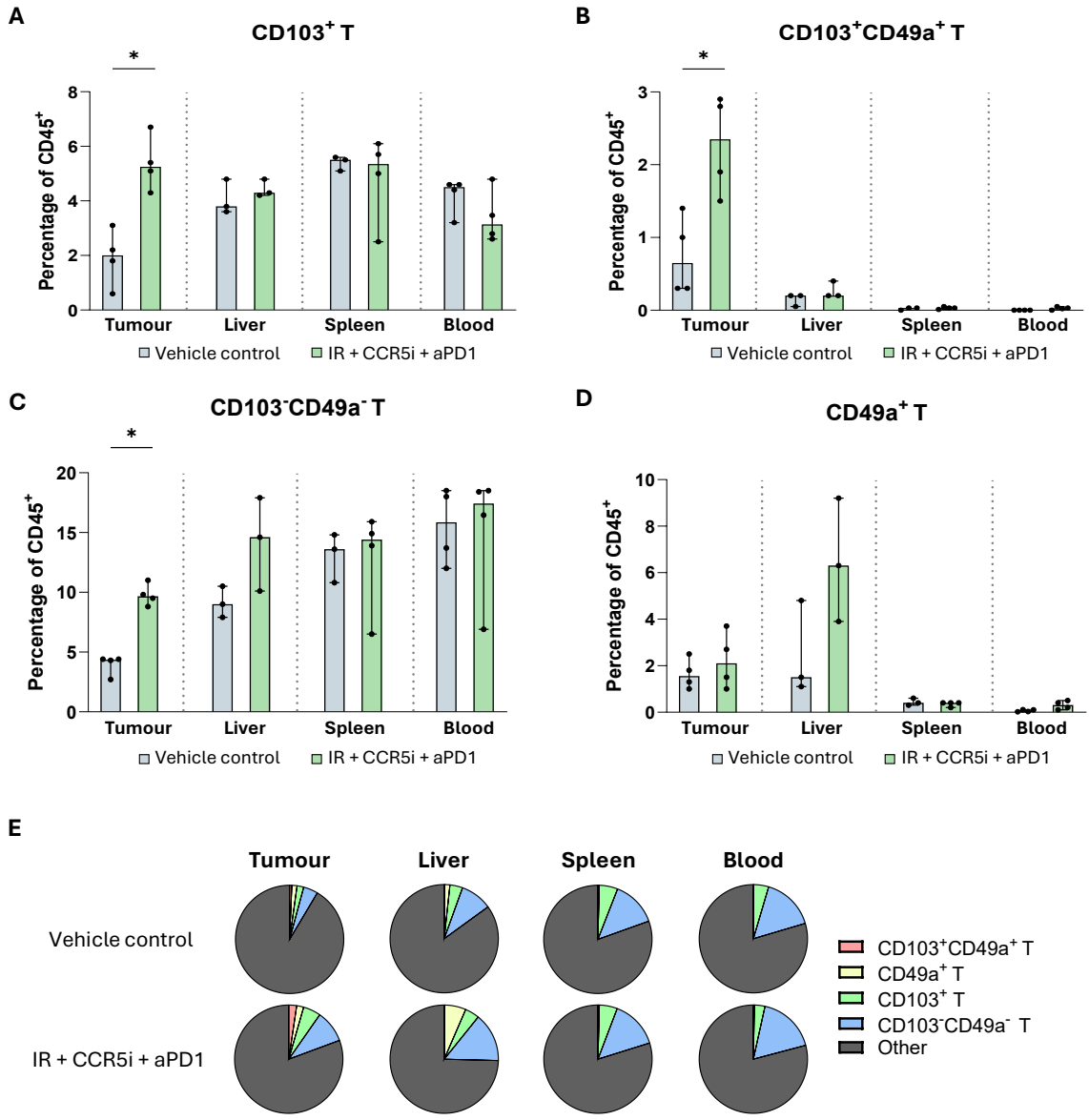

Supplementary Figure 9.3 – CD103 and CD49a expression on T cells relative to the overall immune cell infiltrate

A. Percentage of tumour, liver, spleen, and circulating $CD103^+$ T cells (as a fraction of $CD45^+$ cells). Median and range shown.

B. Percentage of tumour, liver, spleen, and circulating $CD103^+CD49a^+$ T cells (as a fraction of $CD45^+$ cells). Median and range shown.

C. Percentage of tumour, liver, spleen, and circulating $CD103^-CD49a^-$ T cells (as a fraction of $CD45^+$ cells). Median and range shown.

D. Percentage of tumour, liver, spleen, and circulating $CD49a^+$ T cells (as a fraction of $CD45^+$ cells). Median and range shown.

E. Composition of the $CD45^+$ gate, based on median expression of CD103 and CD49a on T cells, in control (upper row) or treated animals (lower row).

All comparisons ($n > 3$) were performed using a two-tailed Mann–Whitney test; *$p<0.05$.

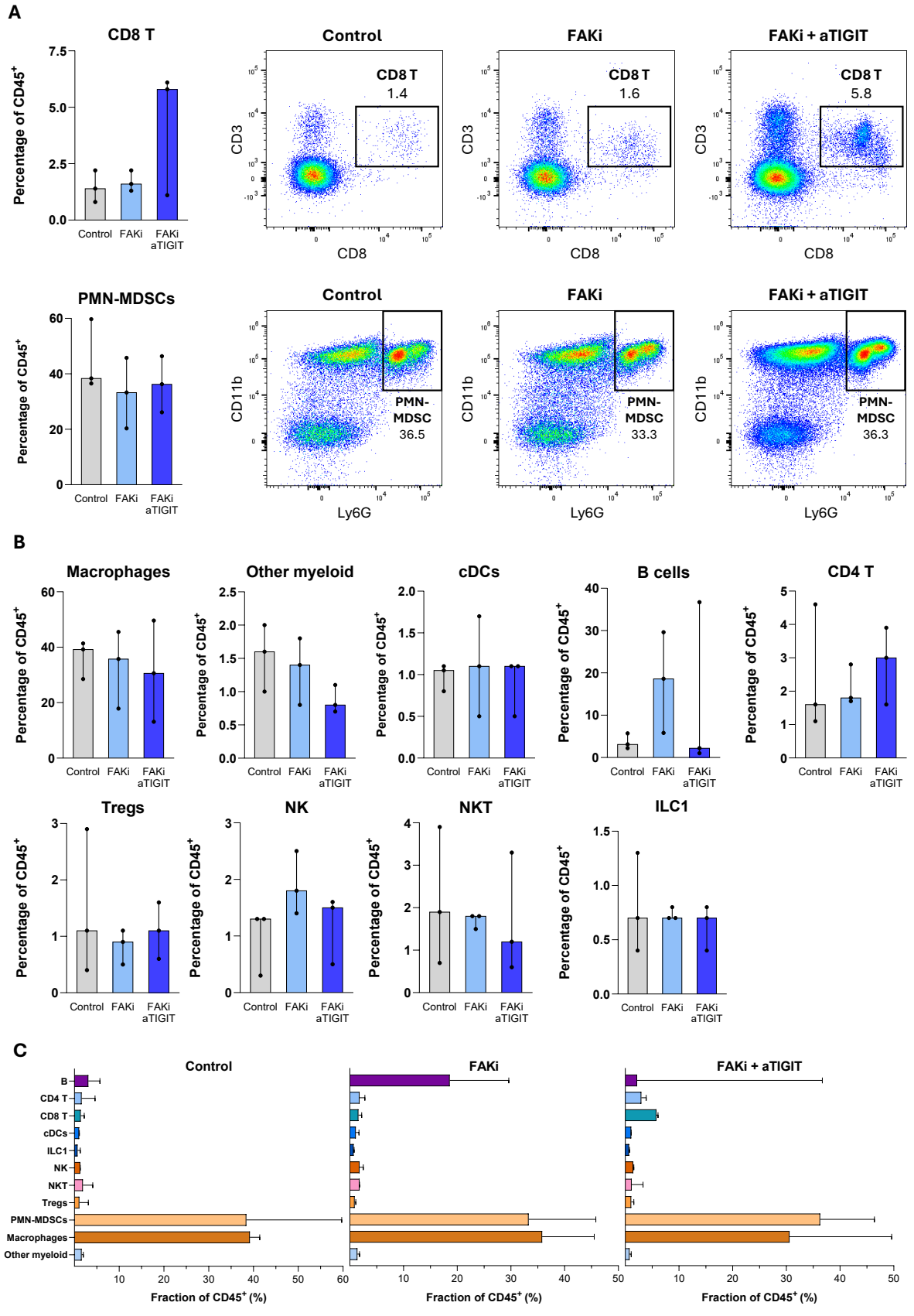
A
CD8 T
Percentage of CD45+
Control
FAKi
FAKi aTIGIT
Control
FAKi
FAKi + aTIGIT
CD8 T 1.4
CD8 T 1.6
CD8 T 5.8
CD3
CD8
PMN-MDSCs
CD11b
Ly6G
PMN-MDSC 36.5
PMN-MDSC 33.3
PMN-MDSC 36.3
B
Macrophages
Other myeloid
cDCs
B cells
CD4 T
Tregs
NK
NKT
ILC1
C
B
CD4 T
CD8 T
cDCs
ILC1
NK
NKT
Tregs
PMN-MDSCs
Macrophages
Other myeloid
Fraction of CD45+ (%)

Supplementary Figure 9.4 – Relative abundance of major tumour leukocyte populations

A. Left: percentage of $CD8^+$ T cells (top) and PMN-MDSCs (bottom) in the TME. Right: representative dot plots showing the percentage of $CD8^+$ T cells and PMN-MDSCs within total $CD45^+$ cells.

B. Relative abundance of each immune cell population in the tumour of mice in the control, FAKi, and FAKi + aTIGIT groups of the immune profiling cohort (*n* = 3 per group). Median and range shown.

C. Relative abundance of each immune cell population in (B), grouped by treatment for ease of comparison. Median and range shown.

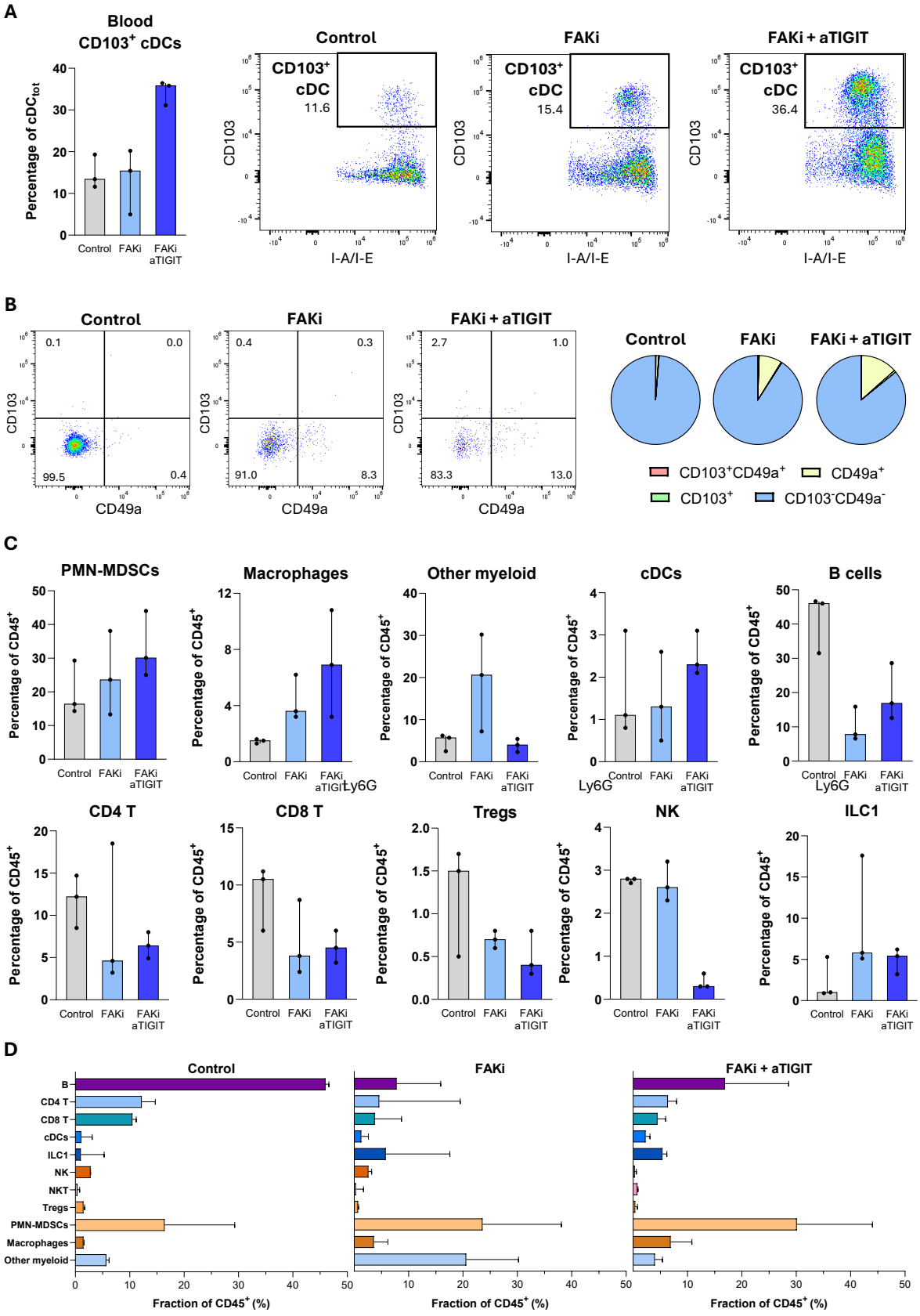
A
Blood
CD103+ cDCs
Percentage of cDCtot
Control
FAKi
FAKi aTIGIT
Control
FAKi
FAKi + aTIGIT
CD103+ cDC
11.6
15.4
36.4
CD103
I-A/I-E
B
Control
FAKi
FAKi + aTIGIT
0.1
0.0
99.5
0.4
0.4
0.3
91.0
8.3
2.7
1.0
83.3
13.0
CD103
CD49a
CD103+CD49a+
CD49a+
CD103+
CD103-CD49a-
C
PMN-MDSCs
Macrophages
Other myeloid
cDCs
B cells
CD4 T
CD8 T
Tregs
NK
ILC1
Percentage of CD45+
Ly6G
D
Control
FAKi
FAKi + aTIGIT
B
CD4 T
CD8 T
cDCs
ILC1
NK
NKT
Tregs
PMN-MDSCs
Macrophages
Other myeloid
Fraction of CD45+ (%)

Supplementary Figure 9.5 – Relative abundance of major blood leukocyte populations

A. Left: percentage of $CD103^+$ cDCs in the blood. Right: representative dot plots showing the percentage of $CD103^+$ cDCs within total blood cDCs.

B. Left: representative dot plots showing the percentage of circulating NK cells expressing CD103 and/or CD49a. Right: Composition of the NK cell gate, based on median expression of CD103 and CD49a.

C. Relative abundance of each immune cell population in the blood of mice in the control, FAKi, and FAKi + aTIGIT groups of the immune profiling cohort (*n* = 3 per group). Median and range shown.

D. Relative abundance of each immune cell population in (C), grouped by treatment for ease of comparison. Median and range shown.

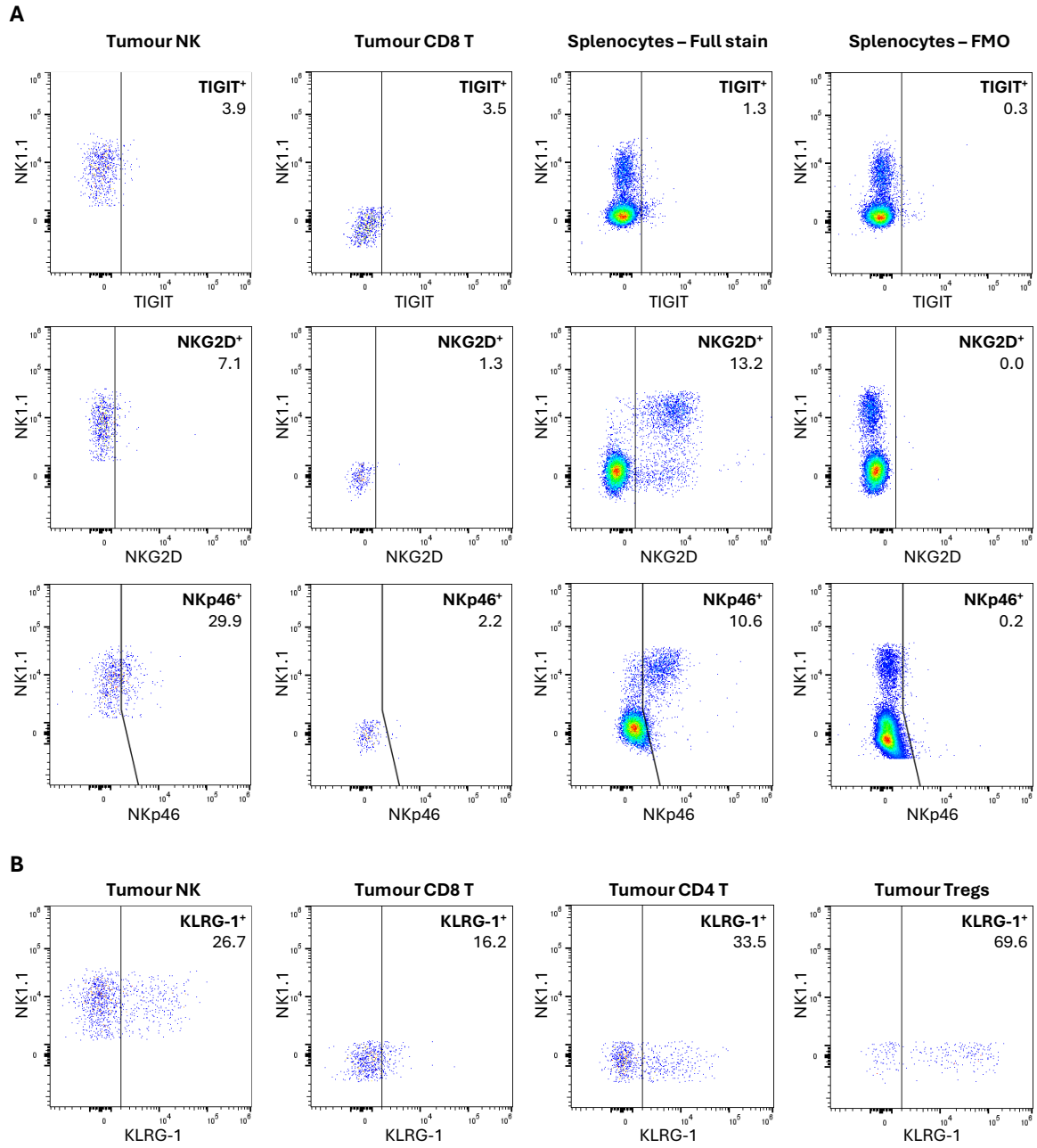

Supplementary Figure 9.6 – Threshold definition for gates in Chapter 5

A. Representative dot plots of tumour NK and CD8$^+$ T cells, and splenocytes from tumour-bearing mice cultured for 18 hours with IL-15 10 ng/mL. Splenocytes were stained with all dyes in the panel (Full stain) or all dyes except the one for which a threshold needed outlining (FMO controls). For splenocytes, pre-gating on NK1.1$^+$ or CD3$^+$ cells using a Boolean "OR" gate was applied to display only T and NK cells.

B. For other markers in the panel (e.g., KLRG-1), FMO controls were not needed, as separation became apparent with side-by-side comparisons of different subsets of marker-expressing cells (e.g., NK cells, CD8 and CD4$^+$ T cells, and Tregs).

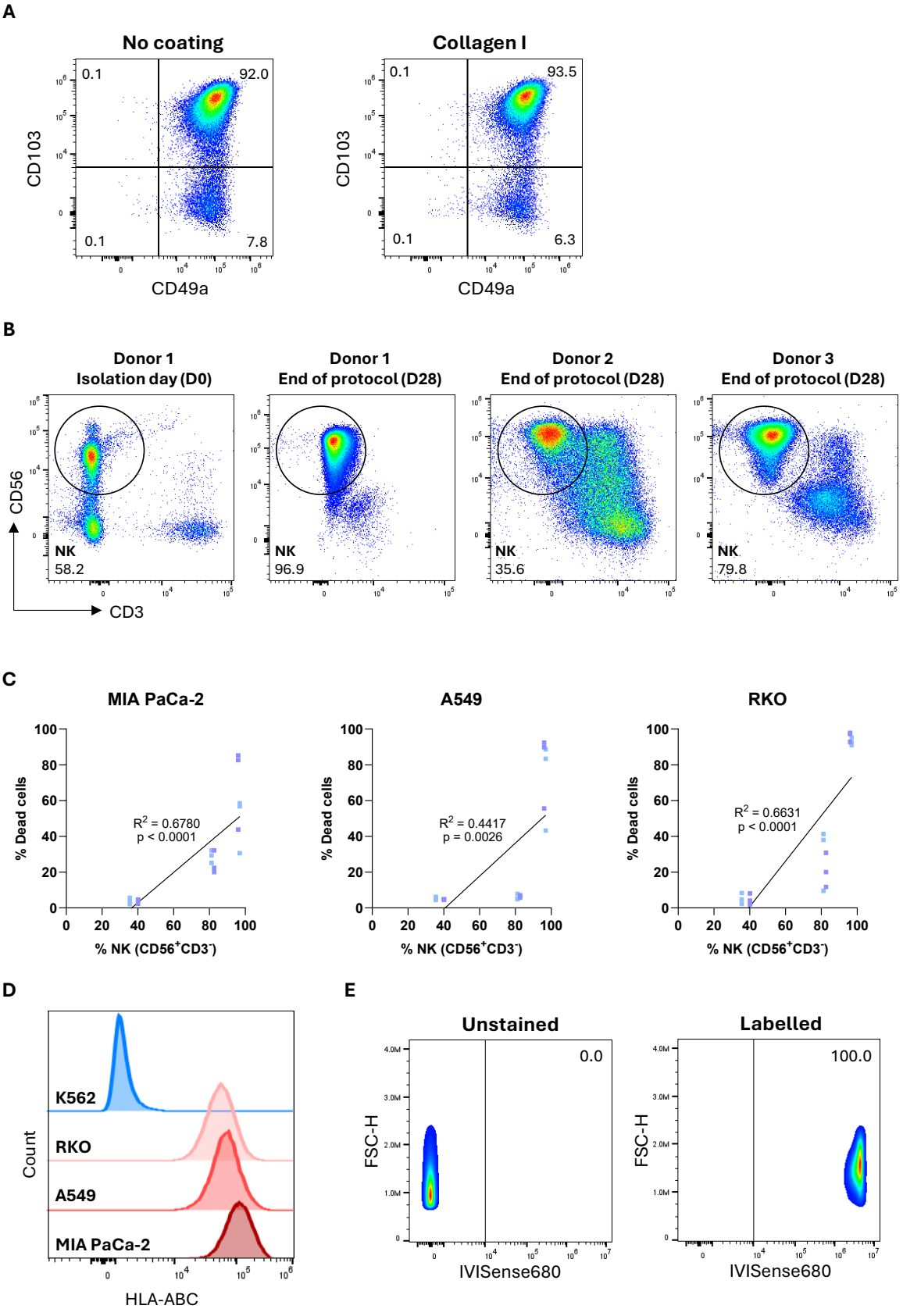
A
No coating
Collagen I
CD103
CD49a
0.1
92.0
0.1
7.8
0.1
93.5
0.1
6.3
B
Donor 1
Isolation day (D0)
Donor 1
End of protocol (D28)
Donor 2
End of protocol (D28)
Donor 3
End of protocol (D28)
CD56
CD3
NK
58.2
NK
96.9
NK
35.6
NK
79.8
C
MIA PaCa-2
A549
RKO
% Dead cells
% NK (CD56+CD3-)
R2 = 0.6780
p < 0.0001
R2 = 0.4417
p = 0.0026
R2 = 0.6631
p < 0.0001
D
K562
RKO
A549
MIA PaCa-2
Count
HLA-ABC
E
Unstained
Labelled
FSC-H
IVISense680
0.0
100.0

Supplementary Figure 9.7 – Generating $CD103^+CD49a^+$ NK cells from PBMCs *in vitro:* factors influencing phenotype and cytotoxicity and *in vivo* monitoring

A. Representative dot plots showing NK cells from one donor (*n* = 1) cultured in an uncoated (left) or collagen-coated (right) plate during the 28-day stimulation protocol.

B. Representative dot plots of the NK cell ($CD56^+CD3^-$) fraction from one donor at baseline (Day 0) and after expansion and stimulation (Day 28). NK cell fractions from two additional donors with suboptimal yield are shown on the right for comparison.

C. Correlation between the NK cell ($CD56^+CD3^-$) fraction and the percentage of dead target cells in the *in vitro* cytotoxicity assay against three solid cancer cell lines. Data from all donors (*n* = 3) and all tested E:T ratios were pooled for the IL-15 + IL-21 (indigo) and IL-15 + IL-21 + TGF-β (pale blue) conditions.

D. HLA-ABC expression in the three solid cancer cell lines compared with the leukaemia cell line K562 (*n* = 1 per cell line).

E. TGF-β–exposed NK cells stimulated as per protocol were labelled with a fluorescent cell tracking dye compatible with IVIS *in vivo* (*n* = 1) prior to injection into R2G2 mice.

BIBLIOGRAPHY

Adeegbe, Dennis O., Shengwu Liu, Maureen M. Hattersley, et al. 2018. 'BET Bromodomain Inhibition Cooperates with PD-1 Blockade to Facilitate Antitumor Response in Kras-Mutant Non–Small Cell Lung Cancer'. *Cancer Immunology Research* 6 (10): 1234–45. https://doi.org/10.1158/2326-6066.CIR-18-0077.

Aglietta, M., C. Barone, M. B. Sawyer, et al. 2014. 'A Phase I Dose Escalation Trial of Tremelimumab (CP-675,206) in Combination with Gemcitabine in Chemotherapy-Naive Patients with Metastatic Pancreatic Cancer'. *Annals of Oncology* 25 (9): 1750–55. https://doi.org/10.1093/annonc/mdu205.

Ai, Lisha, Shidai Mu, Yadan Wang, et al. 2018. 'Prognostic Role of Myeloid-Derived Suppressor Cells in Cancers: A Systematic Review and Meta-Analysis'. *BMC Cancer* 18 (1): 1220. https://doi.org/10.1186/s12885-018-5086-y.

Alba, A., R. Planas, X. Clemente, et al. 2008. 'Natural Killer Cells Are Required for Accelerated Type 1 Diabetes Driven by Interferon-β'. *Clinical and Experimental Immunology* 151 (3): 467–75. https://doi.org/10.1111/j.1365-2249.2007.03580.x.

Allan, David S. J., Ana Sofia Cerdeira, Anuisa Ranjan, et al. 2017. 'Transcriptome Analysis Reveals Similarities between Human Blood CD3− CD56bright Cells and Mouse CD127+ Innate Lymphoid Cells'. *Scientific Reports* 7 (1): 3501. https://doi.org/10.1038/s41598-017-03256-0.

Allan, David S. J., Mala Chakraborty, Giacomo C. Waller, et al. 2021. 'Systematic Improvements in Lentiviral Transduction of Primary Human Natural Killer Cells Undergoing Ex Vivo Expansion'. *Molecular Therapy. Methods & Clinical Development* 20 (March): 559–71. https://doi.org/10.1016/j.omtm.2021.01.008.

Almoguera, Concepcion, Darryl Shibata, Kathleen Forrester, John Martin, Norman Arnheim, and Manuel Perucho. 1988. 'Most Human Carcinomas of the Exocrine Pancreas Contain Mutant C-K-Ras Genes'. *Cell* 53 (4): 549–54. https://doi.org/10.1016/0092-8674(88)90571-5.

Andersen, Dana K., Murray Korc, Gloria M. Petersen, et al. 2017. 'Diabetes, Pancreatogenic Diabetes, and Pancreatic Cancer'. *Diabetes* 66 (5): 1103–10. https://doi.org/10.2337/db16-1477.

Anderson, Kristin G., Katrin Mayer-Barber, Heungsup Sung, et al. 2014. 'Intravascular Staining for Discrimination of Vascular and Tissue Leukocytes'. *Nature Protocols* 9 (1): 1. https://doi.org/10.1038/nprot.2014.005.

Ansari, Mohammed Javeed I., Alan D. Salama, Tanuja Chitnis, et al. 2003. 'The Programmed Death-1 (PD-1) Pathway Regulates Autoimmune Diabetes in Nonobese Diabetic (NOD) Mice'. *Journal of Experimental Medicine* 198 (1): 63–69. https://doi.org/10.1084/jem.20022125.

Antonia, Scott J., Augusto Villegas, Davey Daniel, et al. 2017. 'Durvalumab after Chemoradiotherapy in Stage III Non-Small-Cell Lung Cancer'. *The New England Journal of Medicine* 377 (20): 1919–29. https://doi.org/10.1056/NEJMoa1709937.

Appasamy, P. M., T. W. Kenniston, C. S. Brissette-Storkus, and W. H. Chambers. 1996. 'NKR-P1dim/TCR Alpha Beta + T Cells and Natural Killer Cells Share Expression of NKR-P1A and NKR-P1D'. *Natural Immunity* 15 (5): 259–68.

Arase, Hisashi, Takashi Saito, Joseph H. Phillips, and Lewis L. Lanier. 2001. 'Cutting Edge: The Mouse NK Cell-Associated Antigen Recognized by DX5 Moncoclonal Antibody Is CD49b (A2 Integrin, Very Late Antigen-2)1'. *The Journal of Immunology* 167 (3): 1141–44. https://doi.org/10.4049/jimmunol.167.3.1141.

Arya, Shahrzad, Seyed Amir Sanatkar, Marco Ventin, et al. 2024. 'Abstract 6313: Enhancing CAR T Cell-Based Immunotherapy Outcomes in PDAC: Evaluating iC9.B7-H3 CAR T Cells in Adjuvant, Neoadjuvant, and Monotherapy Settings'. *Cancer Research* 84 (6_Supplement): 6313. https://doi.org/10.1158/1538-7445.AM2024-6313.

Azad, Abul, Su Yin Lim, Zenobia D'Costa, et al. 2017. 'PD-L1 Blockade Enhances Response of Pancreatic Ductal Adenocarcinoma to Radiotherapy'. *EMBO Molecular Medicine* 9 (2): 167–80. https://doi.org/10.15252/emmm.201606674.

Aznar, M. Angela, Charly R. Good, Julie S. Barber-Rotenberg, et al. 2025. 'Clinical and Molecular Dissection of CAR T Cell Resistance in Pancreatic Cancer'. *Cell Reports. Medicine* 6 (9): 102301. https://doi.org/10.1016/j.xcrm.2025.102301.

Banchereau, J., and R. M. Steinman. 1998. 'Dendritic Cells and the Control of Immunity'. *Nature* 392 (6673): 245–52. https://doi.org/10.1038/32588.

Banchereau, Jacques, Francine Briere, Christophe Caux, et al. 2000. 'Immunobiology of Dendritic Cells'. *Annual Review of Immunology* 18 (Volume 18, 2000): 767–811. https://doi.org/10.1146/annurev.immunol.18.1.767.

Barry, Kevin C., Joy Hsu, Miranda L. Broz, et al. 2018. 'A Natural Killer–Dendritic Cell Axis Defines Checkpoint Therapy–Responsive Tumor Microenvironments'. *Nature Medicine* 24 (8): 8. https://doi.org/10.1038/s41591-018-0085-8.

Barry, Simon T., Dmitry I. Gabrilovich, Owen J. Sansom, Andrew D. Campbell, and Jennifer P. Morton. 2023. 'Therapeutic Targeting of Tumour Myeloid Cells'. *Nature Reviews Cancer* 23 (4): 216–37. https://doi.org/10.1038/s41568-022-00546-2.

Baskin, Denis G. 2015. 'A Historical Perspective on the Identification of Cell Types in Pancreatic Islets of Langerhans by Staining and Histochemical Techniques'. *Journal of Histochemistry and Cytochemistry* 63 (8): 543–58. https://doi.org/10.1369/0022155415589119.

Beatty, Gregory L., Shabnam Eghbali, and Rebecca Kim. 2017. 'Deploying Immunotherapy in Pancreatic Cancer: Defining Mechanisms of Response and Resistance'. *American Society of Clinical Oncology Educational Book*, no. 37 (May): 267–78. https://doi.org/10.1200/EDBK_175232.

Bedoui, Sammy, Paul G. Whitney, Jason Waithman, et al. 2009. 'Cross-Presentation of Viral and Self Antigens by Skin-Derived CD103+ Dendritic Cells'. *Nature Immunology* 10 (5): 488–95. https://doi.org/10.1038/ni.1724.

Bergsbaken, Tessa, and Michael J. Bevan. 2015. 'Proinflammatory Microenvironments within the Intestine Regulate the Differentiation of Tissue-Resident CD8+ T Cells Responding to Infection'. *Nature Immunology* 16 (4): 4. https://doi.org/10.1038/ni.3108.

Bernink, Jochem H., Charlotte P. Peters, Marius Munneke, et al. 2013. 'Human Type 1 Innate Lymphoid Cells Accumulate in Inflamed Mucosal Tissues'. *Nature Immunology* 14 (3): 221–29. https://doi.org/10.1038/ni.2534.

Biegert, Greyson, Amanda Rosewell Shaw, Daisuke Morita, et al. 2025. 'Oncolytic Adeno-Immunotherapy Improves Allogeneic Adoptive HER2.CAR-NK Function against Pancreatic Ductal Adenocarcinoma'. *Molecular Therapy Oncology* 33 (2): 201006. https://doi.org/10.1016/j.omton.2025.201006.

Bolm, Louisa, Simon Cigolla, Uwe A. Wittel, et al. 2017. 'The Role of Fibroblasts in Pancreatic Cancer: Extracellular Matrix Versus Paracrine Factors'. *Translational Oncology* 10 (4): 578–88. https://doi.org/10.1016/j.tranon.2017.04.009.

Borrego, F., J. Peña, and R. Solana. 1993. 'Regulation of CD69 Expression on Human Natural Killer Cells: Differential Involvement of Protein Kinase C and Protein Tyrosine Kinases'. *European Journal of Immunology* 23 (5): 1039–43. https://doi.org/10.1002/eji.1830230509.

Bosetti, C., E. Lucenteforte, D. T. Silverman, et al. 2012. 'Cigarette Smoking and Pancreatic Cancer: An Analysis from the International Pancreatic Cancer Case-Control Consortium (Panc4)'. *Annals of Oncology: Official Journal of the European Society for Medical Oncology* 23 (7): 1880–88. https://doi.org/10.1093/annonc/mdr541.

Böttcher, Jan P., Eduardo Bonavita, Probir Chakravarty, et al. 2018. 'NK Cells Stimulate Recruitment of cDC1 into the Tumor Microenvironment Promoting Cancer Immune Control'. *Cell* 172 (5): 1022-1037.e14. https://doi.org/10.1016/j.cell.2018.01.004.

Bottino, Cristina, Roberta Castriconi, Daniela Pende, et al. 2003. 'Identification of PVR (CD155) and Nectin-2 (CD112) as Cell Surface Ligands for the Human DNAM-1 (CD226) Activating Molecule'. *Journal of Experimental Medicine* 198 (4): 557–67. https://doi.org/10.1084/jem.20030788.

Boyman, Onur, Hans Peter Hefti, Curdin Conrad, Brian J. Nickoloff, Mark Suter, and Frank O. Nestle. 2004. 'Spontaneous Development of Psoriasis in a New Animal Model Shows an Essential Role for Resident T Cells and Tumor Necrosis Factor-Alpha'. *The Journal of Experimental Medicine* 199 (5): 731–36. https://doi.org/10.1084/jem.20031482.

Brahmer, Julie R., Scott S. Tykodi, Laura Q. M. Chow, et al. 2012. 'Safety and Activity of Anti–PD-L1 Antibody in Patients with Advanced Cancer'. *New England Journal of Medicine* 366 (26): 2455–65. https://doi.org/10.1056/NEJMoa1200694.

Brauner, Hanna, Marjet Elemans, Sara Lemos, et al. 2010. 'Distinct Phenotype and Function of NK Cells in the Pancreas of Nonobese Diabetic Mice'. *The Journal of Immunology* 184 (5): 2272–80. https://doi.org/10.4049/jimmunol.0804358.

Bronte, Vincenzo, Sven Brandau, Shu-Hsia Chen, et al. 2016. 'Recommendations for Myeloid-Derived Suppressor Cell Nomenclature and Characterization Standards'. *Nature Communications* 7 (1): 1. https://doi.org/10.1038/ncomms12150.

Brownlie, Demi, Marlena Scharenberg, Jeff E. Mold, et al. 2021. 'Expansions of Adaptive-like NK Cells with a Tissue-Resident Phenotype in Human Lung and Blood'. *Proceedings of the National Academy of Sciences* 118 (11): e2016580118. https://doi.org/10.1073/pnas.2016580118.

Burg, Nicole von, Stéphane Chappaz, Anne Baerenwaldt, et al. 2014. 'Activated Group 3 Innate Lymphoid Cells Promote T-Cell–Mediated Immune Responses'. *Proceedings of the National Academy of Sciences* 111 (35): 12835–40. https://doi.org/10.1073/pnas.1406908111.

Burris, H. A., M. J. Moore, J. Andersen, et al. 1997. 'Improvements in Survival and Clinical Benefit with Gemcitabine as First-Line Therapy for Patients with Advanced Pancreas Cancer: A

Randomized Trial'. *Journal of Clinical Oncology: Official Journal of the American Society of Clinical Oncology* 15 (6): 2403–13. https://doi.org/10.1200/JCO.1997.15.6.2403.

Buus, Terkild Brink, Mia Hamilton Jee, and Niels Ødum. 2019. 'OMIP-057: Mouse Γδ T-Cell Development Characterized by a 14 Color Flow Cytometry Panel'. *Cytometry Part A* 95 (7): 726–29. https://doi.org/10.1002/cyto.a.23754.

Callery, Mark P., Kenneth J. Chang, Elliot K. Fishman, Mark S. Talamonti, L. William Traverso, and David C. Linehan. 2009. 'Pretreatment Assessment of Resectable and Borderline Resectable Pancreatic Cancer: Expert Consensus Statement'. *Annals of Surgical Oncology* 16 (7): 1727–33. https://doi.org/10.1245/s10434-009-0408-6.

Camerlingo, Claudia. 2022. 'Prognostic Value of Regulator T Cells in Patients with Pancreatic Cancer: A Systematic Review and Meta-Analysis'. *European Review*, April 29. https://www.europeanreview.org/article/28622.

Canel, Marta, David Taggart, Andrew H. Sims, David W. Lonergan, Irene C. Waizenegger, and Alan Serrels. 2020. 'T-Cell Co-Stimulation in Combination with Targeting FAK Drives Enhanced Anti-Tumor Immunity'. *eLife* 9 (January): e48092. https://doi.org/10.7554/eLife.48092.

Carrega, Paolo, Barbara Morandi, Roberta Costa, et al. 2008. 'Natural Killer Cells Infiltrating Human Nonsmall-Cell Lung Cancer Are Enriched in CD56 Bright CD16(-) Cells and Display an Impaired Capability to Kill Tumor Cells'. *Cancer* 112 (4): 863–75. https://doi.org/10.1002/cncr.23239.

Casanova-Acebes, María, Erica Dalla, Andrew M. Leader, et al. 2021. 'Tissue-Resident Macrophages Provide a pro-Tumorigenic Niche to Early NSCLC Cells'. *Nature* 595 (7868): 578–84. https://doi.org/10.1038/s41586-021-03651-8.

Casbon, Amy-Jo, Damien Reynaud, Chanhyuk Park, et al. 2015. 'Invasive Breast Cancer Reprograms Early Myeloid Differentiation in the Bone Marrow to Generate Immunosuppressive Neutrophils'. *Proceedings of the National Academy of Sciences* 112 (6): E566–75. https://doi.org/10.1073/pnas.1424927112.

Cepek, Karyn L., Sunil K. Shaw, Christina M. Parker, et al. 1994. 'Adhesion between Epithelial Cells and T Lymphocytes Mediated by E-Cadherin and the αEβ7 Integrin'. *Nature* 372 (6502): 190–93. https://doi.org/10.1038/372190a0.

Chaturvedi, Pallavi, Daniele M. Gilkes, Naoharu Takano, and Gregg L. Semenza. 2014. 'Hypoxia-Inducible Factor-Dependent Signaling between Triple-Negative Breast Cancer Cells and Mesenchymal Stem Cells Promotes Macrophage Recruitment'. *Proceedings of the National Academy of Sciences* 111 (20): E2120–29. https://doi.org/10.1073/pnas.1406655111.

Chen, Daniel S., and Ira Mellman. 2017. 'Elements of Cancer Immunity and the Cancer–Immune Set Point'. *Nature* 541 (7637): 7637. https://doi.org/10.1038/nature21349.

Chen, Jichun, and David E. Harrison. 2002. 'Quantitative Trait Loci Regulating Relative Lymphocyte Proportions in Mouse Peripheral Blood'. *Blood* 99 (2): 561–66. https://doi.org/10.1182/blood.V99.2.561.

Cho, Byoung Chul, Delvys Rodriguez Abreu, Maen Hussein, et al. 2022. 'Tiragolumab plus Atezolizumab versus Placebo plus Atezolizumab as a First-Line Treatment for PD-L1-Selected Non-Small-Cell Lung Cancer (CITYSCAPE): Primary and Follow-up Analyses of a Randomised, Double-Blind, Phase 2 Study'. *The Lancet Oncology* 23 (6): 781–92. https://doi.org/10.1016/S1470-2045(22)00226-1.

Clark, Carolyn E., Sunil R. Hingorani, Rosemarie Mick, Chelsea Combs, David A. Tuveson, and Robert H. Vonderheide. 2007. 'Dynamics of the Immune Reaction to Pancreatic Cancer from Inception to Invasion'. *Cancer Research* 67 (19): 9518–27. https://doi.org/10.1158/0008-5472.CAN-07-0175.

Clarke, S. R., M. Barnden, C. Kurts, F. R. Carbone, J. F. Miller, and W. R. Heath. 2000. 'Characterization of the Ovalbumin-Specific TCR Transgenic Line OT-I: MHC Elements for Positive and Negative Selection'. *Immunology and Cell Biology* 78 (2): 110–17. https://doi.org/10.1046/j.1440-1711.2000.00889.x.

Colamartino, Aurelien B. L., William Lemieux, Panojot Bifsha, et al. 2019. 'Efficient and Robust NK-Cell Transduction With Baboon Envelope Pseudotyped Lentivector'. *Frontiers in Immunology* 10: 2873. https://doi.org/10.3389/fimmu.2019.02873.

Colonna, Marco. 2018. 'Innate Lymphoid Cells: Diversity, Plasticity and Unique Functions in Immunity'. *Immunity* 48 (6): 1104–17. https://doi.org/10.1016/j.immuni.2018.05.013.

Conroy, T., P. Pfeiffer, V. Vilgrain, et al. 2023. 'Pancreatic Cancer: ESMO Clinical Practice Guideline for Diagnosis, Treatment and Follow-Up☆'. *Annals of Oncology* 34 (11): 987–1002. https://doi.org/10.1016/j.annonc.2023.08.009.

Conroy, Thierry, Françoise Desseigne, Marc Ychou, et al. 2011. 'FOLFIRINOX versus Gemcitabine for Metastatic Pancreatic Cancer'. *New England Journal of Medicine* 364 (19): 1817–25. https://doi.org/10.1056/NEJMoa1011923.

Cooper, Grace E., Kristoffer Ostridge, Salim I. Khakoo, Tom M. A. Wilkinson, and Karl J. Staples. 2018. 'Human CD49a+ Lung Natural Killer Cell Cytotoxicity in Response to Influenza A Virus'. *Frontiers in Immunology* 9 (July). https://doi.org/10.3389/fimmu.2018.01671.

Cooper, Megan A., Julie M. Elliott, Peter A. Keyel, Liping Yang, Javier A. Carrero, and Wayne M. Yokoyama. 2009. 'Cytokine-Induced Memory-like Natural Killer Cells'. *Proceedings of the National Academy of Sciences of the United States of America* 106 (6): 1915–19. https://doi.org/10.1073/pnas.0813192106.

Cooper, Megan A., Todd A. Fehniger, Sarah C. Turner, et al. 2001. 'Human Natural Killer Cells: A Unique Innate Immunoregulatory Role for the CD56bright Subset'. *Blood* 97 (10): 3146–51. https://doi.org/10.1182/blood.V97.10.3146.

Cortez, Victor, Michelle Robinette, and Marco Colonna. 2015. 'Innate Lymphoid Cells: New Insights into Function and Development'. *Current Opinion in Immunology* 32 (February): 71–77. https://doi.org/10.1016/j.coi.2015.01.004.

Cortez, Victor S., Luisa Cervantes-Barragan, Michelle L. Robinette, et al. 2016. 'Transforming Growth Factor-β Signaling Guides the Differentiation of Innate Lymphoid Cells in Salivary Glands'. *Immunity* 44 (5): 1127–39. https://doi.org/10.1016/j.immuni.2016.03.007.

Cortez, Victor S., Tyler K. Ulland, Luisa Cervantes-Barragan, et al. 2017. 'SMAD4 Impedes the Conversion of NK Cells into ILC1-like Cells by Curtailing Non-Canonical TGF-β Signaling'. *Nature Immunology* 18 (9): 995–1003. https://doi.org/10.1038/ni.3809.

Cossarizza, Andrea, Hyun-Dong Chang, Andreas Radbruch, et al. 2021. 'Guidelines for the Use of Flow Cytometry and Cell Sorting in Immunological Studies (Third Edition)'. *European Journal of Immunology* 51 (12): 2708–3145. https://doi.org/10.1002/eji.202170126.

Croy, B. A., P. Gambel, J. Rossant, and T. G. Wegmann. 1985. 'Characterization of Murine Decidual Natural Killer (NK) Cells and Their Relevance to the Success of Pregnancy'. *Cellular Immunology* 93 (2): 315–26. https://doi.org/10.1016/0008-8749(85)90137-6.

Cui, Kele, Shouxin Hu, Yanfang Zha, et al. 2025. 'CD49a+ NK Cells Promote Esophageal Cancer Development by Inducing MDSCs Infiltration via GM-CSF'. *British Journal of Cancer* 133 (3): 295–304. https://doi.org/10.1038/s41416-025-03065-7.

Dai, Zhenyu, Zheng Zhu, Zhiyao Li, et al. 2025. 'Off-the-Shelf Invariant NKT Cells Expressing Anti-PSCA CAR and IL-15 Promote Pancreatic Cancer Regression in Mice'. *The Journal of Clinical Investigation* 135 (8). https://doi.org/10.1172/JCI179014.

Daussy, Cécile, Fabrice Faure, Katia Mayol, et al. 2014. 'T-Bet and Eomes Instruct the Development of Two Distinct Natural Killer Cell Lineages in the Liver and in the Bone Marrow'. *Journal of Experimental Medicine* 211 (3): 563–77. https://doi.org/10.1084/jem.20131560.

Davidson, Catherine, David Taggart, Andrew H. Sims, David W. Lonergan, Marta Canel, and Alan Serrels. 2022. 'FAK Promotes Stromal PD-L2 Expression Associated with Poor Survival in Pancreatic Cancer'. *British Journal of Cancer* 127 (10): 1893–905. https://doi.org/10.1038/s41416-022-01966-5.

De Rosa, Stephen C., Leonard A. Herzenberg, Leonore A. Herzenberg, and Mario Roederer. 2001. '11-Color, 13-Parameter Flow Cytometry: Identification of Human Naive T Cells by Phenotype, Function, and T-Cell Receptor Diversity'. *Nature Medicine* 7 (2): 245–48. https://doi.org/10.1038/84701.

Dean, Isaac, Colin Y. C. Lee, Zewen K. Tuong, et al. 2024. 'Rapid Functional Impairment of Natural Killer Cells Following Tumor Entry Limits Anti-Tumor Immunity'. *Nature Communications* 15 (1): 683. https://doi.org/10.1038/s41467-024-44789-z.

Demaria, Sandra, Encouse B. Golden, and Silvia C. Formenti. 2015. 'Role of Local Radiation Therapy in Cancer Immunotherapy'. *JAMA Oncology* 1 (9): 1325–32. https://doi.org/10.1001/jamaoncol.2015.2756.

DeNardo, David G., and Brian Ruffell. 2019. 'Macrophages as Regulators of Tumour Immunity and Immunotherapy'. *Nature Reviews Immunology* 19 (6): 369–82. https://doi.org/10.1038/s41577-019-0127-6.

Diefenbach, Andreas, Marco Colonna, and Shigeo Koyasu. 2014. 'Development, Differentiation, and Diversity of Innate Lymphoid Cells'. *Immunity* 41 (3): 354–65. https://doi.org/10.1016/j.immuni.2014.09.005.

DiPiazza, Anthony T., Juliane P. Hill, Barney S. Graham, and Tracy J. Ruckwardt. 2019. 'OMIP-061: 20-Color Flow Cytometry Panel for High-Dimensional Characterization of Murine Antigen-Presenting Cells'. *Cytometry Part A* 95 (12): 1226–30. https://doi.org/10.1002/cyto.a.23880.

Dogra, Pranay, Chiara Rancan, Wenji Ma, et al. 2020. 'Tissue Determinants of Human NK Cell Development, Function, and Residence'. *Cell* 180 (4): 749-763.e13. https://doi.org/10.1016/j.cell.2020.01.022.

Dolina, Joseph S., Natalija Van Braeckel-Budimir, Graham D. Thomas, and Shahram Salek-Ardakani. 2021. 'CD8+ T Cell Exhaustion in Cancer'. *Frontiers in Immunology* 12 (July). https://doi.org/10.3389/fimmu.2021.715234.

Dorner, Brigitte G., Alexander Scheffold, Michael S. Rolph, et al. 2002. 'MIP-1α, MIP-1β, RANTES, and ATAC/Lymphotactin Function Together with IFN-γ as Type 1 Cytokines'. *Proceedings of the National Academy of Sciences* 99 (9): 6181–86. https://doi.org/10.1073/pnas.092141999.

Engblom, Camilla, Christina Pfirschke, and Mikael J. Pittet. 2016. 'The Role of Myeloid Cells in Cancer Therapies'. *Nature Reviews Cancer* 16 (7): 447–62. https://doi.org/10.1038/nrc.2016.54.

Eric, Lutz, Charles J. Yeo, Keith D. Lillemoe, et al. 2011. 'A Lethally Irradiated Allogeneic Granulocyte-Macrophage Colony Stimulating Factor-Secreting Tumor Vaccine for Pancreatic Adenocarcinoma: A Phase II Trial of Safety, Efficacy, and Immune Activation'. *Annals of Surgery* 253 (2): 328. https://doi.org/10.1097/SLA.0b013e3181fd271c.

Erstad, Derek J., Mozhdeh Sojoodi, Martin S. Taylor, et al. 2018. 'Orthotopic and Heterotopic Murine Models of Pancreatic Cancer and Their Different Responses to FOLFIRINOX Chemotherapy'. *Disease Models & Mechanisms* 11 (7): dmm034793. https://doi.org/10.1242/dmm.034793.

Falconi, M., B. Eriksson, G. Kaltsas, et al. 2016. 'ENETS Consensus Guidelines Update for the Management of Patients with Functional Pancreatic Neuroendocrine Tumors and Non-Functional Pancreatic Neuroendocrine Tumors'. *Neuroendocrinology* 103 (2): 153–71. https://doi.org/10.1159/000443171.

Feig, Christine, Aarthi Gopinathan, Albrecht Neesse, Derek S. Chan, Natalie Cook, and David A. Tuveson. 2012. 'The Pancreas Cancer Microenvironment'. *Clinical Cancer Research* 18 (16): 4266–76. https://doi.org/10.1158/1078-0432.CCR-11-3114.

Fernandez, Jessica Lage, Sara Årbogen, Mohammad Javad Sadeghinia, et al. 2023. 'A Comparative Analysis of Orthotopic and Subcutaneous Pancreatic Tumour Models: Tumour Microenvironment and Drug Delivery'. *Cancers* 15 (22): 5415. https://doi.org/10.3390/cancers15225415.

Ferrer-Font, Laura, Sam J. Small, Brittany Lewer, et al. 2021. 'Panel Optimization for High-Dimensional Immunophenotyping Assays Using Full-Spectrum Flow Cytometry'. *Current Protocols* 1 (9): e222. https://doi.org/10.1002/cpz1.222.

Freed-Pastor, William A., Laurens J. Lambert, Zackery A. Ely, et al. 2021. 'The CD155/TIGIT Axis Promotes and Maintains Immune Evasion in Neoantigen-Expressing Pancreatic Cancer'. *Cancer Cell* 39 (10): 1342-1360.e14. https://doi.org/10.1016/j.ccell.2021.07.007.

Fuchs, Anja, William Vermi, Jacob S. Lee, et al. 2013. 'Intraepithelial Type 1 Innate Lymphoid Cells Are a Unique Subset of Cytokine Responsive Interferon-γ-Producing Cells'. *Immunity* 38 (4): 769–81. https://doi.org/10.1016/j.immuni.2013.02.010.

Gao, Yulong, Fernando Souza-Fonseca-Guimaraes, Tobias Bald, et al. 2017. 'Tumor Immunoevasion by the Conversion of Effector NK Cells into Type 1 Innate Lymphoid Cells'. *Nature Immunology* 18 (9): 1004–15. https://doi.org/10.1038/ni.3800.

Garcia, Patrick L., Leona N. Council, John D. Christein, et al. 2013. 'Development and Histopathological Characterization of Tumorgraft Models of Pancreatic Ductal Adenocarcinoma'. *PLOS ONE* 8 (10): e78183. https://doi.org/10.1371/journal.pone.0078183.

Gatti-Mays, Margaret E., Jason M. Redman, Renee N. Donahue, et al. 2020. 'A Phase I Trial Using a Multitargeted Recombinant Adenovirus 5 (CEA/MUC1/Brachyury)-Based Immunotherapy

Vaccine Regimen in Patients with Advanced Cancer'. *The Oncologist* 25 (6): 479-e899. https://doi.org/10.1634/theoncologist.2019-0608.

Gebhardt, Thomas, Linda M. Wakim, Liv Eidsmo, Patrick C. Reading, William R. Heath, and Francis R. Carbone. 2009. 'Memory T Cells in Nonlymphoid Tissue That Provide Enhanced Local Immunity during Infection with Herpes Simplex Virus'. *Nature Immunology* 10 (5): 524–30. https://doi.org/10.1038/ni.1718.

Genkinger, J. M., C. M. Kitahara, L. Bernstein, et al. 2015. 'Central Adiposity, Obesity during Early Adulthood, and Pancreatic Cancer Mortality in a Pooled Analysis of Cohort Studies'. *Annals of Oncology: Official Journal of the European Society for Medical Oncology* 26 (11): 2257–66. https://doi.org/10.1093/annonc/mdv355.

Genkinger, J. M., M. Wang, R. Li, et al. 2014. 'Dairy Products and Pancreatic Cancer Risk: A Pooled Analysis of 14 Cohort Studies'. *Annals of Oncology: Official Journal of the European Society for Medical Oncology* 25 (6): 1106–15. https://doi.org/10.1093/annonc/mdu019.

Giles, Josephine R., Anna-Maria Globig, Susan M. Kaech, and E. John Wherry. 2023. 'CD8+ T Cells in the Cancer-Immunity Cycle'. *Immunity* 56 (10): 2231–53. https://doi.org/10.1016/j.immuni.2023.09.005.

Gilfillan, Susan, Christopher J. Chan, Marina Cella, et al. 2008. 'DNAM-1 Promotes Activation of Cytotoxic Lymphocytes by Nonprofessional Antigen-Presenting Cells and Tumors'. *The Journal of Experimental Medicine* 205 (13): 2965–73. https://doi.org/10.1084/jem.20081752.

Go, Simei, Constantinos Demetriou, Sophie Hughes, et al. 2024. 'Tissue-Resident NK Cells Support Survival in Pancreatic Cancer through Promotion of cDC1-CD8T Activity'. *eLife* 13 (January). https://doi.org/10.7554/eLife.92672.1.

Go, Simei, Constantinos Demetriou, Giampiero Valenzano, et al. 2024. 'Tissue-Resident Natural Killer Cells Support Survival in Pancreatic Cancer through Promotion of cDC1-CD8 T Activity'. *eLife* 13 (December): RP92672. https://doi.org/10.7554/eLife.92672.

Gordon, Scott M., Julie Chaix, Levi J. Rupp, et al. 2012. 'The Transcription Factors T-Bet and Eomes Control Key Checkpoints of Natural Killer Cell Maturation'. *Immunity* 36 (1): 55–67. https://doi.org/10.1016/j.immuni.2011.11.016.

Goswami, Sangeeta, Swetha Anandhan, Deblina Raychaudhuri, and Padmanee Sharma. 2023. 'Myeloid Cell-Targeted Therapies for Solid Tumours'. *Nature Reviews Immunology* 23 (2): 106–20. https://doi.org/10.1038/s41577-022-00737-w.

Goulart, Michelle R., Konstantinos Stasinos, Rachel Elizabeth Ann Fincham, Francesca R. Delvecchio, and Hemant M. Kocher. 2021. 'T Cells in Pancreatic Cancer Stroma'. *World Journal of Gastroenterology* 27 (46): 7956–68. https://doi.org/10.3748/wjg.v27.i46.7956.

Guerin, Marion V., Veronica Finisguerra, Benoit J. Van den Eynde, Nadege Bercovici, and Alain Trautmann. 2020. 'Preclinical Murine Tumor Models: A Structural and Functional Perspective'. *eLife* 9 (January): e50740. https://doi.org/10.7554/eLife.50740.

Guermonprez, Pierre, Jenny Valladeau, Laurence Zitvogel, Clotilde Théry, and Sebastian Amigorena. 2002. 'Antigen Presentation and T Cell Stimulation by Dendritic Cells'. *Annual Review of Immunology* 20: 621–67. https://doi.org/10.1146/annurev.immunol.20.100301.064828.

Gur, Chamutal, Angel Porgador, Moran Elboim, et al. 2010. 'The Activating Receptor NKp46 Is Essential for the Development of Type 1 Diabetes'. *Nature Immunology* 11 (2): 121–28. https://doi.org/10.1038/ni.1834.

Gutierrez, Martin E., Shou-Ching Tang, John D. Powderly, et al. 2025. 'First-in-Human Phase I Open-Label Study of the Anti–TIM-3 Monoclonal Antibody INCAGN02390 in Patients with Select Advanced or Metastatic Solid Tumors'. *The Oncologist* 30 (7): oyaf144. https://doi.org/10.1093/oncolo/oyaf144.

Halfdanarson, T. R., K. G. Rabe, J. Rubin, and G. M. Petersen. 2008. 'Pancreatic Neuroendocrine Tumors (PNETs): Incidence, Prognosis and Recent Trend toward Improved Survival'. *Annals of Oncology* 19 (10): 1727–33. https://doi.org/10.1093/annonc/mdn351.

Hashemi, Elaheh, and Subramaniam Malarkannan. 2020. 'Tissue-Resident NK Cells: Development, Maturation, and Clinical Relevance'. *Cancers* 12 (6): 1553. https://doi.org/10.3390/cancers12061553.

Heiduk, Max, Anna Klimova, Charlotte Reiche, et al. 2023. 'TIGIT Expression Delineates T-Cell Populations with Distinct Functional and Prognostic Impact in Pancreatic Cancer'. *Clinical Cancer Research* 29 (14): 2638–50. https://doi.org/10.1158/1078-0432.CCR-23-0258.

Herberman, Ronald B., Myrthel E. Nunn, and David H. Lavrin. 1975. 'Natural Cytotoxic Reactivity of Mouse Lymphoid Cells against Syngeneic and Allogeneic Tumors. I. Distribution of Reactivity and Specificity'. *International Journal of Cancer* 16 (2): 216–29. https://doi.org/10.1002/ijc.2910160204.

Herbst, Roy S., Jean-Charles Soria, Marcin Kowanetz, et al. 2014. 'Predictive Correlates of Response to the Anti-PD-L1 Antibody MPDL3280A in Cancer Patients'. *Nature* 515 (7528): 563–67. https://doi.org/10.1038/nature14011.

Hildner, Kai, Brian T. Edelson, Whitney E. Purtha, et al. 2008. 'Batf3 Deficiency Reveals a Critical Role for CD8α+ Dendritic Cells in Cytotoxic T Cell Immunity'. *Science (New York, N.Y.)* 322 (5904): 1097–100. https://doi.org/10.1126/science.1164206.

Hilgers, Werner, and Scott E. Kern. 1999. 'Molecular Genetic Basis of Pancreatic Adenocarcinoma'. *Genes, Chromosomes and Cancer* 26 (1): 1–12. https://doi.org/10.1002/(SICI)1098-2264(199909)26:1%3C1::AID-GCC1%3E3.0.CO;2-X.

Hingorani, Sunil R., Emanuel F. Petricoin, Anirban Maitra, et al. 2003. 'Preinvasive and Invasive Ductal Pancreatic Cancer and Its Early Detection in the Mouse'. *Cancer Cell* 4 (6): 437–50. https://doi.org/10.1016/s1535-6108(03)00309-x.

Hingorani, Sunil R., Lifu Wang, Asha S. Multani, et al. 2005. 'Trp53R172H and KrasG12D Cooperate to Promote Chromosomal Instability and Widely Metastatic Pancreatic Ductal Adenocarcinoma in Mice'. *Cancer Cell* 7 (5): 469–83. https://doi.org/10.1016/j.ccr.2005.04.023.

Hiraoka, Nobuyoshi, Kaoru Onozato, Tomoo Kosuge, and Setsuo Hirohashi. 2006. 'Prevalence of FOXP3+ Regulatory T Cells Increases during the Progression of Pancreatic Ductal Adenocarcinoma and Its Premalignant Lesions'. *Clinical Cancer Research: An Official Journal of the American Association for Cancer Research* 12 (18): 5423–34. https://doi.org/10.1158/1078-0432.CCR-06-0369.

Hiroshima, Yukihiko, Ali Maawy, Yong Zhang, et al. 2016. 'Patient-Derived Mouse Models of Cancer Need to Be Orthotopic in Order to Evaluate Targeted Anti-Metastatic Therapy'. *Oncotarget* 7 (44): 71696–702. https://doi.org/10.18632/oncotarget.12322.

Hodi, F. Stephen, Steven J. O'Day, David F. McDermott, et al. 2010. 'Improved Survival with Ipilimumab in Patients with Metastatic Melanoma'. *The New England Journal of Medicine* 363 (8): 711–23. https://doi.org/10.1056/NEJMoa1003466.

Hoffmann, Johanna C., and Michael P. Schön. 2021. 'Integrin αE(CD103)B7 in Epithelial Cancer'. *Cancers* 13 (24): 6211. https://doi.org/10.3390/cancers13246211.

Höglund, P., J. Sundbäck, M. Y. Olsson-Alheim, et al. 1997. 'Host MHC Class I Gene Control of NK-Cell Specificity in the Mouse'. *Immunological Reviews* 155 (February): 11–28. https://doi.org/10.1111/j.1600-065x.1997.tb00936.x.

Hu, Su, Jia Yang, Junjie Shangguan, et al. 2019. 'Natural Killer Cell-Based Adoptive Transfer Immunotherapy for Pancreatic Ductal Adenocarcinoma in a KrasLSL-G12D p53LSL-R172H Pdx1-Cre Mouse Model'. *American Journal of Cancer Research* 9 (8): 1757–65.

Hu, Zhuting, Patrick A. Ott, and Catherine J. Wu. 2018. 'Towards Personalized, Tumour-Specific, Therapeutic Vaccines for Cancer'. *Nature Reviews Immunology* 18 (3): 168–82. https://doi.org/10.1038/nri.2017.131.

Huang, Lei, Lina Jansen, Yesilda Balavarca, et al. 2019. 'Resection of Pancreatic Cancer in Europe and USA: An International Large-Scale Study Highlighting Large Variations'. *Gut* 68 (1): 130–39. https://doi.org/10.1136/gutjnl-2017-314828.

Huang, Patrick, Francisco J. Rodriguez-Matos, Jonathan Qi, et al. 2025. 'Hepatic Immune Environment Differences among Common Mouse Strains in Models of MASH and Liver Cancer'. *JHEP Reports* 7 (5): 101380. https://doi.org/10.1016/j.jhepr.2025.101380.

Hudspeth, Kelly, Matteo Donadon, Matteo Cimino, et al. 2016. 'Human Liver-Resident CD56bright/CD16neg NK Cells Are Retained within Hepatic Sinusoids via the Engagement of CCR5 and CXCR6 Pathways'. *Journal of Autoimmunity*, Special Issue: Honoring the contributions of Professors Diego Vergani and Georgina Mieli-Vergani, vol. 66 (January): 40–50. https://doi.org/10.1016/j.jaut.2015.08.011.

Ilic, Milena, and Irena Ilic. 2016. 'Epidemiology of Pancreatic Cancer'. *World Journal of Gastroenterology* 22 (44): 9694. https://doi.org/10.3748/wjg.v22.i44.9694.

Jaffee, Elizabeth M., Ralph H. Hruban, Barbara Biedrzycki, et al. 2001. 'Novel Allogeneic Granulocyte-Macrophage Colony-Stimulating Factor–Secreting Tumor Vaccine for Pancreatic Cancer: A Phase I Trial of Safety and Immune Activation'. *Journal of Clinical Oncology* 19 (1): 145–56. https://doi.org/10.1200/JCO.2001.19.1.145.

Jelinek, Ivett, Joshua N. Leonard, Graeme E. Price, et al. 2011. 'TLR3-Specific Double-Stranded RNA Oligonucleotide Adjuvants Induce Dendritic Cell Cross-Presentation, CTL Responses, and Antiviral Protection'. *Journal of Immunology* (Baltimore, Md. : 1950) 186 (4): 2422–29. https://doi.org/10.4049/jimmunol.1002845.

Jenne, Dieter E., and Jürg Tschopp. 1988. 'Granzymes, a Family of Serine Proteases Released from Granules of Cytolytic T Lymphocytes upon T Cell Receptor Stimulation'. *Immunological Reviews* 103 (1): 53–71. https://doi.org/10.1111/j.1600-065X.1988.tb00749.x.

Jewett, Anahid, Xiao-Hu Gan, Laura T. Lebow, and Benjamin Bonavida. 1996. 'Differential Secretion of TNF-α and IFN-γ by Human Peripheral Blood-Derived NK Subsets and Association with Functional Maturation'. *Journal of Clinical Immunology* 16 (1): 46–54. https://doi.org/10.1007/BF01540972.

Jia, Hao, Hongmei Yang, Huaxing Xiong, and Kathy Qian Luo. 2023. 'NK Cell Exhaustion in the Tumor Microenvironment'. *Frontiers in Immunology* 14 (November). https://doi.org/10.3389/fimmu.2023.1303605.

Jiang, Hong, Samarth Hegde, Brett L. Knolhoff, et al. 2016. 'Targeting Focal Adhesion Kinase Renders Pancreatic Cancers Responsive to Checkpoint Immunotherapy'. *Nature Medicine* 22 (8): 851–60. https://doi.org/10.1038/nm.4123.

Joffre, Olivier P., Elodie Segura, Ariel Savina, and Sebastian Amigorena. 2012. 'Cross-Presentation by Dendritic Cells'. *Nature Reviews Immunology* 12 (8): 557–69. https://doi.org/10.1038/nri3254.

Joller, Nicole, Jason P. Hafler, Boel Brynedal, et al. 2011. 'Cutting Edge: TIGIT Has T Cell-Intrinsic Inhibitory Functions'. *The Journal of Immunology* 186 (3): 1338–42. https://doi.org/10.4049/jimmunol.1003081.

Joshi, Nikhil S., Weiguo Cui, Anmol Chandele, et al. 2007. 'Inflammation Directs Memory Precursor and Short-Lived Effector CD8(+) T Cell Fates via the Graded Expression of T-Bet Transcription Factor'. *Immunity* 27 (2): 281–95. https://doi.org/10.1016/j.immuni.2007.07.010.

Kamath, Suneel D., Aparna Kalyan, Sheetal Kircher, et al. 2020. 'Ipilimumab and Gemcitabine for Advanced Pancreatic Cancer: A Phase Ib Study'. *The Oncologist* 25 (5): e808–15. https://doi.org/10.1634/theoncologist.2019-0473.

Kamisawa, Terumi, Laura D. Wood, Takao Itoi, and Kyoichi Takaori. 2016. 'Pancreatic Cancer'. *Lancet (London, England)* 388 (10039): 73–85. https://doi.org/10.1016/S0140-6736(16)00141-0.

Kantoff, Philip W., Celestia S. Higano, Neal D. Shore, et al. 2010. 'Sipuleucel-T Immunotherapy for Castration-Resistant Prostate Cancer'. *New England Journal of Medicine* 363 (5): 411–22. https://doi.org/10.1056/NEJMoa1001294.

Kare, Aris J., Lisa Nichols, Ricardo Zermeno, Marina N. Raie, Spencer K. Tumbale, and Katherine W. Ferrara. 2023. 'OMIP-095: 40-Color Spectral Flow Cytometry Delineates All Major Leukocyte Populations in Murine Lymphoid Tissues'. *Cytometry Part A* 103 (11): 839–50. https://doi.org/10.1002/cyto.a.24788.

Karlhofer, Franz M., Randall K. Ribaudo, and Wayne M. Yokoyama. 1992. 'MHC Class I Alloantigen Specificity of Ly-49+ IL-2-Activated Natural Killer Cells'. *Nature* 358 (6381): 66–70. https://doi.org/10.1038/358066a0.

Karoumpalis, Ioannis, and Dimitrios K. Christodoulou. 2016. 'Cystic Lesions of the Pancreas'. *Annals of Gastroenterology* 29 (2): 155–61. https://doi.org/10.20524/aog.2016.0007.

Kastrinos, Fay, Bhramar Mukherjee, Nabihah Tayob, et al. 2009. 'The Risk of Pancreatic Cancer in Families with Lynch Syndrome'. *JAMA : The Journal of the American Medical Association* 302 (16): 1790–95. https://doi.org/10.1001/jama.2009.1529.

Kay, H. D., G. D. Bonnard, W. H. West, and R. B. Herberman. 1977. 'A Functional Comparison of Human Fc-Receptor-Bearing Lymphocytes Active in Natural Cytotoxicity and Antibody-Dependent Cellular Cytotoxicity'. *Journal of Immunology* (Baltimore, Md. : 1950) 118 (6): 2058–66.

Kersten, Kelly, Karin E. de Visser, Martine H. van Miltenburg, and Jos Jonkers. 2017. 'Genetically Engineered Mouse Models in Oncology Research and Cancer Medicine'. *EMBO Molecular Medicine* 9 (2): 137–53. https://doi.org/10.15252/emmm.201606857.

Khalaf, Natalia, and Basim Ali. 2022. 'New-Onset Diabetes as a Signpost of Early Pancreatic Cancer: The Role of Screening'. *Clinical Gastroenterology and Hepatology* 20 (9): 1927–30. https://doi.org/10.1016/j.cgh.2022.02.015.

Khaled, Yazan S., Basil J. Ammori, and Eyad Elkord. 2014. 'Increased Levels of Granulocytic Myeloid-Derived Suppressor Cells in Peripheral Blood and Tumour Tissue of Pancreatic Cancer Patients'. *Journal of Immunology Research* 2014 (January): e879897. https://doi.org/10.1155/2014/879897.

Kiemen, Ashley L., Cristina Almagro-Pérez, Valentina Matos, et al. 2024. '3D Histology Reveals That Immune Response to Pancreatic Precancers Is Heterogeneous and Depends on Global Pancreas Structure'. Preprint, bioRxiv, August 6. https://doi.org/10.1101/2024.08.03.606493.

Kiessling, R., E. Klein, H. Pross, and H. Wigzell. 1975. '"Natural" Killer Cells in the Mouse. II. Cytotoxic Cells with Specificity for Mouse Moloney Leukemia Cells. Characteristics of the Killer Cell'. *European Journal of Immunology* 5 (2): 117–21. https://doi.org/10.1002/eji.1830050209.

Kiessling, R., E. Klein, and H. Wigzell. 1975. '"Natural" Killer Cells in the Mouse. I. Cytotoxic Cells with Specificity for Mouse Moloney Leukemia Cells. Specificity and Distribution According to Genotype'. *European Journal of Immunology* 5 (2): 112–17. https://doi.org/10.1002/eji.1830050208.

Killion, Jerald J., Robert Radinsky, and Isaiah J. Fidler. 1998. *Orthotopic Models Are Necessary to Predict Therapy of Transplantable Tumors in Mice*.

Kim, Hyemin, Jin Ho Choi, Yoojoo Lim, et al. 2025. 'Artificial Intelligence–Powered Spatial Analysis of Immune Phenotypes in Resected Pancreatic Cancer'. *JAMA Surgery* 160 (8): 884–92. https://doi.org/10.1001/jamasurg.2025.1999.

Kinker, Gabriela Sarti, Glauco Akelinghton Freire Vitiello, Ariane Barros Diniz, et al. 2023. 'Mature Tertiary Lymphoid Structures Are Key Niches of Tumour-Specific Immune Responses in Pancreatic Ductal Adenocarcinomas'. Pancreas. *Gut* 72 (10): 1927–41. https://doi.org/10.1136/gutjnl-2022-328697.

Kirchhammer, Nicole, Marcel P. Trefny, Marina Natoli, et al. 2022. 'NK Cells with Tissue-Resident Traits Shape Response to Immunotherapy by Inducing Adaptive Antitumor Immunity'. *Science Translational Medicine* 14 (653): eabm9043. https://doi.org/10.1126/scitranslmed.abm9043.

Kirkegård, Jakob, Frank Viborg Mortensen, and Deirdre Cronin-Fenton. 2017. 'Chronic Pancreatitis and Pancreatic Cancer Risk: A Systematic Review and Meta-Analysis'. *The American Journal of Gastroenterology* 112 (9): 1366–72. https://doi.org/10.1038/ajg.2017.218.

Klose, Christoph S. N., Melanie Flach, Luisa Möhle, et al. 2014. 'Differentiation of Type 1 ILCs from a Common Progenitor to All Helper-like Innate Lymphoid Cell Lineages'. *Cell* 157 (2): 340–56. https://doi.org/10.1016/j.cell.2014.03.030.

Konecny, Andrew J., Peter L. Mage, Aaron J. Tyznik, Martin Prlic, and Florian Mair. 2024. 'OMIP-102: 50-Color Phenotyping of the Human Immune System with in-Depth Assessment of T Cells and Dendritic Cells'. *Cytometry. Part A: The Journal of the International Society for Analytical Cytology* 105 (6): 430–36. https://doi.org/10.1002/cyto.a.24841.

Korsse, Susanne E., Femme Harinck, Margot G. F. van Lier, et al. 2013. 'Pancreatic Cancer Risk in Peutz-Jeghers Syndrome Patients: A Large Cohort Study and Implications for Surveillance'. *Journal of Medical Genetics* 50 (1): 59–64. https://doi.org/10.1136/jmedgenet-2012-101277.

Krejs, Guenter J. 2010. 'Pancreatic Cancer: Epidemiology and Risk Factors'. *Digestive Diseases* 28 (2): 355–58. https://doi.org/10.1159/000319414.

Kroczek, Richard A., and Volker Henn. 2012. 'The Role of XCR1 and Its Ligand XCL1 in Antigen Cross-Presentation by Murine and Human Dendritic Cells'. *Frontiers in Immunology* 3 (February). https://doi.org/10.3389/fimmu.2012.00014.

Kruisbeek, A. M. 2001. 'In Vivo Depletion of CD4- and CD8-Specific T Cells'. *Current Protocols in Immunology* Chapter 4 (May): Unit 4.1. https://doi.org/10.1002/0471142735.im0401s01.

Lanier, L. L., C. Chang, and J. H. Phillips. 1994. 'Human NKR-P1A. A Disulfide-Linked Homodimer of the C-Type Lectin Superfamily Expressed by a Subset of NK and T Lymphocytes'. *Journal of Immunology (Baltimore, Md.: 1950)* 153 (6): 2417–28.

Lanier, L. L., A. M. Le, C. I. Civin, M. R. Loken, and J. H. Phillips. 1986. 'The Relationship of CD16 (Leu-11) and Leu-19 (NKH-1) Antigen Expression on Human Peripheral Blood NK Cells and Cytotoxic T Lymphocytes'. *Journal of Immunology* (Baltimore, Md. : 1950) 136 (12): 4480–86.

Lanier, Lewis L. 2005. 'NK CELL RECOGNITION'. *Annual Review of Immunology* 23 (Volume 23, 2005): 225–74. https://doi.org/10.1146/annurev.immunol.23.021704.115526.

Laskowski, Tamara J., Alexander Biederstädt, and Katayoun Rezvani. 2022. 'Natural Killer Cells in Antitumour Adoptive Cell Immunotherapy'. *Nature Reviews Cancer* 22 (10): 557–75. https://doi.org/10.1038/s41568-022-00491-0.

Le, Dung T., Vincent J. Picozzi, Andrew H. Ko, et al. 2019. 'Results from a Phase IIb, Randomized, Multicenter Study of GVAX Pancreas and CRS-207 Compared with Chemotherapy in Adults with Previously Treated Metastatic Pancreatic Adenocarcinoma (ECLIPSE Study)'. *Clinical Cancer Research* 25 (18): 5493–502. https://doi.org/10.1158/1078-0432.CCR-18-2992.

Leal, Ana S., and Karen T. Liby. 2018. 'Murine Models of Pancreatitis Leading to the Development of Pancreatic Cancer'. *Current Protocols in Pharmacology* 83 (1): e48. https://doi.org/10.1002/cpph.48.

Lee, June-Chul, Kyung-Mi Lee, Dong-Wan Kim, and Dae Seog Heo. 2004. 'Elevated TGF-B1 Secretion and Down-Modulation of NKG2D Underlies Impaired NK Cytotoxicity in Cancer Patients1'. *The Journal of Immunology* 172 (12): 7335–40. https://doi.org/10.4049/jimmunol.172.12.7335.

Lehmann, Frank Michael, Nicole von Burg, Robert Ivanek, et al. 2020. 'Microbiota-Induced Tissue Signals Regulate ILC3-Mediated Antigen Presentation'. *Nature Communications* 11 (1): 1794. https://doi.org/10.1038/s41467-020-15612-2.

Lesch, Stefanie, Viktoria Blumenberg, Stefan Stoiber, et al. 2021. 'T Cells Armed with the C-X-C Chemokine Receptor Type 6 Enhance Adoptive Cell Therapy for Pancreatic Tumours'. *Nature Biomedical Engineering* 5 (11): 1246–60. https://doi.org/10.1038/s41551-021-00737-6.

Liechti, Thomas, and Mario Roederer. 2019. 'OMIP-051 – 28-Color Flow Cytometry Panel to Characterize B Cells and Myeloid Cells'. *Cytometry. Part A : The Journal of the International Society for Analytical Cytology* 95 (2): 150–55. https://doi.org/10.1002/cyto.a.23689.

Lim, Seon Ah, Jungwon Kim, Seunghyun Jeon, et al. 2019. 'Defective Localization With Impaired Tumor Cytotoxicity Contributes to the Immune Escape of NK Cells in Pancreatic Cancer Patients'. *Frontiers in Immunology* 10 (April). https://doi.org/10.3389/fimmu.2019.00496.

Ling, Khoon-Lin, Nicolas Dulphy, Pru Bahl, et al. 2007. 'Modulation of CD103 Expression on Human Colon Carcinoma-Specific CTL'. *Journal of Immunology (Baltimore, Md.: 1950)* 178 (5): 2908–15. https://doi.org/10.4049/jimmunol.178.5.2908.

Liou, Geou-Yarh, Ligia Bastea, Alicia Fleming, et al. 2017. 'The Presence of Interleukin-13 at Pancreatic ADM/PanIN Lesions Alters Macrophage Populations and Mediates Pancreatic Tumorigenesis'. *Cell Reports* 19 (7): 1322–33. https://doi.org/10.1016/j.celrep.2017.04.052.

Liu, Lian, Wenpu Lai, Xiaoling Zhuo, Sihui Chen, Xiaodan Luo, and Huo Tan. 2024. 'Higher Frequency of Peripheral Blood CD103+CD8+ T Cells with Lower Levels of PD-1 and TIGIT Expression Related to Favorable Outcomes in Leukemia Patients'. *Frontiers in Immunology* 15 (September). https://doi.org/10.3389/fimmu.2024.1437726.

Liu, Liyuan, John V. Stokes, Wei Tan, and Stephen B. Pruett. 2022. 'An Optimized Flow Cytometry Panel for Classifying Macrophage Polarization'. *Journal of Immunological Methods* 511 (December): 113378. https://doi.org/10.1016/j.jim.2022.113378.

Liu, Yang, Yelei Guo, Zhiqiang Wu, et al. 2020. 'Anti-EGFR Chimeric Antigen Receptor-Modified T Cells in Metastatic Pancreatic Carcinoma: A Phase I Clinical Trial'. *Cytotherapy* 22 (10): 573–80. https://doi.org/10.1016/j.jcyt.2020.04.088.

Liu, Yihan, Wantao Wu, Changjing Cai, Hao Zhang, Hong Shen, and Ying Han. 2023. 'Patient-Derived Xenograft Models in Cancer Therapy: Technologies and Applications'. *Signal Transduction and Targeted Therapy* 8 (1): 1–24. https://doi.org/10.1038/s41392-023-01419-2.

Liu, Zhaoyuan, Yaqi Gu, Amanda Shin, Shuangyan Zhang, and Florent Ginhoux. 2020. 'Analysis of Myeloid Cells in Mouse Tissues with Flow Cytometry'. *STAR Protocols* 1 (1). https://doi.org/10.1016/j.xpro.2020.100029.

Ljunggren, H. G., and K. Kärre. 1990. 'In Search of the "Missing Self": MHC Molecules and NK Cell Recognition'. *Immunology Today* 11 (7): 237–44. https://doi.org/10.1016/0167-5699(90)90097-s.

Lochem, E. g. van, V. h. j. van der Velden, H. k. Wind, J. g. te Marvelde, N. a. c. Westerdaal, and J. j. m. van Dongen. 2004. 'Immunophenotypic Differentiation Patterns of Normal Hematopoiesis in Human Bone Marrow: Reference Patterns for Age-Related Changes and Disease-Induced Shifts'. *Cytometry Part B: Clinical Cytometry* 60B (1): 1–13. https://doi.org/10.1002/cyto.b.20008.

Loken, Michael R., Jeanne M. Brosnan, Bruce A. Bach, and Kenneth A. Ault. 1990. 'Establishing Optimal Lymphocyte Gates for Immunophenotyping by Flow Cytometry'. *Cytometry* 11 (4): 453–59. https://doi.org/10.1002/cyto.990110402.

Long, Eric O. 1999. 'REGULATION OF IMMUNE RESPONSES THROUGH INHIBITORY RECEPTORS'. *Annual Review of Immunology* 17 (Volume 17, 1999): 875–904. https://doi.org/10.1146/annurev.immunol.17.1.875.

Lowenfels, Albert B., Patrick Maisonneuve, Giorgio Cavallini, et al. 1993. 'Pancreatitis and the Risk of Pancreatic Cancer'. *New England Journal of Medicine* 328 (20): 1433–37. https://doi.org/10.1056/NEJM199305203282001.

Loza, Matthew J., Loris Zamai, Livio Azzoni, Emanuela Rosati, and Bice Perussia. 2002. 'Expression of Type 1 (Interferon Gamma) and Type 2 (Interleukin-13, Interleukin-5) Cytokines at Distinct Stages of Natural Killer Cell Differentiation from Progenitor Cells'. *Blood* 99 (4): 1273–81. https://doi.org/10.1182/blood.V99.4.1273.

Lunemann, Sebastian, Gloria Martrus, Hanna Goebels, et al. 2017. 'Hobit Expression by a Subset of Human Liver-Resident CD56bright Natural Killer Cells'. *Scientific Reports* 7 (1): 6676. https://doi.org/10.1038/s41598-017-06011-7.

Luri-Rey, Carlos, Álvaro Teijeira, Stefanie K. Wculek, et al. 2025. 'Cross-Priming in Cancer Immunology and Immunotherapy'. *Nature Reviews Cancer* 25 (4): 249–73. https://doi.org/10.1038/s41568-024-00785-5.

Lyman, Melissa R., Jacob T. Mitchell, Sidharth Raghavan, et al. 2025. 'Spatial Proteomics and Transcriptomics Reveal Early Immune Cell Organization in Pancreatic Intraepithelial Neoplasia'. *JCI Insight* 10 (15). https://doi.org/10.1172/jci.insight.191595.

Ma, Shoubao, Michael A. Caligiuri, and Jianhua Yu. 2022. 'A Four-Stage Model for Murine Natural Killer Cell Development in Vivo'. *Journal of Hematology & Oncology* 15 (1): 31. https://doi.org/10.1186/s13045-022-01243-1.

Mackay, Laura K., Angus T. Stock, Joel Z. Ma, et al. 2012. 'Long-Lived Epithelial Immunity by Tissue-Resident Memory T (TRM) Cells in the Absence of Persisting Local Antigen Presentation'. *Proceedings of the National Academy of Sciences* 109 (18): 7037–42. https://doi.org/10.1073/pnas.1202288109.

Mackay, Laura K., Erica Wynne-Jones, David Freestone, et al. 2015. 'T-Box Transcription Factors Combine with the Cytokines TGF-β and IL-15 to Control Tissue-Resident Memory T Cell Fate'. *Immunity* 43 (6): 1101–11. https://doi.org/10.1016/j.immuni.2015.11.008.

Malka, D., P. Hammel, F. Maire, et al. 2002. 'Risk of Pancreatic Adenocarcinoma in Chronic Pancreatitis'. Pancreatic Disease. *Gut* 51 (6): 849–52. https://doi.org/10.1136/gut.51.6.849.

Manaster, Irit, Saar Mizrahi, Debra Goldman-Wohl, et al. 2008. 'Endometrial NK Cells Are Special Immature Cells That Await Pregnancy'. *The Journal of Immunology* 181 (3): 1869–76. https://doi.org/10.4049/jimmunol.181.3.1869.

Manfredi, Sylvain, Côme Lepage, Cyril Hatem, Olivier Coatmeur, Jean Faivre, and Anne-Marie Bouvier. 2006. 'Epidemiology and Management of Liver Metastases From Colorectal Cancer'. *Annals of Surgery* 244 (2): 254. https://doi.org/10.1097/01.sla.0000217629.94941.cf.

Marcon, Francesca, Jianmin Zuo, Hayden Pearce, et al. 2020. 'NK Cells in Pancreatic Cancer Demonstrate Impaired Cytotoxicity and a Regulatory IL-10 Phenotype'. *OncoImmunology* 9 (1): 1845424. https://doi.org/10.1080/2162402X.2020.1845424.

Marquardt, Nicole, Vivien Béziat, Sanna Nyström, et al. 2015. 'Cutting Edge: Identification and Characterization of Human Intrahepatic CD49a+ NK Cells'. *The Journal of Immunology* 194 (6): 2467–71. https://doi.org/10.4049/jimmunol.1402756.

Marquardt, Nicole, Eliisa Kekäläinen, Puran Chen, et al. 2019. 'Unique Transcriptional and Protein-Expression Signature in Human Lung Tissue-Resident NK Cells'. *Nature Communications* 10 (1): 1. https://doi.org/10.1038/s41467-019-11632-9.

Masopust, D., V. Vezys, A. L. Marzo, and L. Lefrançois. 2001. 'Preferential Localization of Effector Memory Cells in Nonlymphoid Tissue'. *Science (New York, N.Y.)* 291 (5512): 2413–17. https://doi.org/10.1126/science.1058867.

Masopust, David, Daniel Choo, Vaiva Vezys, et al. 2010. 'Dynamic T Cell Migration Program Provides Resident Memory within Intestinal Epithelium'. *The Journal of Experimental Medicine* 207 (3): 553–64. https://doi.org/10.1084/jem.20090858.

Maude, Shannon L., Theodore W. Laetsch, Jochen Buechner, et al. 2018. 'Tisagenlecleucel in Children and Young Adults with B-Cell Lymphoblastic Leukemia'. *New England Journal of Medicine* 378 (5): 439–48. https://doi.org/10.1056/NEJMoa1709866.

McAllister, Florencia, Jennifer M. Bailey, Janivette Alsina, et al. 2014. 'Oncogenic Kras Activates a Hematopoietic-to-Epithelial IL-17 Signaling Axis in Preinvasive Pancreatic Neoplasia'. *Cancer Cell* 25 (5): 621–37. https://doi.org/10.1016/j.ccr.2014.03.014.

McLaughlin, Martin, Emmanuel C. Patin, Malin Pedersen, et al. 2020. 'Inflammatory Microenvironment Remodelling by Tumour Cells after Radiotherapy'. *Nature Reviews. Cancer* 20 (4): 203–17. https://doi.org/10.1038/s41568-020-0246-1.

Medvedev, A. E., A. C. Johnsen, J. Haux, et al. 1997. 'Regulation of Fas and Fas-Ligand Expression in NK Cells by Cytokines and the Involvement of Fas-Ligand in NK/LAK Cell-Mediated Cytotoxicity'. *Cytokine* 9 (6): 394–404. https://doi.org/10.1006/cyto.1996.0181.

Mele, Dalila, Greta Pessino, Giuseppe Trisolini, et al. 2022. 'Impaired Intratumoral Natural Killer Cell Function in Head and Neck Carcinoma'. *Frontiers in Immunology* 13 (October). https://doi.org/10.3389/fimmu.2022.997806.

Melisi, Davide, Antoine Hollebecque, Do-Youn Oh, et al. 2019. 'A Phase Ib Dose-Escalation and Cohort-Expansion Study of Safety and Activity of the Transforming Growth Factor (TGF) β Receptor I Kinase Inhibitor Galunisertib plus the Anti-PD-L1 Antibody Durvalumab in Metastatic Pancreatic Cancer.' *Journal of Clinical Oncology* 37 (15_suppl): 4124–4124. https://doi.org/10.1200/JCO.2019.37.15_suppl.4124.

Mi, Haoyang, Shamilene Sivagnanam, Courtney B. Betts, et al. 2022. 'Quantitative Spatial Profiling of Immune Populations in Pancreatic Ductal Adenocarcinoma Reveals Tumor Microenvironment Heterogeneity and Prognostic Biomarkers'. *Cancer Research* 82 (23): 4359–72. https://doi.org/10.1158/0008-5472.CAN-22-1190.

Minaga, Kosuke, Tomohiro Watanabe, Ken Kamata, Masatoshi Kudo, and Warren Strober. 2022. 'A Mouse Model of Acute and Chronic Pancreatitis'. *Current Protocols* 2 (4): e422. https://doi.org/10.1002/cpz1.422.

Mincham, Kyle T., and Robert J. Snelgrove. 2023. 'OMIP-086: Full Spectrum Flow Cytometry for High-Dimensional Immunophenotyping of Mouse Innate Lymphoid Cells'. *Cytometry Part A* 103 (2): 110–16. https://doi.org/10.1002/cyto.a.24702.

Mincham, Kyle T., Jacob D. Young, and Deborah H. Strickland. 2021. 'OMIP 076: High-Dimensional Immunophenotyping of Murine T-Cell, B-Cell, and Antibody Secreting Cell Subsets'. *Cytometry Part A* 99 (9): 888–92. https://doi.org/10.1002/cyto.a.24474.

Moffett, Ashley, and Francesco Colucci. 2014. 'Uterine NK Cells: Active Regulators at the Maternal-Fetal Interface'. *The Journal of Clinical Investigation* 124 (5): 1872–79. https://doi.org/10.1172/JCI68107.

Moreno-Nieves, Uriel Y., Joshua K. Tay, Saumyaa Saumyaa, et al. 2021. 'Landscape of Innate Lymphoid Cells in Human Head and Neck Cancer Reveals Divergent NK Cell States in the Tumor Microenvironment'. *Proceedings of the National Academy of Sciences of the United States of America* 118 (28): e2101169118. https://doi.org/10.1073/pnas.2101169118.

Morvan, Maelig G., and Lewis L. Lanier. 2016. 'NK Cells and Cancer: You Can Teach Innate Cells New Tricks'. *Nature Reviews Cancer* 16 (1): 7–19. https://doi.org/10.1038/nrc.2015.5.

Mueller, Scott N., and Laura K. Mackay. 2016. 'Tissue-Resident Memory T Cells: Local Specialists in Immune Defence'. *Nature Reviews Immunology* 16 (2): 2. https://doi.org/10.1038/nri.2015.3.

Muller, Marie, Vincent Haghnejad, Marion Schaefer, et al. 2022. 'The Immune Landscape of Human Pancreatic Ductal Carcinoma: Key Players, Clinical Implications, and Challenges'. *Cancers* 14 (4): 995. https://doi.org/10.3390/cancers14040995.

Nakajima, H., H. L. Park, and P. A. Henkart. 1995. 'Synergistic Roles of Granzymes A and B in Mediating Target Cell Death by Rat Basophilic Leukemia Mast Cell Tumors Also Expressing Cytolysin/Perforin.' *Journal of Experimental Medicine* 181 (3): 1037–46. https://doi.org/10.1084/jem.181.3.1037.

Natalini, Ambra, Sonia Simonetti, Gabriele Favaretto, et al. 2021. 'OMIP-079: Cell Cycle of CD4+ and CD8+ Naïve/Memory T Cell Subsets, and of Treg Cells from Mouse Spleen'. *Cytometry. Part A: The Journal of the International Society for Analytical Cytology* 99 (12): 1171–75. https://doi.org/10.1002/cyto.a.24509.

Naudin, Sabine, Molin Wang, Niki Dimou, et al. 2025. 'Alcohol Intake and Pancreatic Cancer Risk: An Analysis from 30 Prospective Studies across Asia, Australia, Europe, and North America'. *PLOS Medicine* 22 (5): e1004590. https://doi.org/10.1371/journal.pmed.1004590.

Neelapu, Sattva S., Frederick L. Locke, Nancy L. Bartlett, et al. 2017. 'Axicabtagene Ciloleucel CAR T-Cell Therapy in Refractory Large B-Cell Lymphoma'. *New England Journal of Medicine* 377 (26): 2531–44. https://doi.org/10.1056/NEJMoa1707447.

Niehrs, Annika, Laura Hertwig, Marcus Buggert, et al. 2025. 'Transient Tissue Residency and Lymphatic Egress Define Human CD56bright NK Cell Homeostasis'. *Nature Immunology* 26 (11): 2004–15. https://doi.org/10.1038/s41590-025-02290-9.

Niemi, Virginia, Douglas Gaskarth, and Roslyn A. Kemp. 2020. 'Extensive Variability in the Composition of Immune Infiltrate in Different Mouse Models of Cancer'. *Laboratory Animal Research* 36 (November): 43. https://doi.org/10.1186/s42826-020-00075-9.

Nose, Yohei, Takuro Saito, Kei Yamamoto, et al. 2023. 'The Tissue-Resident Marker CD103 on Peripheral Blood T Cells Predicts Responses to Anti-PD-1 Therapy in Gastric Cancer'. *Cancer Immunology, Immunotherapy: CII* 72 (1): 169–81. https://doi.org/10.1007/s00262-022-03240-2.

Ogasawara, Kouetsu, Jessica A. Hamerman, Lauren R. Ehrlich, et al. 2004. 'NKG2D Blockade Prevents Autoimmune Diabetes in NOD Mice'. *Immunity* 20 (6): 757–67. https://doi.org/10.1016/j.immuni.2004.05.008.

Oliphant, Christopher J., You Yi Hwang, Jennifer A. Walker, et al. 2014. 'MHCII-Mediated Dialog between Group 2 Innate Lymphoid Cells and CD4+ T Cells Potentiates Type 2 Immunity and Promotes Parasitic Helminth Expulsion'. *Immunity* 41 (2): 283–95. https://doi.org/10.1016/j.immuni.2014.06.016.

O'Reilly, Eileen M., Do-Youn Oh, Neesha Dhani, et al. 2019. 'Durvalumab With or Without Tremelimumab for Patients With Metastatic Pancreatic Ductal Adenocarcinoma: A Phase 2 Randomized Clinical Trial'. *JAMA Oncology* 5 (10): 1431–38. https://doi.org/10.1001/jamaoncol.2019.1588.

Ozmadenci, Duygu, Jayanth S. Shankara Narayanan, Jacob Andrew, et al. 2022. 'Tumor FAK Orchestrates Immunosuppression in Ovarian Cancer via the CD155/TIGIT Axis'. *Proceedings of the National Academy of Sciences* 119 (17): e2117065119. https://doi.org/10.1073/pnas.2117065119.

Pandha, H., A. Rigg, J. John, and N. Lemoine. 2007. 'Loss of Expression of Antigen-Presenting Molecules in Human Pancreatic Cancer and Pancreatic Cancer Cell Lines'. *Clinical and Experimental Immunology* 148 (1): 127–35. https://doi.org/10.1111/j.1365-2249.2006.03289.x.

Pardoll, Drew M. 2012. 'The Blockade of Immune Checkpoints in Cancer Immunotherapy'. *Nature Reviews. Cancer* 12 (4): 252–64. https://doi.org/10.1038/nrc3239.

Parham, Peter, and Ashley Moffett. 2013. 'Variable NK Cell Receptors and Their MHC Class I Ligands in Immunity, Reproduction and Human Evolution'. *Nature Reviews Immunology* 13 (2): 133–44. https://doi.org/10.1038/nri3370.

Parikh, Aparna R., Annamaria Szabolcs, Jill N. Allen, et al. 2021. 'Radiation Therapy Enhances Immunotherapy Response in Microsatellite Stable Colorectal and Pancreatic Adenocarcinoma in a Phase II Trial'. *Nature Cancer* 2 (11): 1124–35. https://doi.org/10.1038/s43018-021-00269-7.

Park, Lily M., Joanne Lannigan, Quentin Low, Maria C. Jaimes, and Diana L. Bonilla. 2024. 'OMIP-109: 45-Color Full Spectrum Flow Cytometry Panel for Deep Immunophenotyping of the Major Lineages Present in Human Peripheral Blood Mononuclear Cells with Emphasis on the T Cell Memory Compartment'. *Cytometry. Part A: The Journal of the International Society for Analytical Cytology* 105 (11): 807–15. https://doi.org/10.1002/cyto.a.24900.

Pauls, Katrin, Margarete Schön, Robert C. Kubitza, et al. 2001. 'Role of Integrin αE(CD103)B7 for Tissue-Specific Epidermal Localization of CD8+ T Lymphocytes'. *Journal of Investigative Dermatology* 117 (3): 569–75. https://doi.org/10.1046/j.0022-202x.2001.01481.x.

Peng, Hui, Xiaojun Jiang, Yonglin Chen, et al. 2013. 'Liver-Resident NK Cells Confer Adaptive Immunity in Skin-Contact Inflammation'. American Society for Clinical Investigation, April 1. https://doi.org/10.1172/JCI66381.

Peng, Hui, Lijin Li, Chong Zuo, et al. 2022. 'Combination TIGIT/PD-1 Blockade Enhances the Efficacy of Neoantigen Vaccines in a Model of Pancreatic Cancer'. *Frontiers in Immunology* 13 (December). https://doi.org/10.3389/fimmu.2022.1039226.

Permert, J., I. Ihse, L. Jorfeldt, H. von Schenck, H. J. Arnqvist, and J. Larsson. 1993. 'Pancreatic Cancer Is Associated with Impaired Glucose Metabolism'. *The European Journal of Surgery = Acta Chirurgica* 159 (2): 101–7.

Peterson. 2023. 'A Method of NIR Fluorescent Cell Labeling for in Vivo Cell Tracking.' *Revvity Application Note*. https://resources.revvity.com/pdfs/app-a-method-of-nir-fluorescent-cell-labeling-for-in-vivo-cell-tracking.pdf.

Pham, Thao N. D., Mario A. Shields, Christina Spaulding, et al. 2021. 'Preclinical Models of Pancreatic Ductal Adenocarcinoma and Their Utility in Immunotherapy Studies'. *Cancers* 13 (3): 440. https://doi.org/10.3390/cancers13030440.

Phillips, Phoebe. 2012. 'Pancreatic Stellate Cells and Fibrosis'. In *Pancreatic Cancer and Tumor Microenvironment*, edited by Paul J. Grippo and Hidayatullah G. Munshi. Transworld Research Network. http://www.ncbi.nlm.nih.gov/books/NBK98937/.

Polani, Faran, Patrick M. Grierson, and Kian-Huat Lim. 2021. 'Stroma-Targeting Strategies in Pancreatic Cancer: Past Lessons, Challenges and Prospects'. *World Journal of Gastroenterology* 27 (18): 2105–21. https://doi.org/10.3748/wjg.v27.i18.2105.

Pour, P., J. Althoff, F. W. Krüger, and U. Mohr. 1977. 'A Potent Pancreatic Carcinogen in Syrian Hamsters: N-Nitrosobis(2-Oxopropyl)Amine'. *Journal of the National Cancer Institute* 58 (5): 1449–53. https://doi.org/10.1093/jnci/58.5.1449.

Pouxvielh, Kévin, Marie Marotel, Annabelle Drouillard, et al. 2024. 'Tumor-Induced Natural Killer Cell Dysfunction Is a Rapid and Reversible Process Uncoupled from the Expression of Immune Checkpoints'. *Science Advances* 10 (35): eadn0164. https://doi.org/10.1126/sciadv.adn0164.

Probst, Hans Christian, Patrizia Stoitzner, Lukas Amon, et al. 2023. 'Guidelines for DC Preparation and Flow Cytometry Analysis of Mouse Nonlymphoid Tissues'. *European Journal of Immunology* 53 (11): 2249819. https://doi.org/10.1002/eji.202249819.

Purdy, Amanda K., and Kerry S. Campbell. 2009a. 'Natural Killer Cells and Cancer: Regulation by the Killer Cell Ig-like Receptors (KIR)'. *Cancer Biology & Therapy* 8 (23): 13–22. https://doi.org/10.4161/cbt.8.23.10455.

Purdy, Amanda K., and Kerry S. Campbell. 2009b. 'Natural Killer Cells and Cancer: Regulation by the Killer Cell Ig-like Receptors (KIR)'. *Cancer Biology & Therapy* 8 (23): 13–22. https://doi.org/10.4161/cbt.8.23.10455.

Pylayeva-Gupta, Yuliya, Kyoung Eun Lee, Cristina H. Hajdu, George Miller, and Dafna Bar-Sagi. 2012. 'Oncogenic Kras-Induced GM-CSF Production Promotes the Development of Pancreatic Neoplasia'. *Cancer Cell* 21 (6): 836–47. https://doi.org/10.1016/j.ccr.2012.04.024.

Qiu, Wanglong, and Gloria H. Su. 2013. 'Development of Orthotopic Pancreatic Tumor Mouse Models'. *Methods in Molecular Biology (Clifton, N.J.)* 980: 215–23. https://doi.org/10.1007/978-1-62703-287-2_11.

Quinn, E., N. Hawkins, Y. L. Yip, C. Suter, and R. Ward. 2003. 'CD103+ Intraepithelial Lymphocytes--a Unique Population in Microsatellite Unstable Sporadic Colorectal Cancer'. *European Journal of Cancer (Oxford, England: 1990)* 39 (4): 469–75. https://doi.org/10.1016/s0959-8049(02)00633-0.

Rahib, Lola, Benjamin D. Smith, Rhonda Aizenberg, Allison B. Rosenzweig, Julie M. Fleshman, and Lynn M. Matrisian. 2014. 'Projecting Cancer Incidence and Deaths to 2030: The Unexpected Burden of Thyroid, Liver, and Pancreas Cancers in the United States'. *Cancer Research* 74 (11): 2913–21. https://doi.org/10.1158/0008-5472.CAN-14-0155.

Raulet, David H. 2003. 'Roles of the NKG2D Immunoreceptor and Its Ligands'. *Nature Reviews Immunology* 3 (10): 781–90. https://doi.org/10.1038/nri1199.

Rawla, Prashanth, Tagore Sunkara, and Vinaya Gaduputi. 2019. 'Epidemiology of Pancreatic Cancer: Global Trends, Etiology and Risk Factors'. *World Journal of Oncology* 10 (1): 10–27. https://doi.org/10.14740/wjon1166.

Rebuffet, Lucas, Janine E. Melsen, Bertrand Escalière, et al. 2024. 'High-Dimensional Single-Cell Analysis of Human Natural Killer Cell Heterogeneity'. *Nature Immunology*, July 2, 1–15. https://doi.org/10.1038/s41590-024-01883-0.

Reck, Martin, Delvys Rodríguez-Abreu, Andrew G. Robinson, et al. 2016. 'Pembrolizumab versus Chemotherapy for PD-L1-Positive Non-Small-Cell Lung Cancer'. *The New England Journal of Medicine* 375 (19): 1823–33. https://doi.org/10.1056/NEJMoa1606774.

Renouf, Daniel J., Jonathan M. Loree, Jennifer J. Knox, et al. 2022. 'The CCTG PA.7 Phase II Trial of Gemcitabine and Nab-Paclitaxel with or without Durvalumab and Tremelimumab as Initial Therapy in Metastatic Pancreatic Ductal Adenocarcinoma'. *Nature Communications* 13 (1): 5020. https://doi.org/10.1038/s41467-022-32591-8.

Rio, Maria-Luisa del, Jose-Ignacio Rodriguez-Barbosa, Elisabeth Kremmer, and Reinhold Förster. 2007. 'CD103- and CD103+ Bronchial Lymph Node Dendritic Cells Are Specialized in Presenting and Cross-Presenting Innocuous Antigen to CD4+ and CD8+ T Cells'. *Journal of Immunology* (Baltimore, Md. : 1950) 178 (11): 6861–66. https://doi.org/10.4049/jimmunol.178.11.6861.

Rittmeyer, Achim, Fabrice Barlesi, Daniel Waterkamp, et al. 2017. 'Atezolizumab versus Docetaxel in Patients with Previously Treated Non-Small-Cell Lung Cancer (OAK): A Phase 3, Open-Label, Multicentre Randomised Controlled Trial'. *Lancet* (London, England) 389 (10066): 255–65. https://doi.org/10.1016/S0140-6736(16)32517-X.

Robert, Caroline, Georgina V. Long, Benjamin Brady, et al. 2015. 'Nivolumab in Previously Untreated Melanoma without BRAF Mutation'. *New England Journal of Medicine* 372 (4): 320–30. https://doi.org/10.1056/NEJMoa1412082.

Roberts, A. I., R. E. Brolin, and E. C. Ebert. 1999. 'Integrin Alpha1beta1 (VLA-1) Mediates Adhesion of Activated Intraepithelial Lymphocytes to Collagen'. *Immunology* 97 (4): 679–85. https://doi.org/10.1046/j.1365-2567.1999.00812.x.

Roberts, Edward W., Miranda L. Broz, Mikhail Binnewies, et al. 2016. 'Critical Role for CD103+/CD141+ Dendritic Cells Bearing CCR7 for Tumor Antigen Trafficking and Priming of T Cell Immunity in Melanoma'. *Cancer Cell* 30 (2): 324–36. https://doi.org/10.1016/j.ccell.2016.06.003.

Robertson, Michael J. 2002. 'Role of Chemokines in the Biology of Natural Killer Cells'. *Journal of Leukocyte Biology* 71 (2): 173–83.

Robinson, William A. 1974. 'Granulocytosis in Neoplasia'. *Annals of the New York Academy of Sciences* 230 (1): 212–18. https://doi.org/10.1111/j.1749-6632.1974.tb14451.x.

Roche, Paul A., and Kazuyuki Furuta. 2015. 'The Ins and Outs of MHC Class II-Mediated Antigen Processing and Presentation'. *Nature Reviews Immunology* 15 (4): 203–16. https://doi.org/10.1038/nri3818.

Rose, Shawn, Alexander Misharin, and Harris Perlman. 2012. 'A Novel Ly6C/Ly6G-Based Strategy to Analyze the Mouse Splenic Myeloid Compartment'. *Cytometry Part A* 81A (4): 343–50. https://doi.org/10.1002/cyto.a.22012.

Rosenberg, Steven A., Nicholas P. Restifo, James C. Yang, Richard A. Morgan, and Mark E. Dudley. 2008. 'Adoptive Cell Transfer: A Clinical Path to Effective Cancer Immunotherapy'. *Nature Reviews. Cancer* 8 (4): 299–308. https://doi.org/10.1038/nrc2355.

Royal, Richard E., Catherine Levy, Keli Turner, et al. 2010. 'Phase 2 Trial of Single Agent Ipilimumab (Anti-CTLA-4) for Locally Advanced or Metastatic Pancreatic Adenocarcinoma'. *Journal of Immunotherapy* 33 (8): 828. https://doi.org/10.1097/CJI.0b013e3181eec14c.

Roychoudhuri, Rahul, Robert L. Eil, and Nicholas P. Restifo. 2015. 'The Interplay of Effector and Regulatory T Cells in Cancer'. *Current Opinion in Immunology*, Lymphocyte development and activation * Tumour immunology, vol. 33 (April): 101–11. https://doi.org/10.1016/j.coi.2015.02.003.

Ryan, David P., Theodore S. Hong, and Nabeel Bardeesy. 2014. 'Pancreatic Adenocarcinoma'. *New England Journal of Medicine* 371 (11): 1039–49. https://doi.org/10.1056/NEJMra1404198.

Sadr-Azodi, Omid, Viktor Oskarsson, Andrea Discacciati, Per Videhult, Johan Askling, and Anders Ekbom. 2018. 'Pancreatic Cancer Following Acute Pancreatitis: A Population-Based Matched Cohort Study'. *Official Journal of the American College of Gastroenterology | ACG* 113 (11): 1711. https://doi.org/10.1038/s41395-018-0255-9.

Sagebiel, Adrian F., Fenja Steinert, Sebastian Lunemann, et al. 2019. 'Tissue-Resident Eomes+ NK Cells Are the Major Innate Lymphoid Cell Population in Human Infant Intestine'. *Nature Communications* 10 (1): 975. https://doi.org/10.1038/s41467-018-08267-7.

Sakamoto, Naoyuki, Takeshi Ishikawa, Satoshi Kokura, et al. 2015. 'Phase I Clinical Trial of Autologous NK Cell Therapy Using Novel Expansion Method in Patients with Advanced Digestive Cancer'. *Journal of Translational Medicine* 13 (August): 277. https://doi.org/10.1186/s12967-015-0632-8.

Sakuishi, Kaori, Lionel Apetoh, Jenna M. Sullivan, Bruce R. Blazar, Vijay K. Kuchroo, and Ana C. Anderson. 2010. 'Targeting Tim-3 and PD-1 Pathways to Reverse T Cell Exhaustion and Restore Anti-Tumor Immunity'. *The Journal of Experimental Medicine* 207 (10): 2187–94. https://doi.org/10.1084/jem.20100643.

Salmon, Hélène, Juliana Idoyaga, Adeeb Rahman, et al. 2016. 'Expansion and Activation of CD103+ Dendritic Cell Progenitors at the Tumor Site Enhances Tumor Responses to Therapeutic PD-L1 and BRAF Inhibition'. *Immunity* 44 (4): 924–38. https://doi.org/10.1016/j.immuni.2016.03.012.

Sanos, Stephanie L., Viet L. Bui, Arthur Mortha, et al. 2009. 'RORγt and Commensal Microflora Are Required for the Differentiation of Mucosal Interleukin 22–Producing NKp46+ Cells'. *Nature Immunology* 10 (1): 83–91. https://doi.org/10.1038/ni.1684.

Santis, Ana G., Miguel R. Campanero, Jose L. Alonso, et al. 1992. 'Tumor Necrosis Factor-α Production Induced in T Lymphocytes through the AIM/CD69 Activation Pathway'. *European Journal of Immunology* 22 (5): 1253–59. https://doi.org/10.1002/eji.1830220521.

Saxena, Mansi, Sjoerd H. van der Burg, Cornelis J. M. Melief, and Nina Bhardwaj. 2021. 'Therapeutic Cancer Vaccines'. *Nature Reviews Cancer* 21 (6): 360–78. https://doi.org/10.1038/s41568-021-00346-0.

Schneble, Erika J., John S. Berry, Francois A. Trappey, et al. 2014. 'The HER2 Peptide Nelipepimut-S (E75) Vaccine (NeuVax™) in Breast Cancer Patients at Risk for Recurrence: Correlation of Immunologic Data with Clinical Response'. *Immunotherapy* 6 (5): 519–31. https://doi.org/10.2217/imt.14.22.

Sender, Ron, Yarden Weiss, Yoav Navon, et al. 2023. 'The Total Mass, Number, and Distribution of Immune Cells in the Human Body'. *Proceedings of the National Academy of Sciences* 120 (44): e2308511120. https://doi.org/10.1073/pnas.2308511120.

Serafini, Nicolas, Christian A. J. Vosshenrich, and James P. Di Santo. 2015. 'Transcriptional Regulation of Innate Lymphoid Cell Fate'. *Nature Reviews Immunology* 15 (7): 415–28. https://doi.org/10.1038/nri3855.

Serrels, Alan, Tom Lund, Bryan Serrels, et al. 2015. 'Nuclear FAK Controls Chemokine Transcription, Tregs, and Evasion of Anti-Tumor Immunity'. *Cell* 163 (1): 160–73. https://doi.org/10.1016/j.cell.2015.09.001.

Serreze, David V., and Edward H. Leiter. 1994. 'Genetic and Pathogenic Basis of Autoimmune Diabetes in NOD Mice'. *Current Opinion in Immunology* 6 (6): 900–906. https://doi.org/10.1016/0952-7915(94)90011-6.

Sert, Nathalie Percie du, Amrita Ahluwalia, Sabina Alam, et al. 2020. 'Reporting Animal Research: Explanation and Elaboration for the ARRIVE Guidelines 2.0'. *PLOS Biology* 18 (7): e3000411. https://doi.org/10.1371/journal.pbio.3000411.

Sethna, Zachary, Pablo Guasp, Charlotte Reiche, et al. 2025. 'RNA Neoantigen Vaccines Prime Long-Lived CD8+ T Cells in Pancreatic Cancer'. *Nature* 639 (8056): 1042–51. https://doi.org/10.1038/s41586-024-08508-4.

Shi, L., R. P. Kraut, R. Aebersold, and A. H. Greenberg. 1992. 'A Natural Killer Cell Granule Protein That Induces DNA Fragmentation and Apoptosis.' *Journal of Experimental Medicine* 175 (2): 553–66. https://doi.org/10.1084/jem.175.2.553.

Shiow, Lawrence R., David B. Rosen, Nadezda Brdicková, et al. 2006. 'CD69 Acts Downstream of Interferon-Alpha/Beta to Inhibit S1P1 and Lymphocyte Egress from Lymphoid Organs'. *Nature* 440 (7083): 540–44. https://doi.org/10.1038/nature04606.

Singh, Santosh Kumar, Manoj K. Mishra, Isam-Eldin A. Eltoum, Sejong Bae, James W. Lillard, and Rajesh Singh. 2018. 'CCR5/CCL5 Axis Interaction Promotes Migratory and Invasiveness of Pancreatic Cancer Cells'. *Scientific Reports* 8 (1): 1323. https://doi.org/10.1038/s41598-018-19643-0.

Sivakumar, Shivan, Enas Abu-Shah, David J. Ahern, et al. 2021. 'Activated Regulatory T-Cells, Dysfunctional and Senescent T-Cells Hinder the Immunity in Pancreatic Cancer'. *Cancers* 13 (8): 1776. https://doi.org/10.3390/cancers13081776.

Skak, Kresten, Klaus Stensgaard Frederiksen, and Dorthe Lundsgaard. 2008. 'Interleukin-21 Activates Human Natural Killer Cells and Modulates Their Surface Receptor Expression'. *Immunology* 123 (4): 575–83. https://doi.org/10.1111/j.1365-2567.2007.02730.x.

Slattery, Karen, Cong-Hui Yao, Eimear Mylod, et al. 2025. 'Uptake of Lipids from Ascites Drives NK Cell Metabolic Dysfunction in Ovarian Cancer'. *Science Immunology* 10 (107): eadr4795. https://doi.org/10.1126/sciimmunol.adr4795.

Smyth, Mark J., Erika Cretney, Kazuyoshi Takeda, et al. 2001. 'Tumor Necrosis Factor–Related Apoptosis-Inducing Ligand (Trail) Contributes to Interferon γ–Dependent Natural Killer Cell Protection from Tumor Metastasis'. *The Journal of Experimental Medicine* 193 (6): 661–70. https://doi.org/10.1084/jem.193.6.661.

Sojka, Dorothy K., Beatrice Plougastel-Douglas, Liping Yang, et al. 2014. 'Tissue-Resident Natural Killer (NK) Cells Are Cell Lineages Distinct from Thymic and Conventional Splenic NK Cells'. *eLife* 3 (April): e01659. https://doi.org/10.7554/eLife.01659.

Song, Shanshan, Baosheng Wang, Xin Zhang, et al. 2015. 'Long-Term Diabetes Mellitus Is Associated with an Increased Risk of Pancreatic Cancer: A Meta-Analysis'. *PloS One* 10 (7): e0134321. https://doi.org/10.1371/journal.pone.0134321.

Sparano, Colin, Darío Solís-Sayago, Nathan Sébastien Zangger, et al. 2024. 'Autocrine TGF-B1 Drives Tissue-Specific Differentiation and Function of Resident NK Cells'. *Journal of Experimental Medicine* 222 (3): e20240930. https://doi.org/10.1084/jem.20240930.

Sparano, Colin, Darío Solís-Sayago, Nathan Sébastien Zangger, et al. 2025. 'Autocrine TGF-B1 Drives Tissue-Specific Differentiation and Function of Resident NK Cells'. *Journal of Experimental Medicine* 222 (3). https://doi.org/10.1084/jem.20240930.

Spear, Sarah, Juliana B. Candido, Jacqueline R. McDermott, et al. 2019. 'Discrepancies in the Tumor Microenvironment of Spontaneous and Orthotopic Murine Models of Pancreatic Cancer Uncover a New Immunostimulatory Phenotype for B Cells'. *Frontiers in Immunology* 10 (March). https://doi.org/10.3389/fimmu.2019.00542.

Speiser, Daniel E., Obinna Chijioke, Karin Schaeuble, and Christian Münz. 2023. 'CD4+ T Cells in Cancer'. *Nature Cancer* 4 (3): 317–29. https://doi.org/10.1038/s43018-023-00521-2.

Spits, Hergen, Jochem H. Bernink, and Lewis Lanier. 2016. 'NK Cells and Type 1 Innate Lymphoid Cells: Partners in Host Defense'. *Nature Immunology* 17 (7): 758–64. https://doi.org/10.1038/ni.3482.

Stanietsky, Noa, Hrvoje Simic, Jurica Arapovic, et al. 2009. 'The Interaction of TIGIT with PVR and PVRL2 Inhibits Human NK Cell Cytotoxicity'. *Proceedings of the National Academy of Sciences* 106 (42): 17858–63. https://doi.org/10.1073/pnas.0903474106.

Steele, Nina G., Eileen S. Carpenter, Samantha B. Kemp, et al. 2020. 'Multimodal Mapping of the Tumor and Peripheral Blood Immune Landscape in Human Pancreatic Cancer'. *Nature Cancer* 1 (11): 11. https://doi.org/10.1038/s43018-020-00121-4.

Stokes, Jayme B., Sara J. Adair, Jill K. Slack-Davis, et al. 2011. 'Inhibition of Focal Adhesion Kinase by PF-562,271 Inhibits the Growth and Metastasis of Pancreatic Cancer Concomitant with Altering the Tumor Microenvironment'. *Molecular Cancer Therapeutics* 10 (11): 2135–45. https://doi.org/10.1158/1535-7163.MCT-11-0261.

Street, Shayna E. A., Erika Cretney, and Mark J. Smyth. 2001. 'Perforin and Interferon-γ Activities Independently Control Tumor Initiation, Growth, and Metastasis'. *Blood* 97 (1): 192–97. https://doi.org/10.1182/blood.V97.1.192.

Sudan, Raki, Susan Gilfillan, and Marco Colonna. 2024. 'Group 1 ILCs: Heterogeneity, Plasticity, and Transcriptional Regulation'. *Immunological Reviews* 323 (1): 107–17. https://doi.org/10.1111/imr.13327.

Sun, Cheng, Hao-yu Sun, Wei-hua Xiao, Cai Zhang, and Zhi-gang Tian. 2015. 'Natural Killer Cell Dysfunction in Hepatocellular Carcinoma and NK Cell-Based Immunotherapy'. *Acta Pharmacologica Sinica* 36 (10): 1191–99. https://doi.org/10.1038/aps.2015.41.

Sun, Haoyu, Lianxin Liu, Qiang Huang, et al. 2019. 'Accumulation of Tumor-Infiltrating CD49a+ NK Cells Correlates with Poor Prognosis for Human Hepatocellular Carcinoma'. *Cancer Immunology Research* 7 (9): 1535–46. https://doi.org/10.1158/2326-6066.CIR-18-0757.

Sung, Hyuna, Jacques Ferlay, Rebecca L. Siegel, et al. 2021. 'Global Cancer Statistics 2020: GLOBOCAN Estimates of Incidence and Mortality Worldwide for 36 Cancers in 185 Countries'. *CA: A Cancer Journal for Clinicians* 71 (3): 209–49. https://doi.org/10.3322/caac.21660.

Syed, Jihad, Jack Ashton, Jesuchristopher Joseph, et al. 2019. 'Multiplex Immunohistochemistry: The Importance of Staining Order When Producing a Validated Protocol'. *Immunotherapy: Open Access* 5 (2): 1–9.

Tang, Fei, Jinhu Li, Lu Qi, et al. 2023. 'A Pan-Cancer Single-Cell Panorama of Human Natural Killer Cells'. *Cell* 0 (0). https://doi.org/10.1016/j.cell.2023.07.034.

Tarannum, Mubin, Khanhlinh Dinh, Juliana Vergara, et al. 2024. 'CAR Memory–like NK Cells Targeting the Membrane Proximal Domain of Mesothelin Demonstrate Promising Activity in Ovarian Cancer'. *Science Advances* 10 (28): eadn0881. https://doi.org/10.1126/sciadv.adn0881.

Tessmer, Marlowe S., Emma C. Reilly, and Laurent Brossay. 2011. 'Salivary Gland NK Cells Are Phenotypically and Functionally Unique'. *PLOS Pathogens* 7 (1): e1001254. https://doi.org/10.1371/journal.ppat.1001254.

Torcellan, Tommaso, Christin Friedrich, Rémi Doucet-Ladevèze, et al. 2024. 'Circulating NK Cells Establish Tissue Residency upon Acute Infection of Skin and Mediate Accelerated Effector Responses to Secondary Infection'. *Immunity* 57 (1): 124-140.e7. https://doi.org/10.1016/j.immuni.2023.11.018.

Torelli, Giovanni Fernando, Sabina Chiaretti, Nadia Peragine, et al. 2022. 'Repeated Infusions of Escalating Doses of Expanded and Activated Autologous Natural Killer Cells in Minimal Residual Disease-Positive Ph+ Acute Lymphoblastic Leukemia Patients. A GIMEMA Phase 1 Trial'. *American Journal of Hematology* 97 (6): E204–7. https://doi.org/10.1002/ajh.26537.

Trovato, Rosalinda, Alessandra Fiore, Sara Sartori, et al. 2019. 'Immunosuppression by Monocytic Myeloid-Derived Suppressor Cells in Patients with Pancreatic Ductal Carcinoma Is Orchestrated by STAT3'. *Journal for ImmunoTherapy of Cancer* 7 (1). https://doi.org/10.1186/s40425-019-0734-6.

Tumeh, Paul C., Christina L. Harview, Jennifer H. Yearley, et al. 2014. 'PD-1 Blockade Induces Responses by Inhibiting Adaptive Immune Resistance'. *Nature* 515 (7528): 568–71. https://doi.org/10.1038/nature13954.

Ulrich, Alexis B., Jens Standop, Bruno M. Schmied, Matthias B. Schneider, Terence A. Lawson, and Parviz M. Pour. 2002. 'Expression of Drug-Metabolizing Enzymes in the Pancreas of

Hamster, Mouse, and Rat, Responding Differently to the Pancreatic Carcinogenicity of BOP'. *Pancreatology* 2 (6): 519–27. https://doi.org/10.1159/000066094.

Valenzano, Giampiero, Shannon N. Russell, Simei Go, Eric O'Neill, and Keaton I. Jones. 2024. 'Using Spectral Flow Cytometry to Characterize Anti-Tumor Immunity in Orthotopic and Subcutaneous Mouse Models of Cancer'. *Current Protocols* 4 (10): e70032. https://doi.org/10.1002/cpz1.70032.

Van Gassen, Sofie, Britt Callebaut, Mary J. Van Helden, et al. 2015. 'FlowSOM: Using Self-Organizing Maps for Visualization and Interpretation of Cytometry Data'. *Cytometry Part A* 87 (7): 636–45. https://doi.org/10.1002/cyto.a.22625.

Veglia, Filippo, Emilio Sanseviero, and Dmitry I. Gabrilovich. 2021. 'Myeloid-Derived Suppressor Cells in the Era of Increasing Myeloid Cell Diversity'. *Nature Reviews Immunology* 21 (8): 485–98. https://doi.org/10.1038/s41577-020-00490-y.

Victorino, Francisco, Dorothy K. Sojka, Kelley S. Brodsky, et al. 2015. 'Tissue-Resident NK Cells Mediate Ischemic Kidney Injury and Are Not Depleted by Anti–Asialo-GM1 Antibody'. *The Journal of Immunology* 195 (10): 4973–85. https://doi.org/10.4049/jimmunol.1500651.

Viel, Sébastien, Antoine Marçais, Fernando Souza-Fonseca Guimaraes, et al. 2016. 'TGF-β Inhibits the Activation and Functions of NK Cells by Repressing the mTOR Pathway'. *Science Signaling* 9 (415): ra19. https://doi.org/10.1126/scisignal.aad1884.

Vilches, Carlos, and Peter Parham. 2002. 'KIR: Diverse, Rapidly Evolving Receptors of Innate and Adaptive Immunity'. *Annual Review of Immunology* 20 (Volume 20, 2002): 217–51. https://doi.org/10.1146/annurev.immunol.20.092501.134942.

Visser, Karin E. de, and Johanna A. Joyce. 2023. 'The Evolving Tumor Microenvironment: From Cancer Initiation to Metastatic Outgrowth'. *Cancer Cell* 41 (3): 374–403. https://doi.org/10.1016/j.ccell.2023.02.016.

Walsh, Daniel A., Henrique Borges da Silva, Lalit K. Beura, et al. 2019. 'The Functional Requirement for CD69 in Establishment of Resident Memory CD8+ T Cells Varies with Tissue Location'. *Journal of Immunology (Baltimore, Md. : 1950)* 203 (4): 946–55. https://doi.org/10.4049/jimmunol.1900052.

Walzer, Thierry, Mathieu Bléry, Julie Chaix, et al. 2007. 'Identification, Activation, and Selective in Vivo Ablation of Mouse NK Cells via NKp46'. *Proceedings of the National Academy of Sciences of the United States of America* 104 (9): 3384–89. https://doi.org/10.1073/pnas.0609692104.

Walzer, Thierry, Sébastien Jaeger, Julie Chaix, and Eric Vivier. 2007. 'Natural Killer Cells: From CD3(-)NKp46(+) to Post-Genomics Meta-Analyses'. *Current Opinion in Immunology* 19 (3): 365–72. https://doi.org/10.1016/j.coi.2007.04.004.

Wang, Jian, Fengqi Li, Meijuan Zheng, Rui Sun, Haiming Wei, and Zhigang Tian. 2012. 'Lung Natural Killer Cells in Mice: Phenotype and Response to Respiratory Infection'. *Immunology* 137 (1): 37–47. https://doi.org/10.1111/j.1365-2567.2012.03607.x.

Wang, Xiaowei, Jun Gao, Yan Ren, et al. 2011. 'Detection of KRAS Gene Mutations in Endoscopic Ultrasound-Guided Fine-Needle Aspiration Biopsy for Improving Pancreatic Cancer Diagnosis'. *The American Journal of Gastroenterology* 106 (12): 2104–11. https://doi.org/10.1038/ajg.2011.281.

Wang, Yifan, Weiye Deng, Nan Li, et al. 2018. 'Combining Immunotherapy and Radiotherapy for Cancer Treatment: Current Challenges and Future Directions'. *Frontiers in Pharmacology* 9 (March). https://doi.org/10.3389/fphar.2018.00185.

Wang-Gillam, Andrea, Kian-Huat Lim, Robert McWilliams, et al. 2022. 'Defactinib, Pembrolizumab, and Gemcitabine in Patients with Advanced Treatment Refractory Pancreatic Cancer: A Phase I Dose Escalation and Expansion Study'. *Clinical Cancer Research* 28 (24): 5254–62. https://doi.org/10.1158/1078-0432.CCR-22-0308.

Weber, Jeffrey S., Matteo S. Carlino, Adnan Khattak, et al. 2024. 'Individualised Neoantigen Therapy mRNA-4157 (V940) plus Pembrolizumab versus Pembrolizumab Monotherapy in Resected Melanoma (KEYNOTE-942): A Randomised, Phase 2b Study'. *Lancet* (London, England) 403 (10427): 632–44. https://doi.org/10.1016/S0140-6736(23)02268-7.

Weiss, Glen J., Jordan Waypa, Lisa Blaydorn, et al. 2017. 'A Phase Ib Study of Pembrolizumab plus Chemotherapy in Patients with Advanced Cancer (PembroPlus)'. *British Journal of Cancer* 117 (1): 33–40. https://doi.org/10.1038/bjc.2017.145.

Willenbrock, Frances, Catrin M. Cox, Eileen E. Parkes, et al. 2021. 'Circulating Biomarkers and Outcomes from a Randomised Phase 2 Trial of Gemcitabine versus Capecitabine-Based Chemoradiotherapy for Pancreatic Cancer'. *British Journal of Cancer* 124 (3): 581–86. https://doi.org/10.1038/s41416-020-01120-z.

Wolf, Natalie K., Djem U. Kissiov, and David H. Raulet. 2023. 'Roles of Natural Killer Cells in Immunity to Cancer, and Applications to Immunotherapy'. *Nature Reviews Immunology* 23 (2): 90–105. https://doi.org/10.1038/s41577-022-00732-1.

Xie, Changqing, Austin G. Duffy, Gagandeep Brar, et al. 2020. 'Immune Checkpoint Blockade in Combination with Stereotactic Body Radiotherapy in Patients with Metastatic Pancreatic Ductal Adenocarcinoma'. *Clinical Cancer Research : An Official Journal of the American Association for Cancer Research* 26 (10): 2318–26. https://doi.org/10.1158/1078-0432.CCR-19-3624.

Xu, W., G. Birch, A. Meliki, et al. 2025. 'Progressive Natural Killer Cell Dysfunction in Advanced-Stage Clear-Cell Renal Cell Carcinoma and Association with Clinical Outcomes'. *ESMO Open* 10 (2). https://doi.org/10.1016/j.esmoop.2024.104105.

Yamamoto, Keisuke, Anthony Venida, Julian Yano, et al. 2020. 'Autophagy Promotes Immune Evasion of Pancreatic Cancer by Degrading MHC-I'. *Nature* 581 (7806): 100–105. https://doi.org/10.1038/s41586-020-2229-5.

Yamazaki, Chihiro, Masanaka Sugiyama, Tomokazu Ohta, et al. 2013. 'Critical Roles of a Dendritic Cell Subset Expressing a Chemokine Receptor, XCR1'. *Journal of Immunology* (Baltimore, Md. : 1950) 190 (12): 6071–82. https://doi.org/10.4049/jimmunol.1202798.

Yang, Baibing, Joy M. Davis, Thomas H. Gomez, et al. 2021. 'Characteristic Pancreatic and Splenic Immune Cell Infiltration Patterns in Mouse Acute Pancreatitis'. *Cell & Bioscience* 11 (1): 28. https://doi.org/10.1186/s13578-021-00544-1.

Yokoyama, Wayne M., Marcus Altfeld, and Katharine C. Hsu. 2010. 'Natural Killer Cells: Tolerance to Self and Innate Immunity to Viral Infection and Malignancy'. *Biology of Blood and Marrow Transplantation : Journal of the American Society for Blood and Marrow Transplantation* 16 (1 0): S97–105. https://doi.org/10.1016/j.bbmt.2009.10.009.

Youn, Je-In, Srinivas Nagaraj, Michelle Collazo, and Dmitry I. Gabrilovich. 2008. 'Subsets of Myeloid-Derived Suppressor Cells in Tumor-Bearing Mice'. *Journal of Immunology (Baltimore, Md.: 1950)* 181 (8): 5791–802. https://doi.org/10.4049/jimmunol.181.8.5791.

Yu, Min, Renguo Guan, Weifeng Hong, et al. 2019. '<p>Prognostic Value of Tumor-Associated Macrophages in Pancreatic Cancer: A Meta-Analysis</P>'. *Cancer Management and Research* 11 (May): 4041–58. https://doi.org/10.2147/CMAR.S196951.

Zaghdoudi, Sonia, Emilie Decaup, Ismahane Belhabib, et al. 2020. 'FAK Activity in Cancer-associated Fibroblasts Is a Prognostic Marker and a Druggable Key Metastatic Player in Pancreatic Cancer'. *EMBO Molecular Medicine* 12 (11): e12010. https://doi.org/10.15252/emmm.202012010.

Zecca, Alessandra, Valeria Barili, Danila Rizzo, et al. 2021. 'Intratumor Regulatory Noncytotoxic NK Cells in Patients with Hepatocellular Carcinoma'. *Cells* 10 (3): 614. https://doi.org/10.3390/cells10030614.

Zeng, Juan, Lu Zhang, Shiqi Ma, et al. 2024. 'Dysregulation of Peripheral and Intratumoral KLRG1+ CD8+ *T* Cells Is Associated with Immune Evasion in Patients with Non-Small-Cell Lung Cancer'. *Translational Oncology* 45 (July): 101968. https://doi.org/10.1016/j.tranon.2024.101968.

Zhang, Angela L., Paula Colmenero, Ulrich Purath, et al. 2007. 'Natural Killer Cells Trigger Differentiation of Monocytes into Dendritic Cells'. *Blood* 110 (7): 2484–93. https://doi.org/10.1182/blood-2007-02-076364.

Zhao, Jiangang, Hans A. Schlößer, Zhefang Wang, et al. 2019. 'Tumor-Derived Extracellular Vesicles Inhibit Natural Killer Cell Function in Pancreatic Cancer'. *Cancers* 11 (6): 874. https://doi.org/10.3390/cancers11060874.

Zhen, David Bing, Martin Whittle, Paul S. Ritch, et al. 2022. 'Phase II Study of PEGPH20 plus Pembrolizumab for Patients (Pts) with Hyaluronan (HA)-High Refractory Metastatic Pancreatic Adenocarcinoma (mPC): PCRT16-001.' *Journal of Clinical Oncology* 40 (4_suppl): 576–576. https://doi.org/10.1200/JCO.2022.40.4_suppl.576.

Zhu, Yu, John M. Herndon, Dorothy K. Sojka, et al. 2017. 'Tissue Resident Macrophages in Pancreatic Ductal Adenocarcinoma Originate from Embryonic Hematopoiesis and Promote Tumor Progression'. *Immunity* 47 (2): 323-338.e6. https://doi.org/10.1016/j.immuni.2017.07.014.

Zhu, Yu, Brett L. Knolhoff, Melissa A. Meyer, et al. 2014. 'CSF1/CSF1R Blockade Reprograms Tumor-Infiltrating Macrophages and Improves Response to T-Cell Checkpoint Immunotherapy in Pancreatic Cancer Models'. *Cancer Research* 74 (18): 5057–69. https://doi.org/10.1158/0008-5472.CAN-13-3723.

Zinger, Assaf, Lilach Koren, Omer Adir, et al. 2019. 'Collagenase Nanoparticles Enhance the Penetration of Drugs into Pancreatic Tumors'. *ACS Nano* 13 (10): 11008–21. https://doi.org/10.1021/acsnano.9b02395.